Mechanisms of Ventricular Fibrillation

The role of mechano-electrical feedback
and tissue heterogeneity

Rikkert Keldermann

Omslag Rikkert Keldermann
Druk Ipskamp Drukkers B.V.
ISBN 978-90-393-5020-1

Mechanisms of Ventricular Fibrillation

The role of mechano-electrical feedback
and tissue heterogeneity

Mechanismen van Ventrikelfibrilleren

De rol van mechano-elektrische terugkoppeling
en weefselheterogeniteit

(met een samenvatting in het Nederlands)

Proefschrift

ter verkrijging van de graad van doctor aan de Universiteit Utrecht
op gezag van de rector magnificus, prof. dr. J. C. Stoof,
ingevolge het besluit van het college voor promoties
in het openbaar te verdedigen op
dinsdag 31 maart 2009 des middags te 2.30 uur.

door

Rik Hubert Keldermann

geboren op 9 april 1980
te Heerlen

Promotor:
Prof. dr. P. Hogeweg

Co-Promotor:
Dr. A.V. Panfilov

The studies described in this thesis were financially supported by the Netherlands Organisation for Scientific Research (NWO) through grant number 814.02.014 of the Earth and Life Sciences program.

Ter herinnering aan onze moeders, Loes en Nelline

Contents

CHAPTER 1

Introduction

The heart is a muscular organ that pumps blood throughout the body. The human heart contracts approximately once per second, adding up to more than 2.5 billion contractions over 80 years. Failure in cardiac contraction leads to sudden cardiac death, which is one of the most common causes of death in the industrialized world. In most cases this is caused by ventricular fibrillation (VF) [31, 202]. During VF turbulent excitation patterns occur, causing uncoordinated contraction of the ventricles. If VF is not halted by means of defibrillation, blood circulation will cease, causing cardiac death within minutes.

One important tool to study the mechanisms underlying cardiac physiology, is mathematical modeling. Over the last decades mathematical models ranging from single cell dynamics to complex three-dimensional whole organ models have been used to study cardiac arrhythmias. The focus of this thesis is to gain more insight in the underlying mechanisms of VF using electrophysiological and mechanical models of the human heart. We are especially interested in mechano-electrical feedback and in the role of tissue heterogeneity in the onset of cardiac arrhythmias.

As a general introduction in this thesis we briefly discuss in this chapter the anatomy of the human heart, the underlying electrophysiological and mechanical processes, and their feedback mechanisms. Next, we provide basic information on cardiac arrhythmias and discuss their mechanisms. We then focus on modeling cardiac arrhythmias. At the end we provide a short outline of the modeling studies described in this thesis.

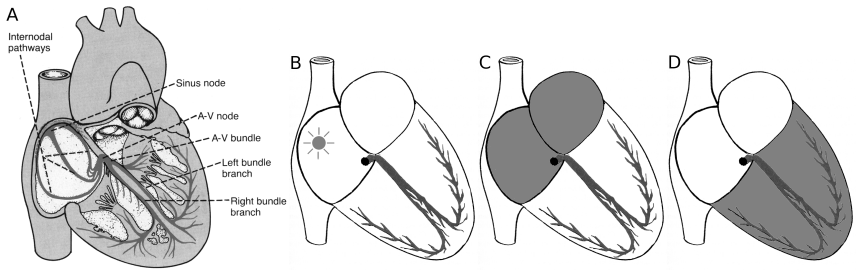

Figure 1.1: (A) Excitation system of the heart showing the sino-atrial node and the Purkinje system of the heart. Also the AV-node, internodal pathways and the ventricular bundle branches are shown. Reprinted with permission from [52] (Figure 10-1, page 122). (B-D) Transmission of the cardiac impulse through the heart. Adapted and reprinted with permission from [52] (Figure 10-4, page 125).

1.1 The Heart

The vertebrate heart is a muscular organ consisting of four chambers: the left and right atrium and the left and right ventricles. The right atrium receives deoxygenated blood from the superior vena cava, inferior vena cava and coronary sinus, whereas the left atrium receives oxygenated blood from the left and right pulmonary veins. The atria pump the blood to the ventricles. The right ventricle pumps blood into the pulmonary circulation, and the left ventricle pumps blood into the systemic circulation through the aorta. For effective pumping of the heart it is important that both the atria and the ventricles are synchronized. During a heart cycle, the timing of mechanical contraction of the heart is regulated via electrical excitation of cardiac myocytes. This is known as excitation-contraction coupling and is mediated via the generation and propagation of action potentials.

During a normal heart beat, the electrical excitation signal originates from the sino-atrial (SA) node that is located in the upper right atrium (see Figure 1.1A). The SA node consists of special cells that are capable of generating spontaneous action potentials with a certain frequency (automaticity). Once an action potential is generated in the SA node (Figure 1.1B), the initial electrical wave propagates to the surrounding cells in the atria (Figure 1.1C), and subsequently the atria start to contract and pump the blood into the ventricles. The atria and the ventricles are electrically isolated and electrically connected via the atrio-ventricular (AV) node. It takes some time for the ventricles to fill, and therefore it is important that there is a delay in activation and contraction between the ventricles and the atria. This delay is regulated by the AV node, which has slower conduction velocity properties. From the AV node, the electrical wave propagates to the bundle of His, the left and right bundle branches and to the Purkinje network (see Figure 1.1A). Finally, the electrical signal is passed on via the Purkinje network to the entire ventricular myocardium. As a result the ventricles contract synchronously pumping the blood from the ventricles through the pulmonary and systemic circulation (Figure 1.1D) [52].

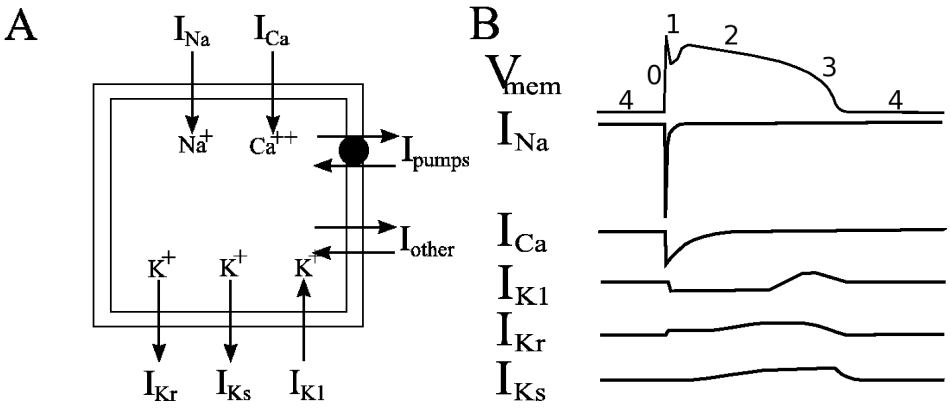

Figure 1.2: (A) Schematic overview of inward and outward ion currents across the surface cell membrane. (B) Schematic time plot of the membrane potential (top, phase 0-4) and the corresponding major ionic currents during the action potential phase. Phase 4 represents the resting membrane potential (typically, -90 mV). Phase 0 represents the rapid depolarization phase increasing the membrane potential to around +10 mV. This phase is due to the opening of the fast sodium channels causing a rapid influx of sodium ions into the cell (I_{Na}). Phase 1 represents the inactivation of the fast sodium channels. As a result there is a net transient outward current due to the outflux of potassium ions (I_{to}, not shown) causing a small downward notch. Phase 2 represents the plateau phase, in which there is a balance between the inward calcium ions (I_{Ca}) through the L-type calcium channels and the outward potassium ions through the slow delayed rectifier potassium channels (I_{Ks}). During phase 3, the L-type calcium channels close, while the slow delayed rectifier potassium channels are still open, resulting in a net outward current. As a consequence even more types of potassium channels open (I_{Kr},I_{K1}) causing the cell to repolarize. These delayed rectifier potassium channels close once the resting membrane potential is reached.

Electrical excitation of a cardiac cell is a sudden change of its transmembrane potential, from its resting state (which is around -90 mv), to an excited state (around +10 mv). This generates an action potential generation and is the result of a complex interaction of different membrane ionic channels and pumps, which are time and voltage dependent. Excitation of a cardiac cell can be initiated by an electrical stimulus that leads to an initial depolarization of the cell membrane from its resting state to exceed a certain threshold value (approximately -60 mv). Once this threshold value is reached, a very rapid "all or none" response follows, bringing the membrane potential up to +10 mv (depolarization). After depolarization, there is a repolarization phase during which the membrane potential is restored to its resting value. During the repolarization phase cells are unable to respond to a subsequent stimulus, because the ionic channels have not yet recovered from the depolarization phase. This is called the refractory period. In Figure 1.2 a schematic overview is given of the ventricular action potential as well as a description of the major ions involved in each phase. In cardiac tissue, muscle cells are electrically coupled via gap junctions such that if one cell becomes depolarized, the resulting ionic flux depolarizes its neighboring cells. If the threshold is reached in these cells, they also become depolarized and in turn raise the membrane potentials of their neighbors. This results in the formation of a propagating wave of excitation.

In the heart, the coupling of excitation to contraction is regulated via the intracellular calcium concentration. During depolarization, the concentration of intracellular calcium ions increases through the so called L-type calcium channels, which are located on the cell membrane. These calcium ions give rise to a subsequent release of a much higher quantity of calcium ions from the sarcoplasmatic reticulum. The increase of the intracellular calcium concentration initiates cardiac contraction via several conformational changes of interacting proteins: troponin C, actin, and myosin.

Contraction of cardiac tissue also affects the process of wave propagation [83]. This process known as mechano-electrical feedback. Mechano-electrical feedback is among others regulated via mechano-sensitive ion channels, such as the stretch-activated channels, which are activated by stretch and alter electrophysiological properties of the action potential. These channels can open as a result from conformational changes mediated via stretch or pressure, or can be pulled open due to tension of the cell membrane. Opening of these channels allows ions to flow in or out of the cell, causing a change in membrane potential [61, 150]. Mechano-electrical feedback may have both anti-arrhythmic and arrhythmogenic consequences. Mechanical deformation has been shown to alter the electrical properties of myocytes [160] and plays an important role during cardiac arrhythmias [35].

1.2 Cardiac Arrhythmias

Cardiac arrhythmias are a condition in which there is abnormal electrical activity in the heart, which can result in irregular fast or slow heart rates. As a consequence, the mechanical pump function of the heart is affected, which can make the heart tremble or not pump at all.

There are many different types of cardiac arrhythmias, which can be either present in the atria or ventricles. *Bradycardias* represent cardiac arrhythmias with a slow heart rhythm (less than 60 beats/min), whereas *tachycardias*, represent cardiac arrhythmias with a fast heart rhythm (more than 100 beats/min). Tachycardias are usually the result of abnormal formation of excitation waves and/or abnormal propagation of excitation waves in addition to the normal cardiac rhythm, and can be the result of automaticity, reentry or triggered activity. Many arrhythmias are driven by reentry, in which the electrical impulse recurrently travels in a tight circle within the heart, rather than moving from one end of the heart to the other and then stopping.

Reentrant arrhythmias can be classified into tachycardias, flutter and fibrillation and can occur in both the atria and ventricles and lead to a decrease in cardiac output. Tachycardias are characterized by high but regular excitation and contraction rates ($> 100/min$), flutter is characterized by even higher but still regular rhythms and contraction rates ($> 250/min$), and fibrillation is characterized by even higher uncoordinated depolarizations leading to loss of contraction. Arrhythmias occurring in the ventricles are more dangerous, because they normally destabilize into VF. During VF, there is uncoordinated contraction of the ventricles making them tremble rather than contract properly, and as a consequence the ventricles fail to pump blood into the pulmonary and systemic circulation. Ventricular tachycardia (VT) can be classified into monomorphic and polymorphic VT. During monomorphic VT, all heart beats match each other in each lead of a surface electrocardiogram (ECG), whereas during polymorphic VT there are variations in morphology. Both monomorphic and polymorphic VT can destabilize into VF.

1.2.1 Mechanisms of Cardiac Arrhythmias

Several mechanisms have been proposed to explain the dynamics of cardiac arrhythmias. In most cases, arrhythmias are driven by reentrant circuits, in which an electrical wave recurrently propagates into a circle, leading to continuously activated zones in which sinus rhythm is suppressed. In 1D, a reentrant circuit is represented as a wave rotating around a ring of cardiac tissue [188]. This is demonstrated in Figure 1.3A in which an action potential travels around a ring of cardiac tissue. The black regions represent high values of the membrane potential, the gray areas represent the tail of the action potential (intermediate membrane potentials), and the white regions represent the resting membrane potential. If the size of the ring is larger than the size of the wavelength (i.e., the black and gray areas), then the action potential can continuously rotate within the circular ca-

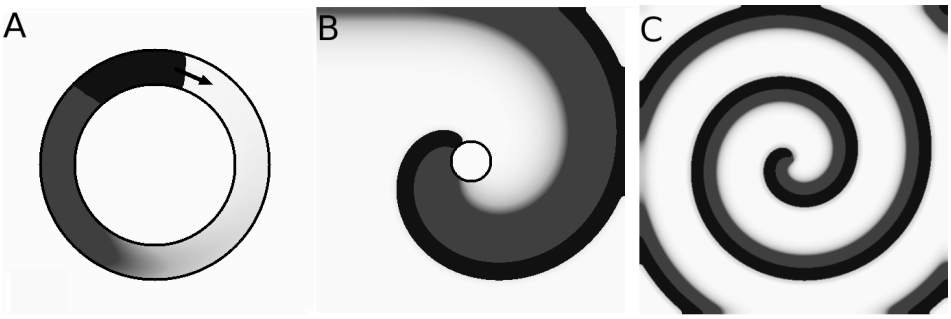

Figure 1.3: (A) Reentrant circuit in a 1D cable. (B) Spiral wave rotating around an inexcitable object. (C) Spiral wave rotating around its core. Darker areas represent higher membrane potentials.

ble. In 2D and 3D, reentrant waves can circulate around anatomically inexcitable object (i.e., anatomical reentry, see Figure 1.3B) [188] or they can be rotating spiral waves around a core formed by the refractory properties of the tip of the spiral (i.e., functional reentry, see Figure 1.3C) [156]. Experimental evidence of reentrant circuits in cardiac tissue was first provided by Allessie et al. [3], and were later also found by Davidenko et al. [29] and Pertsov et al. [132].

Reentrant waves are dependent on the velocity of the wave front (i.e., conduction velocity), the duration of the refractory period and the size of the reentrant circuit (i.e., the size of the ventricles). The wavelength of reentrant circuits is defined as the product of the refractory period and the conduction velocity. If the refractory period or the conduction velocity decreases then the wavelength will reduce thereby increasing the number of smaller reentrant circuits that can be sustained in the ventricles. During tachycardia and flutter there is often one reentrant circuit present, while during fibrillation many reentrant circuits are present.

1.2.2 Mechanisms of Ventricular Fibrillation

In the ventricles, many arrhythmias are driven by reentrant circuits. Ventricular tachycardia is driven by a single reentrant circuit, while VF is driven by many turbulent reentrant circuits. Normally, ventricular fibrillation occurs as a result of deterioration of ventricular tachycardia. There are two main hypotheses, which can explain such VT/VF transition.

The first hypothesis explains the onset of VF due to turbulent wave propagation induced by heterogeneity in refractoriness of cardiac tissue [86, 106]. The important role of heterogeneity in VF is supported by the strong association of VF with diseases that lead to increased heterogeneity, such as coronary artery disease, cardiomyopathies, and congenital heart disease [26, 31, 202]. These diseases are associated with structural and/or electrophysiological changes of the cardiac tissue which increase the degree of heterogeneity in the heart. These

changes involve among others the formation of inexcitable tissue (fibrosis), gap junction remodeling and changes in ionic currents. Furthermore, VF is associated with diseases such as Long QT, Short QT, and Brugada syndrome [26, 31, 202], in which ion channel mutations lead to an increase of action potential duration (APD) dispersion.

The second hypothesis explains the onset of VF by the occurrence of dynamical instabilities (alternans) induced by steep APD restitution [50, 125, 128, 131, 140, 184]. This is known as the restitution hypothesis [140, 184]. According to the original restitution hypothesis, alternans instability occurs when the slope of the APD restitution curve, which relates the APD to its previous diastolic interval (DI), exceeds one [50, 125]. However, recent experimental and modeling studies have demonstrated that although steepness of restitution curve is an important determinant of instability [10, 11, 192], other factors such as electrotonic coupling, cardiac memory, and conduction velocity restitution should also be taken into account [33, 138, 171, 174].

The restitution hypothesis and refractoriness hypothesis of VF are related. Alternans instability induces dynamic heterogeneities that can lead to wavebreaks, whereas static anatomically defined heterogeneities can also lead to wavebreaks.

Several mechanisms have been proposed to explain the underlying dynamics of VF. One widely studied mechanism is known as *multiple wavelet* VF [105, 106] and is characterized by the presence of multiple self-sustained electrical wavelets in the heart (see Figure 1.4(left)). These wavelets may be initiated due to pre-existing heterogeneity [105, 106] or due to dynamical instabilities, which are associated with APD restitution properties [36, 50, 125, 128, 131, 140, 184]. In Figure 1.4(left) we show an example of turbulent wave patterns occurring during multiple wavelet VF using a simplified model.

Another well-established mechanism is known as *mother rotor* fibrillation, in which VF is driven by a dominant fast source of excitation [19, 69, 200]. This rapid reentrant electrical source (i.e., the mother rotor) is responsible for maintaining VF and causes conduction block in the surrounding tissue due to heterogeneity in refractory periods [8]. The activation source is so fast that it is unable to conduct in some regions where it blocks but manages to conduct in other regions where the tissue is no longer in its refractory period. As a result, multiple small wavebreaks and irregular activation patterns are generated [69]. Thus both the speed of the activation source as well as the extent of heterogeneity in refractoriness are important for mother rotor fibrillation. In Figure 1.4(right) we show an example of turbulent wave patterns occurring during mother rotor VF using a simplified model.

Although wave patterns during multiple wavelet VF and mother rotor fibrillation are to some extent similar, there are some important differences between the two mechanisms. For example, it is believed that mother rotor VF can be stopped by elimination of the mother rotor, i.e., by local intervention, while for multiple wavelet VF such an intervention will not work because of the independence of the different wavelets.

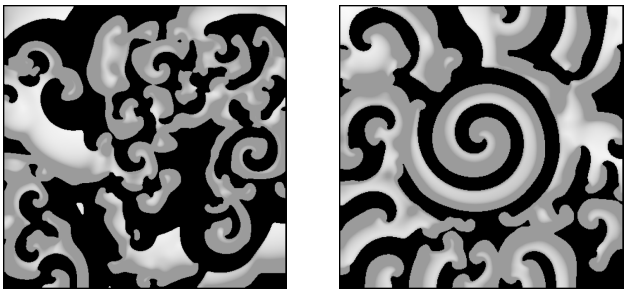

Figure 1.4: Multiple wavelet VF (left) and mother rotor fibrillation (right). Wave patterns were generated using a FitzHugo-Nagumo type of model. For the mother rotor simulation, the medium is heterogeneous such that the spiral wave rotates faster in the center of the medium. Note that during mother rotor fibrillation the initial spiral in the middle of the tissue remains intact. From [169].

1.2.3 Cardiac Arrhythmias and Mechano-Electrical Feedback

Mechano-electrical feedback can play an important role in cardiac arrhythmias, in which tissue deformation changes electrophysiological properties of the tissue. The cellular mechanism underpinning mechano-electrical feedback is believed to be the modulation of the transmembrane potential via mechano-sensitive ionic channels activated by stretch of cardiac myocytes [83].

One of the most known arrhythmogenic effects of mechano-electrical feedback is Commotio Cordis, in which a sudden precordial impact of a small object into the chest can cause a cardiac arrhythmia [96]. Alternatively, a strong impact using the human fist on the chest during a cardiac arrhythmia (precordial thump), may terminate a cardiac arrhythmia. Both effects are believed to have a feedback on excitation mainly via stretch and the stretch-activated channels [38, 84, 94, 96].

Franz et al. [35] showed that mechanical stimulation of the heart induced by periodic expansion of a balloon placed into the heart ventricle results in the induction of electrical excitation. A subsequent study by Hansen et al. [55] confirmed that these excitations were caused by the depolarizing current of the stretch-activated channels.

1.3 Modeling Cardiac Arrhythmias

Modeling can be a valuable tool to study the complex processes that occur in the human heart during cardiac arrhythmias. Using models, we can not only gain insight in the underlying mechanisms of cardiac arrhythmias, but also gain information complementary to experimental and clinical research. The use of computer models allows us to control parameters in a systematic manner and to analyze which components are important for the obtained results, while in experimental and clinical studies it is almost impossible to control all conditions. Furthermore,

in experiments it is not always possible to obtain all data that would be required to understand the underlying dynamics of cardiac arrhythmias. Cardiac arrhythmias have a 3D structure, and current experimental procedures mostly allow measurements in patients on the endocardial [198] and epicardial [112, 114, 116] surface of the heart, and often have a poor spatial resolution. Computer models allow us to investigate cardiac arrhythmias in 3D with an accurate spatial resolution that can lead to new insights. Because models and experiments can lead to different insights, it is important that experimentalists and theoreticians work together to unravel the underlying mechanisms that occur during cardiac arrhythmias.

1.3.1 Modeling Electrophysiology

Many basic concepts regarding cardiac arrhythmias have been explained using computer models. One of the first models to study excitable behavior or cardiac tissue were based on cellular automata (CA) models [106, 187]. In these models cells were described by discrete states (resting, excited, refractory), and rules describing state transitions. Some important hypotheses regarding cardiac arrhythmias were studied using simple CA models, such as the multiple wavelet hypothesis [105, 106]. However, to study the onset and more complex dynamics of VF in cardiac tissue, CA models are not always accurate enough to describe additional effects such as action potential duration and conduction velocity restitution properties. In order to describe cardiac excitable behavior in more detail, partial differential equations (PDE) are often used.

Electrical activity in the heart can be described by a system of reaction-diffusion equations. A standard monodomain model for cardiac tissue is given below [74]:

$$C_m \frac{\partial V_m}{\partial t} = \frac{\partial}{\partial x_i}\left(D_{ij}\frac{\partial V_m}{\partial x_j}\right) - I_{ion}(V_m, g_i) \tag{1.1}$$

where, V_m denotes the transmembrane voltage, C_m the membrane capacitance, D_{ij} the diffusion tensor describing the conductivity of the tissue, and I_{ion} the sum of the ionic transmembrane currents describing the excitable behavior of the individual cardiac cell. In addition to Equation 1.1 there are one or more equations for g_i needed to calculate the dynamics of the transmembrane current.

The minimal number of equations to reproduce the transmembrane voltage is two: one equation that reproduces the transmembrane current and one equation that describes the recovery processes [34]. Such low dimensional models can reproduce some important measurable characteristics of cardiac tissue, such as action potential restitution properties, the general shape of the action potential, and the effects of tissue anisotropy and heterogeneity [2, 173]. These models can be used to reproduce tissue patterns such as spiral waves or wave breakup. By adding one or two extra variables these models can also reproduce experimentally measured conduction velocity restitution and the exact shape of the action potential [32]. However, low dimensional models do not describe detailed biophysical mechanisms of excitation that occur due to different dynamics of ionic channels on the cardiac membrane. To describe ionic channel dynamics one should use

so-called ionic models for cardiac tissue that are based on the founding paper by Hodgkin and Huxley [59]. Ionic models describe the properties of each individual ionic channel and are based on experimental studies of voltage and time dynamics using voltage clamp techniques. Recent ionic models for cardiac tissue include around 60-100 variables to model many details of ionic channel dynamics identified in cardiac cells [124]. One of the models used in this thesis is the ionic model developed by Ten Tusscher et al. [171, 174], which calculates the following ionic currents:

$$\begin{aligned} I_{ion} &= I_{Na} + I_{to} + I_{CaL} + I_{Kr} + I_{Ks} + I_{K1} + I_{NaCa} \\ &\quad + I_{NaK} + I_{pCa} + I_{pK} + I_{Na,b} + I_{Ca,b} \end{aligned} \tag{1.2}$$

where, I_{Na} denotes the fast sodium current, I_{to} the transient outward current, I_{CaL} the L-type calcium current, I_{Kr} the slow rectifier current, I_{Ks} the slow delayed rectifier current, I_{K1} the inward rectifier current, I_{NaCa} the sodium/calcium exchanger current, I_{NaK} the sodium/potassium pump current, I_{pCa} and I_{pK} are the plateau calcium and potassium currents, and $I_{Na,b}$ and $I_{Ca,b}$ are background currents (see also Figure 1.2).

Both low dimensional and ionic models can be used to study wave dynamics in cardiac tissue. Low dimensional models are used as a tool for more general qualitative studies of possible new effects, while ionic models are used for detailed quantitative studies of specific effects for which molecular membrane mechanisms are important. In this thesis we use both low dimensional (chapters 2-5) and ionic models (chapter 6-8) to describe the excitable behavior of cardiac cells.

1.3.2 Modeling Cardiac Contraction

During a normal heart beat, cardiac cells deform up to 15% [103]. In order to model cardiac deformation, finite deformation elasticity theory should be applied. The motion of a continous and deformable medium can be described by a continuous displacement field resulting from a set of forces that act on the medium. These forces (and hence the resulting displacements) can vary continuously over time. In order to apply finite deformation elasticity we define two states of the solid body. The *reference* state (also referred to as *undeformed* state) describes the initial unloaded state of the material. In this state there are no active forces and all displacements are zero. Under the influence of applied forces the reference state will deform into a new equilibrium state, which is known as the *deformed* state. In finite deformation elasticity theory there are two concepts often used: *strain* is a measure of length change and *stress* represents a force per unit area acting on an infinitely small plane of surface within the material. In this thesis we use the second Piola-Kirchhoff stress tensor T^{MN}, which represents the force acting on an element of surface in the reference configuration measured per unit undeformed area.

The equations that govern finite deformation elasticity arise from the conservation of linear momentum following Newton's laws of motion [101]. For static

stress equilibrium in the absence of body forces, the governing equations expressed in terms of the second Piola-Kirchhoff stress components T^{MN} are described by:

$$\frac{\partial}{\partial X_M}\left(T^{MN}\frac{\partial x_j}{\partial X_N}\right)=0 \tag{1.3}$$

where, $\{x_i\}$ describes the present (deformed) position in rectangular Cartesian coordinates of a material particle that occupied the location $\{X_M\}$ in the reference (undeformed) configuration.

In general, deformation of cardiac cells due to external forces is split into two components. *Active stresses* are generated by the contractile apparatus during the systole of the cardiac cycle, and are generally responsible for shortening of the cardiac cells. *Passive stresses* represent the resistance of cardiac cells to deform due to the dense network of connective tissue that binds them together. In a modeling context the second Piola-Kirchhoff stress tensor T^{MN} is split up in a passive (T_p) and active stress (T_a) component:

$$T^{MN}=T_p{}^{MN}(\mathbf{C})+T_a{}^{MN}(\mathbf{C},V_a) \tag{1.4}$$

where $\mathbf{C}$ is a mechanical tensor accounting for the deformation of the tissue and V_a is a function that controls the amplitude, delay and recovery of the active stress components.

The relationship between the stress (T^{MN}) and strain (covered by $\mathbf{C}$) is given by constitutive equations. Constitutive equations are empirical relations used to represent stress-deformation behavior of a material, which are independent of the choice of the coordinate system, between experimentally observed stress and strain tensors.

1.3.3 Modeling Excitation-Contraction Coupling and Mechano-Electrical Feedback

In order to mathematically couple the reaction diffusion system and the mechanical equations, the relationship between Eqs. 1.1 and 1.3 must be considered. In general, each term in Eq. 1.1 may depend on the state of deformation, resulting in:

$$\frac{\partial \mathbf{V_m}}{\partial t}=\nabla\cdot(\mathbf{D}(\mathbf{C})\nabla\mathbf{V_m})+\mathbf{F}(\mathbf{V_m},\mathbf{C}) \tag{1.5}$$

The effects of the reaction diffusion equations on the mechanics equations (i.e., excitation-contraction coupling) arise from the fact that some variables in Eq. 1.1 control the development of the active stress in the medium. For example, the contractile force developed by cardiac myocytes is determined by the intracellular concentration of calcium ions $[Ca^{2+}]_i$, which is one of the variables of the reaction diffusion model describing cardiac cells [66].

The direct influence of contraction on excitation (i.e., mechano-electrical feedback) is given by the stretch-activated current I_s, which is added to I_{ion} in Eq. 1.1.

The effect of contraction on the stretch-activated current has been investigated in several studies [94, 129, 177, 181]. Stretch-activated channels have quite simple properties compared to other ionic channels. Their conductivity is time independent and only affected by stretch of the cardiac cell membrane and the experimentally measured current-voltage relationship for the stretch-activated channels is almost linear [201]. This resulted in the following expression for stretch-activated current, that was introduced in [94, 177, 181], and was modified for strain dependency [129]:

$$I_s = G_s(\sqrt{g} - 1)(V_m - E_s) \tag{1.6}$$

where G_s and E_s are the maximal conductance and reversal potential of the stretch-activated channels, respectively. g is the determinant of the covariant metric tensor (that is directly related to $\mathbf{C}$), and accounts for the local deformation. The stretch-activated current in Eq. 1.6 is only present during dilatation (i.e., $g > 1$), and is zero during contraction (i.e., $g < 1$).

Additionally, contraction also affects the metric tensor of the coordinate system, which becomes curvilinear. Due to motion of the material coordinate system, a general curvilinear expression can be used that is corrected for the deformation of the local area, to evaluate the Laplacian in Eq. 1.5.

1.4 Thesis Outline

In this thesis we study mechanisms of ventricular fibrillation focusing on the effect of mechano-electrical feedback and tissue heterogeneity on VF dynamics. In **part I**, consisting of **chapters 2-5**, we investigate the basic effects of mechano-electrical feedback in 2D systems using simple low dimensional models to describe cardiac excitable behavior. In **part II**, consisting of **chapters 6-8**, we use anatomically based models of the human ventricles to study the mechanisms and dynamics of VF and investigate the effects of tissue heterogeneity (**chapters 6-7**) and mechano-electrical feedback (**chapter 8**). The contents of each chapter are summarized in more detail below.

Part I

Chapter 2 is a general review article about the concept of mechano-electrical feedback. We introduce the general framework needed to model mechano-electrical feedback and discuss some of the basic effects of deformation on cardiac excitable behavior. In particular those mechanisms relating to the effects of deformation on pacemaker activity and spiral wave dynamics are discussed.

In **chapters 3** and **4** we study one of the basic effects of mechano-electrical feedback, which is the induction of electrical excitation due to depolarization of cardiac tissue via the stretch-activated channels. We refer to this as automatic pacemakers. Our aim is to investigate the organization and interaction of these automatic pacemakers in a 2D sheet of cardiac tissue. For these studies we use

a low dimensional Aliev-Panfilov model [2] to describe the membrane kinetics of the cardiac tissue and extend this model with a description of the stretch-activated current. The Aliev-Panfilov model describes key characteristics of cardiac tissue such as shape of the action potential, refractoriness and restitution of action potential duration. This model is coupled to a mechanical finite element model to describe the deforming tissue. The mechanical model gives rise to approximately 10-15% deformation following excitation, consistent with contracting tissue. We show that local deformations can depolarize cardiac tissue via the stretch-activated current, which can lead to the induction of automatic pacemakers. These automatic pacemakers are self-organized and can drift throughout the medium.

In **chapter 5** we find that mechano-electrical feedback can induce breakup of spiral waves. It turns out that mechanically induced breakup occurs via specific inactivation properties of the sodium current. In order to observe this effect, it is important to use a model that has a proper description of the inactivation kinetics of the sodium current. The standard Aliev-Panfilov model [2] only contains a description of the activation of the sodium current, but lacks a description of the inactivation kinetics. Therefore, for this study we used a three-variable Fenton-Karma model [33], that contains a more detailed description of the sodium current (inactivation and activation kinetics). We extend this model with a description of the stretch-activated current. The Fenton-Karma model also describes key characteristics of cardiac tissue such as shape of the action potential, refractoriness and restitution of action potential duration. This model is coupled to the same mechanical finite element model as is used in **chapters 3** and **4**. We show that local deformation can induce breakup of an otherwise stable spiral into complex spatio-temporal patterns due to block of the sodium current as a result of the the slow depolarizing current of the stretch-activated channels. Furthermore, we show that mechanical deformations can lead to spiral wave drift throughout the medium. We study the mechanisms of these effects and discuss their applicability to the theory of cardiac arrhythmias.

Part II

In **chapter 6** we study the organization of VF using a heterogeneous anatomical model of the human ventricles. For this, we develop an anatomical model of the human ventricles that incorporates clinically measured restitution data [114]. This model contains a realistic description of the human ventricles, including a detailed description of cell electrophysiology, ventricular anatomy and fiber direction anisotropy. For this, we use the ionic model developed by Ten Tusscher et al. [171, 174] to describe membrane kinetics of the cardiac tissue. We extend this model by mapping clinically observed epicardial restitution data to our anatomical representation and extrapolate these properties throughout the ventricles using a diffusion based algorithm. Restitution properties are fitted by regionally varying parameters of the electrophysiological model. We show that an increased level of heterogeneity leads to a greater number of filaments and a broader distribution

of excitation periods, thereby increasing the complexity and dynamics of VF.

In **chapter 7** we continue our study of VF using our heterogeneous model of the human ventricles developed in **chapter 6**. In this study we use a profile of a patient that contained a large degree of heterogeneity in restitution slopes, and study the effects of different initial conditions on VF dynamics. For this, we initiate spiral waves in steep and shallow restitution areas. We show that mother rotor VF can occur in the human heart and that ablation of the mother rotor terminates VF. Furthermore, we show that both mother rotor and multiple wavelet VF can occur in the same heart depending on the initial conditions at the onset of VF. We study the organization of these two types of VF in terms of filament numbers, excitation periods and frequency domains.

In **chapter 8** we develop an integrative 3D electro-mechanical model of the left ventricle of the human heart and use this model to study the initiation and organization of VF due to mechano-electrical feedback. For the reaction diffusion part, we use a 3D finite difference geometry of the human left ventricle that is based on data from [60], and contains a detailed description of the left ventricle as well as fiber direction anisotropy. To describe the membrane kinetics of the cardiac tissue we use the ionic model developed by Ten Tusscher et al. [171, 174] and extend this model with a description of the stretch-activated current. For the mechanical part, we create an equivalent 3D finite element model of the human left ventricle that is also based on the finite difference data from [60]. The finite element mesh also contains fiber direction anisotropy. The coupling between the electrical activity and the mechanical active tension is accomplished via the intracellular calcium concentration. Active tension is then determined by the Niederer-Hunter-Smith model [119], that approximates active tension developed as a result of cellular cross-bridge cycling. The passive mechanical response is determined via the Guccione transversely isotropic constitutive relations [49]. Mechano-electrical feedback is represented via the stretch-activated channels which are modulated by local deformation. We verify our model by simulating a normal heart beat and comparing the resulting strains in the cardiac wall with experimentally measured strains reported in the literature. Furthermore, we show that an otherwise stable spiral wave can break up into VF via mechano-electrical feedback of the stretch-activated channels. We identify the mechanisms of this transition and study the 3D organization of mechanically induced VF.

Finally, in **chapter 9** we end this thesis with a summarizing discussion in which we discuss the major findings found in this thesis. We then give a short overview about the complexity of the numerical models used and discuss some of the underlying model assumptions. We conclude that mechano-electrical feedback and tissue heterogeneity can play an important role in the initiation and dynamics of ventricular fibrillation.

Part I

Modeling Basic Mechanisms of Mechano-Electrical Feedback in 2D

CHAPTER 2

Modeling Cardiac Mechano-Electrical Feedback using Reaction-Diffusion-Mechanics Systems

R.H. Keldermann[1], M.P. Nash[2] and A.V. Panfilov[1]

[1] *Theoretical Biology/Bioinformatics Group*
Utrecht University
Padualaan 8, 3584 CH Utrecht, The Netherlands

[2] *Bioengineering Institute and Department of Engineering Science*
University of Auckland
Private Bag 92019, Auckland, New Zealand

Physica D. Accepted for publication (2008)
DOI:10.1016/j.physd.2008.08.017

Abstract

In many practically important cases, wave propagation described by reaction-diffusion equations initiates deformation of the medium. Mathematically, such processes are described by coupled reaction-diffusion-mechanics (RDM) systems. RDM systems were recently used to study the effects of deformation on wave propagation in cardiac tissue, so called mechano-electrical feedback (MEF). In this article, we review the results of some of these studies, in particular those relating to the effects of deformation on pacemaker activity and spiral wave dynamics in the heart. We also provide brief descriptions of the numerical methods used, and the underlying cardiac physiology.

2.1 Introduction

Reaction-diffusion (RD) equations describe a wide variety of non-linear systems in physics, chemistry and biology. They describe non-linear wave patterns in the Belousov-Zhabotinsky (BZ) chemical reaction [199], in the processes of morphogenesis of the mould *Dictyostelium discoideum* (Dd) [183], of electrical activity in cardiac tissue [43], and in many other biological systems. More information about reaction-diffusion systems can be found in [48, 74]. Propagation of non-linear waves is usually accompanied by other important processes. One of the most fundamental is the mechanical deformation of the medium. In the human heart, non-linear electrical waves propagate through the cardiac tissue and initiate cardiac contraction. In turn, mechanical deformation also affects the electrical waves of the heart. This sets up a complex system of feedback between both of these processes, and is known as mechano-electrical feedback (MEF) [83, 89, 90]. In this article, we review modeling approaches used to study MEF using coupled reaction-diffusion-mechanics systems. We start with a description of the physiological basis of cardiac excitation, contraction and MEF. We then outline the modeling approach and its numerical implementation, and present results on the effects of MEF on the initiation of ectopic beats, pacemaking activity, and spiral wave dynamics in the heart. We limit our studies to wave dynamics in two dimensions. Review articles discussing other aspects of MEF can be found in [65, 82, 120]

2.1.1 Biophysics of Cardiac Excitation and Contraction

Cardiac contraction is initiated by the propagation of electrical waves. The waves are a result of timed excitation of billions of cardiac cells (myocytes), which are electrically coupled together via conducting gap junctions.

Electrical activation of a cardiac cell is a sudden change of its transmembrane potential, from the resting state (around -90 mV), to an excited state (around +10 mV). This change of transmembrane potential occurs as a result of several transmembrane currents carried by various ions (Na^+, K^+, Ca^{2+}, Cl^-, etc.) across the cell membrane. These currents can be subdivided into two large groups:

inward currents, which depolarize (excite) cardiac cells, and outward currents, which repolarize the membrane to its resting state. The inward currents are carried mainly by Na^+ and Ca^{2+} ions, and the outward current are mainly carried by K^+ ions. Excitation of the cell occurs if the transmembrane potential exceeds the threshold value (approximately -60 mV). After that the inward Na^+ current is activated and brings the membrane potential to its fully activated state of around 10 mV. After depolarization, a repolarization phase follows, in which the membrane potential slowly recovers to its resting membrane potential due to inactivation of Na^+ current and activation of the outward K^+ currents. The timecourse of excitation of a cardiac cell and the main inward (negative) and outward (positive) currents involved are schematically shown in Figure 2.1.

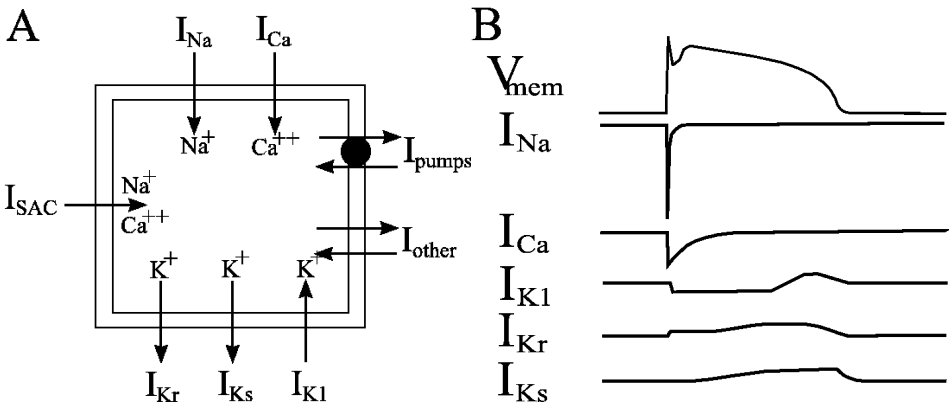

Figure 2.1: (A) Schematic overview of inward and outward ion currents across the surface cell membrane. (B) Schematic time plot of currents during the action potential phase.

If a cell becomes excited (depolarized), current from this cell propagates to neighboring cells via the gap junctions, which in turn cause neighboring cells to depolarize. As soon as the threshold value of the transmembrane potential is reached, these cells also become excited and in a similar way transmit excitation to their neighbors. This results in a propagating wave of excitation.

Excitation of the heart initiates cardiac contraction in the following way. During depolarization, a small amount of calcium ions flows into the cell through the calcium channels. This calcium current causes a subsequent release of a larger quantity of calcium stored within specialized cellular compartments called the sarcoplasmatic reticulum. This increases the calcium concentration initiates contraction of the heart via calcium mediated conformational changes in contractile proteins (troponin C, actin, myosin) [83]. Initiation of contraction via excitation is called electro-mechanical (or excitation-contraction) coupling.

There is also a feedback effect of contraction on excitation of cardiac cells, which is known as mechano-electrical feedback. The main physiological mechanism underpinning this is believed to be mechano-sensitive ion channels, such as the stretch-activated channels (SAC), which have been identified in cardiac

cells [61, 150]. In response to cell stretch, these channels produce an inward current [83] which as we discussed above, tends to depolarize the cell and in some cases can even initiate cardiac excitation. Franz et al. [35] showed that mechanical stimulation of the heart induced by periodic expansion of a balloon placed into the heart ventricle results in the induction of electrical excitation (see Figure 2.2). A subsequent study by Hansen et al. [55] confirmed that these excitations were caused by the depolarizing current of the SAC.

It is also believed that SAC play a role during a mechanical impact to the chest, which may be either lethal or life saving. It is known that a sudden precordial impact of a small object into the chest can cause Commotio Cordis [96]: an arrhythmia which is lethal. Alternatively, a strong impact using the human fist on the chest during a cardiac arrhythmia (precordial thump), may terminate a cardiac arrhythmia. Both effects are believed to have a feedback on excitation mainly via stretch and SAC and are discussed in [38, 84, 94–96, 100].

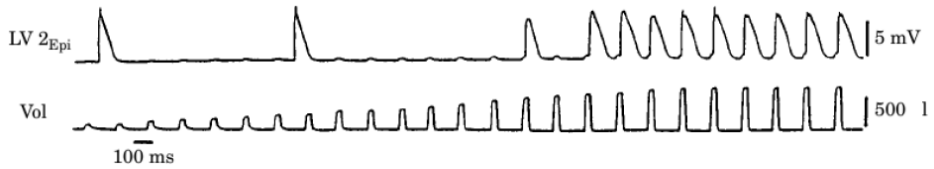

Figure 2.2: Mechanically induced ectopic (abnormal) excitation in a Langendorff perfused rabbit heart (i.e., the aorta is cannulated and the heart is maintained by perfusion with an oxygen and nutrient rich solution.) Monophasic action potential (MAP) (top) and changes in left ventricular volume (LVP) (bottom). Once a critical volume (i.e., stretch) is reached, an action potential is triggered. Reprinted with permission from [35].

2.2 Modeling Reaction-Diffusion-Mechanics

2.2.1 Modeling Electrical Activity

Electrical activity of the heart can be described by a system of reaction-diffusion (RD) equations and has been reviewed previously (see for example [74, 123, 148]). A standard monodomain model for cardiac tissue is given below.

$$\begin{aligned} C\tfrac{\partial V}{\partial t} &= \nabla\cdot(\mathbf{D}\nabla V) + I_m(V, g_i) \\ \tfrac{dg_i}{dt} &= \phi(g_i, V) \end{aligned} \tag{2.1}$$

The first equation describes changes of the transmembrane potential V on the cell membrane (with capacitance C) as a result of inward and outward transmembrane ionic currents I_m, and currents between adjacent cardiac cells $\nabla\cdot(\mathbf{D}\nabla V)$, where $\mathbf{D}$ is the conductivity tensor that accounts for the electrical anisotropy of cardiac tissue. For details and derivation of this equation see [74]. The ionic current I_m is a sum of all currents that flow across the cardiac membrane (see

Figure 2.1) (e.g., $I_m = I_{Na} + I_{Ca} + I_K + ...$). Each of these currents depend on other variables, which are called gating variables g_i and account for experimentally measured activation and inactivation kinetics of that specific current. There are many different types of models available for cardiac cells, which differ in complexity and details on the representation of ionic currents I_m. The first *biophysical* or ionic models were developed by Hodgkin-Huxley (for nerve cells) [59] and Noble (for cardiac cells) [122], and describe individual ion currents across the cell membrane based on detailed experimental observations. Modern ionic models in addition to ionic currents also describe concentration changes of the major ions involved. These models produce accurate properties of the cardiac action potential such as action potential shape, refractoriness, rate dependence, and describe the various detailed biophysical mechanisms of excitation that occur due to different dynamics of ion channels. These models often contain many ODEs (10-100) and can be computationally intensive. Ionic models can be used to study detailed quantitative effects of ion channels, e.g. drug applications, genetic disorders, etc. Some examples of these models are [28, 99, 172]. More simple *phenomenological* models describe basic macroscopic properties of cardiac tissue such as shape, refractoriness, etc. These models contain fewer ODEs (<4) and can be used to study more general qualitative effects. Some examples of these models are [2, 12, 33, 34].

2.2.2 Modeling Mechanical Deformation

Cardiac cells change their length by up to 15% [103] during cardiac contraction. In order to model deformation, finite deformation elasticity theory should be applied to describe the kinematics of deformation and stress equilibrium and model the relationship between stress and strain.

Equations that describe finite deformation elasticity arise from the conservation of linear momentum following Newton's law of motion [101]. For static stress equilibrium in the absence of body forces, the governing equations expressed in terms of the second Piola-Kirchhoff stress components T^{MN} regarding mechanics are described by:

$$\frac{\partial}{\partial X_M}\left(T^{MN}\frac{\partial x_j}{\partial X_N}\right) = 0 \tag{2.2}$$

where, x_m is the deformed space, and X_m the undeformed space. The second Piola-Kirchhoff stress tensor describes material behavior independent of rigid body rotation and contains passive (T_p) and active stress (T_a) components described by:

$$T^{MN} = {T_p}^{MN}(\mathbf{E}) + {T_a}^{MN}(\mathbf{E}, V_a) \tag{2.3}$$

where, $\mathbf{E}$ is the Green-Lagrange deformation tensor, that accounts for mechanical deformation and V_a is a function that controls the amplitude, delay and recovery of the active stress [117, 129]. Passive properties are described by (nonlinear) constitutive relations, which are determined by experimental models. Experimental evidence has shown that cardiac tissue exhibits different responses

along various material axes [161], and this has important implications for both cardiac mechanics [115] and electrical activation in myocardial tissue [85]. Active properties (i.e., contraction) are related to the intracellular calcium concentration, which is typically one of the variables of the RD model (see Niederer et al. [119] for an extensive model description).

2.2.3 Modeling Mechano-Electrical Feedback

Mechanical deformation affects the electrical properties in various ways: first, the coordinate system is changed during deformation thereby affecting diffusion properties; second, passive electrical properties such as capacitance and diffusion may change during deformation and third, ionic currents, such as SAC are affected by deformation. The effects of deformation ($\mathbf{E}$) on the RD equation is schematically shown in Eq. 2.4:

$$C(\mathbf{E})\frac{\partial V}{\partial t} = \nabla\cdot(\mathbf{D}(\mathbf{E})\nabla V) + I(V,\mathbf{E}) \tag{2.4}$$

In [67, 115, 117, 129] a modeling framework for MEF has been introduced. In Eq. 2.4 the system does not move. However, contraction of the coordinate system also affects the metric tensor of the coordinate system, which becomes curvilinear. Due to motion of the material coordinate system, we use a general curvilinear expression that is corrected for the deformation of the local area, to evaluate the Laplacian in Eq. 2.4. This is described in Eq 2.5:

$$\nabla\cdot(\nabla\mathbf{V}) = \frac{\partial}{\partial X_M}\left(\sqrt{g}g^{-1}_{MN}\frac{\partial V}{\partial X_N}\right) \tag{2.5}$$

where, $g_{MN} = \{\frac{\partial x_k}{\partial X_M}\frac{\partial x_k}{\partial X_N}\}$ is the covariant metric tensor of the coordinate system, (which is directly related to the Green Lagrange deformation tensor $\mathbf{E}$ [101]); and g is the determinant of the metric tensor which accounts for local deformation.

The effect of contraction on the ionic current (SAC) has been investigated in several studies [94, 129, 177, 181]. SAC have quite simple properties compared to other ionic channels. Their conductivity is time independent and only affected by stretch of the cardiac membrane and the experimentally measured current-voltage relationship for the SAC is almost linear (see Figure 2.3a) [201]. Furthermore, the conductivity of the SAC is dependent on the cell's sarcomere length (SL) [201] and can also be approximated by a linear function (see Figure 2.3b). This resulted in the following expression for SAC current, that was introduced in [94, 177, 181] and modified for strain dependency [129]:

$$I_{SAC} = G_{SAC}(\sqrt{g}-1)(V - E_{SAC}) \tag{2.6}$$

where, G_{SAC} and E_{SAC} are the conductance and reversal potential for the SAC, respectively. Furthermore, it is widely believed that the current through the SAC occurs mainly during stretch and thus it is assumed that the current in Eq. 2.6 is

only present if $\sqrt{g} > 1$. Adding Eq. 2.6 to the right hand side of Eq. 2.4 provides a description of the direct effect of stretch on the membrane current.

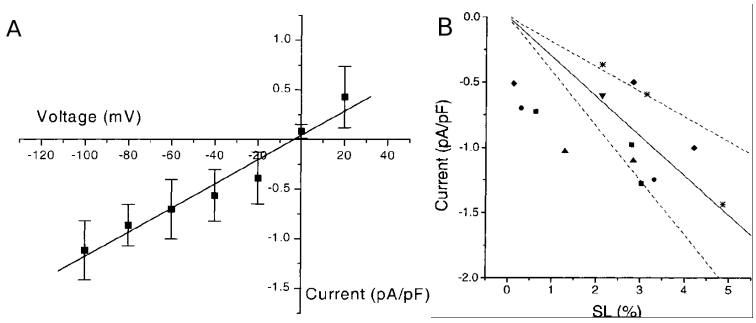

Figure 2.3: (A) SAC current-voltage relationship normalized to cell capacitance [201]. (B) Linear regression of % change in SL vs. current density. Reprinted with permission from [201]

2.2.4 Numerical Formulation

To solve the RDM model Nash and Panfilov [117] introduced a hybrid method in which an explicit Euler scheme was used for the RD system, with non-linear finite element techniques for the large deformation mechanics. The solution procedure is described below.

After N time integration steps (a value of 3 was used in [129]) for solving the RD equations (Eq. 2.4), the equations governing tissue mechanics are solved (Eqs. 2.2 and 2.3), using active stress components produced by the variable V_a of the RD equations. Non-linear Newton iterations are performed to solve the stress equilibrium equations (Eq. 2.2) and provide updated values of the Green-Lagrange deformation tensor, which modulate the excitation properties via Eqs. 2.4 and 2.6 for the subsequent N excitation time-steps. A detailed description of the solution procedure is given in [75, 117].

Recently, a more extensive mathematical analysis involving numerical issues of soft tissue modeling on coupled electric-mechano systems was published in [186]. They showed in a more detailed numerical analysis that in some cases a more accurate integration scheme should be used to enforce stability of coupled reaction diffusion mechanics systems. This topic definitely requires more attention in the future for both stability issues and numerical efficiency.

2.3 Reaction-Diffusion-Mechanics without SAC

One of the first studies regarding RDM were performed by Nash and Panfilov [117]. They used the Aliev-Panfilov model [2] to describe membrane kinetics for cardiac tissue. Material properties were given by Mooney-Rivlin material law [163] to describe mechanical isotropic material behavior. To couple the reaction-diffusion

system with the mechanical part Nash and Panfilov [117] introduced an additional equation for active tension that described qualitatively consistent timing and amplitude of cardiac tissue contraction. The formulation did not include SAC nor the effects of mechanics on passive properties, and thus the only effects studied were the direct geometric effects of tissue deformation on wave propagation.

Nash and Panfilov investigated electromechanical activity following a point stimulus at the center of the tissue and compared this with the activity from a rotating spiral in the center of the tissue. They found that for the central location the overall mechanical deformation caused by a centrally located rotating spiral wave was an order of magnitude less than that of periodic radial waves, but deformations became comparable for non-central locations. They also studied the effects of MEF on spiral wave rotation. They found that spiral waves with MEF had a larger variation of periods compared to spiral wave periods in the non-contracting model and that the mean spiral wave period during contraction was slightly increased. They also found that in the absence of mechanical deformation spirals had a stationary circular meandering pattern, whereas with MEF spiral wave meandering was non-stationary and drifted along the boundary of the medium. The magnitude of these effects are small and no significant effect of MEF on spiral wave breakup was found. However, the effects of SAC on MEF was not investigated in that study.

2.4 Reaction-Diffusion-Mechanics with SAC

In this section we review the effects of SAC on electrophysiological properties of cells and the effects of SAC on 1D and 2D wave propagation, which were studied using various modeling approaches and using various models of cardiac tissue.

2.4.1 The Effects of SAC on Electrophysiological Properties

During stretch, SAC produce an inward current which tends to depolarize a cardiac cell and has various effects on electrophysiological properties. The effects of a constant, time independent current via SAC on general electrophysiological properties was studied by Trayanova et al. [177]. The model did not include active contraction and the effect of SAC was studied using only a RD model. With reference to Figure 2.4, the paper [177] reports the following effects of SAC (for $G_{SAC} = 30\mu S/\mu F$ and $E_{SAC} = -20mV$): 1) A slight decrease of resting membrane potentials (around -75mV vs. -85mV); 2) Elongation of the action potential for short cycle lengths (CL) (i.e., for a CL of 100ms action potential duration is around 82ms vs. 77ms); 3) A slight flattening of the restitution curve; 4) A slight increase of the effective refractory period (up to 1-2ms); 5) An increase of conduction velocity and wavelength for cycle lengths longer than 115 ms, and a decrease for cycle lengths smaller than 115 ms; 6) An increase in the activation threshold. These findings reported by Trayanova et al. [177] are broadly consistent to those reported experimentally in [88, 141, 142].

Other studies [130, 181] have shown that in extreme cases the current through SAC can prevent formation of action potentials. This occurs as a result of the accommodation affect, in which the threshold of activation increases due to a slower depolarizing current [58, 59]. This has also been reported in experiments [59]. Possible consequences of accommodation for wave propagation in cardiac tissue were studied by Biktashev et al. [14]. As we point out below, such blocks of propagation can cause breakup of spiral waves.

Studies have also investigated the effects of SAC on the action potential. Different responses are possible, which are determined by the timing of the stretch and the magnitude of I_{SAC} generated. If stretch is applied during the plateau (excitation) phase of the action potential, it will change the time course of repolarization, which leads to either shortening or lengthening of the action potential. This change in duration depends on the value of E_{SAC} and the magnitude of the transmembrane potential during the plateau phase; I_{SAC} can be either an outward or inward current. This also has been reported in both experimental [78, 201] and modeling studies [38, 80, 177]. If SAC are activated when the cell is already repolarized, SAC may result in either a prolonged excitatory phase or a new action potential [80, 129, 177] (see Figure 2.4).

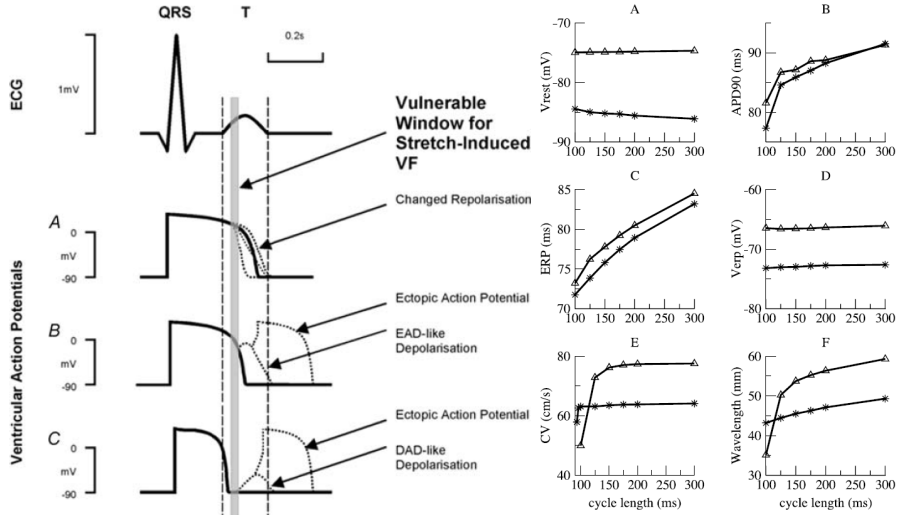

Figure 2.4: (Left) Effects of mechanical impact action on mechano-sensitive channels on AP shape during a critical time window. Reprinted with permission from [84]. (Right) Basic electrophysiological properties with (triangles) and without SAC (stars). (A) Resting membrane potential. (B) Action potential duration at the level of 90% repolarization (APD_{90}). (C) Effective refractory period (ERP). (D) Transmembrane potential at the end of ERP. (E) Conduction velocity (CV). (F) Wavelength (ERP × CV). Reprinted with permission from [177].

2.4.2 Pacemakers

The idea of action potentials induced by SAC was further investigated in [75, 129] where it was shown that in some conditions electrical waves can induce stretch of cardiac tissue, which in turn may be sufficient to initiate a new action potential resulting in the onset of periodical pacemaker activity. Panfilov et al. [75, 129], used an Aliev-Panfilov [2] model to describe membrane kinetics, which was modified to describe SAC in accordance with Eq. 2.6. Figure 2.5 shows wave propagation after application of a single stimulus at the center of a 2D medium, with and without mechanical activity. We see that without mechanics the initial wave vanished, while with mechanics a stable pacemaker sets up at the center of the medium. The mechanism of pacemaker activity here is simple and related to depolarization of tissue by the SAC. With reference to Figure 2.5, we observed stretch at the center of the medium after the wave had traveled away from the center. This stretch resulted in an inward current via SAC and depolarized the resting tissue at the center, which resulted in the onset of subsequent periodic activations [129].

It was also shown that pacemaker activity occurred at locations pre-determined by the medium size, its electrical and mechanical properties and that the location of a pacemaker slowly drifts until it reaches a stationary position. Figure 2.5 shows a comprehensive picture of pacemaker drift from different initial conditions to stable attractors for one set of parameter values. Further details on the effect of medium size on this process can be found in [129]. It was also shown in [75] that in a heterogeneous medium containing a gradient of excitability, pacemakers drift to the region with lower period values. Furthermore, mechanical deformation not only induces pacemakers but also has a pronounced effect on the spatial organization of excitation patterns (see Figure 2.6) [75]. Paper [75] also reports on the interaction of multiple pacemakers. For example, for one parameter set multiple pacemakers were shown to drift toward each other and merge to form one stable pacemaker at the center of the tissue (see Figure 2.6) [75].

Note that these studies were performed in simplified models of cardiac tissue and it remains to be determined whether these effects will be present using ionic models, as well as in experiments. Recently, it was shown in neonatal rat ventricular cell cultures that calcium overload can lead to pacemaker activity and that in some cases pacemakers drift throughout the medium [18]. Mechanisms of this drift require further investigations.

2.4.3 Drift of Spirals

In the previous section, we discussed drift of spiral waves due to mechanical deformation in the absence of SAC [117]. A more recent article [130] studied the effects of mechanical deformation and SAC on spiral wave behavior. For this study, a different RD model was used: a modified version of the three variable Fenton-Karma model [33], which contains a more detailed description of the sodium current in comparison to the previous used Aliev-Panfilov model. In this model, SAC were

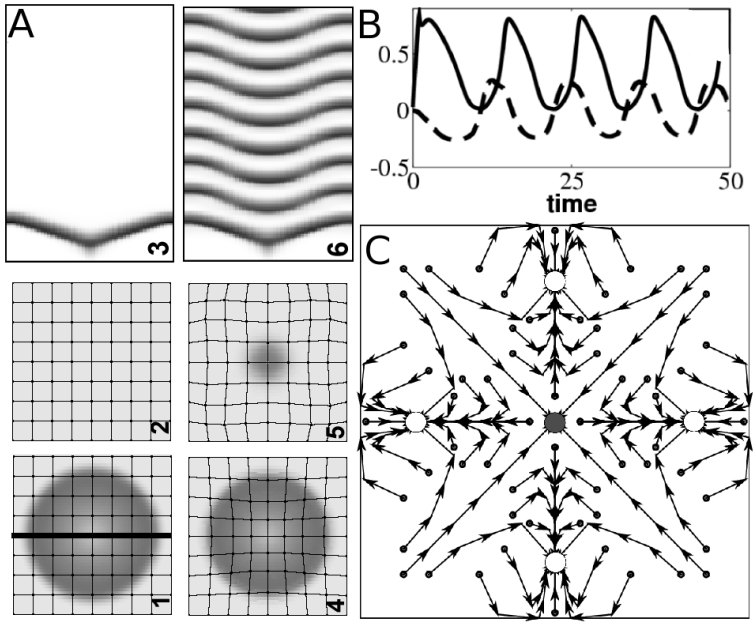

Figure 2.5: (A) Development of pacemaker activity due to mechanics. (B) Time course of the excitation variable (solid line) and dilatation ($\sqrt{g}-1$) (dashed line). (C) Drift of pacemakers from different initial conditions. Reprinted with permission from [129]

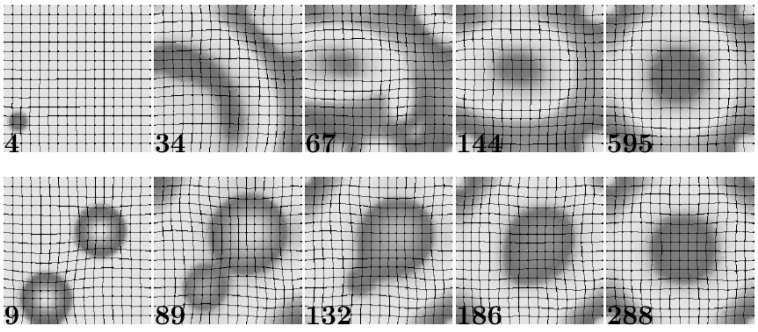

Figure 2.6: (Top) Drift of a single pacemaker. (Bottom) Interaction and drift of multiple pacemakers. Reprinted with permission from [75]

modeled using Eq. 2.6. Panfilov et al. [130] showed that in the presence of mechanical deformation, the spiral wave drifted to the center of the medium, which was an attractor of this system independent of the initial starting position (see Figure 2.7A). After arriving at the attractor, the tip of the spiral wave underwent a bi-periodic hypo-cycloidal motion. The drift was primarily due to the SAC. When SAC were removed from the model (i.e., the model had only geometrical feedback as in [117]), the spiral wave drift was still present, but the tip was no longer directed to the stable attractor in the center of the tissue. Instead, it drifted along the boundary. Drift velocity was also much smaller. When I_{SAC} alone was used (i.e., no geometrical feedback), drift and meander to the center of the medium were observed in a way similar to Figure 2.7A. It was also shown that different medium sizes did not affect the position of the stable attractor, but did affect the drift velocity.

As suggested in [130], spiral wave drift is induced by a periodic modulation of the properties of the medium due to contraction. This mechanism is similar to the resonant drift mechanism of spiral waves and has been studied in [1, 47]. In particular, it was shown in [1, 47] that if the properties of the excitable medium are changed periodically, this results in the onset of spiral wave meander. If this period is close to the period of the spiral wave, then spiral wave drift is observed. In our case, contraction induced by a rotating spiral provides such a periodical modulation with a period equal to that of the spiral wave. Thus spiral wave drift is expected. Resonant drift of spirals have been observed in detailed ionic models of cardiac tissue [15, 16] and in BZ experiments [47].

2.4.4 Breakup of Spirals

The study of Nash and Panfilov [117] did not report any effects of mechanical deformation on spiral wave breakup. However, the subsequent study of Panfilov et al. [130], which included SAC and a different description of the RD model, reported that mechanical deformation can induce breakup of spiral waves. Figure 2.7B shows a typical pattern of mechanically induced breakup using a three variable Fenton-Karma model [33]. Here, we see that after a few rotations, the initial spiral wave blocked at certain positions, which caused the spiral to breakup into fragmented spirals. Mechanically induced spiral breakup was due to the SAC. When SAC were removed (i.e., leaving just the geometry feedback), the spiral remained stable and did not break up. On the other hand, when only I_{SAC} was used (with no geometrical feedback), the spiral wave broke-up.

Spiral wave fragmentation was shown to occur due the accommodation effect of the SAC. The sodium current is the main determinant in the generation of a new action potential, and its magnitude is proportional to the product of the sodium activation and inactivation gates, which are time and voltage dependent. If at any time there is a voltage difference between two neighboring cells (e.g., if one cell is excited and the other cell remains in its resting state), then ion current flows from one cell to the other via the gap junctions and slowly raises the membrane potential. When the threshold value (approximately -60 mV) is

reached, the inward sodium current is activated and a new action potential is generated, which in turn activates the next neighboring cell. However, due to the accommodation effect, SAC have already *slowly* depolarized the tissue (before any neighboring cell is excited) thereby effecting the inactivation kinetics of the sodium channel. Thus, when a fully excited neighboring cell tries to depolarize this cell via the gap junctions (which is a faster process compared to the SAC), the sodium current cannot be activated, because the inactivation gates are already closed due to the slow rising potential of the SAC. This is shown in Figure 2.7C by the black arrow. A similar mechanism was reported in [87] for a 1D setup using a more accurate ionic model of cardiac tissue (Courtemanche model [28]). Inactivation of the sodium current has also been observed in experiments [59].

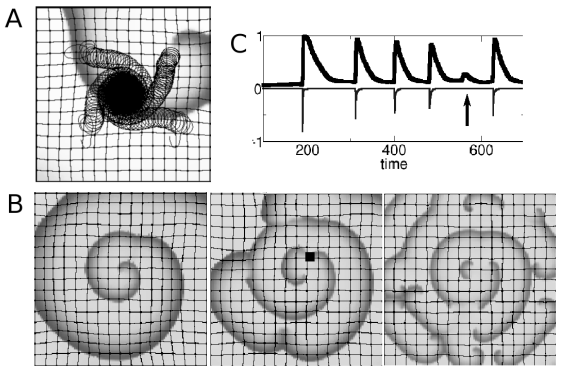

Figure 2.7: Spiral drift and breakup caused by mechanical activity. See text for explanation. (A) Drift of spirals from different initial conditions. (B) Spiral wave breakup due to accommodation effect. (C) Time course of the excitation variable and the sodium current measured in the black square of figure B. The black arrow denotes the point in which the SAC blocks the sodium current. Modified from [130].

2.4.5 Inducing Spiral Waves by Mechanical Stimulation (Commotio Cordis)

In order to understand the possible mechanisms of the initiation of ventricular arrhythmias after a mechanical impact (Commotio Cordis), Garny and Kohl [38] investigated the effects of a mechanical impact on the initiation of spiral waves using a 2D model. They used a guinea pig ventricular cell model [124] for the RD model and added SAC to a bell shaped profile of external forces to simulate a region of impact. Within this region the current of the SAC was described using $I_{SAC} = G_{SAC}(V - E_{SAC})$ and this current was activated during the impact (for details see [38]). They found that various responses can occur, depending on the timing of the impact during the action potential. Garny and Kohl showed that if the mechanical impact was applied between 10% and 50% repolarization of the action potential (i.e., which is similar to the vulnerable window in the left panel of Figure 2.4), this can lead to the initiation of self sustaining spiral waves.

This is shown in Figure 2.8. The SAC depolarize the tissue behind the action potential, and a new action potential arises that propagates in some directions, but is blocked in other directions (see Fig 2.8 at 17 and 31 ms). As a result two spirals are born. Garny and Kohl showed that there is only a very narrow time window for which such spiral waves can be initiated [38, 80]. This has also been observed in experiments by Link et al. [96].

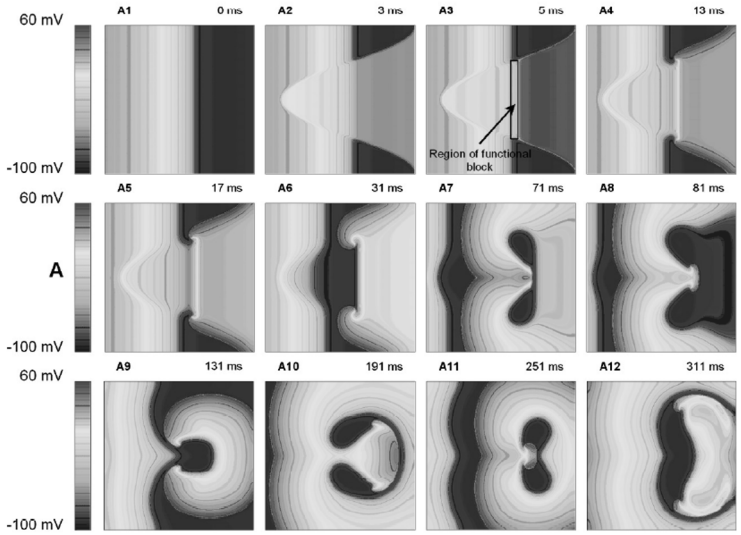

Figure 2.8: Initiation of spiral waves after a mechanical impact. See text for explanation. Reprinted with permission from [38]. For color see page 203.

Similar results have been reported by Li et al. [94], who investigated the induction of ventricular arrhythmias after a mechanical impact using a 3D bidomain model of the human ventricles. Membrane kinetics were represented by the LR1-A model [5], which is a modified version of the Luo-Rudy-1 model [98]. Impact effects were modeled via the SAC activation in the region representing the impact region. They showed that the impact region can lead to different cellular responses such as: new action potentials, shortening or lengthening of the AP. Furthermore, they showed that a mechanical impact can induce re-entry via the activation of the SAC.

In addition to the induction of spiral waves, some studies have also considered how MEF affects the termination of spiral waves using a large amplitude stimulus (i.e., defibrillation). In [51, 177], it was shown that SAC can lead to an increase in defibrillation threshold, which has also been reported in clinical and experimental studies [63, 97, 182].

2.5 Conclusion

This review addresses some of the fundamental effects of deformation on wave propagation in RD systems. We provide a general description of the framework used to model MEF and give necessary physiological background regarding the underlying processes, with particular focus on cardiac muscle. Furthermore, we discuss several studies that have shown that deformation has an effect on many important aspects of wave propagation. Studies on MEF are still in their infancy and much needs to be done to further understand the resulting feedback dynamics. In particular, more realistic biophysical models need to be developed to more accurately describe the processes that occur during contraction, and how passive properties of RD systems such as the capacitance C and diffusion $\mathbf{D}$ tensor are affected by deformation. Additionally, a more realistic description of the passive mechanical properties of the tissue should be pursued. Cardiac muscle exhibits orthotropic and heterogeneous material properties, which play a significant role during tissue deformation. The description of active cell tension requires improvement to better represent the relationship between contractile tension, the intracellular calcium transient, and changes in cell length. Furthermore, anisotropic active stresses may be important for MEF. It would be interesting to investigate the effects of MEF in 3D models using more realistic 3D anatomical representations. There are already several models that at least partially address some of these processes [79, 118, 119], but more needs to be done in this direction. In addition to such numerical studies, many interesting questions may be addressed using analytical methods such as singular perturbation theory, which may be extended to the study of RDM systems.

Acknowledgments

This review was funded by the Netherlands Organization for Scientific Research (NWO grant number 814.02.014). M.P.N. was supported by the Marsden Fund Council from New Zealand government funding, administered by the Royal Society of New Zealand.

CHAPTER 3

Self-Organized Pacemakers in a Coupled Reaction-Diffusion-Mechanics System

A.V. Panfilov[1], R.H. Keldermann[1] and M.P. Nash[2]

[1] *Theoretical Biology/Bioinformatics Group*
Utrecht University
Padualaan 8, 3584 CH Utrecht, The Netherlands

[2] *Bioengineering Institute and Department of Engineering Science*
University of Auckland
Private Bag 92019, Auckland, New Zealand

Phys. Rev. Lett. 95: 258104 (2005)

Abstract

Using a computational model of a coupled reaction-diffusion-mechanics system, we found that mechanical deformation can induce automatic pacemaking activity. Pacemaking was shown to occur after a single electrical or mechanical stimulus in an otherwise non-oscillatory medium. We have studied the mechanisms underpinning this effect and conditions for its existence. We show that self-organized pacemakers drift throughout the medium to approach attractors with locations that depend of the size of the medium, and on the location of the initial stimulus.

3.1 Introduction

Reaction-diffusion equations describe a wide variety of non-linear systems in physics, chemistry and biology. They describe non-linear wave patterns in the Belousov-Zhabotinsky (BZ) chemical reaction [199], in the processes of morphogenesis of the mould *Dictyostelium discoideum* (Dd) [183], of electrical activity in cardiac tissue [43], and in many other biological systems. Propagation of non-linear waves is usually accompanied by other important processes. One of the most fundamental is the mechanical deformation of the medium. Indeed, the primary physiological function of the electrical waves in the heart is the initiation of cardiac contraction. Contraction of the heart in turn affects the process of wave propagation resulting in a complex global feedback phenomenon known as mechano-electrical feedback, which has been studied in electrophysiology for well over a century [83]. Non-linear waves during Dd morphogenesis induce motion of the cells, which substantially affects wave dynamics [183]. Waves in the BZ reaction in gels cause deformation [197], which in turn affects spiral wave dynamics [109]. Furthermore, a 'chain reaction' of spiral wave births and deaths can result from an externally controlled deformation of a medium [17]. Although the interplay of mechanical deformations with the dynamics of reaction-diffusion systems is an important phenomenon, most studies have separately considered the mechanical deformation or non-linear wave propagation in reaction-diffusion systems.

Recently, we introduced a general framework to study the effects of mechanical deformation on reaction-diffusion systems [117]. We described a deformable, excitable medium capable of conducting non-linear waves of excitation, which initiate contraction. The reaction-diffusion system was defined using a general curvilinear coordinate system, with a metric determined using the equations of continuum mechanics. In turn, deformations were initiated and controlled by the reaction-diffusion system. We illustrated this concept using simple reaction-diffusion models of cardiac excitation that have been successfully applied in electrophysiology [36, 205]. However, the formulation in [117] lacks several important feedback mechanisms, including a description of the stretch-activated channels, which are considered to be the main physiological basis of mechano-electrical feedback in cardiac tissue [83].

This chapter reports a novel phenomenon for coupled reaction-diffusion mechanics systems: the formation of self-organized pacemakers. To this end, we have extended the electro-mechanical framework in [117] to include a description of the stretch-activated transmembrane currents. We have investigated the mechanisms underpinning these self-organized pacemakers, and have studied their dynamical properties, such as drift patterns and the dependence of drift on the initial conditions and medium size. Self-organization of pacemakers is important to the general theory of reaction-diffusion systems [104, 165] as well as for applications, such as for pacemaker activity in cardiac tissue to initiate the normal heart beat [83].

3.2 Methods

3.2.1 Electro-Mechanical Model

We start with the three-variable reaction-diffusion-mechanics model of excitable tissue introduced in [117]:

$$\frac{\partial u}{\partial t} = \nabla^2 u - ku(u-a)(u-1) - uv - I_s \tag{3.1}$$

$$\frac{\partial v}{\partial t} = \varepsilon(u)(ku - v) \tag{3.2}$$

$$\frac{\partial T_a}{\partial t} = \varepsilon(u)(k_T u - T_a) \tag{3.3}$$

$$\frac{\partial}{\partial X_M}\left(T^{MN}\frac{\partial x_j}{\partial X_N}\right) = 0 \tag{3.4}$$

$$T^{MN} = \frac{1}{2}\left(\frac{\partial W}{\partial E_{MN}} + \frac{\partial W}{\partial E_{NM}}\right) + T_a C^{-1}_{MN} \tag{3.5}$$

$$\nabla^2 u = \frac{\partial}{\partial X_M}\left(\sqrt{C}C^{-1}_{MN}\frac{\partial u}{\partial X_N}\right) \tag{3.6}$$

Eqs. 3.1-3.2 provide a standard low-dimensional model of cardiac electrical propagation: u and v are normalized variables representing the transmembrane potential and recovery properties of the tissue, respectively; $(-ku(u-a)(u-1) - uv)$ is the total transmembrane ionic current per unit area [117]. The parameters are a, which represents the threshold of activation (and is a key control parameter in the simulations), k which controls the magnitude of transmembrane current ($k = 8$ in all simulations), and $\varepsilon(u)$, which sets the time scale of the recovery process: $\varepsilon(u) = 1$ for $u < 0.05$, and $\varepsilon(u) = 0.1$ for $u \geq 0.05$. For the parameter values used in this chapter, Eqs. 3.1-3.2 describe non-oscillatory cardiac tissue that supports stable propagation of excitation waves.

The excitable tissue in our model contracts and the mechanics is modulated by the variable T_a (described by Eq. 3.3), which represents the active stress generated by the medium. k_T governs the rate of tension development ($k_T = 10$ for all simulations).

Following standard continuum mechanics [101], we use two coordinate systems to define the deformation. $\{X_M\}$ are material coordinates embedded in the contracting tissue, and $\{x_i\}$ are the spatial reference Cartesian coordinates. The equations of continuum mechanics provide the relationship between these two coordinate systems ($x_i(X_M)$), i.e., they determine the deformed position of a point x_i that was initially located at X_M. This is achieved using the equations of stress equilibrium (Eq. 3.4) that arise from the physical laws of motion (conservation of linear momentum). In this work, we use a stress tensor of finite elasticity theory, T^{MN} (the second Piola-Kirchhoff stress tensor in Eq. 3.5), which contains two parts: (i) the active stress components, $T_a C^{-1}_{MN}$, where $C_{MN} = \partial x_k/\partial X_M \cdot \partial x_k/\partial X_N$ is the right Cauchy-Green deformation (metric) tensor of the $\{X_M\}$ coordinate system [67], and (ii) the passive elastic stress components, which are expressed in terms of the derivatives of a strain energy function (W) with respect to components of the Green's strain tensor, $E_{MN} = \frac{1}{2}(C_{MN} - \delta_{MN})$, where δ_{MN} is the unitary tensor. For this study, the strain energy function was chosen to be the Mooney-Rivlin constitutive law [67], $W = c_1(I_1 - 3) + c_2(I_2 - 3)$, where I_1 and I_2 are principal invariants of C_{MN}, and c_1 and c_2 are stiffness coefficients ($c_1 = 2$ and $c_2 = 6$ for all simulations, chosen to give rise to relative local deformations of approximately 15% following excitation, consistent with contracting cardiac tissue). Due to motion of the material coordinate system, we used a general curvilinear expression for the evaluation of the Laplacian in Eq. 3.1, given by Eq. 3.6, where $C = det(C_{MN})$.

The direct influence of contraction on excitation is given by a stretch-activated current I_s, known to be present in cardiac tissue [83]. In this study, we have incorporated a generic description of the stretch-activated currents into the model using:

$$I_s = G_s(\sqrt{C} - 1)(u - E_s), \tag{3.7}$$

where G_s and E_s are the maximal conductance and reversal potential of the stretch-activated channels, respectively. This type of relation is similar to that used in [177], but in our model the deformation of the medium is computed as a part of the mechanics solution procedure, therefore we use an explicit dependence of the conductance on the local dilatation ($\sqrt{C} - 1$). Furthermore, since the current through the stretch-activated channels occurs mainly during stretch, we assume that the current in Eq. 3.7 is present only if $\sqrt{C} > 1$. The value of the parameter E_s in our model was typically 1, and describes the depolarizing effect of the current observed experimentally [83, 177]. The value of G_s is one of the main determinants of the effects of deformation on wave propagation and was varied in our computations.

3.2.2 Numerical Integration Methods

The coupled electro-mechanical model was solved using a hybrid approach that combines an explicit Euler time integration scheme to compute the excitation characteristics of the medium, with non-linear finite element techniques to determine the large deformation mechanics of the tissue. The solution procedure is

as follows: after N_{mech} time integration steps for Eq. 3.1-3.3, the equations governing tissue mechanics (Eq. 3.4) are solved, subject to the active stresses T_a due to Eq. 3.3. The solution of Eq. 3.4 provides updated values of the metric tensor components C_{MN}, which in turn modulate excitation properties (via Eqs. 3.6 and 3.7) for the subsequent N_{mech} excitation time-steps.

The model solution parameters were the following: Euler computations were performed using a time integration step of $\Delta t = 0.03$ (dimensionless time units) and a space integration step of $\Delta x = \Delta y = 0.6$ (dimensionless space units), consistent with previous studies [117]. The mechanics mesh was defined using up to 15x15 finite elements. Each mechanical element contained up to 7x7 electrical grid points, and the value of $N_{mech} = 3$ was used. Thus, the finite difference mesh was up to 91x91 grid points. These parameters were chosen following a solution convergence study to ensure that the main results of this chapter (i.e., the onset of pacemakers) were insensitive to these parameter choices. No-flux boundary conditions were imposed for Eq. 3.1, and the boundaries of the medium were fixed in space for Eq. 3.4. Mechanically, the fixed boundaries are consistent with an isometric contraction regime: a standard experimental procedure for muscle mechanics, during which end-points of the tissue are fixed to maintain constant length. Full details of the mechanical and electrical coupling of the model, and the numerical (finite element) methods used to solve the equations of mechanics are given in [117].

3.3 Results

The upper panels of Figure 3.1 show the process of wave propagation after application of a single stimulus at the center of the medium, and in the absence of mechanical activity. We observed that the stimulus initiated a single wave of excitation (Figure 3.1.1) that vanished following propagation (Figure 3.1.2). The spatio-temporal evolution of this pulse is presented in Figure 3.1.3. In the presence of mechanical activity of the medium, we observed that the same initial conditions resulted in the onset of a stable pacemaker at the center of the medium (Figures 3.1.4 and 3.1.5). Following a single stimulus, the initial propagating wave gave rise to subsequent waves that spontaneously appeared at the center of the medium (Figure 3.1.6). Thus, mechanical deformation can initiate self-oscillatory activity in a reaction-diffusion system. The mechanism of this phenomenon is explained in Figure 3.2a, which illustrates the excitation variable u (solid line) and local dilatation (dashed line) at the center of the medium during the pacemaking activity given in Figures 3.1.4-6. We observed contraction (negative dilatation) following excitation, but as the wave traveled away from the center, electrical recovery and localized stretch (positive dilatation) occurred in this region. This central stretch resulted from contraction of the surrounding parts of the medium and led to an inward current produced by the stretch-activated channels I_s (Eq. 3.7). This current depolarized the central tissue resulting in the onset of a subsequent excitation.

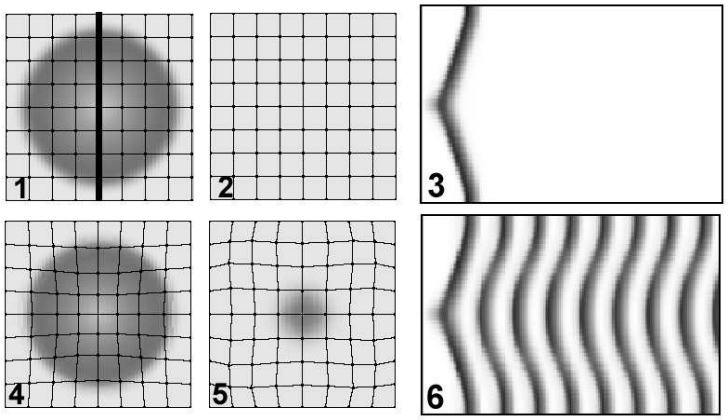

Figure 3.1: Development of a stable pacemaker due to mechanical deformation. The upper panels show wave propagation in the absence of mechanical activity at time 10.17 time units (panel 1), and 16.17 time units (panel 2). Panel 3 shows the time-space plot for the bold vertical line marked in panel 1. The medium size was 28.8 space units and the total integration time spanning left-to-right in panel 3 is 100 time units. Panels 4-6 show a similar simulation to that in panels 1-3, but including mechanical deformation of the medium, with $G_s = 0.5$, $E_s = 1$ and $a = 0.05$. The period of the pacemaker was 11.1 time units. For the time-space plots (panels 3 and 6), time runs along the horizontal axis.

The period of the pacemaker induced by the mechanical deformation was modulated by the parameter values. Increasing the stretch-activated current I_s by increasing G_s led to a decrease in the pacemaker period (Figure 3.2b). On the other hand, decreasing the excitation threshold a also decreased the period of the pacemaker.

The parameters G_s and E_s that modulate the stretch-activated channels in Eq. 3.7 were both important for the pacemaking effect we observed. From Eq. 3.7, one can expect that the threshold value of the I_s current necessary to initiate new excitations is proportional to $-G_s(u^* - E_s)$ (where u^* is some constant). In order to test this, Figure 3.3a illustrates the boundary of the onset of oscillations in the parametric space for G_s^{-1}, E_s. As expected, we see that G_s^{-1} linearly increases with E_s. The relationship between G_s and a required for pacemaking was more complex (Figure 3.3b). We observed the onset of oscillations only for $a < 0.08$. For $0.08 \leq a < 0.12$ (above the dashed line), we obtained only one extra excitation that failed to propagate through the medium, and for $a \geq 0.12$ the propagation of the first wave also failed.

We found that if a pacemaker was established at any point other than the center of the medium, then it drifted to other locations in the medium. We performed computations by initiating the first pulse at 56 different locations throughout the medium. Almost all stimuli resulted in pacemakers that drifted to approach one of four attractors that were symmetrically located on the center-lines across the medium, and at approximately 1/6 of the medium size from the boundary, as illustrated in Figure 3.4a. In the cases where the stimulus was initiated on the

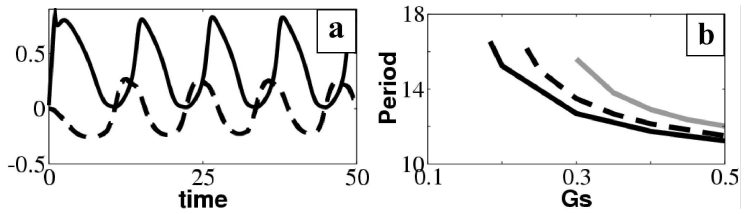

Figure 3.2: (a) The time course of the excitation variable u (solid line) and local dilatation ($\sqrt{C}-1$) (dashed line) at the center of the medium for the computation presented in Figures 3.1.4-6. (b) Period of the pacemaker as a function of G_s for $a=0.05$ (solid line), $a=0.06$ (dashed line), and $a=0.07$ (gray line).

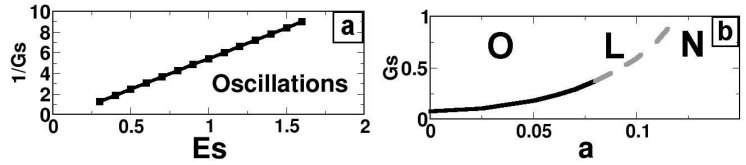

Figure 3.3: Values of the parameters (a) G_s^{-1}, E_s, and (b) G_s, a, required for pacemaking oscillations. Symbols in panel (b) denote: **O**- oscillations regime; **L**- single additional local response; and **N** - no wave propagation. Other parameter values were the same as those for Figure 3.1.

diagonals of the medium, the pacemaker drifted to the central point, where it became stationary. The attractor locations were not affected by the size of mechanical elements. A 50% decrease in the element size resulted in negligible (less than 5%) changes in the attractor locations. However, we found that the arrangement of attractor locations depended on the medium size (Figure 3.4b). If the medium size was decreased, then the peripheral attractors (open circles in Figure 3.4a) shifted toward the boundaries of the medium. If the size was less than 25 space units, the pacemaking activity settled at the boundary of the medium (defined as shift=1 in Figure 3.4b) at the middle of the corresponding side, similar to Figure 3.4a. For larger sizes, the four peripheral attractors approached the center of the medium. For media larger than 34 space units, a single attractor was located at the center of the medium (shift=0). This attractor persisted for all larger sizes of the medium for which computations were performed (up to 54 space units). It is reasonable to expect that in the limit of very large system size (when the relative influence of boundary will be negligible), the pacemaker drift will either disappear or become independent of a specific location. However, we were not able to approach this limit, nor find a substantial decrease in drift velocity towards the center for medium sizes larger than 34 space units. We found that pacemaker drift was due to a complex interaction between the depolarizing stretch-activated current and the recovery dynamics of the medium. For example, if the contraction was substantially delayed with respect to the excitation (more than 5 time units), then the pacemaker drift was always directed toward the boundary of the

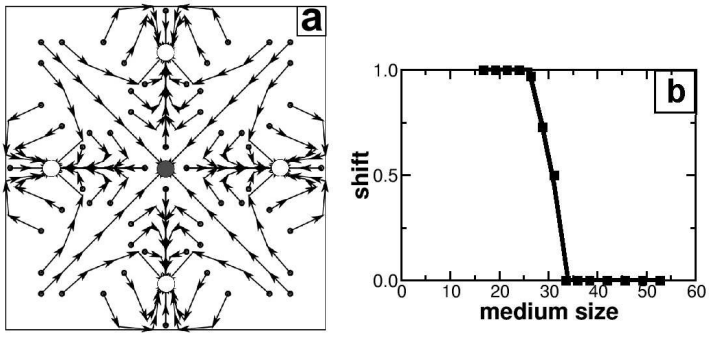

Figure 3.4: Pacemaker drift. (a) Depending on the site of initiation, pacemakers drifted to one of five attractors symmetrically located throughout the medium. Computations were carried out using a medium of size 28.8x28.8 space units; the size of each mechanical element was 7x7 electrical grid points. The arrows show the pacemaker trajectories, and filled black circles mark the initial sites of stimulation. (b) Relative shift - defined as the distance from the center of the medium to the peripheral attractors (denoted by white circles in (a)) divided by half of the medium size - plotted against medium size. Computations were carried out for $G_s = 0.5, E_s = 1$ and $a = 0.05$.

medium. We also found that the magnitude of the stretch-activated current at the point of initial stimulation was greater for a smaller medium compared to that for a larger medium. However, it remains to be determined how these observations can be used to robustly predict drift direction for a given model.

Finally, note that we were also able to initiate pacemaking activity using a single mechanical stimulus (i.e., a rapid local stretch of the tissue) instead of electrical stimulation.

3.4 Discussion

We found that mechanical deformation can induce pacemakers in excitable tissue, and that this effect is due to the depolarization action of the stretch-activated current. Although we use very general descriptions of the medium's excitation-mechanics properties and the dynamics of stretch-activated channels, we propose that this effect could be important in cardiac tissue. Indeed, as shown in detailed biophysical models of cardiac tissue [177], and in experimental studies [83], stretch-activated channels can depolarize cardiac tissue in a manner similar to that in our computations. The induction of a pacemaker depends on the relation of the depolarizing effect of I_s with the excitation properties of cardiac cells. These properties differ substantially throughout the heart [83], and many types of cardiac cells show self-oscillating behavior, even in the absence of applied stretch. Therefore, given the wide variety of properties of cardiac cells and the depolarizing action of the stretch-activated channels in the heart, we propose that the effects of induction of pacemaking activity can exist for some types of cardiac cells, particularly those that exhibit self-oscillation dynamics.

One of limitations of our study is that our formulation neglects the fibrous anisotropy of cardiac tissue, which is important both for the electrical and the mechanical properties of the heart. We chose not to consider these effects, since the main aim of this study was to investigate the basic effects of deformation on a general reaction-diffusion system. The influence of cardiac anisotropy is likely to add additional effects, and will be addressed in future studies.

Acknowledgments

We are grateful to Prof. P.J. Hunter, Dr. P. Kohl and Prof. H. Verschelde for valuable discussions. This research was funded by the Netherlands Organization for Scientific Research (NWO grant number 814.02.014). M.P.N. was supported by the Marsden Fund Council from New Zealand government funding, administered by the Royal Society of New Zealand.

CHAPTER 4

Pacemakers in a Reaction-Diffusion-Mechanics System

R.H. Keldermann[1], M.P. Nash[2] and A.V. Panfilov[1]

[1] *Theoretical Biology/Bioinformatics Group*
Utrecht University
Padualaan 8, 3584 CH Utrecht, The Netherlands

[2] *Bioengineering Institute and Department of Engineering Science*
University of Auckland
Private Bag 92019, Auckland, New Zealand

J. Stat. Phys. 128: 375-392 (2007)

Abstract

Non-linear waves of excitation are found in various biological, physical and chemical systems and are often accompanied by deformations of the medium. In this chapter, we numerically study wave propagation in a deforming excitable medium using a two-variable reaction-diffusion system coupled with equations of continuum mechanics. We study the appearance and dynamics of different excitation patterns organized by pacemakers that occur in the medium as a result of deformation. We also study the interaction of several pacemakers with each other and the effects of pacemakers in the presence of heterogeneities in the medium. We found that mechanical deformation not only induces pacemakers, but also has a pronounced effect on spatial organization of various excitation patterns. We show how these effects are modulated by the size of the medium, the location of the initial stimulus, and the properties of the reaction-diffusion-mechanics feedback

4.1 Introduction

Reaction-diffusion (RD) equations are one of the most studied classes of partial differential equations (PDEs) in mathematics applied to biological, chemical and physiological sciences [110]. They describe various processes of spatial organization in different systems with the most important solutions being non-linear waves, vortices and stationary Turing patterns. Each of these solutions have been studied extensively over the years using both analytical and numerical approaches. Non-linear waves can be found in many biological, physical and chemical systems. Examples of such waves include: chemical waves in the Belousov-Zhabotinsky (BZ) chemical reaction [199], and waves of carbon monoxide oxidation on platinum catalytic surfaces [68], both of which organize spatio-temporal patterns; and electrical waves in retinal and cortical nerve tissue [42], where they may underlie neurological diseases such as epilepsy [3, 29]. Non-linear waves also control the morphogenesis of the *Dictyostelium discoideum* (Dd) amoeba [40] and the initiation of the development of *Xenopus* oocytes after fertilization [91]. One of the most practically important applications of non-linear waves are activation waves in the heart that give rise to cardiac muscle contraction.

The main function of the heart is to pump blood, which is achieved by the coordinated contraction of millions of cardiac cells (myocytes). This coordination is achieved via non-linear electrical waves that propagate through the cardiac tissue and initiate cardiac contraction. Problems in the electrical system of the heart may result in cardiac arrhythmias, e.g. rapid activation and spatial desynchronization of mechanical contractions in the heart [116, 136], which cause the mechanical pump function of the heart to malfunction. In the US alone, more than 450,000 people die suddenly each year as a result of cardiac arrhythmias [204].

Electrical excitation of a cardiac cell is a sudden change of its transmembrane potential, from its resting state (which is around -90 mv), to an excited state (around +10 mv). This rapid change of the membrane potential is a result of a

complex interaction of different membrane ionic channels and pumps, which are time and voltage dependent. Excitation of a cardiac cell can be initiated by an electrical stimulus that produces an initial depolarization of the cell membrane from its resting state to exceed a certain threshold value (approximately -60 mv). Once this threshold value is reached, a very rapid "all or none" response follows that brings the membrane potential up to +10 mv. This is called the depolarization phase. After depolarization, there is a repolarization phase during which the resting membrane potential is restored. However, during the repolarization phase cells are unable to respond to a subsequent stimulus, because not all the ionic channels have yet recovered from the depolarization phase. This is called the refractory period. In cardiac tissue, muscle cells are electrically coupled such that if one cell becomes excited (depolarized), the membrane potential of its neighboring cells also increases. If the threshold is reached in these cells, then they also become depolarized and in turn the membrane potentials of their neighbors is also raised, and so on. This results in the formation of a propagating wave of excitation.

Normally, cardiac excitation is produced by a specialized group of cells in the heart (the sinus node) consisting of self-oscillating cells that periodically initiate propagating waves of excitation. The sinus node is a complex heterogeneous structure and the precise details of its function are not completely understood.

Mathematical modeling is widely used to study wave propagation in the heart. There are many models available that describe the action potential of single cells [2, 12, 28, 33, 98, 172]. Important for these models is that they should cover the fundamental features, which we described above. In particular cells must be excitable, they require a refractory phase, and depolarization must propagate as a non-linear wave [43].

Usually, propagation of non-linear waves is accompanied by other important processes of which one of the most fundamental is mechanical deformation. Non-linear waves during Dd morphogenesis induce cell-motion, which substantially affects wave dynamics [183]. Waves in BZ reactions cause deformation of the gel [197], which in turn affects spiral wave dynamics [109]. In the heart, electrical waves initiate contraction of cardiac tissue.

The process by which cellular depolarization causes myocytes to contract is called excitation-contraction coupling (ECC). During depolarization the concentration of intracellular calcium ions increases through the so called L-type calcium channels, which are located on the cell membrane. This calcium current causes a subsequent release of a much larger quantity calcium stored within specialized cellular compartments called the sarcoplasmatic reticulum. The increase of the intracellular calcium concentration initiates cardiac contraction via several conformational changes of interacting proteins: troponin C, actin, and myosin [83].

Contraction of cardiac tissue also affects the process of wave propagation [83], which is called mechano-electrical feedback (MEF). MEF may have both anti-arrhythmic and arrhythmogenic consequences, and has been studied for well over a century [83]. For example, mechanical deformation has been shown to alter the electrical properties of myocytes [160] and plays an important role during

arrhythmias [35]. Two phenomena that involve MEF are *Commotio Cordis* [94] and the *precordial thump*. Commotio Cordis is a situation in which a blunt, non-penetrating object strikes the chest and produces cardiac arrhythmias that may lead to sudden cardiac death. The precordial thump is a life saving technique during cardiac arrest in which the heart beat can be re-activated by delivering a sharp blow to the chest.

The precise mechanisms underpinning the role of MEF in arrhythmogenesis remain unclear. Modeling can be a helpful tool to investigate the underlying mechanisms of cardiac arrhythmias. Although the interplay of mechanical deformation with the dynamics of RD systems is an important phenomenon, most studies have separated mechanical deformation from non-linear wave propagation.

We have previously presented a general framework for studying the effects of mechanical deformation on RD systems [117]. There we described a deformable, excitable medium capable of conducting non-linear waves of excitation. We did not aim to perform a detailed study that combines physiologically detailed excitation models with biophysically-based contraction models and realistic cardiac anatomy. Rather, we have started from a fundamental description of the electromechanical coupling using basic models of these processes together with simple rectangular geometries. This is because our aim was to study the fundamental effects that MEF may have on wave propagation, and thus elucidate the underlying mechanisms. The RD system was defined in a general curvilinear coordinate system, with a metric tensor determined by the equations of continuum mechanics. In turn, deformations were initiated and controlled by the RD system. We illustrated this concept of a coupled reaction-diffusion-mechanics (RDM) system using a simple two variable RD model of cardiac excitation. However, the model in [117] lacks several important feedback mechanisms, including a representation of the stretch-activated channels, which describe one of the main effects of MEF in cardiac tissue.

In a subsequent study [129], we introduced another RDM model, which contained a description of the stretch-activated channels. There, we found that mechanical deformation can induce automatic pacemaking activity. Pacemaking was shown to occur after a single electrical or mechanical stimulus in an otherwise non-oscillatory medium. We showed that pacemaking activity resulted from stretch of the medium and subsequent depolarization via the stretch-activated channels. However, we restricted our study to a small parameter region and only investigated the onset and behavior of a single pacemaker.

In this article we extend the results of our previous chapter [129] and study the effects of different conductivities for stretch-activated channels, multiple pacemaker sites and parametric gradients on drift and excitation patterns.

4.2 Methods

4.2.1 Reaction-Diffusion Equations

Reaction-Diffusion equations are given by the following expression:

$$\partial \mathbf{V}/\partial t = \nabla\cdot(\mathbf{D}\nabla\mathbf{V}) + \mathbf{F}(\mathbf{V}) \tag{4.1}$$

where $\mathbf{V}$ is a vector of concentrations, $\mathbf{D}$ is a diffusion tensor and $\mathbf{F}(\mathbf{V})$ is a non-linear vector function. The number of components and properties of the diffusion tensor are different for different types of systems.

For cardiac tissue, the minimal number of components of $\mathbf{V}$ is two: one variable that describes the transmembrane potential and one variable that controls the recovery processes [34]. Such low dimensional models can reproduce some important measurable characteristics of cardiac tissue, such as action potential restitution properties, the general shape of the action potential in the heart, and the effects of tissue anisotropy and heterogeneity [2, 173]. By adding one or two extra variables these models can also describe experimentally measured conduction velocity restitution and the exact shape of the action potential [32]. However, low dimensional models do not describe detailed biophysical mechanisms of excitation that occur due to different dynamics of ionic channels on the cardiac membrane. To describe ionic channel dynamics one should use so-called ionic models for cardiac tissue that are based on the founding paper by Hodgkin and Huxley [59]. Ionic models describe the properties of each individual ionic channel and are based on experimental studies of voltage and time dynamics using voltage clamp techniques. Recent ionic models for cardiac tissue include around 60-100 variables to model many details of ionic channel dynamics identified in cardiac cells [124]. Both low dimensional and ionic models can be used to study wave dynamics in cardiac tissue. Low dimensional models are used as tools for more general qualitative studies of possible new effects, while ionic models are used for detailed quantitative studies of specific effects for which molecular membrane mechanisms are established, e.g. drug applications, genetic disorders, etc.

4.2.2 Modeling Elastic Deformations

During a normal heart beat, cardiac cells deform up to the order of 15% [103]. Therefore, finite deformation elasticity theory must be applied to describe the deformations in the medium. Following standard continuum mechanics, we use two coordinate systems to describe the deformations. Assume that $\mathbf{x} = \{x_i\}$ describes the present (deformed) position in rectangular Cartesian coordinates of a material particle that occupied the location $\mathbf{X} = \{X_M\}$ in the reference (undeformed) configuration. The deformation gradient tensor, $\mathbf{F}$, transforms the undeformed line segment, $d\mathbf{X}$, into the deformed line segment, $d\mathbf{x}$, by $d\mathbf{x} = \mathbf{F}d\mathbf{X}$ with $F^i_M = \frac{\partial x_i}{\partial X_M}$. The right Cauchy-Green deformation tensor, $\mathbf{C}$, describes how each component of the undeformed line segment $d\mathbf{X}$ contributes to the squared length of the deformed

line segment $d\mathbf{x}$ and is defined in terms of the deformation gradient tensor:

$$\mathbf{C} = \mathbf{F}^T\mathbf{F} \qquad \text{or} \qquad C_{MN} = \left\{ \frac{\partial x_k}{\partial X_M} \frac{\partial x_k}{\partial X_N} \right\} \tag{4.2}$$

The right Cauchy-Green deformation tensor is independent of rigid body motion. We can define three principal components, which remain unchanged under coordinate rotations at a given state of deformation: $I_1 = tr\mathbf{C}$, $I_2 = 1/2[(tr\mathbf{C})^2 - tr\mathbf{C^2}]$ and $I_3 = \det\mathbf{C}$. Next, we introduce the Lagrangian Green's strain tensor, $\mathbf{E}$, which is defined by:

$$\mathbf{E} = \frac{1}{2}(\mathbf{C} - \mathbf{I}) \qquad \text{or} \qquad E_{MN} = \frac{1}{2}(C_{MN} - I_{MN}) \tag{4.3}$$

where $\mathbf{I}$ is the unitary tensor. Note that both $\mathbf{C}$ and $\mathbf{E}$ are symmetric tensors by definition. To represent material behavior independent of rigid body motion, we use the second Piola-Kirchhoff stress tensor, T^{MN} [101], that represents the force per unit undeformed area, acting on an infinitesimal element of surface in the reference configuration.

The equations that govern finite deformation elasticity arise from the conservation of linear momentum following Newton's laws of motion [101] and for static equilibrium are given by:

$$\frac{\partial}{\partial X_M}\left(T^{MN}F_N^j\right) = 0 \tag{4.4}$$

The relationship between the stress and strain (T^{MN}, and C_{MN} or E_{MN}) is given by an appropriate constitutive relation and is described later.

4.2.3 Coupled Reaction-Diffusion-Mechanics Equations

Our model is based on the concept of a deforming RD medium, which we introduced in [117]. In order to mathematically couple the RD system and the mechanical equations, the relationship between Eqs. 4.1 and 4.4 must be considered. In general, each term in Eq. 4.1 may depend on the state of deformation, resulting in:

$$\partial\mathbf{V}/\partial t = \nabla\cdot(\mathbf{D}(\mathbf{C})\nabla\mathbf{V}) + \mathbf{F}(\mathbf{V},\mathbf{C}) \tag{4.5}$$

where $\mathbf{C}$ is the right Cauchy-Green deformation tensor, defined by Eq. 4.2.

The effects of the RD equations on the mechanics equations arise from the fact that some variables V_i in Eq. 4.1 control the development of the active stress in the medium. For example, the contractile force developed by cardiac myocytes is determined by the intracellular concentration of calcium ions $[Ca^{2+}]_i$, which is one of the variables of the RD model describing cardiac cells [66]. In a modeling context, we split the second Piola-Kirchhoff tensor into active and passive stress components (see [117]), and use one or more of the variables of Eq. 4.5 to modulate the active stress development:

$$T^{MN} = {T_p}^{MN}(\mathbf{C}) + {T_a}^{MN}(\mathbf{C}, V_a) \tag{4.6}$$

where ${T_p}^{MN}(\mathbf{C})$ and ${T_a}^{MN}(\mathbf{C},V_a)$ represent the passive and the active tissue response, respectively. In [117], passive tissue properties were chosen to obey the isotropic Mooney-Rivlin constitutive law, and active tissue properties were also considered to be isotropic, and was determined using ${T_a}^{MN}(\mathbf{C},V_a) = V_a C^{MN}$. Other mechanical conditions, such as non-isotropic active stress, non-linear passive tissue properties, etc. can be implemented by modifying the terms in Eq. 4.6.

In this study, we used the following RDM model:

$$\frac{\partial u}{\partial t} = \nabla^2 u - ku(u-a)(u-1) - uv - I_s \tag{4.7}$$

$$\frac{\partial v}{\partial t} = \varepsilon(u)(ku - v) \tag{4.8}$$

$$\frac{\partial T_a}{\partial t} = \varepsilon(u)(k_T u - T_a) \tag{4.9}$$

$$\frac{\partial}{\partial X_M}\left(T^{MN}\frac{\partial x_j}{\partial X_N}\right) = 0 \tag{4.10}$$

$$T^{MN} = \frac{1}{2}\left(\frac{\partial W}{\partial E_{MN}} + \frac{\partial W}{\partial E_{NM}}\right) + T_a C^{-1}_{MN} \tag{4.11}$$

$$\nabla^2 u = \frac{\partial}{\partial X_M}\left(\sqrt{C}C^{-1}_{MN}\frac{\partial u}{\partial X_N}\right) \tag{4.12}$$

To describe non-linear waves of cardiac excitation we use a low dimensional model based on the Aliev-Panfilov model [2]. Here, u is a dimensionless representation of the transmembrane potential and v is a dimensionless variable that describes the recovery properties of the tissue. The term $(-ku(u-a)(u-1)-uv)$ represents the total transmembrane ionic current per unit area and controls the fast processes, such as the initiation and upstroke of the action potential [117]. The threshold value a represents the excitability of the tissue and is an important parameter for pacemaking [129] ($a = 0.05$ unless otherwise noted). k controls the magnitude of the transmembrane current ($k = 8$ in all simulations), and $\varepsilon(u)$ determines the time scale of the recovery process and active stress: $\varepsilon(u) = 1$ for $u < 0.05$, and $\varepsilon(u) = 0.1$ for $u \geq 0.05$. The other parameters do not have a clear physiological meaning, but are chosen in order to reproduce key characteristics of cardiac tissue, such as the shape of the action potential, refractoriness and restitution of action potential duration. I_s represents the stretch-activated current, which is described below.

The Aliev-Panfilov model [2] is a low dimensional model for cardiac tissue that qualitatively describes the process of excitation and recovery of cardiac cells. However, the model does provide an experimentally based description of the restitution properties of action potential duration, which is important for the stability of wave propagation in the heart. The model presented in Eqs. 4.7-4.12 reproduces the shape of the action potential and the phenomenon of refractoriness as well as the effects of the stretch-activated current I_s, which is described below. The values of the parameters of the model were found by fitting the overall characteristics of cardiac propagation. Although the Aliev-Panfilov model uses

dimensionless units, simulation results can be compared to dimensional observations from experimental studies by comparing specific (dimensionless) model characteristics with experimental observations.

Deformation is modulated by the variable T_a (described by Eq. 4.9), which represents the active stress generated by the medium. The rate of tension development is determined by k_T ($k_T = 10$ for all simulations).

The mechanical part of this model is unchanged from [129]. The active stress component of the second Piola-Kirchhoff stress tensor T^{MN} in Eq. 4.11, is $T_a C^{-1}_{MN}$, and the passive elastic stress component, is expressed in terms of the derivatives of the strain energy function (W) with respect to components of the Green's strain tensor from Eq. 4.3. The strain energy function was chosen to obey the Mooney-Rivlin constitutive law [67]: $W = c_1(I_1 - 3) + c_2(I_2 - 3)$, where I_1 and I_2 are the first two principal invariants of C_{MN}, and c_1 and c_2 are stiffness coefficients, which together with the parameter k_T from Eq. 4.9 modulate the local deformations during contraction ($c_1 = 2$, $c_2 = 6$ for all simulations, chosen to give rise to relative local deformations of approximately 15% following excitation). Due to motion of the material coordinate system, we used a general curvilinear expression given by Eq. 4.12 to evaluate the Laplacian in Eq. 4.7, with $C = \det(C_{MN})$, which provides a diffusive membrane current per unit undeformed area.

The direct influence of contraction on excitation is given by the stretch-activated current I_s, known to be present in cardiac tissue [83]. As in [129] we use a generic description of the stretch-activated current into the model:

$$I_s = G_s(\sqrt{C} - 1)(u - E_s) \tag{4.13}$$

where G_s and E_s are the maximal conductance and reversal potential of the stretch-activated channels, respectively. The stretch-activated current in Eq. 4.13 is only present during stretch (i.e., when $\sqrt{C} > 1$). The value of the parameter E_s in our model was typically 1, and describes the depolarizing effect of the current observed experimentally [83, 177]. G_s determines the outcome of the simulations with respect to drift and excitation patterns ($G_s = 0.6$ unless otherwise noted).

4.2.4 Numerical Integration Methods

The coupled electro-mechanical model was solved using a hybrid approach that combines an explicit Euler time integration scheme to compute RD equations of the medium, with non-linear finite element techniques to determine the large deformation mechanics of the tissue. To formulate the finite element integral equations, we introduced a weighting field of virtual displacements, $\delta\mathbf{v} = \{\delta v_j\}$, and the weak form of the stress equilibrium equations (4.4) is given by:

$$\int_{V_0} T^{MN} F^j_N \frac{\partial \delta v_j}{\partial X_M} \, dV_0 = \int_{S_2} \mathbf{s} \cdot \delta\mathbf{v} \, dS \tag{4.14}$$

where V_0 is the undeformed volume and S_2 is the portion of the boundary subject to external tractions $\mathbf{s}$. Eq. 4.14 was solved using the finite element method described in [117].

The solution procedure is as follows: after N_{mech} time integration steps for the RD equations (Eqs. 4.7-4.9), the equations governing tissue mechanics are solved, using active stress components produced by the variable V_a of the RD equations (Eq. 4.9). Non-linear Newton iterations are performed to solve the stress equilibrium equations (Eq. 4.14) and provide updated values of the deformation tensor $\mathbf{C}$, which modulates excitation properties (via Eqs. 4.12 and 4.13) for the subsequent N_{mech} excitation time-steps.

The model solution parameters were the following: Euler computations were performed using a time integration step of $\Delta t = 0.03$ (dimensionless time units) and a space integration step of $\Delta x = \Delta y = 0.6$ (dimensionless space units), consistent with previous studies [129]. The mechanics mesh was defined using up to 16x16 finite elements. Each mechanical element contained 7x7 electrical grid points, and the value of $N_{mech} = 3$ was used. Thus, the finite difference mesh was up to 97x97 grid points. No-flux boundary conditions were imposed for Eq. 4.7, and the boundaries of the medium were fixed in space for Eq. 4.14. Mechanically, the fixed boundaries are consistent with an isometric contraction regime.

4.3 Results

4.3.1 Single Pacemaker

In Figure 4.1, we illustrate the development of various patterns due to pacemaking in a deforming medium. The wave was initiated at the center of the medium at $t = 0$. The upper panels show the process of wave propagation after one single stimulus in the absence of mechanical deformations. We see that the wave disappeared after propagating across the medium, after which the medium returned to a spatially homogeneous steady state configuration. Thus, in the absence of mechanical activity the reaction-diffusion model did not show oscillatory activity. The middle and lower panels of Figure 4.1 illustrate the results obtained from the same initial stimulus, but in the presence of mechanical deformations. The middle panels show wave propagation from the same initial conditions for $G_s = 0.2$. We see that in this case the mechanical deformation generates a pacemaker at the center of the medium, similar to that reported in [129]. Comparing the upper and middle panels at $t = 12$, we observed that the conduction velocity of the propagating wave was slightly slower in the presence of mechanical deformation. This is because contraction initiates stretch in front of the wave (see also Figure 4.2), thus the effective propagation distance is slightly increased. In the lower panels, we show a similar simulation with a higher value of $G_s = 0.6$. We also observed the onset of a pacemaker, but the spatial activation pattern was altered: as the wave propagated away from the center, stretch was generated near the boundaries, which caused local activations in these regions, resulting in a diamond like pattern of excitation (see $t = 12$, $t = 23$, lower panels).

The mechanism of pacemaking is explained in Figure 4.2, which shows the excitation variable u (black line), active stress T_a (dashed line) and the stretch activated current (gray line) for a point in the center of the medium.

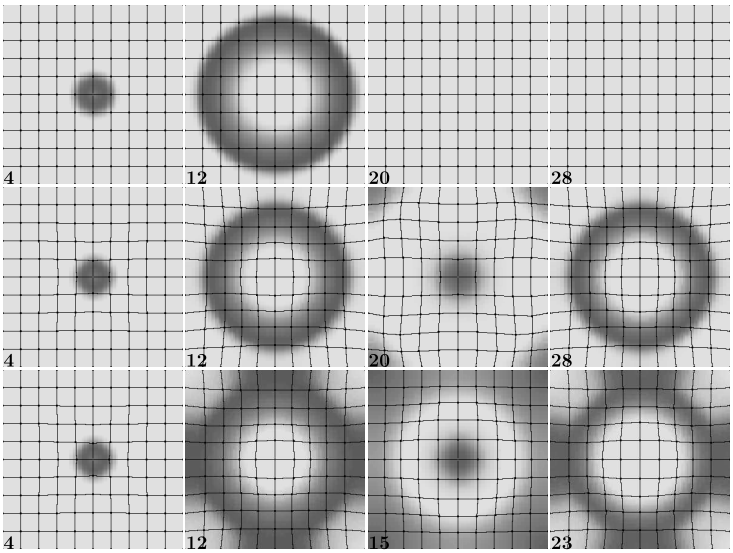

Figure 4.1: Excitation patterns after application of a single stimulus at the center of the medium in Eqs. 4.7-4.12. The upper panels show wave propagation in the absence of mechanical deformation. The middle panels show wave propagation in the presence of mechanical deformation with $G_s = 0.2$. In the lower panels, $G_s = 0.6$. The size of the medium is 61x61 grid points and $a = 0.05$ for all simulations. Dark shadings represent regions where $u > 0.6$. The period of the pacemakers in the middle and lower panels were 15.42 and 9.3 [t.u.], respectively. Times in time units [t.u.] are indicated at the lower left of each panel.

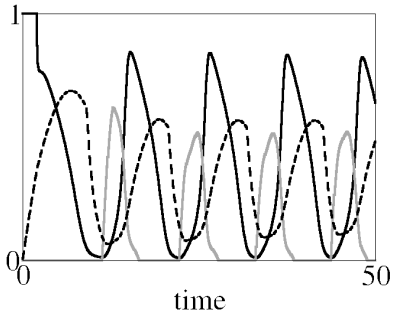

Figure 4.2: Time course of the excitation variable u (black line), active stress T_a (divided by 5; dashed line) and stretch-activated current (multiplied by 5; gray line) at the center of the medium for the computation presented in the lower panels of Figure 4.1.

Shortly after electrical activation, active stress T_a was generated in the center causing contraction/shortening of the tissue. Because I_s is only activated when tissue is elongated, no stretch-activated current I_s is generated during contraction (the gray line coincides with the x-axis). However, when the excitation wave propagated to some distance from the center, the contraction at the back of this wave caused stretch at the center, which led to an I_s current in accordance with Eq. 4.13. As a result of this inward current, the tissue depolarized and generated a new action potential, which resulted in subsequent excitations. Note, that because the stretch of the tissue occurs after the contraction this results in a substantial delay between the activation wave and I_s, and that the tissue at that point recovers from the refractory period and is capable for new excitations. Therefore, mechanical deformation acting via the stretch-activated current can initiate self-oscillatory activity in a RDM system. The activation patterns depend on the strength of the stretch-activated channel, which is modulated by the value of G_s. In [129], we showed that other parameters that increase I_s, or increase the excitability of the tissue, cause the onset of oscillations.

4.3.2 Drift of a Single Pacemaker

In Figure 4.1 the initial stimulus was in the center of the medium. We have shown that if the initial excitation is not located in the center, then the pacemaker will drift, and for a large size medium it will approach the center [129]. We show the results of such a simulation in Figure 4.3. Here, the primary point of excitation is located at the lower left corner of the medium. We see that the pacemaker drifts to the center, however, this occurs in a few stages. We observe that the site of the second activation was substantially shifted from the site of the initial activation and that this second activation occurred in a large arc-shaped area (see $t = 34$). The subsequent activation was again located closer to the center and occurred in a smaller area (see $t = 67$). Note, however, that the overall excitation pattern still remained complex. Following the next excitation, at $t = 100$, we observed a regular 'target' pattern type of excitations similar to that at $t = 144$. Finally, the pacemaker drifted to the center of the medium where it stabilized (see $t = 595$).

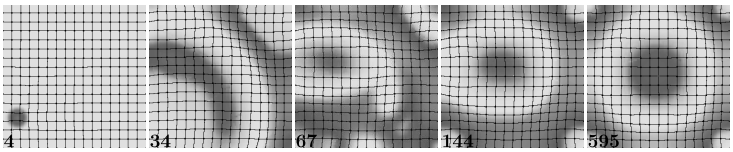

Figure 4.3: Drift of a pacemaker starting at the point located in the lower-left corner. The size of the medium is 97x97 grid points, $G_s = 0.6$ and $a = 0.05$.

We have also performed a similar simulation with a decreased value of $G_s = 0.5$. We obtained excitation patterns that were qualitatively similar to that shown in Figure 4.3. We also observed an arc shaped area, which in turn was reduced to a point. Similarly, the point drifted to the center of the medium where it stabilized.

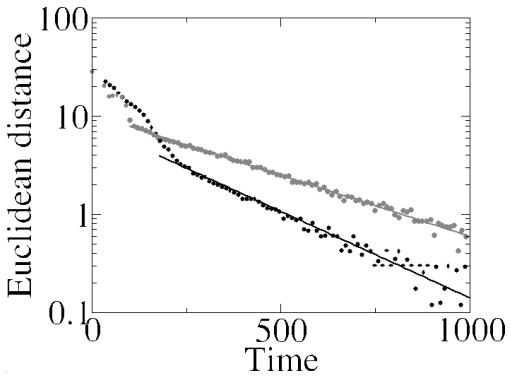

Figure 4.4: Distance ([s.u.]) from the pacemaker site to the center of the tissue as a function of time in [t.u.] for $G_s = 0.5$ (black line) and $G_s = 0.6$ (gray line).

To study the convergence of pacemaker drift, we determined the distance from the subsequent locations of the pacemakers to the center of the tissue. We show this for both $G_s = 0.5$ (black) and $G_s = 0.6$ (gray) on a logarithmic scale vs time in Figure 4.4. The last part of the curves can be well fitted to a straight line, indicating exponential convergence of pacemaking activity to the center. Furthermore, we see that for $G_s = 0.5$ the dependency has a steeper slope than $G_s = 0.6$, and drifts faster to the center of the medium.

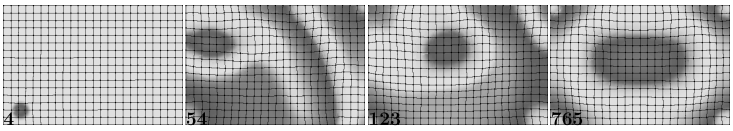

Figure 4.5: Drift of a pacemaker starting at the point located in the lower-left corner. The size of the medium is 145x97 grid points, $G_s = 0.6$ and $a = 0.05$.

In the above simulations we used a square domain to investigate pacemaker drift. We also studied pacemaker drift in a rectangular domain with the horizontal side being 1.5 times longer than the vertical side (see Figure 4.5). The primary point of excitation here is located at the lower left corner of the medium. We observed that the pacemaker drifted toward the center and that excitation patterns are qualitatively similar to that shown in Figure 4.3: drift occurred in few stages, with fast initial drift and slower secondary drift. We also observed arc shaped areas during drift. When drift of the pacemaker stabilized in the center of the tissue, we see that the shape of the wave is elliptical, while this is circular in Figure 4.3. This is a result of anisotropic stretch distribution in the horizontal and vertical directions for such domain shape.

4.3.3 Drift of Two Pacemakers

We also studied the dynamics of two coexisting pacemakers and their interaction (Figure 4.6). The initial starting points were located symmetrically about the vertical mid-line at the left and the right boundaries (see $t = 6$). We observed that both pacemakers drifted to the center of the tissue and merged with each other to form one stable single pacemaker (see $t = 480$). Note that the final pattern of excitation was the same as that in Figure 4.3.

We have also studied the interaction and drift of two non-symmetrically located pacemakers, which started from the initial conditions as illustrated in Figure 4.7 (see $t = 9$). Due to this non-symmetry, the upper pacemaker depolarized more tissue than the lower pacemaker (see $t = 89$). In this case, we also observed drift of both pacemakers to the center of the tissue, but this proceeded differently. We observed an initial drift of the 'small' lower pacemaker to the 'large' upper pacemaker, which eventually formed one single pacemaking site on the diagonal away from the center (see $t = 132$). Then, the single pacemaker drifted to the center of the medium where it stabilized (see $t = 288$). The final pattern in Figure 4.6 is the same as that shown in Figure 4.3.

From this we conclude that two coexisting pacemakers do not constitute a stable configuration. They merge to form one stable pacemaker that drifts to the center of the medium.

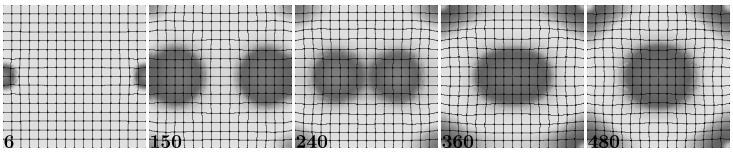

Figure 4.6: Drift of two simultaneously initiated pacemakers located symmetrically about the vertical mid-line. The size of the medium was 97x97 grid points. Other parameter values were the same as those for Figure 4.3.

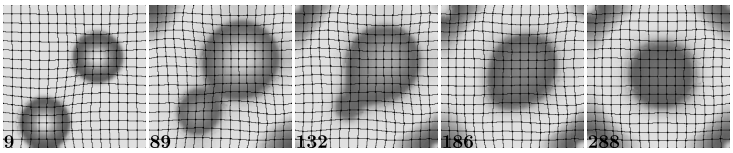

Figure 4.7: Drift of two pacemakers starting from non-symmetric locations. Other parameter values were the same as those for Figure 4.6.

4.3.4 Pacemaker Activity Resulting from Non-Local Stimulation

In the previous simulations, we only investigated single or multiple pacemaker sites. We now focus on an initial non-local stimulus. To this end, we studied

the excitation patterns that occurred as a result of applying an initial stimulation along the vertical mid-line of the tissue as is shown in Figure 4.8. We see that during the course of time the oscillating site becomes elliptic (see $t = 60$), then the asymmetry of the ellipse decreases, and finally we obtained a stable point source that was located in the center of the medium (see $t = 180$). We also observed that if the initial condition of the line was not located in the center, the line developed to a single point source, which then drifted to the center of the medium, and stabilized (results not shown). Therefore, as for the case of two pacemakers, non-local stimulation also approaches to one stable point pacemaker at the center of the medium.

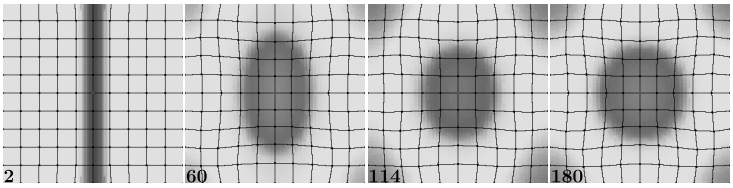

Figure 4.8: Pacemaker activity resulting from a non-local stimulation. The size of the medium is 61x61 grid points. Other parameter values were the same as those for Figure 4.3.

Pacemaking activity of the heart normally occurs in the sinus node. The sinus node has a complex heterogeneous structure and consists of different cell types, which have different properties with respect to excitability, coupling conductance and oscillation cycle lengths [203]. We studied pacemaker dynamics in a heterogeneous excitable medium with a gradient in excitability induced by changing the parameter a in Eq. 4.7. The value of a vs x is shown in Figure 4.9(left), the lower the value the higher the excitability. Figure 4.9(right) shows the dynamics of a single pacemaker in such a heterogeneous medium. We studied the dynamics initiated from two different initial conditions (marked by the black squares). The drift trajectories are represented by the black lines, and the directions of the pacemakers are indicated by the black arrows. In both cases, the pacemaker drifted from the initial location to the region located in the middle of the medium in the vertical direction and to the center of the horizontal region where the value of a was minimal. Drift patterns were qualitatively similar to the pattern shown in Figure 4.3. For the first few excitations following the initial stimulus, we also observed arc shaped areas of activation, which were subsequently reduced to a point source. For both initial conditions, it took approximately 500 time units to drift to the stable end configuration. We varied the gradient-location in our simulations, and the pacemaker always drifted to the lower value of a (results not shown). The excitability appeared to have a strong influence on the final position of the pacemaker. Note, that for smaller values of a, the pacemaker period was shorter. Thus, observed that pacemakers drifted to regions with shorter period.

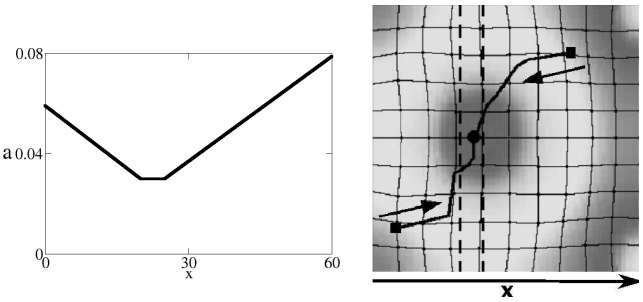

Figure 4.9: Pacemaker drift in a heterogeneous medium with respect to the excitability parameter a. (Left) value of a as function of x. (Right) Trajectories of drift (solid black lines). The initial starting points are marked with a black square and the end point is marked with a black circle. The arrows denote the direction of drift and the dashed lines represent the minimal value of a. The gray-scale picture shows the final state of the pacemaker drift. Other parameter values were the same as those for Figure 4.8.

4.4 Discussion

In this chapter, we studied drift of a single pacemaker and multiple pacemakers in a homogeneous medium. We observed that mechanical deformation has a pronounced effect on drift of pacemakers and induces different excitation patterns. Independent of the initial conditions, multiple pacemakers merged with each other to form one stable pacemaker at the center of the medium. Single pacemakers in a homogeneous medium always drifted to the center of the medium, where they stabilized. Thus, in a homogeneous model the center of the medium is a single global attractor for pacemaking activity. Note that in [129] the attractors for a smaller medium are located differently. We did not study this in this chapter, but it would be interesting to investigate this in more detail. Also, here we have only considered pacemaker drift in square/rectangular domains. It would be interesting to study these effects in domains with different shapes and different parametric gradients.

In the presence of a gradient of excitability, we found that pacemaker-drift no longer stabilized at the center, but drifted to the region with the lowest period (as determined by the excitability parameter a).

Although we use very general descriptions of the medium's excitation and mechanical properties, and the dynamics of stretch-activated channels, we propose that their effects may be important in cardiac tissue. Indeed, as shown in detailed biophysical models of cardiac tissue [177], and in experimental studies [83], stretch-activated channels can depolarize cardiac tissue in a manner similar to that in our computations. The induction of a pacemaker depends on the relation of the depolarizing effect of I_s with the excitation properties of cardiac cells. These properties differ substantially throughout the heart [83], and many types of cardiac cells show self-oscillating behavior, even in the absence of applied stretch. Therefore, given the wide variety of properties of cardiac cells and the depolar-

izing action of the stretch-activated channels in the heart, we propose that the effects of deformation on pacemaking activity can exist for some types of cardiac cells, particularly those that exhibit or are close to self-oscillation dynamics.

Recently, it was shown that calcium overload can lead to pacemaker activity in neonatal rat ventricular myocytes in the form of delayed after depolarizations and that in some cases pacemaker activity drifted throughout the medium [18]. However, the exact cause of the observed pacemaker activity drift is unresolved, and it remains to be seen whether this is a mechanical or electrophysiological effect.

One of the limitations in this study is that we neglected the anisotropic behavior of cardiac tissue, which is important for both the RD and mechanics systems. We chose not to consider these effects, because the main aim of this study was to investigate the basic effects of deformation on pacemaker dynamics.

The onset of pacemaker activity here is probably due to some type of supercritical Hopf bifurcation. Therefore it is reasonable to assume, that close to that bifurcation point the system is sensitive to small spatial and temporal variations and it would be interesting to study that using methods of statistical physics. Note also, that stochastic effects can be also important even for normal wave propagation in the heart as indicated in [162]. The influence of these features will likely add additional effects and will be addressed in future studies.

Acknowledgments

We are grateful to Prof. P.J. Hunter and Dr. P. Kohl for valuable discussions. This research was funded by the Netherlands Organization for Scientific Research (NWO grant number 814.02.014). M.P.N. was supported by the Marsden Fund Council from New Zealand government funding, administered by the Royal Society of New Zealand.

CHAPTER 5

Drift and Breakup of Spiral Waves in Reaction-Diffusion-Mechanics Systems

A.V. Panfilov[1], R.H. Keldermann[1] and M.P. Nash[2]

[1] *Theoretical Biology/Bioinformatics Group*
Utrecht University
Padualaan 8, 3584 CH Utrecht, The Netherlands

[2] *Bioengineering Institute and Department of Engineering Science*
University of Auckland
Private Bag 92019, Auckland, New Zealand

Proc. Natl. Acad. Sci. U.S.A. 104: 7922-7926 (2007)

Abstract

Rotating spiral waves organize excitation in various biological, physical and chemical systems. They underpin a variety of important phenomena, such as cardiac arrhythmias, morphogenesis processes and spatial patterns in chemical reactions. Important insights into spiral wave dynamics have been obtained from theoretical studies of the reaction-diffusion (RD) partial differential equations. However, most of these studies have ignored the fact that spiral wave rotation is often accompanied by substantial deformations of the medium. Here we show that joint consideration of the RD equations with the equations of continuum mechanics for tissue deformations (reaction-diffusion-mechanics (RDM) systems), yield important new effects on spiral wave dynamics. We show that deformation can induce the breakup of spiral waves into complex spatio-temporal patterns. We also show that mechanics leads to spiral wave drift throughout the medium approaching dynamical attractors, which are determined by the parameters of the model and the size of the medium. We study mechanisms of these effects and discuss their applicability to the theory of cardiac arrhythmias. Overall, we demonstrate the importance of RDM systems for mathematics applied to life sciences.

5.1 Introduction

Rotating spiral waves have been found in a wide variety of non-linear systems in physics, chemistry and biology. For example, they occur in Belousov-Zhabotinsky (BZ) chemical reactions [189, 199], and on platinum surfaces during the process of catalytic oxidation of carbon monoxide [68]. Biological examples of spiral waves include: spiral waves during morphogenesis of the *Dictyostelium discoideum* amoebae [183], spiral waves of calcium-induced calcium-release in *Xenopus* oocytes [91] and spiral waves in retinal and cortical nerve tissue [189]. Another important example is in the heart, for which spiral waves of electrical activity are thought to lead to life-threatening cardiac arrhythmias [29, 189].

Spiral waves have been studied extensively using mathematical modeling. In this context, spiral waves are solutions of the reaction-diffusion (RD) equations in two dimensions. There are a wide range of analytical and numerical approaches to study the basic features of these systems, as well as specific models for a variety of biological or chemical processes.

Spiral wave rotation is typically accompanied by other important processes. One of the most fundamental is the mechanical deformation of the medium. For example, spiral waves during *Dictyostelium discoideum* morphogenesis are relayed by chemotactically moving cells [183]; and chemical spiral waves cause deformation of the medium in which they rotate [197]. In the heart, the electrical waves initiate muscle contraction resulting in substantial local deformations. These deformations in turn affect the process of wave propagation in the heart, which is known as the phenomenon of mechano-electrical feedback. Mechano-electrical feedback has been studied in electrophysiology for over a century (see reviews

in [85]), and may have both anti- and pro-arrhythmic consequences. Whilst deformation is known to be important in the above-mentioned systems, most previous theoretical and experimental studies have not addressed the combined effects of medium mechanics and spiral wave dynamics.

To study the interactive effects of deformation and RD systems, one needs to combine two classes of partial differential equations: the RD equations (as above), and the equations of continuum mechanics, which govern the deformation of the medium. Furthermore, one must define the feedback relations that exist between them. In the heart, local deformations of up to 10-15% have been experimentally observed [103], thus finite deformation elasticity theory must be used to describe the tissue mechanics. The detailed coupling of the RD processes and mechanical deformations is complex and not completely understood, however general relationships have been established. For example, it is well known that heart tissue contraction is initiated by an influx of calcium ions into the cardiac myocytes, which is a typical state variable of biophysical RD models [30]. On the other hand, deformation changes the geometry of cardiac cells and ionic currents through the cardiac membrane (via stretch-activated channels [83]), thereby affecting the parameters of the RD system. We have proposed the concept of a reaction-diffusion-mechanics (RDM) system [117], which combines a very general description of deformation with a low dimensional RD system in order to study the basic effects of mechanics on non-linear wave propagation.

In this article, we apply our RDM modeling approach in order to study the fundamental effects of deformation on spiral wave dynamics. We find two new types of dynamics: mechanically induced breakup of spiral waves; and drift of spiral waves toward dynamical attractors due to mechanical deformation. These types of dynamics may be important in many applications. For example, in cardiac tissue, spiral breakup is considered as a likely mechanism of ventricular fibrillation, whilst meander and drift of spiral waves are believed to determine the type of cardiac arrhythmia [37, 44].

5.2 Methods

5.2.1 Mathematical Model

Our RDM model consists of a RD model with currents I_{so} and I_{si} developed by Dr. Flavio H. Fenton (personal communication), and is based on a three-variable Fenton-Karma RD model for cardiac excitation [33], coupled with the soft tissue mechanics equations described in [117, 129]:

$$\frac{\partial u}{\partial t} = \nabla^2 u - I_{fi}(u,v) - I_{so}(u) - I_{si}(u,w) - I_s(u,C) \tag{5.1}$$

$$\frac{\partial v}{\partial t} = \frac{\Theta(u_c - u) - v}{\tau_v(u)} \tag{5.2}$$

$$\frac{\partial w}{\partial t} = \frac{\Theta(u - 0.25) - w}{\tau_w(u)} \tag{5.3}$$

$$\frac{\partial T_a}{\partial t} = \varepsilon(u)(k_T u - T_a) \tag{5.4}$$

$$\frac{\partial}{\partial X_M}\left(T^{MN}\frac{\partial x_j}{\partial X_N}\right) = 0 \tag{5.5}$$

$$T^{MN} = \frac{1}{2}\left(\frac{\partial W}{\partial E_{MN}} + \frac{\partial W}{\partial E_{NM}}\right) + T_a C^{-1}_{MN} \tag{5.6}$$

$$\nabla^2 u = \frac{\partial}{\partial X_M}\left(\sqrt{C}C^{-1}_{MN}\frac{\partial u}{\partial X_N}\right) \tag{5.7}$$

where $\Theta(x)$ is the standard Heaviside step function: $\Theta(x) = 1$ for $x \geq 0$, and $\Theta(x) = 0$ for $x < 0$. Eqs. 5.1-5.3 provide a standard low-dimensional model of cardiac electrical propagation, which includes a qualitative description of three main ionic currents that modulate the activation of cardiac tissue: the fast inward current $I_{fi} = -g_{fi} v \Theta(u - 0.25)(1 - u)(u - 0.25)$, with a maximal conductance of $g_{fi} = 7.2$, determines the primary excitation of a cell; the slow outward current $I_{so}(u) = 0.05u^{1.4}\Theta(0.2 - u)$ accounts for recovery of cell properties after excitation; the slow inward current $I_{si}(u,w) = \Theta(u - 0.2)uw(0.23 + 0.085 \cdot tanh[k(u - 0.65)])$ determines the duration of the excitation pulse; and I_s represents the stretch-activated current, which will be described later. The variable u represents the transmembrane potential scaled to the interval [0,1].

The Hodgkin-Huxley type gating variable v determines inactivation of I_{fi}, with the time constant given by: $\tau_v(u) = \tau_1$ for $u \leq 0.085$; $\tau_v(u) = \tau_2$ for $0.085 < u < 0.125$; $\tau_v(u) = \tau_3$ for $0.125 \leq u < u_c$; and $\tau_v(u) = \tau_4$ for $u \geq u_c$. The gating variable w determines activation of I_{si}, with the time constant $\tau_w(u) = 125$ for $u \leq 0.25$ and $\tau_w(u) = 170$ for $u > 0.25$. The currents I_{fi}, I_{so} and I_{si} may be regarded as general descriptions of the sodium, potassium and calcium currents, respectively, of an excitable cardiac cell.

Following excitation, the tissue in our model contracts and the mechanics are modulated by the variable T_a (given by Eq. 5.4), which represents the active stress generated by the medium. The function $\varepsilon(u) = 1$ for $u \leq 0.05$; and $\varepsilon(u) = 0.1$ for $u > 0.05$; governs the delay between activation and active force development. k_T governs the rate of tension development during excitation and thus the maximal value of active tension. Doubling k_T results in an approximate two-fold increase in active tension.

The mechanical part of our model is unchanged from [129]. The main equations here are the equations of stress equilibrium (Eq. 5.5) formulated using the second Piola-Kirchhoff stress tensor, T^{MN} in Eq. 5.6, which contains two parts: (i) the active stress components, $T_a C^{-1}_{MN}$, where $C_{MN} = \partial x_k / \partial X_M \cdot \partial x_k / \partial X_N$ is the right Cauchy-Green deformation (metric) tensor, and C is its determinant; and (ii) the passive elastic stress components, which are expressed in terms of the

derivatives of a strain energy function (W) with respect to components of Green's strain tensor, $E_{MN} = \frac{1}{2}(C_{MN} - \delta_{MN})$, where δ_{MN} is the unitary tensor. For the purposes of this study, the strain energy function was chosen to be the isotropic Mooney-Rivlin constitutive law [67], $W = c_1(I_1 - 3) + c_2(I_2 - 3)$, where I_1 and I_2 are principal invariants of C_{MN}, and c_1 and c_2 are stiffness coefficients, that together with the parameter k_T from Eq. 5.4 determine local deformation during contraction ($c_1 = 2$, $c_2 = 6$, and $k_T = 10$ for all simulations, chosen to give rise to relative local deformations of approximately 15%).

The direct influence of deformation on the excitation properties is given by the stretch-activated current I_s. In general there are three groups of mechanically activated channels in the heart, but only two of them (the cation non-selective channels, and the potassium-selective channels) are activated by stretch [83]. The overall physiological action of these channels is depolarization of the membrane in response to stretch, as shown in the majority of experimental observations from isolated cardiac tissue and the whole heart. Experimental studies of the electrophysiological properties of stretch-activated channels show that they are instantly activated by mechanical stimulation, and the current-voltage (I-V) relationship for the most important nonspecific cation channel is linear [61, 203]. On basis of these observations, linear ionic models for I_s have been proposed [177, 181]. These linear models have been used to study effects of mechanical stretch on heart tissue using detailed ionic models of the cardiac myocyte. Therefore, we believe that a linear time-independent description will also be sufficient for our low-dimensional formulation for cardiac cells. Thus we use:

$$I_s = G_s(\sqrt{C} - 1)(u - E_s), \tag{5.8}$$

where G_s and E_s are the maximal conductance and reversal potential, respectively, of the stretch-activated channels. Following [129], the current in Eq. 5.8 is present only if $\sqrt{C} > 1$ (which indicates stretch).

The value of E_s in most biophysically accurate models is assumed to be around -20 mV [61, 181], and describes the experimentally observed depolarizing effect of the stretch-activated current. In our model we used values close to $E_s \sim 1$ to provide the depolarizing effect. However, the exact value of the reversal potential may depend on the cell type [61, 83, 203], therefore we performed simulations with lower values of E_s to investigate the possible effects on the main results of this study.

The value of G_s is one of the main determinants of the effects of deformation on wave propagation and was varied in our computations. The complete list of parameters of the models used in this study is given in Table 5.1 (Supplementary Material).

5.2.2 Numerical Integration Method

The coupled RDM model was solved using a hybrid approach that combines an explicit Euler scheme for the RD system, with finite element techniques for large

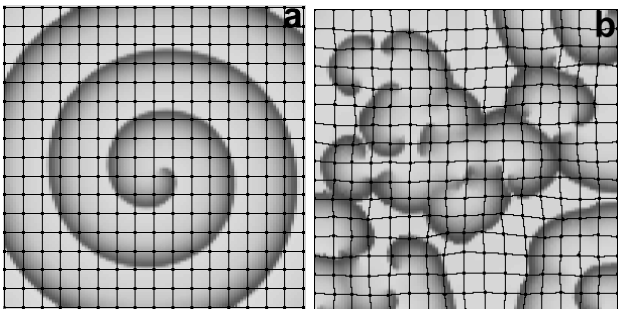

Figure 5.1: Spiral wave breakup due to mechanical activity. (a) Spiral wave rotation in a RD system based on Eqs. 5.1-5.3 and in the absence of deformation with $u_c = 0.15$, $\tau_1 = \tau_2 = \tau_3 = 30$, $\tau_4 = 3$. (b) Similar computations in a deforming medium using Eqs. 5.1-5.8 with $G_s = 0.03$. Both snapshots are taken at 1800 time units. The medium consists of 513x513 grid points and 16x16 mechanical elements, each containing 33x33 grid points.

deformation mechanics. Full details are given in [117, 129]. The numerical parameters were the following: Euler computations were performed on a deforming grid of up to 513x513 finite difference points using no-flux boundary conditions. For all simulations, we used a time integration step of $\Delta t = 0.1$ (dimensionless time units [t.u.]), and a space integration step of $\Delta x = \Delta y = 0.8$ (dimensionless space units [s.u.]), consistent with previous studies involving a similar RD model [33]. Each mechanical element contained between 6x6 and 33x33 electrical grid points, and the mechanics solution steps were separated by between 10 and 80 excitation integration steps (consistent with [117, 129]). When solving Eq. 5.5, the boundaries of the medium were fixed in space, which is consistent with an isometric contraction regime: a standard experimental procedure for muscle mechanics, during which end-points or edges of the tissue are fixed to maintain a constant overall dimension. Isometric contraction is appropriate for isovolumic phases of contraction and relaxation during the cardiac cycle, for which the overall dimension of the heart is approximately constant, whilst regional deformations are heterogeneously distributed.

5.3 Results

5.3.1 Spiral Wave Breakup

In the absence of deformation, Eqs. 5.1-5.3 describe non-oscillatory cardiac tissue that supports stable rotating spiral waves (Figure 5.1a). We found that in the presence of deformation (Eqs. 5.1-5.8), rotation of spiral waves became unstable and broke up into complex spatio-temporal patterns (Figure 5.1b) that persisted for the duration of our simulations (approximately 50 rotations).

We investigated the factors underpinning the transition from a stable rotating spiral into spiral breakup. In Eqs. 5.1-5.3, the main influence of mechanical defor-

mation on excitation appears in two ways: (i) via the stretch-activated current I_s in Eq. 5.1; and (ii) due to deformation of the tissue, as expressed in Eq. 5.7. We studied the relative contributions of these two factors to the spiral wave instability. We performed one simulation using the same parameter values and initial conditions as the simulation in Figure 5.1b, but in the absence of I_s. In this case, spiral wave stability persisted despite the tissue deformations (Supplementary Material, Figure 5.6a).

In another simulation, I_s was maintained similar to the computation illustrated in Figure 5.1b, but the effect of tissue deformation on wave propagation was neglected (i.e. rather than using Eq. 5.7, the Laplacian was evaluated using $\nabla^2 u = \frac{\partial^2}{\partial X^2} + \frac{\partial^2}{\partial Y^2}$, as for the undeformed configuration). In this case, we observed that the onset of spiral breakup, and its subsequent complexity, was similar to the simulation in Figure 5.1b (Supplementary Material, Figure 5.6b).

In additional sets of computations, we found that spiral breakup occurred only if the conductance of the stretch-activated channel was $G_s \geq 0.028$. We found that this threshold value (which we denote as G_{sTH}) was modulated by other parameters of the model that influence the stretch-activated current in Eq. 5.8. If the reversal potential for the stretch-activated current was decreased to $E_s = 0.75$, then the conductance threshold for breakup increased to $G_{sTH} = 0.039$, and a further decrease to $E_s = 0.5$ resulted in $G_{sTH} = 0.065$. Clearly, decreasing E_s in Eq. 5.8 reduces the magnitude of the stretch-activated current, thus a larger value of G_s is necessary for breakup to occur. The complete dependence of G_{sTH} on E_s is illustrated in Figure 5.7 (Supplementary Material).

The observation that mechanically-induced spiral wave breakup was primarily due to the stretch-activated current was somewhat unexpected, since it is a depolarizing current, and such currents typically promote excitation in cardiac tissue. Thus, we investigated how propagation block could be caused by the stretch-activated current, and it turns out that the mechanism of this effect is related to the so-called "accommodation phenomenon", whereby the threshold for activation increases as the rate of depolarization is decreased, which has been studied in electrophysiology since 1936 [58, 59].

We illustrate this effect using an example that incorporates a recent detailed ionic model for human cardiac cells [172]. This model uses a widely accepted biophysical description of the sodium current, for which conductance of the sodium channels is proportional to the product of activation (m) and inactivation (h, j) gates: $I_{Na} \sim m^3 hj$. Following the Hodgkin-Huxley approach [59], the dynamics of the gating variables are given by equations of the form: $\frac{dm}{dt} = \frac{m_\infty(u) - m}{\tau_m(u)}$, where the parameters of the voltage-dependent functions $m_\infty(u)$ and $\tau_m(u)$ are fitted to experimental measurements. Similar exponential relaxation equations are used for the h and j gates. The steady-state values $m_\infty(u)$, $h_\infty(u)$, and $j_\infty(u)$ depend on the transmembrane voltage and are shown in Figure 5.2a. As voltage increases, we see that the activation gate goes from 0 to 1, and the inactivation gate goes from 1 to 0. It is important to note that the inactivation curve approaches zero at a voltage of around $u \sim 0.15$, whereas the activation curve starts to increase

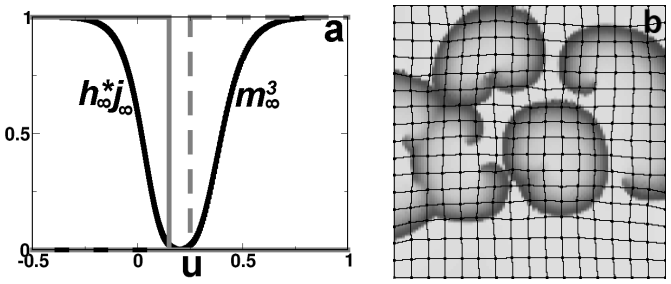

Figure 5.2: Breakup in a model with biophysical activation and inactivation of the fast inward current I_{fi}. (a) The scaled activation and inactivation curves from the TNNP model [172] (the black lines). (The values are scaled from the original values of voltage to the interval of voltage between 0 and 1 for the Fenton-Karma model). Plotted are the scaled curves of $h_\infty(u) * j_\infty(u)$ (the black solid line) and of $m_\infty^3(u)$ (the black dashed line) from [172]. The gray lines show the Heaviside description of the activation (the gray dashed line) and inactivation (the gray solid line) curves in Eqs. 5.1-5.3. (b) Spiral wave breakup in a model with biophysical activation and inactivation of the fast inward current I_{fi} (see text for details). The snapshot is taken at 1200 time units, $g_{fi} = 14.2$, all other parameters and initial conditions are the same as in Figure 5.1.

for higher values of voltage above about $u \sim 0.25$. Thus if cardiac tissue is *slowly* depolarized from the resting state $u = 0$ such that the gating variables approximately follow their steady-state values, then I_{Na} will be inactivated (at $u = 0.15$) before the voltage reaches the activation threshold ($u = 0.25$). A similar situation will occur if cardiac tissue is incompletely repolarized after excitation, such that the resting potential is above the inactivation value of $u = 0.15$. This type of I_{Na} inactivation occurs in our simulations and results in spiral wave breakup.

This is illustrated in Figure 5.3a, which shows the time-course of the transmembrane voltage u, the Fenton-Karma variable v (which accounts for inactivation of the fast inward current I_{fi}), and the currents I_{fi} and I_s at a point where the wave block occurs (marked by the filled square in Figure 5.3b). The horizontal gray lines in the upper panels show the voltage above which I_{fi} is inactivated by the v gating variable ($u = 0.15$). Since I_{fi} is responsible excitation and thus wave propagation, inactivation of I_{fi} results in wave block.

Now let us explain the onset of new wavebreaks. During spiral wave rotation (Figure 5.3a upper panel and insert 5.3c), we see that the minimal diastolic value of the transmembrane potential is initially slightly below the gray (inactivation) line, resulting in recovery of the variable v up to values of approximately 0.6 (Figure 5.3a lower panel), which allows recovery of I_{fi} required for generation of a new action potential. However, we also observed that the minimal diastolic voltage increased, and after the third action potential the transmembrane potential did not decrease below the inactivation value. As a result, the inactivation variable v was not recovered and remained at zero and thus I_{fi} did not recover as well (Figure 5.3a lower panel around the vertical dashed line). In the absence of the fast inward current, excitation is not possible and wave propagation was blocked. This non-recovery of the transmembrane potential was caused by the stretch-activated

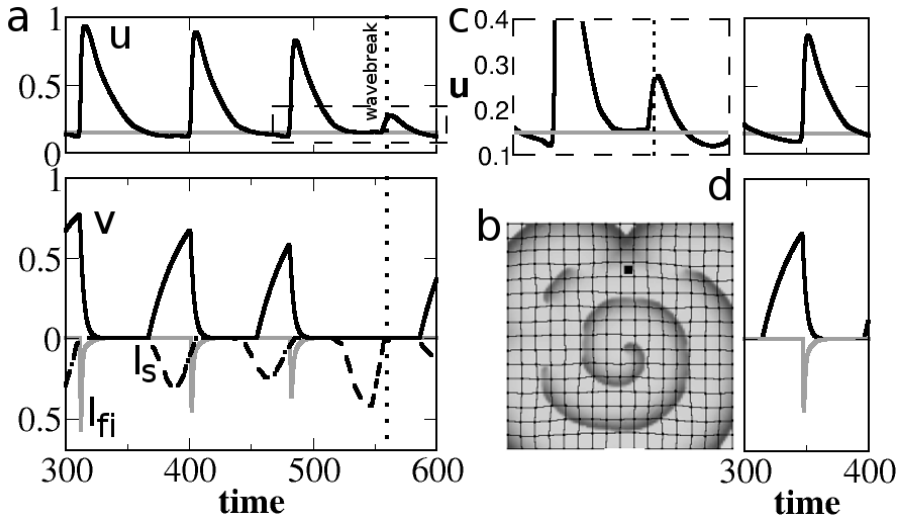

Figure 5.3: Mechanism of breakup due to mechanical activity. (a) Time courses of: voltage u (upper black trace); stretch-activated current I_s multiplied by 100 (lower dashed black line); the fast inward current I_{fi} (lower gray trace); and the variable v (lower black trace), which is responsible for the inactivation of I_{fi} at the point marked by the filled square in panel (b). The vertical dotted line is located at 560 time units and the horizontal upper gray line at $u = 0.15$. (b) Fragmentation of the spiral wave, showing the same simulation as in Figure 5.1b, but at time 560 time units. All parameters and conditions are the same as in Figure 5.1b. (c) Magnification of the dashed rectangular region from fig (a). (d) A similar computation as in panel (a), but in the absence of I_s ($G_s = 0$ in Eq. 5.8).

current. We can see that I_s was maximal during the late repolarization phase, and this prevented the voltage from decreasing below the gray line. To confirm this effect, we performed a similar simulation, but with I_s blocked (Figure 5.3d). In this case, repolarization continued below the inactivation threshold. Thus, the I_{fi} current was not inactivated, and the spiral wave did not break up.

The breakup we observed was due to sodium current inactivation. However, whilst the representation of the sodium current in the Fenton-Karma model provides a qualitatively correct description of the activation-inactivation properties of this current, it is not based on experimental data of these processes. To underline the importance of the activation-inactivation processes for our mechanisms, we developed a modification of the Fenton-Karma model, which included biophysically based activation and inactivation curves of the fast sodium current. We replaced the Heaviside based activation function $\Theta(u-0.25)(u-0.25)$ from Eq. 5.1 by the activation curve (m^3) from the TNNP model [172], scaled to the interval [0,1] (Figure 5.2a); and the Heaviside inactivation function $\Theta(u_c-u)$ from Eq. 5.2 by the voltage-dependent inactivation curve $h*j$ (Figure 5.2a). Thus, in this modified model activation and inactivation processes are based on experimentally measured properties of the sodium current. We studied spiral wave rotation using this new model and found that with these modifications we also obtained

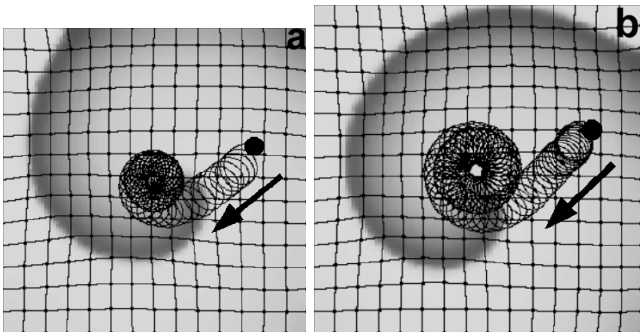

Figure 5.4: Spiral wave drift due to mechanical activity. (a) Initial position of a spiral wave tip (black circle) and the final state of the spiral wave after 120 rotations (shaded image) in a medium the containing 141x141 grid points with 11x11 points per mechanics element, and $G_s = 0.01$. The arrow indicates the direction of spiral wave drift. The solid curve illustrates the trajectory of the spiral tip. (b) A similar simulation to that in panel (a), but in a medium containing 151x151 grid points. Other parameter values were the same as those for Figure 5.1b, except $u_c = 0.25, \tau_1 = 95, \tau_3 = 300$

mechanically-induced breakup of the spiral wave. As in the case of the Fenton-Karma model, the spiral wave did few rotations and broke down into a complex spatio-temporal pattern (Figure 5.2b). Overall, the breakup process was similar to that observed in the Fenton-Karma model, however modification of I_{fi} resulted in some increase in the wavelength of the spiral waves.

5.3.2 Spiral Wave Drift

We studied the dynamics of spiral wave rotation using parameter values for which spiral breakup was absent and in the absence of deformation. Under these conditions, the spiral wave rotation was stationary with a circular motion of the spiral tip (Figure 5.1a). Using the same parameter values in the presence of mechanical activity, we observed drift of the spiral wave to the center of the medium (Figure 5.4a) and subsequent meander of the spiral around the center. The meander pattern in Figure 5.4a was a combination of two motions: a counter-clockwise rotation of the spiral wave tip along a circular trajectory (similar to that in Figure 5.1a), with the motion of the center of rotation of this circle following another circular trajectory in the clockwise direction. This tip trajectory was accurately reproduced in the complex plane $Z = X + iY$ (up to initial phases) using:

$$Z(t) = R_0 exp(i2\pi f_0 t) + R_1 exp(-i2\pi f_1 t) \tag{5.9}$$

This equation describes a cycloidal motion that is a superposition of a clockwise spiral wave rotation with frequency f_0 along a circle of radius R_0, and a counter-clockwise circular motion along the radius R_1 with frequency f_1. For Figure 5.4a, these parameters are $R_0 = 7.50[s.u.], f_0 = 11.95 * 10^{-3}[t.u.]^{-1}, R_1 = 4.86[s.u.], f_1 = 0.56 * 10^{-3}[t.u.]^{-1}$. We performed several simulations with different initial spi-

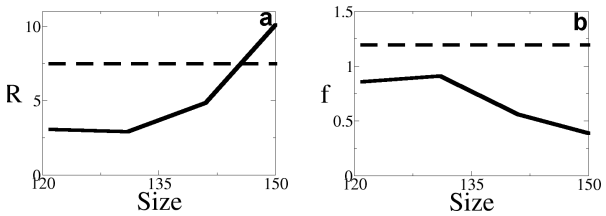

Figure 5.5: Characteristics of meander patterns. (a) R_0 and R_1 in $[s.u.]$ vs. medium size (in grid points). (b) f_0 and f_1 in $[t.u.]^{-1}$vs. medium size.

ral wave locations and in all cases the spiral wave approached the center of the medium, and meandered along a similar trajectory to that in Figure 5.4a.

We have also studied how the size of the medium effects spiral wave drift. Figure 5.4b illustrates the behavior of a spiral wave in a larger medium (151x151 grid points; compared to the 141x141 grid in Figure 5.4b). In this case, the spiral wave also drifted to the center, but its meander pattern was of larger overall dimension. This meander was also reproduced using Eq. 5.9 with $R_0 = 7.50[s.u.], f_0 = 11.95 * 10^{-3}[t.u.]^{-1}, R_1 = 10.67[s.u.], f_1 = 0.37 * 10^{-3}[t.u.]^{-1}$. Thus, the change in medium size did not affect the spiral wave rotation (R_0 and f_0 are the same for Figures 5.4a,b), however the radius and the period of the circular meander trajectory were greater for the larger medium..

Figure 5.5a shows the effect of medium size on the characteristics of the meander pattern. We observed that R_0 and f_0 remained constant, whilst R_1 increased and f_1 decreased with the increase in medium size. As a result, the radius of the meander pattern increased, whilst the speed along the circular trajectory $2\pi * R_1 * f_1$ increased only slightly with size (not shown).

In a similar manner to the spiral breakup analysis, we studied how this drift was modulated by the two feedback effects of deformation: the stretch-activated current I_s; and the effect of tissue deformation of wave propagation. We observed that drift of the spiral wave occurred in the absence of I_s, although the meander pattern was not cycloidal (Supplementary Material, Figure 5.8a). However, the drift speed was much slower than that in Figure 5.4a. After 120 rotations, the spiral wave had drifted approximately one-third of the medium width, whilst by the same time in Figure 5.4b the spiral had approached and made several rotations about the center of the medium. In Figure 5.8b, we see that I_s alone induced drift and meander of the spiral wave similar to that in Figure 5.4a. The characteristics of the meander trajectories were also similar ($R_0 = 7.36[s.u.], f_0 = 12.07 * 10^{-3}[t.u.]^{-1}, R_1 = 4.23[s.u.], f_1 = 0.56 * 10^{-3}[t.u.]^{-1}$), although there was a small increase in the spiral wave frequency f_0, and a slight decrease in the radius of the circular motion R_1, compared with that of Figure 5.4a. Thus for these parameters, we conclude that the dominant factor driving spiral drift is the stretch-activated current.

We believe that the mechanism of this drift is similar to the resonant drift of

spiral waves reported in [1, 47]. As demonstrated in [47], a periodical variation of the properties of an excitable medium in synchrony with the period of a spiral wave, resulted in drift and subsequent stable meandering of the spiral wave tip. In our model, deformation of the medium also produced a periodical modulation of the tissue properties in synchrony with the spiral wave period, due to the excitation-contraction coupling. Thus, the effects of mechanics in the present study are likely to be similar to the effects of periodical forcing during resonant drift, leading to drift and meandering attractors for spiral wave rotation.

5.4 Discussion

We have demonstrated that deformation has a pronounced effect on spiral wave rotation and can induce either breakup, or drift and meander of spiral waves.

Using very general descriptions of the excitation-mechanics properties, our modeling has demonstrated that stretch-activated channels can induce spiral wave breakup. This conclusion requires confirmation both experimentally and using modeling studies involving detailed ionic descriptions of cardiac tissue. In support of the latter, we have shown that spiral breakup occurred as a result of inactivation of the fast inward current I_{fi}, which was due to diastolic depolarization mediated by the stretch-activated current. Furthermore, the notion that the stretch-activated current can block action potential has been demonstrated using the Beeler-Reuter ionic model for ventricular cells [181], for which it was shown that increasing the conductance of the stretch-activated current resulted in failure of excitation of cardiac cells (see Figure 3 from [181]). Note also that inactivation of the fast sodium current by depolarization has been observed experimentally (e.g. [59]), and reproduced using ionic models of cardiac tissue [14], for which it can cause block of propagation.

We suggest that the mechanism of spiral drift is similar to the resonant drift mechanism. Resonant drift of spiral waves in cardiac tissue has not been experimentally studied in biological tissues, but has been shown to exist in detailed ionic models of cardiac tissue [15], as well as in experiments involving BZ reactions [47]. Therefore, it is likely that these effects of mechanics on spiral wave dynamics could also be reproduced using more detailed experimental and modeling studies in cardiac tissue and in BZ reaction.

Here we have presented the first general study of spiral wave dynamics in a deforming medium, but many potentially important factors have been neglected, such as the fibrous anisotropy of cardiac tissue, which is important both for the electrical and the mechanical properties of the heart. We chose not to consider this factor, because the main aim of this study was to investigate the basic effects of mechanics on a general reaction-diffusion system. The influence of cardiac anisotropy is likely to add additional effects, and will be addressed in future studies.

Acknowledgments

We are grateful to Dr. F.H. Fenton who kindly provided the equations used in the construction of our RDM model, and to Prof. P.J. Hunter and Dr. P. Kohl, for valuable discussions. This research is funded by the Netherlands Organization for Scientific Research (grant 814.02.014). M.P.N. was supported by the Marsden Fund Council from New Zealand government funding, administered by the Royal Society of New Zealand.

5.5 Supplementary Material

Table 5.1

Excitation parameters:	$u_c = 0.15$	$k_T = 10.0$	$\varepsilon(u) = 1$ if $u < 0.05$
	$E_s = 1.0$	$G_s = 0.03$	$\varepsilon(u) = 0.1$ if $u \geq 0.05$
	$\tau_1 = 30$	$\tau_2 = 30$	$\tau_3 = 30$
	$\tau_4 = 3$	$g_{fi} = 7.2$	$k = 10$
FDM parameters:	$\Delta t = 0.1$	$\Delta x = \Delta y = 0.8$	up to 513x513 points
Mechanics parameters:	$c_1 = 2$	$c_2 = 6$	
FEM parameters:	up to 32x32 elements		

Table 5.1: Default parameters for the coupled electro-mechanics model. Any variations on these parameters for the various models are explicitly indicated. FDM: finite difference method (excitation model); FEM: finite element method (mechanics model).

Figure 5.6

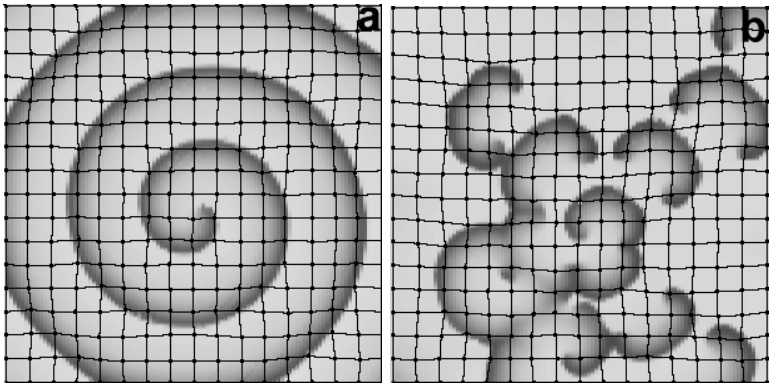

Figure 5.6: Patterns of activation for the same time as in Figure 5.1b, and using the same initial conditions and parameter values. For (a) the stretch-activated current I_s was omitted. For (b) the dependence of excitation propagation on tissue deformation was neglected.

Figure 5.7

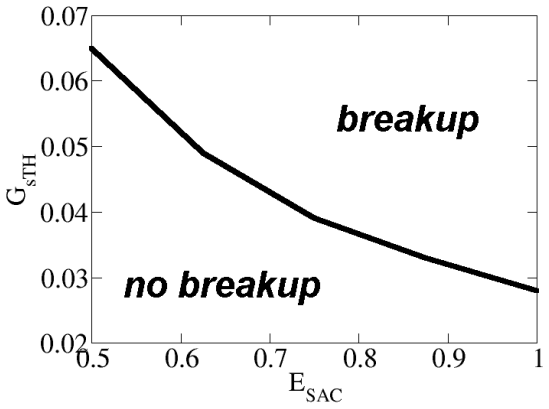

Figure 5.7: The threshold value G_{sTH} of the conductance of the stretch-activated channel above which the breakup occurs, as a function of the reversal potential for the stretch-activated current E_s.

Figure 5.8

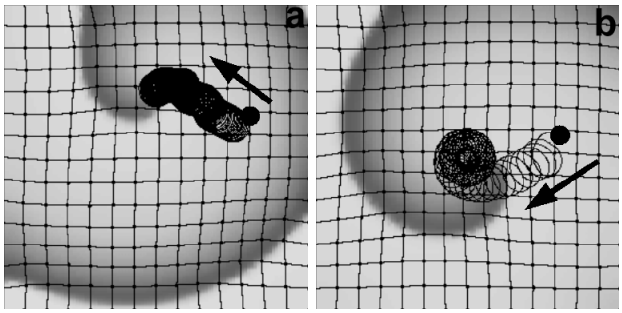

Figure 5.8: Dynamics of spiral wave rotation over the same period of time as in Figure 5.4a, from the same initial conditions and parameter values except for: (a) the stretch-activated current I_s in Eq. 5.1 was omitted; (b) the effects of deformation on excitation propagation tissue was omitted.

Part II

Mechanisms of Ventricular Fibrillation in Anatomically Based Models of the Human Ventricles:

The Role of Tissue Heterogeneity and Mechano-Electrical Feedback

CHAPTER 6

Effect of Heterogeneous APD Restitution on VF Organization in a Model of the Human Ventricles

R.H. Keldermann[1], K.H.W.J. Ten Tusscher[1], M.P. Nash[2], R. Hren[3], P. Taggart[4], A.V. Panfilov[1]

[1] *Theoretical Biology/Bioinformatics Group*
Utrecht University
Padualaan 8, 3584 CH Utrecht, The Netherlands

[2] *Bioengineering Institute and Department of Engineering Science*
University of Auckland
Private Bag 92019, Auckland, New Zealand

[3] *Institute of Mathematics, Physics, and Mechanics*
University of Ljubljana, Ljubljana, Slovenia

[4] *Department of Cardiology and Cardiothoracic Surgery*
University College Hospital, London, United Kingdom

Am. J. Physiol. Heart Circ. Physiol. 294: H764-H774 (2008)

Abstract

The onset of ventricular fibrillation (VF) has been associated with steep action potential duration (APD) restitution in both clinical and computational studies. Recently, detailed clinical restitution properties in cardiac patients were reported showing a substantial degree of heterogeneity in restitution slopes at the epicardium of the ventricles. The aim of the present study was to investigate the effect of heterogeneous restitution properties in a 3D model of the ventricles using these clinically measured restitution data. We used a realistic model of the human ventricles, including detailed descriptions of cell electrophysiology, ventricular anatomy, and fiber direction anisotropy. We extended this model by mapping the clinically observed epicardial restitution data to our anatomical representation using a diffusion based algorithm. Restitution properties were then fitted by regionally varying parameters of the electrophysiological model. We studied the effects of restitution heterogeneity on the organization of VF by analyzing filaments and the distributions of excitation periods. We found that the number of filaments and the excitation periods were both dependent on the extent of heterogeneity. An increased level of heterogeneity leads to a greater number of filaments and a broader distribution of excitation periods, thereby increasing the complexity and dynamics of VF. Restitution heterogeneity may play an important role in providing a substrate for cardiac arrhythmias.

6.1 Introduction

Sudden cardiac death is the most common cause of death in the industrialized world and in most cases it is due to ventricular fibrillation (VF) [202]. During VF, excitation waves are disturbed and chaotic, causing the contraction of the ventricles to become rapid and uncoordinated.

It has been shown in clinical and experimental studies that these turbulent wave patterns are underpinned by re-entrant sources of excitation [29, 45, 62, 107, 178, 190]. If VF is not halted by means of defibrillation, this condition can be lethal within minutes.

Historically, it has been hypothesized that VF is due to turbulent wave propagation induced by heterogeneity in refractoriness of cardiac tissue [86, 106]. The important role of heterogeneity in VF is supported by the strong association of VF with diseases that lead to increased heterogeneity, such as coronary artery disease, cardiomyopathies, and congenital heart disease [26, 202]. Due to these pathologies, remodeling of the cellular ionic currents, calcium handling and gap junction coupling in cardiac tissue results in increased heterogeneity. Furthermore, VF is associated with diseases such as Long QT, Short QT, and Brugada syndrome [26, 202], in which ion channel mutations lead to an increase of action potential duration (APD) dispersion.

In the last decade, it has been proposed that VF is caused by the occurrence of dynamical instabilities (alternans) induced by steep APD restitution [50, 125, 128,

131, 140, 184], which became known as the restitution hypothesis of VF [140, 184]. More recently, intracellular calcium cycling has been shown to cause alternans in APD [139, 185], which may lead to dynamical instabilities and VF. According to the original restitution hypothesis, alternans instability occurs when the slope of the APD restitution curve, which relates the APD to its previous diastolic interval (DI), exceeds one [50, 125]. Recent experimental and modeling studies show that although steepness of restitution curve is an important determinant of instability [10, 11, 192], other factors such as electrotonic coupling, cardiac memory, and conduction velocity restitution should also be taken into account [33, 138, 171, 174]. The restitution hypothesis and refractoriness hypothesis of VF are related. Alternans instability induces dynamic heterogeneities that can lead to wavebreak, whereas static anatomically defined heterogeneities can also lead to wavebreak.

Restitution induced VF has been the subject of a variety of computational studies. Because the restitution hypothesis does not require pre-existing heterogeneity for the onset of VF, most of the computational studies regarding the restitution hypothesis have assumed that cardiac tissue is homogeneous. However, recent clinical studies have demonstrated that APD restitution properties on the ventricular epicardium and endocardium have a complex spatially non-uniform distribution [102, 114, 198]. These studies showed that: 1) APD restitution properties are spatially heterogeneous containing multiple sites of steep and shallow restitution slopes; 2) Maximum restitution slopes range from almost zero to well over two; 3) Restitution properties differ between patients and are dependent on the underlying pathology. Some studies on the effects of heterogeneous APD restitution in cardiac tissue have shown that spatial dispersion in APD restitution may result in wavebreak and initiation of VF [22, 24, 196]. However, the influence of restitution heterogeneity on VF dynamics and organization has not yet been investigated.

In this chapter, we study the effects of heterogeneous APD restitution data measured in clinical studies [114] on VF organization in the human heart. We use our integrative anatomical model of the human ventricles [170], which was recently developed and verified against available clinical data on human VF. The model describes action potential characteristics of human ventricular myocytes [171, 174], combined with an anatomically detailed geometry of the human ventricles that incorporates fiber direction anisotropy [60]. We introduce APD restitution heterogeneity into our model by incorporating clinically measured restitution data from patients who were undergoing surgery for aortic valve replacement as reported in [114]. Clinical restitution curves were mapped and interpolated to our 3D ventricular geometry and reproduced by our cell model using appropriate regional variations of the parameters of the electrophysiological model. We used this human ventricular model to study the effects of spatial heterogeneity of APD restitution on the dynamics of VF and found that the organization of VF became more complex with increased heterogeneity. We have quantified these effects in terms of the number of filaments and the local excitation periods.

6.2 Methods

We developed a heterogeneous model of the human ventricles by incorporating clinically measured spatially heterogeneous APD restitution properties [114] into our integrative model of the human ventricles [170, 171, 174]. Below we describe in detail the main features of our heterogeneous model.

6.2.1 Ventricular Model

Excitation of the ventricles in a monodomain model can be described using the following partial differential equation [74]:

$$C_m \frac{\partial V_m}{\partial t} = \frac{\partial}{\partial x_i}\left(D_{ij}\frac{\partial V_m}{\partial x_j}\right) - I_{ion} \tag{6.1}$$

where V_m denotes the transmembrane voltage, C_m the membrane capacitance, D_{ij} the diffusion tensor, and I_{ion} the sum of the ionic transmembrane currents describing the excitable behavior of the individual ventricular cell. There are different models available to describe action potential characteristics of the cell membrane [2, 12, 33, 98, 99, 171]. In this study, we used the human ventricular ionic model published by Ten Tusscher et al. [171, 174] and refer to this as the TNNP model. This model provides a detailed description of voltage, ionic currents and intracellular ion concentrations, and is based on a wide range of human based electrophysiological data. The most recent version of the TNNP model [174] includes a more extensive description of intracellular calcium dynamics. However, the model does not describe calcium alternans nor spontaneous calcium release. The model reproduces experimentally measured APD [108] and conduction velocity restitution curves [41]. The TNNP model contains the following ionic currents:

$$\begin{aligned} I_{ion} &= I_{Na} + I_{to} + I_{CaL} + I_{Kr} + I_{Ks} + I_{K1} + I_{NaCa} \\ &\quad + I_{NaK} + I_{pCa} + I_{pK} + I_{Na,b} + I_{Ca,b} \end{aligned} \tag{6.2}$$

A complete list of all equations and parameter settings can be found in Appendix A. We used the 'default' parameter settings from [174]; all changes from these default settings are detailed in the text below. More information about homogeneous 2D and 3D spiral wave dynamics and spiral wave breakup can be found in [170, 174].

Geometric data describing the 3D ventricular anatomy and fiber direction field were derived from a normal healthy human heart [60]. From this heart, a voxel description of approximately 13.5 million points with a spatial resolution of 0.25 *mm* was obtained. We assume that the transverse conductivity is the same in all directions orthogonal to the direction of the muscle fiber axis and that local conductivity tensors D_{ij} can be derived from local muscle fiber directions using:

$$D_{ij} = D_T * \delta_{i,j} + (D_L - D_T)\alpha_i\alpha_j \tag{6.3}$$

where, D_L and D_T are the longitudinal and transverse conductivity, respectively and α is the muscle fiber direction. For D_L we used 162 Ωcm and for D_T we used 40.5 Ωcm, which resulted in conduction velocities of 68 cm/s in the longitudinal direction and 32 cm/s in the transverse direction. Thus the resulting anisotropy ratio was approximately 2:1, which is consistent with clinical measurements [71].

6.2.2 Clinical Human Restitution Data

A recent clinical study by Nash et al. [114] has provided global epicardial restitution properties in 14 cardiac patients. In this study, activation-recovery intervals (ARI) were recorded over the entire ventricular epicardial surface using an epicardial sock containing 256 unipolar contact electrodes (inter-electrode spacing approximately 10 mm). These ARI values can be compared to action potential durations (APD) measured at approximately 50% repolarization (APD_{50}) [56]. They applied a standard S1-S2 protocol to determine restitution properties. A train of 9 S1 stimuli at a basic cycle length (BCL) of 600 ms were applied, followed by a S2 stimulus at various intervals ranging from 600 ms to 240 ms. For each electrode, up to 24 pairs of values for the diastolic interval (DI) and subsequent APD_{50} were recorded. We fitted the clinical ARI data of Nash et al. [114] using a least-squares mono-exponential fit as this was the same approach used by Nash et al. [114]:

$$APD_{50} = APD_{50(SS)} - a * exp(-DI/b) \tag{6.4}$$

where the steady state $APD_{50(SS)}$, a and b are parameters of the fit. The maximum restitution slope S_{max} was determined for each electrode using [114]:

$$S_{max} = (a/b) * exp(-DI_{min}/b) \tag{6.5}$$

where DI_{min} is the minimum measured non-refractory DI. Note that this method for maximum restitution slope determination differs from the method used in Ten Tusscher et al. [174] who used a piecewise linear approximation to determine the maximum restitution slope. We compared both methods and found that the piecewise calculation systematically underestimated the maximum restitution slope by around 0.2-0.3 compared to the least squares mono-exponential fit method (Nash et al. [114]).

6.2.3 Mapping and Extrapolating Clinical Restitution Data

In the present study, we used datasets of two patients undergoing replacement surgery for aortic valve disease, for which the most complete APD restitution recordings were available, with more than 85% of valid electrode recordings for each dataset. An electrode was defined to be valid if the data contained at least 18 pairs of DI and APD_{50} values and the mono-exponential fit had at least a correlation coefficient of 0.6 or higher, with 1 meaning perfect statistical correlation and

0 meaning there is no correlation at all. Maximum restitution slopes (S_{max}) with a slope smaller than 0.4 or greater than 3 were manually evaluated and corrected if needed. Dataset 1 (i.e., Figure 4 in [114]) had a mean +/- SD S_{max} of 1.78 +/- 1.04, based on $n = 238$ (93%) valid restitution curves. For dataset 2, the mean +/- SD S_{max} was 0.97 +/- 0.97 based on $n = 227$ (89%) valid restitution curves.

To map the clinical restitution data to our human ventricles, we first mapped the positions of the 256 sock electrodes to the surface of our ventricular model. Coordinates of both the epicardial sock and the anatomical model were normalized about the center of the apex taking into account the anterior, posterior, left and right sides of the ventricles. Electrode sites were then projected on the epicardial surface of our ventricular model by minimizing the distance to the epicardial surface.

For our study, we needed to assign restitution properties of cardiac tissue throughout the entire 3D ventricular mass. However, data on the full 3D organization of APD restitution in the human ventricles are presently not available. Observations have been reported only for surfaces of the heart, and measuring restitution properties on the epi- and endocardium require different clinical methods. To date, either epicardial or endocardial recordings (but not both) have been reported for individual hearts. Nash et al. [114] used an epicardial sock with electrodes to measure restitution data at 256 locations spread across most of the epicardium. Yue et al. [198] used a catheter balloon with electrodes to measure restitution data at 128 locations on the endocardium of the heart. The epi- and endocardial data sets each show regional organization of restitution slopes into 3-5 different areas. Slopes varied between regions and the spatial arrangement of these regions varied considerably from patient to patient. Given these observations regarding restitution slope patterns on the epi- and endocardial surfaces, it is likely that this heterogeneity has a 3D structure. In the absence of experimental 3D data, we extrapolated the 2D surface patterns across the 3D mass. Rather than using different data sets from two different hearts (i.e., one set of data for the epicardial surface, and another for the endocardial surface), we used only the epicardial data from Nash et al. [114]. In order to extrapolate the data into 3D, we developed a diffusion based algorithm to extend the epicardial profile smoothly across the ventricular walls (described below). We do not claim that our algorithm will reproduce the quantitatively correct 3D restitution profile for a particular patient. However, we believe that this is a reasonable first step until more detailed data on 3D organization of human restitution becomes available.

6.2.4 Diffusion Domain Algorithm

Our diffusion algorithm contains the following three steps.

Firstly, we extended the measured S_{max} values (maximum 256 electrode points on the epicardium) to all heart points by solving the diffusion equations for the maximum restitution slopes in the domain given by the heart anatomy. We used the clinically measured maximum restitution slopes as constraints, i.e., the variable S_{max} was kept constant at each electrode position during the diffusion process.

We used a value for the non-dimensional diffusion coefficient of $D = 400$, which provided the desired spatial smoothness of interpolation. The diffusion equations were solved until the average square of residual at the non-constraint points decreased below 10^{-10}. As a result, we obtained a smooth spatial interpolation of S_{max} across all points in the 3D model except for the regions immediately adjacent to the initial electrodes.

The second step was to remove these sharp local gradients by applying a moving average window of $3 \times 3 \times 3$ voxels in the domain given by the heart anatomy. Note that this averaging also changed the values of S_{max} at the reference electrodes (see Figure 6.1, column 2). As a third step, we scaled back S_{max} values for all points using a linear transformation function, which was found from the data presented in Figure 6.2. More specifically, we found the best least square linear fit of the original, clinically measured maximum restitution slope values and the S_{max} values found after step 2 of our interpolation procedure. We then scaled back our data using this linear transformation. Thus, we obtained a smooth distribution of S_{max} across all heart points in our anatomical model, which corresponded well with the clinical data at the epicardial surface.

Figure 6.1 shows the application of our algorithm for dataset 1 (the upper row) and dataset 2 (the lower row). In the first column, we show a direct linear surface interpolation of the clinical data using Matlab's GRIDDATA function. In the second column, we show how S_{max} values are distributed after the diffusion algorithm and the $3 \times 3 \times 3$ moving average window were applied. The third column shows the maximum restitution slopes after the linear transformation step. Comparing the raw data set shown in Figure 6.1 column 1 with the interpolated data shown in column 3, we see that we were able to obtain a profile of heterogeneity in all heart points that corresponded well with the clinical data, but was spatially smooth. We chose to use this smoothed representation as it provided a robust general description of heterogeneity in the heart that helped guard against possible spurious recordings. (Note that the patient 1 dataset we use here is the same as the one used in Figure 4 in [114]).

For dataset 1, a large region of the posterior wall of the left ventricle contained steep restitution slopes, with values close to 3. The right ventricle contains more shallow restitution slopes, with values around 0.5-1. Between these regions, intermediate values were present. The mean +/- SD restitution slope was 1.78 +/- 0.65. Dataset 2 had a relatively small region on the anterior wall with high slope values, whereas the rest of the bulk tissue was characterized by shallow restitution. The mean +/- SD restitution slope was 1.01 +/- 0.48. Both profiles are illustrated in Figure 6.3, where red areas correspond to steep restitution slopes ($S_{max} = 2.5 - 3$), whilst blue areas correspond to shallow restitution slopes ($S_{max} = 0.5 - 1$). Figure 6.11 illustrates two short-axis slices with maximum restitution slopes that have been interpolated from the epicardium through to the endocardium (for dataset 1).

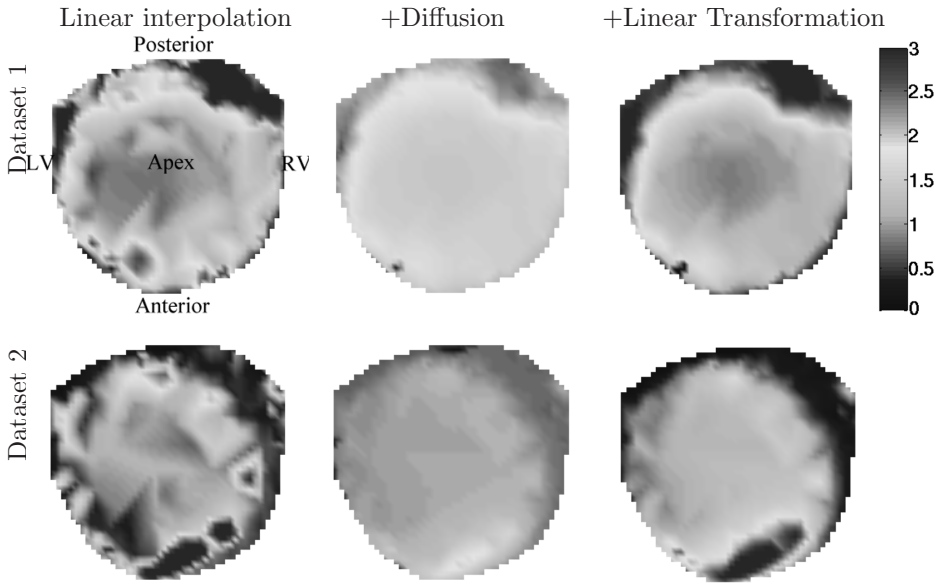

Figure 6.1: Distribution of epicardial restitution, S_{max} shown on the polar projection, with the epicardial apex at the center of each plot and the ventricular base at the outer circumference. For the polar projections, the anterior, posterior, LV, and RV portions of the ventricular epicardium are shown at the bottom, top, left, and right, respectively. (Top) Dataset 1. (Bottom) Dataset 2. (Column 1) Simple triangle based linear surface interpolation using Matlab's GRIDDATA function. (Column 2) After diffusion and application of the $3 \times 3 \times 3$ moving average window. (Column 3) After linear transformation. For color see page 204.

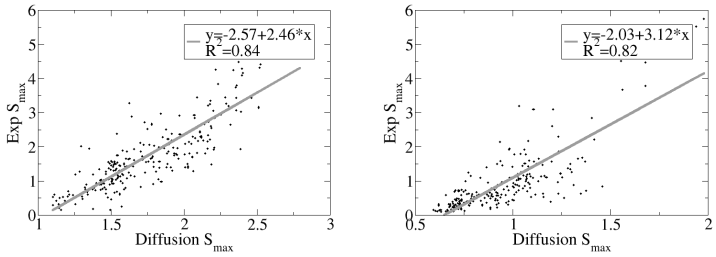

Figure 6.2: Correlation plots of clinical S_{max} values versus model S_{max} values after diffusion and moving average window procedures. (Left) Dataset 1. (Right) Dataset 2.

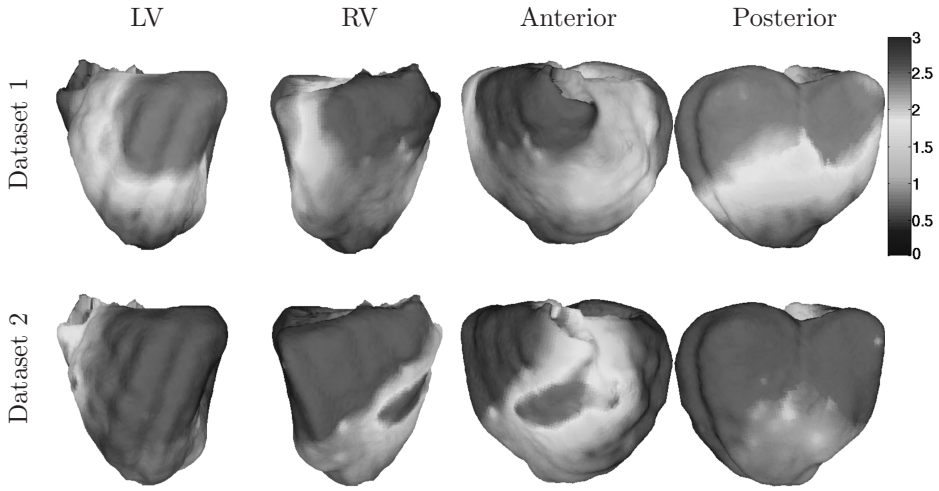

Figure 6.3: 3D plots of restitution S_{max}. (Top) Dataset 1. (Bottom) Dataset 2. From left to right: LV, RV, anterior and posterior views. For color see page 204.

6.2.5 Parameters of the Cell Model

To model cardiac tissue with the desired regional APD restitution properties we fitted parameters of the TNNP model to different maximum restitution slopes. For each computational point of the ventricular geometry, the value of S_{max} was used to individually assign cell model parameters. To generate restitution curves, we paced a single cell model with a series of 10 S1 stimuli at a BCL of 600 ms, followed by a single S2 stimulus delivered at a specified DI after the last S1 action potential. The restitution curve was generated by decreasing the S1-S2 interval (and hence DI), and plotting the APD_{50} of the S2 action potential versus the preceding DI value. We reproduced a variety of slopes between 0.4 and 3 by varying the parameters $G_{Kr}, G_{Ks}, G_{pCa}, G_{pK}$ and τ_f. Figure 6.4 shows the values of these parameters used to obtain the given maximum restitution slopes. Note, that for slopes $S_{max} < 0.4$ we used $S_{max} = 0.4$, and for slopes $S_{max} > 3$ we used $S_{max} = 3$ (gray lines in Figure 6.4). Figure 6.5 shows an example of some APD and APD restitution curves for different parameter settings, together with experimental data to which these restitution curves were fitted. More information about fitting of experimental restitution curves using the TNNP model can be found in Ten Tusscher et al. [174].

6.2.6 Numerical Approach

Equations for the gating variables in the TNNP model were integrated using a Rush and Larsen integration scheme [149]. To integrate Equation 6.1, we used a forward Euler scheme with a time step of $\Delta t = 0.02$ ms and a space step of $\Delta x = 0.25$ mm, and the following Laplacian was evaluated at each point in the

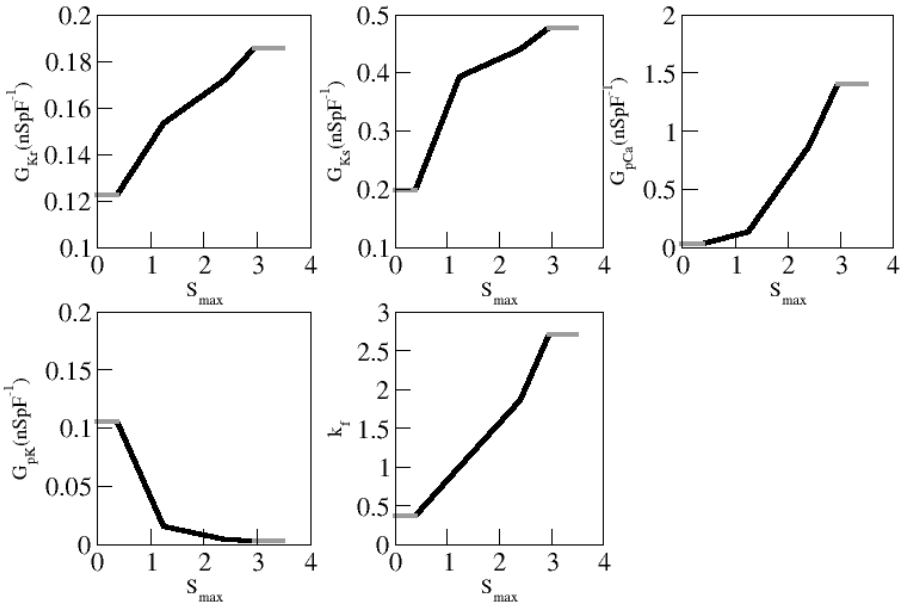

Figure 6.4: Model parameters determining the maximum slope of the APD restitution curve. The y-axes are G_{Kr}, G_{Ks}, G_{pCa}, G_{pK} (in $nSpF^{-1}$) and k_f, respectively. The parameter k_f is the multiplication factor of τ_f. The x-axis shows the maximum slope of the restitution curve S_{max}. Gray lines represent cutoff values (see text for further explanation).

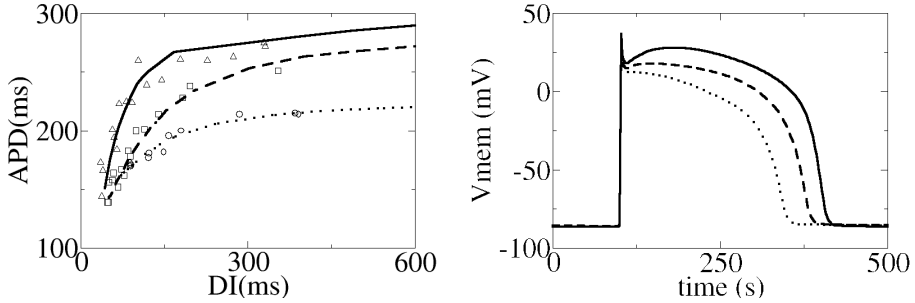

Figure 6.5: Example of restitution curves (left) and corresponding action potentials (right) (using a basic cycle length of 600 ms with a S1-S2 protocol) for different parameter settings of the model. Maximum restitution slopes are 2.70, 1.00 and 0.42, respectively. For comparison, experimental data points to which the model restitution curves were fitted are shown, using triangles (slope 2.70), squares (slope 1.00) and circles (slope 0.42).

human ventricular geometry:

$$\Delta(i,j,k) = \frac{\partial}{\partial x_i}\left(D_{ij}\frac{\partial V_m}{\partial x_j}\right) \tag{6.6}$$

which can be discretized to the following equation:

$$L(i,j,k) = \sum_{l=0}^{l=18} w_l V_m(l) \tag{6.7}$$

where l is an index running over the 18 neighbors of the point (i,j,k) and the point itself, and w_l are the weights defined for each neighbor point containing information about the voltage contributed to the Laplacian at each point (i,j,k). Weights are calculated at each point using the local conductivity tensors calculated by Equation 6.3. To ensure a zero axial current flow from heart points to non-heart points, no flux boundary conditions were imposed by setting weights to zero if a neighbor lay outside the heart geometry.

To initiate 3D scroll waves, we used an S1-S2 protocol, in which the S2 stimulus was activated in the refractory tail of the S1 stimulus, thereby creating a scroll wave. Stimulus currents were applied at twice the diastolic threshold value. For each restitution slope profile, we performed simulations of VT/VF by initiating a scroll wave in the free wall of the left ventricle. Simulations lasted for 8 seconds or were terminated if there was no activity present.

Assuming that the medium is an infinite volume conductor, electrograms can be calculated using the dipole source density of the membrane potential in all voxel points using [135]:

$$ECG = \int_V \frac{D\nabla V_m \cdot \overrightarrow{r}}{r^3} dV \tag{6.8}$$

where, V is the domain of integration (i.e., the ventricular volume), and $\overrightarrow{r}$ is the vector from each point to the recording electrode, which was placed 10 cm from the center of the ventricles in the anterior direction of the transverse plane.

Scroll wave filaments were detected using an algorithm proposed by Fenton and Karma [33]. If there is a spiral wave in 2D (a scroll wave in 3D) present, the core (filament) can be defined as the point(s) for which the excitation wavefront and waveback meet. This can be calculated as the intersection points of the -60 mV isopotential line and the $dV/dt = 0$ iso-line. Voxel data corresponding to these intersection points were then stored. Individual filaments were detected by iteratively joining neighboring voxels that were designated as filament points. All voxels that belonged to the same filament were assigned a unique identifier. Filaments were determined at 10 ms intervals. Of these filaments, we tracked: the time of birth, time of death, time of bifurcation, time of amalgamation, lifespan, filament from which a filament bifurcated, filament into which a filament amalgamated, and ultimate filament to which a filament can be traced back through the bifurcations events.

All simulations were coded in C++ and MPI and were run on 16 processors of a Beowulf cluster consisting of 16 Dell 650 Precision Workstations (dual Intel Xeon 2.66 GHz). Simulating 1 second of wave propagation in the ventricles took approximately 6.5 hours of wall-clock computation time. Ventricular geometry, wave patterns and scroll wave filaments were visualized using the marching cubes algorithms for isosurface detection in voxel data, and OpenGL for isosurface rendering.

6.3 Results

6.3.1 Wavefronts and ECG Signal

In the first series of simulations we initiated a spiral in the free wall of the left ventricle using a S1-S2 protocol. In Figure 6.6, we show snapshots of consecutive wavefronts and the ECG pattern for both patient datasets (dataset 1 in the top row, and dataset 2 in the bottom row). For dataset 1, we observed that the initial spiral broke down into a chaotic fibrillatory pattern, and that the ECG signal was irregular and complex (dominant frequency of 4.6 Hz). For dataset 2, the initial spiral remained stable in the LV. Note that the spiral was not anchored, and did not (hyper)meander nor drift during the entire simulation. The ECG signal was periodic (dominant frequency of 4.5 Hz), which resembles ECG signals during ventricular tachycardia (VT). The frequency spectra of both ECG signals are shown in Figure 6.7. Although the simulations had similar dominant frequencies, the frequency spectrum of dataset 1 was broader in comparison to that of dataset 2, which had a single dominant peak. These observations are characteristic of the differences between VF and VT, respectively, and the frequencies are similar to those reported in clinical [23, 112, 116, 195] and numerical studies [170].

6.3.2 Number of Filaments

A convenient way to quantify the complexity of excitation patterns in the thick walled ventricles of the heart is by determining the number of scroll wave filaments of the excitation sources [21, 25, 73, 127, 144, 146, 170, 178]. A scroll wave filament is a line around which a 3D spiral wave rotates. When such a filament intersects with the surface of the heart, a phase singularity (PS) manifests on the heart surface. For dataset 2, we observed just one reentrant source, represented by a single filament.

In Figure 6.8, we show a snapshot of the filaments present for dataset 1 after 5 seconds of simulation time. Here the excitation pattern was organized by approximately 15 filaments. Most of these filaments extended from the epicardium to the endocardium, with only 5 filaments located entirely within the myocardial walls. We observed that the majority of filaments were located near the base of the heart, whereas very few filaments were present near the apex. Furthermore, most filaments were present in the left ventricular wall, i.e., the region with high restitution slope values. The filament numbers and shapes fluctuated during the

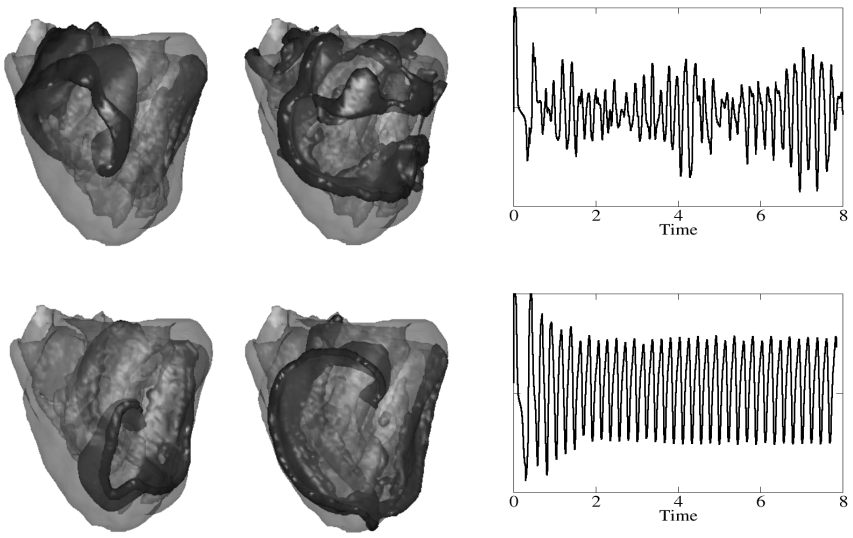

Figure 6.6: Wavefronts (in red on the left) and ECG signals (right). (Top) Dataset 1. (Bottom) Dataset 2. The first snapshot shows the spiral after initiation on the left ventricular free wall and the second snapshot shows wavefronts after 5 seconds of simulation time. For color see page 205.

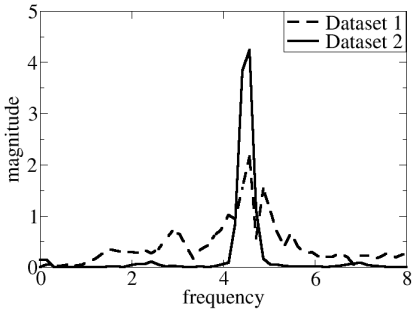

Figure 6.7: Frequency spectra of ECG signals. (Dashed) Dataset 1. (Solid) Dataset 2.

course of the simulation. In Figure 6.8, we show the time dynamics of the number of filaments during 8 seconds of simulation. After an initial phase of growth, the number of filaments fluctuated around 12-20. The average number of filaments was 14.9, which is within the range reported by Ten Tusscher et al. [170]. We also show the number of PS visible on the epicardium. The average number of PS was 10.7, thus the ratio of the number of filaments to PS was approximately 1.4, consistent with [170].

We analyzed how filaments were created and destroyed over time through death, birth, bifurcation and amalgamation events. This is shown in Figure 6.9 for dataset 1. Horizontal lines indicate individual filaments and their lifespan. The start of a line is determined by the birth of a filament or the bifurcation from another filament. The end of the line occurs when the filaments disappear, i.e., the death or the amalgamation of a filament with another filament. Short horizontal lines in Figure 6.9 correspond to short living filaments, and long lines correspond to long living filaments. During the simulation we detected 1463 filaments and 379 births, 547 deaths, 1085 bifurcations and 917 amalgamation events. In figure 6.9 we can see that most of the filaments exist only for a short periods of time, although there are small number of long lived filaments.

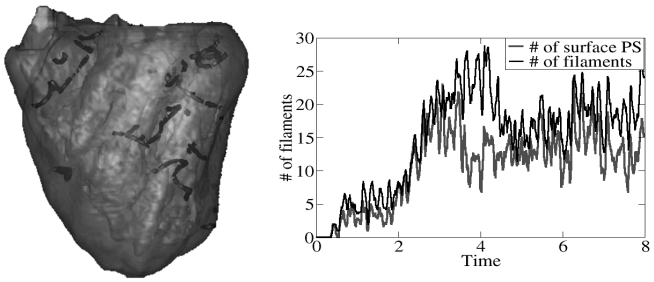

Figure 6.8: Filaments of dataset 1. (A) Snapshot after 5 seconds of simulation time. (B) Number of PSs (red) and filaments (black) over time. For color see page 205.

6.3.3 Role of Tissue Heterogeneity

To determine the effect of tissue heterogeneity on wave patterns during VF we performed a series of simulations in which we varied the degree of APD restitution heterogeneity in the heart. We did this by using the following linear transformation:

$$S_{new} = S_{avg} + \varepsilon(S_{max} - S_{avg}) \tag{6.9}$$

where, S_{new} is the new value of the maximum restitution slope at each given point, the average maximum slope taken over all points of dataset 1 is $S_{avg} = 1.78$, ε is a variable that scales the degree of heterogeneity and S_{max} is the original value of the maximum restitution slope at each given point for dataset 1. Clearly, $\varepsilon = 1$

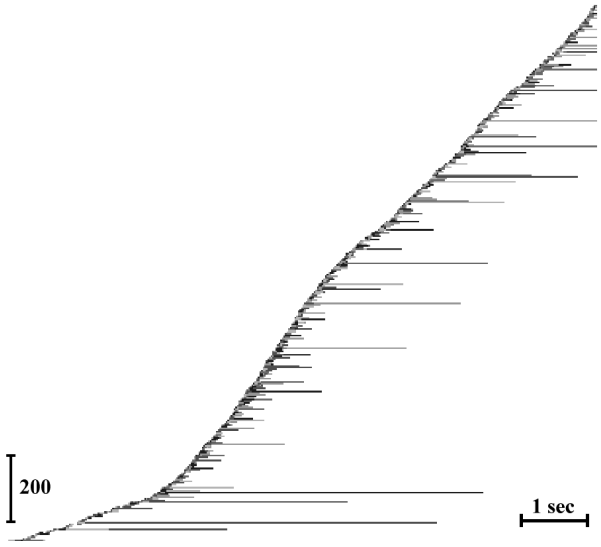

Figure 6.9: Filament history for simulated VF. Horizontal lines correspond to individual filaments and start at the time a filament appears (through birth or bifurcation) and stop at the time a filament disappears (through death or amalgamation). Filaments get assigned unique identity numbers that are not reused once a filament has died. Different colors are used to indicate clusters of filaments that can be traced back through bifurcation events to the same initial filament, which is the first filament of that color. We use different colors for filaments with the same ancestor only if the filament cluster has a size of 5 or more filaments. All other filaments that either have arisen through birth rather than bifurcation, or belong to a small cluster are colored black.

corresponds to the fully heterogeneous simulation of dataset 1 (presented above), $\varepsilon = 0$ corresponds to a spatially homogeneous restitution model with a slope of 1.78, and intermediate values of ε scale the degree of heterogeneity: larger values of ε correspond to more heterogeneous properties.

We performed a series of computations similar to that shown in Figure 6.6. The spiral was initiated in the LV wall using a S1-S2 protocol. We used ε values of 0, 0.25, 0.5, 0.75 and 1. The duration of all simulations was 8 seconds. We investigated the maximum number of filaments, average number of filaments, maximum number of epicardial PS and average number of epicardial PS for each simulation. The results are shown in Figure 6.10 and we see that for $\varepsilon = 0$ (homogeneous setting) full blown breakup did not occur for the given slope (1.78). We found that to induce breakup for our heart model, we needed to increase the restitution slope to above 1.8 (results not shown). This is consistent with the slope value reported by Ten Tusscher et al. [174], given the difference in the methods used for slope determination (see methods section). We see that the maximum number of filaments and the average number of filaments increased for increasing heterogeneity. Similar results were found for the epicardial PS.

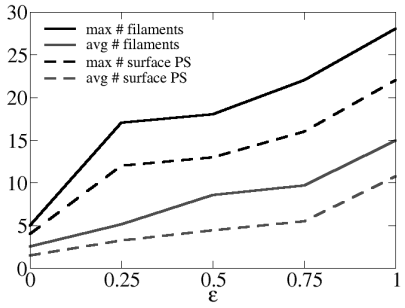

Figure 6.10: Number of filaments and epicardial phase singularities (PS) for different degrees of APD restitution heterogeneity ($\varepsilon = 0$, homogeneous; $\varepsilon = 1$, heterogeneous).

To understand the mechanism of increased filament numbers with increasing heterogeneity, we investigated filament locations in the heart. Figure 6.11 shows all the locations of filament voxels across two slices of the heart together with the maximum restitution slopes (for the 8 second run with $\varepsilon = 1$). The majority of the filaments were located in regions containing steep restitution slopes, and they were evenly distributed across these steep slope regions. Indeed, the mean +/- SD restitution slope taken across all voxels traversed by the filaments was significantly steeper (2.17 +/- 0.55) than that for the voxels spanning the remainder of the model (1.76 +/- 0.65, $p < 0.005$, 2-tailed Student t-test).

In our model, the slope of the restitution curve is related to APD (see Figure 6.5) and thus gradients in restitution slopes are associated with gradients in APD. Such APD heterogeneities could potentially induce new wavebreaks by

themselves (even without steep restitution) and this would be expected to occur in areas of abrupt APD variation. However, we did not observe this in our simulations. We observed comparatively fewer numbers of filaments in regions containing restitution slope gradients. Thus the increase in complexity of VF is more likely to be directly due to the increase in size of regions with a steep enough restitution slope (> 1.80), rather than an increased occurrence of new breaks at larger gradients of heterogeneities in APD.

An additional fact in favor of this hypothesis is that the electrical turbulence induced by steep restitution would be expected to be homogeneously distributed across entire regions of steep restitution, and this is what we have observed (Figure 6.11).

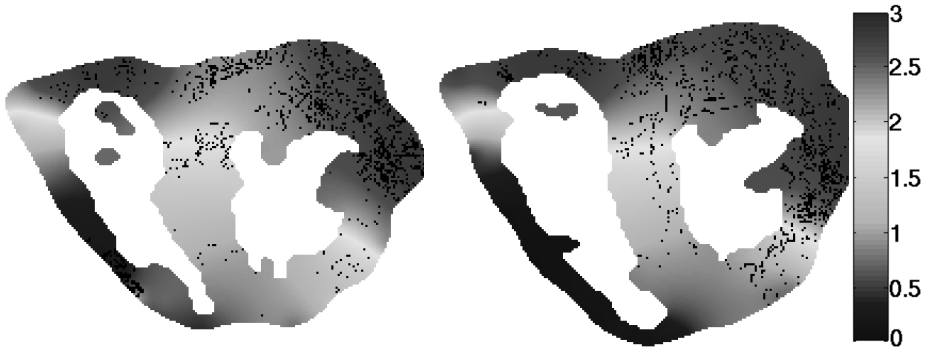

Figure 6.11: Location of filament voxels (black) for the entire 8 seconds run. Illustrated are short-axis slices mid-way between base-to-apex (left), and one-third of the distance from the base-to-apex (right). Maximum restitution slopes are represented using a pseudo-color spectrum. For color see page 205.

We finally investigated the spatial-temporal distribution of excitation periods for all voxels in the 3D ventricular anatomy for different extents of heterogeneity (ε). For this, we determined excitation periods in every voxel after 2 seconds of transient processes using a 2 second window. Figure 6.12 shows the distribution of excitation periods on the epicardium, averaged in a time interval between 2-4 seconds for $\varepsilon = 1$. We see that there are several distinct regions with different excitation frequencies. We followed this distribution until the end of the simulation and found that these regions with different periods are not anatomically predefined and that their location changes in the course of time (not shown).

We compared the spatial distribution of excitation periods in the interval 2-4 seconds for all values of ε. For the homogeneous simulation ($\varepsilon = 0$), we found that the average period values were distributed homogeneously and did not change over time. For ε values between 0 and 1 we found that the number of regions with different periods increased as the heterogeneity (ε) in APD slopes increased.

To quantify this increased heterogeneity in excitation period regions, we determined the average period value (dots) and the 95% confidence interval period values (bars) for different values of ε (see Figure 6.13). We did this both for

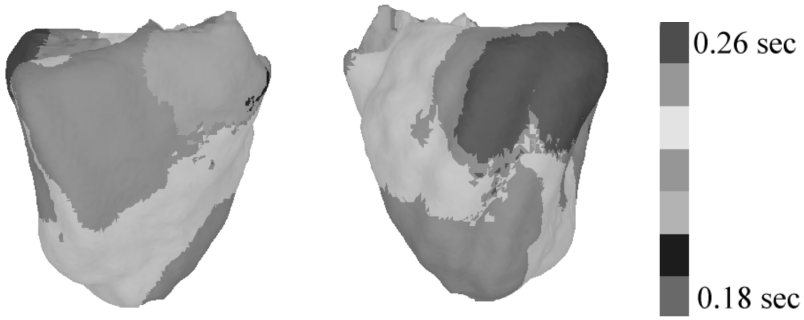

Figure 6.12: Average excitation periods for $\varepsilon = 1$ in a time interval between 2-4 seconds of simulation time. LV (left) and RV (right) views are shown. For color see page 206.

excitation periods distributions across the entire ventricular mass (gray) and for distributions across the ventricular epicardium (dark gray). Comparing the gray and dark gray bars, we see that the period distributions on the epicardial surface were similar to those measured over the entire ventricular mass. We see that the average periods (gray and dark gray dots, respectively) remained approximately equal for all values of ε, but that the width of the period distributions increased with increased ε (gray and dark gray bars, respectively).

Given the observed temporal variations in excitation period domains and our results on filament locations, we conclude that the increase in complexity of excitation period patterns is primarily caused by the increased number of filaments under increased heterogeneity rather than the increased heterogeneity in anatomically defined APD restitution regions itself.

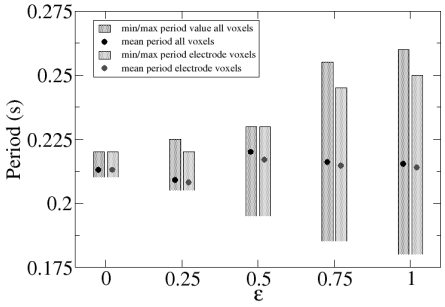

Figure 6.13: 95% confidence interval period values. Gray bars: minimum and maximum periods found in 95% confidence interval period values for all voxels in the entire ventricular anatomy. Dark gray bars: minimum and maximum period found in 95% confidence interval period values only for the 256 electrode positions on the epicardial surface.

6.4 Discussion

We have used a detailed human ventricular model to study wave organization during VF in the presence of APD restitution heterogeneity. The model contains a detailed description of human ventricular anatomy, fiber direction anisotropy, and the electrophysiological behavior of human ventricular cells. Recent clinical studies by Nash et al. [114] provided APD restitution properties at 256 locations spanning the entire ventricular epicardium for different patients. This study showed that APD restitution slopes are organized into different regions with slopes ranging from 0 to well over 3.

We incorporated the clinical data of Nash et al. [114] into our anatomically realistic model of the human ventricles by mapping from the 256 electrode locations to our ventricular geometry and interpolating the projected data using a diffusion based algorithm. Restitution slopes were then fitted by tuning selected parameters of the TNNP model, which were individually specified at each voxel based on the interpolated restitution slopes. For this study, we used datasets of 2 patients: dataset 1 contained regions of shallow and steep restitution slopes, while dataset 2 contained mostly shallow restitution slopes. Thus, the heterogeneity profiles of both datasets were different.

Heterogeneities are not necessary to induce VF in the human heart. As reported by Ten Tusscher et al. [170] VF can occur in a homogeneous heart if the slope of the restitution curve is higher than 1.5. In our model, a slope value of 1.8 or higher is necessary to induce VF. This difference in slope value is due to the difference in slope determination method used between Ten Tusscher et al. [170] and this chapter (see methods). Note, that the minimum slope value necessary to induce VF in a homogeneous heart is substantially higher than the value of 1, predicted from the original restitution hypothesis. As shown by Cherry and Fenton [20] in a Fenton-Karma model [33] and by Ten Tusscher et al. [174] in the TNNP model, this higher slope value can be explained by electrotonic interactions and CV restitution properties influencing APD alternans.

We analyzed the dynamics of filaments during VF, the formation via birth and bifurcations and the disappearance via death and amalgamation, and the duration of their lifespan. We found that most rotors were short lived, whereas only a small number of long lived rotors were present during VF. This is in agreement with the findings of [170] and experimental observations on epicardially manifested rotors in animal hearts [73, 145, 146].

We found that APD restitution heterogeneity is not only important for the initiation of wavebreak and re-entry [22, 24], but also affects the number of filaments during VF. We found that an increased level of APD restitution slope heterogeneity leads to more filaments and a broader and more dynamical distribution of excitation periods. We conclude that there is an interplay between the dynamical organization and complexity of VF, and the underlying APD restitution heterogeneity. Furthermore, our results are consistent with the notion that the increase in wavebreaks caused by increasing heterogeneity (ε) is predominantly due to the presence of larger areas with steep restitution slope, rather

than increased gradients in restitution slope or APD. However, we do not exclude that other factors such as geometric effects, anisotropy or more pronounced APD gradients potentially play a role in wavebreak formation.

Finally, we found that the number of epicardial PSs correlated well with the total number of filaments, and that distribution of epicardial excitation periods, provides a good estimate of the period distribution within the entire ventricular mass.

6.4.1 Limitations

Clinical data were only available for the epicardial surface of the ventricles. There was no information on restitution properties in the mid-myocardium nor endocardium. To overcome this, the epicardial restitution slope data was extrapolated across the entire ventricular walls using a diffusion based algorithm. Note that a variety of interpolation schemes could have been used to achieve a similar degree of variation. The use of different parameters in our diffusion algorithm may lead to different gradients in slope values for the same set of clinical data. It remains to be investigated how these different heterogeneity profiles with different slope gradients affect the results presented in this study.

Other heterogeneities such as epi-, endocardial and M-cells, Purkinje fibers, laminar sheets and disease conditions (such as fibrosis and gap junction remodeling) were not taken into account in our model and may also contribute to the complexity of excitation patterns during VF.

It should be noted that the mapping of the TNNP model parameters to the restitution slope values that we used is not unique, and that the same slopes may likely be obtained using other combinations of parameter settings. However, we believe that this non-uniqueness should not qualitatively affect the results of our study, as it is the slope of the restitution curve that is the main determinant of the instabilities in our model.

Another limitation is that TNNP model used in our study does not reproduce calcium driven alternans [137, 158, 159], which is an additional source of instability that can lead to VF.

Acknowledgments

The authors would like to thank Dr. R. Clayton for his valuable comments. This research was funded by the Netherlands Organization for Scientific Research (NWO grant number 814.02.014). M.P.N. was supported by the Marsden Fund Council from New Zealand government funding, administered by the Royal Society of New Zealand.

CHAPTER 7

A Computational Study of Mother Rotor VF in the Human Ventricles

R.H. Keldermann[1], K.H.W.J. Ten Tusscher[2], M.P. Nash[3], C.P. Bradley[4], R. Hren[5], P. Taggart[6], A.V. Panfilov[1]

[1] *Theoretical Biology/Bioinformatics Group, Utrecht University Padualaan 8, 3584 CH Utrecht, The Netherlands*

[2] *Department of Scientific Computing Simula Research Laboratory P.O. Box 134, 1325 Lysaker, Norway*

[3] *Bioengineering Institute and Department of Engineering Science University of Auckland Private Bag 92019, Auckland, New Zealand*

[4] *Department of Physiology, Anatomy and Genetics University of Oxford, Oxford, United Kingdom*

[5] *Institute of Mathematics, Physics, and Mechanics*
University of Ljubljana, Ljubljana, Slovenia

[6] *Department of Cardiology and Cardiothoracic Surgery*
University College Hospital, London, United Kingdom

Am. J. Physiol. Heart Circ. Physiol. 296: H370-H379 (2009)

Abstract

Sudden cardiac death is one of the major causes of death in the industrialized world. It is most often caused by a cardiac arrhythmia called ventricular fibrillation (VF). Despite its large social and economical impact, the mechanisms for VF in the human heart yet remain to be identified. Two of the most frequently discussed mechanisms observed in experiments with animal hearts are the multiple wavelet and the mother rotor hypotheses. Most recordings of VF in animal hearts are consistent with the multiple wavelet mechanism. However, in animal hearts, mother rotor fibrillation has also been observed. For both multiple wavelet and mother rotor VF, cardiac heterogeneity plays an important role.

Clinical data of action potential restitution measured from the surface of human hearts were recently published. These in vivo data show a substantial degree of spatial heterogeneity. Using these clinical restitution data, we study the dynamics of VF in the human heart using a heterogeneous computational model of the human ventricles. We hypothesized that this observed heterogeneity can serve as a substrate for mother rotor fibrillation.

We found that, based on these data, mother rotor VF can occur in the human heart and that ablation of the mother rotor terminates VF. Furthermore, we found that both mother rotor and multiple wavelet VF can occur in the same heart depending on the initial conditions at the onset of VF. We studied the organization of these two types of VF in terms of filament numbers, excitation periods and frequency domains.

We conclude that mother rotor fibrillation is a possible mechanism in the human heart.

7.1 Introduction

Sudden cardiac death is the most common cause of death in the industrialized world and in most cases it is due to ventricular fibrillation (VF) [202]. During VF, excitation waves are disturbed causing the contraction of the ventricles to become rapid and uncoordinated. It has been shown in clinical and experimental studies that these turbulent wave patterns are underpinned by re-entrant sources of excitation [29, 45, 62, 107, 178, 190]. If VF is not halted by means of defibrillation, this condition will be lethal within several minutes.

Several mechanisms have been proposed to explain the dynamics of VF. One widely studied mechanism is known as *multiple wavelet* VF [105, 106] and is characterized by the presence of multiple self-sustained electrical wavelets in the heart. These wavelets may be arise due to dynamical instabilities, which are associated with action potential duration (APD) restitution properties (the so called restitution hypothesis) [36, 50, 125, 128, 131, 140, 184] and intracellular calcium dynamics [185]

Another well-established mechanism is known as *mother rotor* fibrillation, in which VF is driven by a dominant fast source of excitation [19, 69, 200]. This rapid reentrant electrical source (i.e., the mother rotor) is responsible for maintaining VF and causes conduction block in the surrounding tissue due to heterogeneity in refractory periods [8]. The activation source is so fast that it is unable to conduct in some regions where it blocks but manages to conduct in other regions where refractoriness allows. As a result, multiple small wavebreaks and irregular activation patterns are generated [69].

Mother rotors have been observed in VF experiments in animal hearts. Samie et al. [152] reported the presence of a high frequency rotor in the left ventricle responsible for maintaining VF in guinea pig hearts. They also demonstrated that a spatial left-right gradient in I_{K1} provides a robust ionic mechanism for rotor stabilization in the left ventricle and wavebreak generation in the right ventricle. Mother rotor fibrillation has also been reported in rabbit hearts [19, 193]. Furthermore, long-lived, stationary rotors have been reported in isolated right ventricular slaps of sheep [200]. Multiple attempts to find similar mother rotor VF in the pig heart were not successful [64, 72, 73]. Although these studies showed the presence of long lasting epicardial rotors, they were not consistently present throughout VF. The authors concluded that epicardial mother rotors did not drive VF in their experimental model, however the presence of a transmural mother rotor could not be ruled out. In the human heart, several clinical studies have investigated VF organization on the epicardial and/or endocardial surface [102, 111, 112, 116]. In particular, the study by Nash et al. [116] reported persistent epicardial rotors that lasted over 5 seconds, corresponding to 20 reentrant cycles or more. However, similar to studies on pig hearts [64, 72, 73], these rotors were not consistently present throughout the measured VF episodes. The study by Masse et al. [102] showed an example of a persistent rotor on the endocardium co-existing with multiple reentrant patterns occurring on the epicardium, and suggested that this could be a recording of mother rotor fibrillation. However, as in the study of

Nash et al. [116] this persistent rotor was not consistently present throughout the measured VF episode. Finally both these studies [102, 116] could not determine whether these long lasting rotors were responsible for driving VF or represented only part of the multiple wavelet activity.

One factor contributing to the plausibility of mother rotor VF is electrophysiological tissue heterogeneity [200]. In heterogeneous tissue the period of rotation varies spatially, and if a rotor is placed in a region where rotation is fastest, then it may serve as a mother rotor that drives VF [152]. Recently, in clinical studies [114, 198], large degree of electrophysiological tissue heterogeneity were also reported in human hearts.

The primary aim of this chapter was to study whether the electrophysiological tissue heterogeneity recorded by Nash et al. [114] could provide a substrate to support mother rotor VF in the human heart. We define mother rotor VF as a stationary persistent source that lasted for at least 5 seconds and actively induced wavebreaks. In addition, elimination of the mother rotor must result in VF termination. Having identified such rotors, we also studied the organization of the resulting mother rotor VF and compared this with multiple wavelet VF in the human heart.

This study utilized an integrative model of the human ventricles, which incorporates a detailed ionic model of the human ventricular myocyte [171, 174], combined with an anatomically realistic geometry of the human ventricles, which includes fiber direction anisotropy [60]. Recently, this model was extended [77] to include heterogeneous APD restitution data from the human ventricles obtained from [114]. Our modeling framework allows us to check whether VF in the human heart can be driven by a mother rotor, and to study how properties of the mother rotor (such as its frequency) affect the VF excitation patterns. Performing such studies experimentally is difficult, if not impossible.

7.2 Materials and Methods

We use a realistic model of the human ventricles, which contains a detailed description of cell electrophysiology, ventricular anatomy and fiber direction anisotropy [171, 174]. We have extended this model to include clinically measured restitution data of the human ventricles [114] using our previously developed diffusion based algorithm [77].

Human Ventricular Model

We model excitable behavior using a monodomain description of cardiac tissue [74]:

$$C_m \frac{\partial V_m}{\partial t} = \frac{\partial}{\partial x_i}\left(D_{ij}\frac{\partial V_m}{\partial x_j}\right) - I_{ion} \tag{7.1}$$

where V_m denotes the transmembrane voltage, C_m the membrane capacitance, D_{ij} the diffusion tensor accounting for the anisotropy of cardiac tissue, and I_{ion} the sum of the ionic transmembrane currents describing the excitable behavior of the individual ventricular cells. To represent human ventricular electrophysiological properties we used the ionic model developed by Ten Tusscher et al. [174] (see Appendix A) and refer to this as the TNNP model. This model provides a detailed description of voltage, ionic currents and intracellular ion concentrations. The model represents the intracellular calcium dynamics by including subspace calcium dynamics, which controls the L-type calcium current and the calcium-induced calcium release (CICR). CICR is modeled with a four-state Markov model for the ryanodine receptor, and both the fast and slow voltage-gated inactivation of the L-type calcium current are also incorporated (see [174] for detailed information). The model reproduces experimentally measured APD [108, 114] and conduction velocity restitution curves [41].

Geometric data describing the 3D ventricular anatomy and fiber direction field are derived from a normal healthy human heart [60] and is described in more detail in [170]. Overall, the heart was represented by approximately 13.5 million points with a spatial resolution of 0.25 *mm*. As in [170], we assume that the transverse conductivity is the same in all directions orthogonal to the longitudinal direction of the muscle fiber axis and that local conductivity tensors D_{ij} can be derived from local muscle fiber directions using:

$$D_{ij} = D_T * \delta_{i,j} + (D_L - D_T)\alpha_i\alpha_j \tag{7.2}$$

where, D_L and D_T are the longitudinal and transverse conductivity, respectively and α is the muscle fiber direction. For D_L we used 162 Ωcm and for D_T we used 40.5 Ωcm, which resulted in conduction velocities of 68 cm/s in the longitudinal direction and 32 cm/s in the transverse direction, similar to the values reported by [167]. The resulting anisotropy ratio was approximately 2:1, which is also consistent with clinical measurements [71].

7.2.1 Clinical Data on Restitution Heterogeneity

We have used clinical restitution data from [114], which provided global epicardial APD restitution properties in cardiac patients undergoing aortic valve replacement or coronary artery bypass graft procedures. Activation-recovery intervals (ARI) were recorded on the entire ventricular epicardial surface using an epicardial sock containing 256 unipolar contact electrodes (inter electrode spacing ∼10

mm). ARI values have been shown to correlate with the 50% action potential duration repolarization values (APD_{50}) [56]. In each electrode, restitution properties were determined using a standard S1-S2 protocol. Then, clinical restitution data was fitted using a least-squares mono-exponential fit, and maximum restitution slopes (S_{max}) were determined for each electrode. For more information about the clinical data and procedures used we refer to [114].

For this study, we used data from a single patient. This dataset contains a large degree of heterogeneity and steep slopes of measured APD restitution (see Supplementary Material, Figure 1). The mean ± SD S_{max} was 2.01 ± 1.20 based on $n = 243$ (95%) valid restitution curves (see [77]). We assigned these restitution properties throughout the entire 3D ventricular mass. However, data on the full 3D organization of APD restitution in the human ventricles are presently not available. Observations have been reported only for surfaces of the heart. To date, either epicardial or endocardial recordings for individual hearts have been reported [114, 198]. For both the epicardial and endocardial data, the maximum restitution slopes varied markedly between regions and the spatial arrangement of these regions varied considerably within and between patients. It is likely that this heterogeneity has a 3D structure.

In the absence of a 3D restitution profile, we extrapolated the epicardial data from Nash et al. [114] across the 3D mass. To this end, we developed a diffusion based algorithm to smoothly extend the epicardial profile across the ventricular muscle. We first extended the 243 clinically measured surface S_{max} values across the entire ventricular walls by solving a diffusion problem. The variable S_{max} was kept constant at each electrode position during the diffusion process. As a result, we obtained a smooth spatial interpolation of S_{max} across the ventricles, except for regions immediately adjacent to the recording electrodes. The second step was to remove these sharp gradients by applying a $3 \times 3 \times 3$ voxel moving average window. The third step involved a linear scaling to correct all 13.5 million S_{max} values based on the original known 243 S_{max} values at the recording electrode locations. For a more extensive description of the diffusion algorithm, we refer to [77]. We believe that this is a reasonable first step to qualitatively describe APD restitution heterogeneity until more detailed data on the 3D organization of restitution in the human restitution becomes available.

The results of this interpolation for the current dataset are shown in Figure 7.1. We see that a large region of the posterior wall contains steep restitution slopes, with maximum slope values up to 3. The left ventricle contains more shallow restitution slopes, with maximum slope values of approximately 0.5-1. Between these regions, intermediate values are present. The mean ± SD restitution slope is 2.01 ± 0.25 ($n = 13.5$ million).

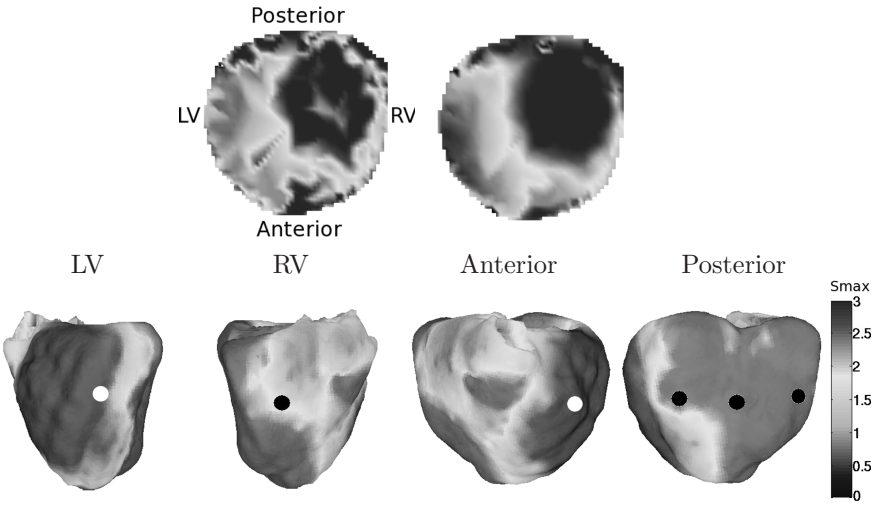

Figure 7.1: Polar and 3D plots of maximum restitution slope values S_{max}. (Top) Distribution of epicardial restitution, S_{max} shown on polar projections, with the epicardial apex at the center of each plot and the ventricular base at the outer circumference. (Top left) 243 *experimental* S_{max} values interpolated across the polar plot using MATLAB's griddata. (Top right) *model* S_{max} values after the diffusion based algorithm. (Bottom) *model* 3D plots of maximum restitution curves S_{max}. From left to right: LV, RV, anterior and posterior views. The circles denote the positions of initial wavebreaks leading to the formation of the first spiral wave. Black circles indicate positions of the first wavebreak that lead to multiple wavelet VF dynamics, whereas white circles indicate positions of first wavebreak that lead to mother rotor fibrillation type dynamics. Maximum restitution slope values range from 0.5 (blue) to 3 (red). For color see page 206.

7.2.2 Numerical Approach

Equations for the gating variables in the TNNP model were integrated using a Rush and Larsen integration scheme [149]. To integrate Equation 7.1, we used a forward Euler scheme with a time step of $\Delta t = 0.02$ ms and a space step of $\Delta x = 0.25$ mm. No-flux boundary conditions were used so that the axial current flow from heart points to non-heart points was set zero. For more details we refer to [77, 170]

7.2.3 Induction of Ventricular Fibrillation

To initiate 3D scroll waves, we used a S1-S2 protocol, for which a S1 stimulus was applied at either the right ventricles or on the posterior junction of the right and left ventricles. The S2 stimulus was activated during the refractory tail of the S1 stimulus and was extended from the base for approximately 50% of the base-apex dimension, thereby creating a single scroll wave. We varied the position of the S2 stimulus such that the core of the initial scroll wave was located in different regions of the ventricles, with either shallow or steep restitution curves (see Figure 7.1). Stimulus currents were applied at twice the diastolic threshold value. We performed different simulations of VF by initiating the scroll wave at different locations (see Figure 7.1, black and white circles). The difference between these black and white circles will be described later. Furthermore, we also initiated a scroll wave in the septum (not shown in Figure 7.1). Simulations were run for 8 seconds or were terminated if there was no activity present.

7.2.4 Electrograms

Assuming that the medium is an infinite volume conductor, electrograms can be calculated using the dipole source density of the membrane potential in all voxel points using [135]:

$$ECG = \int_V \frac{D\nabla V_m \cdot \overrightarrow{r}}{r^3} dV \tag{7.3}$$

where, V is the domain of integration (i.e., the ventricular volume), and $\overrightarrow{r}$ is the vector from each point to the recording electrode, which was placed 10 cm from the center of the ventricles in the anterior direction of the transverse plane.

7.2.5 Filaments and Phase Singularities

Scroll wave filaments were detected using an algorithm proposed by Fenton and Karma [33]. If there is a spiral wave in 2D (a scroll wave in 3D) present, the core (filament) can be defined as the point(s) for which the excitation wavefront and waveback meet. This can be calculated as the intersection points of an isopotential line (we used -60 mV) and the $dV/dt = 0$ iso-line. Voxel data corresponding to these intersection points were then stored. Individual filaments were detected

by iteratively joining neighboring voxels that were designated as filament points. Filaments were determined at 10 *ms* intervals. Of these filaments, we tracked: the time of birth, time of death, time of bifurcation, time of amalgamation, lifespan, filament from which a filament bifurcated, filament into which a filament amalgamated, and ultimate filament to which a filament can be traced back through the bifurcations events [170]. Filaments were categorized based on their geometrical position and assigned to either the left ventricle, right ventricle or septum.

7.2.6 Period Distribution and Frequency Domains

For all simulations we calculated the interbeat interval between successive action potentials in every heart point ($n = 13.5$ million points) following the initiation of VF (i.e., after the first 2 seconds of simulation time). For the histograms (Figures 7.6 and 7.10) the mean period was calculated in every point between 2-6 seconds of simulation time. The histogram range is 0.16-0.28 seconds and the bin size 1 ms. Note that this method is different from experimental methods which calculate the dominant frequency via fast Fourier transformations of optical action potential mappings [116, 152, 193, 200]. Because experimental recordings are often measured during time intervals which exceed our simulation time (minutes vs seconds) we prefer to use direct measurement of period values.

7.2.7 Implementation

All simulations were coded in C++ and MPI and were run on 16 processors of a Beowulf cluster consisting of 16 Dell 650 Precision Workstations (dual Intel Xeon 2.66 GHz). Simulating 1 second of wave propagation in the ventricles took approximately 6.5 hours of wall-clock computation time. Ventricular geometry, wave patterns and scroll wave filaments were visualized using the marching cubes algorithms for isosurface detection in voxel data, and OpenGL for isosurface rendering.

7.3 Results

7.3.1 Multiple Wavelet and Mother Rotor VF Wavefronts

Scroll waves were initiated at different locations of the ventricles (see Figure 7.1, white and black circles). After investigating the results of the different starting locations, we found that we could distinguish two different types of VF dynamics which were dependent on the location of the first spiral.

The first type of VF dynamics we found is *multiple wavelet* VF and was investigated in our previous publication [77]. The starting locations of the initial spiral for this type of VF are denoted by the black circles in Figure 7.1. These initial locations were located in regions containing steep restitution slopes. Figure 7.2 shows a typical example of these dynamics. After initiation, we observed that the spiral wave broke up into multiple wavelets that were predominantly located

in the right ventricle, where APD restitution was steepest (slopes of 2.5-3). The chaotic spatio-temporal patterns that arose persisted throughout the simulations and were similar to the restitution induced multiple wavelet VF dynamics we studied in [77, 170].

The second type of VF we found is *mother rotor* VF. For several other initial conditions (denoted by the white circles in Figure 7.1), located in regions with shallow restitution slopes, we found patterns of excitation that were different from the patterns described above. In both cases the mother rotor was similar in size. Figure 7.3 shows an example of such an excitation pattern. After an initial transient, we observed a persistent (single) stable spiral wave located in the left ventricle, where restitution slopes were shallow (slopes of 0.5-1.0). At the same time, we observed the continuous formation of wavebreaks occurring on the other side of the heart (the free wall of the right ventricle and posterior wall), where restitution slopes were steep (slopes of 2.5-3). These wave patterns are consistent with mother rotor fibrillation. In order to verify this, we show below that these wavebreaks were indeed driven by the single stable spiral in the left ventricle.

During mother rotor VF wavebreaks were induced by dynamical heterogeneity (due to steep slopes of the APD restitution curves). Indeed, we found that wavebreaks occurred not immediately, but after several cycles of mother rotor rotation. Moreover, APD alternans instability was clearly evident at the locations of onset of wavebreaks. This wavebreak mechanism differs from the mechanism of wavebreaks due to conduction blocks between regions with different refractoriness that is usually reported to underlie mother rotor fibrillation.

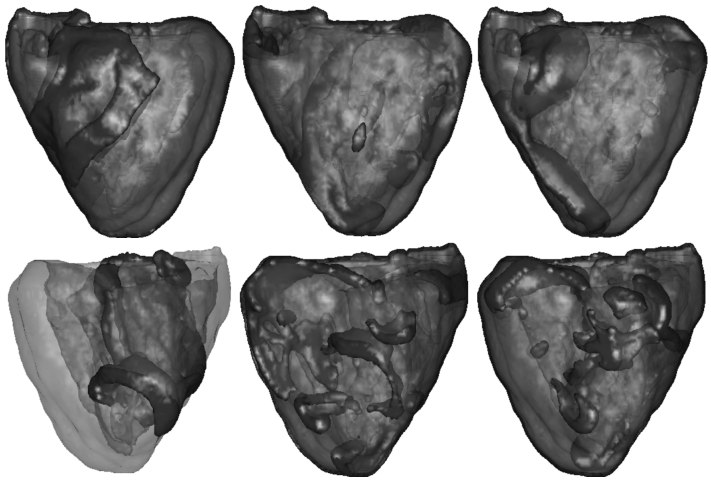

Figure 7.2: Multiple wavelet VF. Wavefronts are shown in red. (Top) LV view. (Bottom) RV view. (First column) Location of the initial spiral. (Second column) After 5 seconds. (Third column) After 7 seconds. Most wavebreaks occur in the RV free wall and exist independently. For color see page 207.

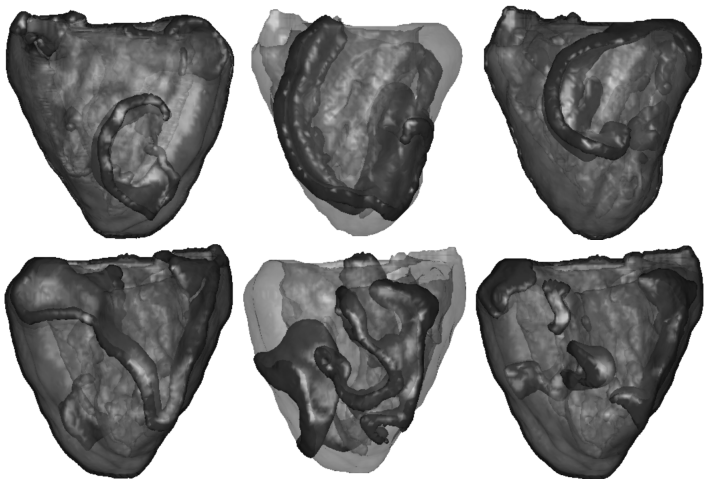

Figure 7.3: Mother rotor fibrillation. Wavefronts are shown in red. (Top) LV view. (Bottom) RV view. (First column) Location of the initial spiral. (Second column) After 3.5 seconds. (Third column) After 10 seconds. Note the stable spiral in the LV free wall, while breaks occurred in the RV free wall. The spiral in the LV wall remained stable until the end of the simulation (up to 12 seconds simulated). Breaks in the RV were driven by the mother rotor spiral. For color see page 207.

7.3.2 Ablation of the Mother Rotor

To test the hypothesis that the wavebreaks observed in Figure 7.3 are driven by the mother rotor, we eliminated the mother rotor spiral 3 seconds after its onset by removing approximately 20% of the left ventricular free wall of the left ventricle that contained this rotor (see Figure 7.4). We found that after removal, the wavebreaks did not complete rotation and that the wavetips of the rotors ran into the refractory tails of the waves and disappeared. After 0.5 seconds there was no wave activity present in the heart. Thus, the wavebreaks in the right ventricle (Figure 7.3) seem to be driven by the stable spiral wave in the left ventricle implying that this is indeed mother rotor fibrillation. We tested this removal procedure further by applying it at different phases of the mother rotor rotation, and by removing different sized regions (10-20% of the LV free wall). We found that as soon as the mother rotor activity was eliminated, the wavebreaks in the right ventricle died out.

Clearly, removing part of the myocardium decreased the overall ventricular mass of the heart, which could potentially terminate wave activity during fibrillation (critical mass hypothesis). To verify that this was not the case here, we repeated the multiple wavelet simulations shown in Figure 7.2 and removed the same part of the left ventricle as we did for the mother rotor simulation. We found that multiple wavelet VF did not terminate after the removal of tissue, and that the right ventricle sustained multiple independent sources, which could complete a rotation and were not terminated by the tissue removal procedure

(Figure 7.5). Thus termination of mother rotor VF was not related to the critical mass phenomenon, but to the removal of a persistent rotor that was responsible for actively inducing wavebreaks.

These results demonstrate that VF in Figure 7.3 is driven by a single spiral and represents mother rotor VF. Interestingly, our simulations show that multiple wavelet and mother rotor VF can occur in the same heart, depending on the initial location of the spiral.

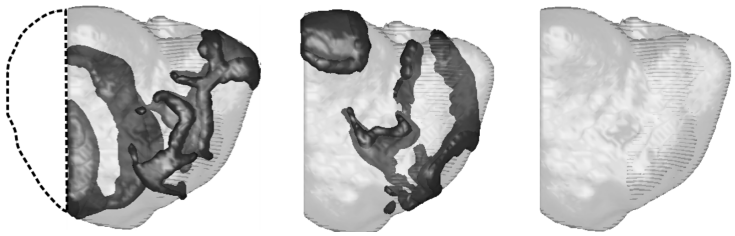

Figure 7.4: Ablation of the mother rotor spiral in the LV (posterior view). The black dashed line denotes the part of the ventricles that was removed. The first snapshot is at approximately 3 seconds of simulation time (i.e., the time when part of the LV was removed), the second snapshot at 3.3 seconds and the third snapshot is at 3.5 seconds, after which there was no longer any wave activity. For color see page 208.

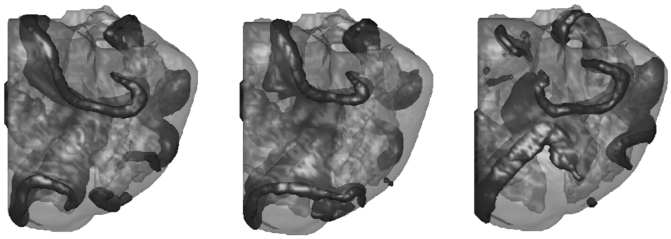

Figure 7.5: Ablation of the LV (posterior view) during multiple wavelet VF. The first snapshot is at approximately 3 seconds of simulation time (i.e., the time when part of the LV was removed), the second snapshot at 3.5 seconds and the third snapshot is at 4.0 seconds. Clearly it can be seen that after ablation there are multiple independent sources of wave activity present. As a consequence, wave activity did not terminate due to the ablation procedure and the underlying wave dynamics did not change. For color see page 208.

7.3.3 VF Dynamics and Organization

ECG, Period Distribution and Frequency Domains

In Figure 7.6 we show the ECG and period distributions for both the multiple wavelet and the mother rotor simulations. For multiple wavelet VF (Figure 7.6A) the ECG had a mean frequency of 4.4-4.5 Hz, similar to clinically recorded frequencies [23, 112, 116, 195]. For the mother rotor fibrillation (Figure 7.6B) the

mean frequency was very similar and had a mean frequency of 4.6-4.7 Hz. Both ECGs have similar complexity. Note, that the shape of the FFT spectra for the ECGs shown in Figure 7.6A,B were similar (Supplementary Material 7.13), and there did not appear to be any relationship between period distribution and underlying heterogeneity profile (Supplementary Material 7.12).

We also determined period values for every point ($n = 13.5$ million heart points) from 2 to 6 seconds and constructed a histogram of mean period values for these simulations (Figure 7.6C,D). We see that histograms for the mother rotor and for the multiple wavelet VF differ substantially. For multiple wavelet VF (Figure 7.6C) we see a broad period distribution with mean period of 0.223 (4.48 Hz)(box-plot stats: median= 0.217, interquartile-range= 0.016, $n = 13.5$ million), while for the mother rotor VF (Figure 7.6D) the distribution has a clear peak at 0.216 seconds, corresponding to the period of the mother rotor, and a narrow distribution. Overall the mean was 0.216 (4.63 Hz)(box-plot stats: median= 0.216, interquartile-range= 0.002, $n = 13.5$ million).

In Figure 7.7, we show the corresponding 3D spatial distribution of the mean period values for the multiple wavelet and mother rotor simulation measured between 2-4 and 4-6 seconds, respectively. Indeed, during multiple wavelet VF period values are grouped into different domains with different frequencies (Figure 7.7A). However, these domains are not anatomically pre-defined and change during the course of the simulation (Figure 7.7B) as they are determined by dynamical processes [77]. For the mother rotor simulations, we did not observe distinct frequency domains for the durations between 2-4 (Figure 7.7C) or 4-6 seconds. In this case, the period distribution was mainly determined by the frequency of the mother rotor.

Number of Filaments

A convenient way to quantify the complexity of excitation patterns in the ventricles of the heart is by determining the number of the excitation sources (scroll wave filaments) [21, 25, 73, 127, 144, 146, 170, 178]. A scroll wave filament is a line around which a 3D spiral wave rotates. When such a filament intersects with the surface of the heart, a phase singularity (PS) manifests on the heart surface. In Figure 7.8, we compare the time dynamics of the total number of filaments and epicardial PSs for both the multiple wavelet and the mother rotor simulation.

For the multiple wavelet simulation, the number of filaments varied between 10-30. The mean number of filaments was 11.2 and the mean number of PS was 8.0. Initially there were only filaments detected in the right ventricle, but after approximately 4.5 seconds of simulation time there were also filaments detected in the left ventricle. Most wavebreaks were found in high restitution areas, but sometimes wavebreaks also occurred in areas with shallow restitution slopes at the boundary between steep and shallow restitution regions. Additional characteristics of multiple wavelet VF organization such as location of breaks have been previously discussed in [77]. The ratio of the number of filaments to PSs was approximately 1.4, consistent with earlier findings [170].

For the mother rotor VF, the number of filaments varied between 2-8, which

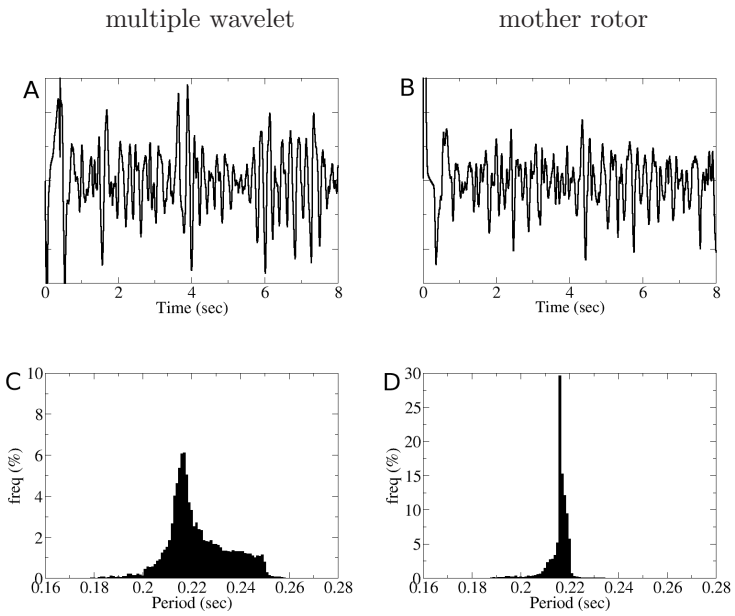

Figure 7.6: ECG (A,B). Histogram of the mean period distribution measured in all heart points between 2-6 seconds of simulation time (C,D). Left: multiple wavelet simulation. Right: mother rotor simulation.

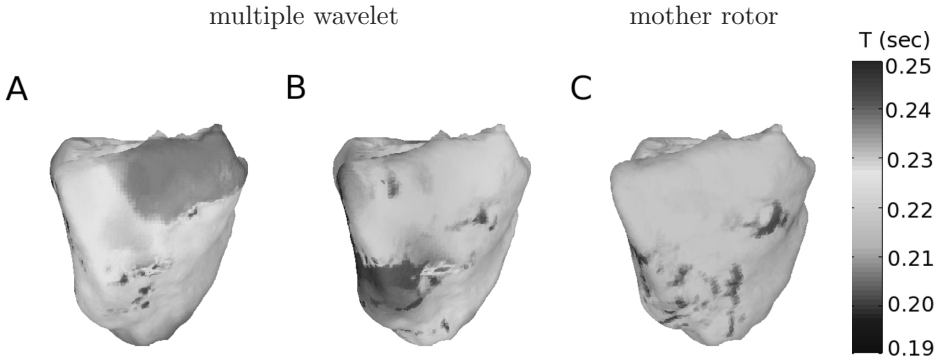

Figure 7.7: Spatial distribution of mean period values. (A) and (B) Multiple wavelet simulation, period distribution shown between 2-4 and 4-6 seconds. (C) Mother rotor simulation, period distribution shown between 2-4 seconds. Similar pattern occurs for the time interval between 4-6 seconds. Right ventricular free wall is shown. Period values range from 0.19 s (blue) to 0.25 s (red). For color see page 208.

is lower compared to multiple wavelet VF. The mean number of filaments was 3.8 and the mean number of PS was 2.3, resulting in a 1.65 ratio between filaments and epicardial PS. Apart from the mother rotor filament in the left ventricle, most filaments occurred in the right ventricle.

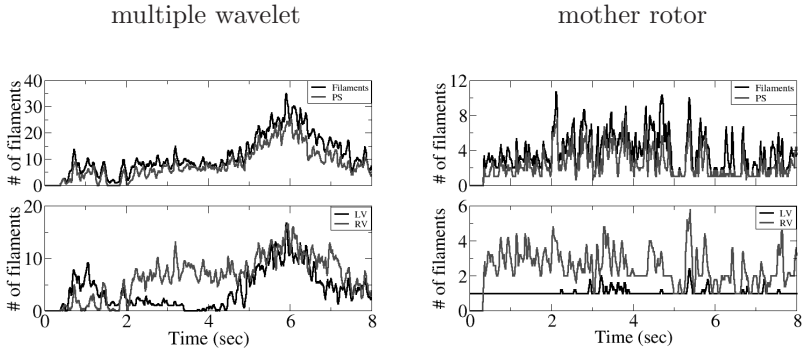

Figure 7.8: Total number of filaments and epicardial PSs. (Left) Multiple wavelet VF. (Right) Mother rotor fibrillation. (Top) Total number of filaments and epicardial PSs. (Bottom) Number of filaments in the LV and RV are shown (filaments in the septum not included). For color see page 209.

Filament History

We also analyzed filament history by tracing the events of filament creation and elimination over 8 seconds of time through death, birth, bifurcation and amalgamation events. This is shown in Figure 7.9 for both the multiple wavelet and the mother rotor fibrillation simulations.

For the multiple wavelet VF simulation, we detected 1025 filaments. Most of the filaments existed only for short periods of time (< 0.5 seconds). However, we also observed few long living filaments, which lasted for several cycles (up to 2-3 seconds). The mean lifespan of a filament was 0.084 seconds ($n = 1025$).

For the mother rotor fibrillation simulation, we detected 388 filaments. During this simulation the mother rotor filament was stable and was present until the end of the simulation. All other filaments existed for short periods of time ($< 0.25 - 0.5$ seconds). Similar results have been reported for rabbit hearts where VF was driven by a mother rotor [19]. The mean lifespan of a filament was 0.068 seconds ($n = 387$, mother rotor filament excluded).

We find that the total number of filaments during mother rotor fibrillation is 2-3 times smaller compared to the multiple wavelet fibrillation. In addition, during mother rotor fibrillation filaments have a shorter lifetime ($p < 0.05$, unpaired Student t-test). Furthermore, during multiple wavelet VF there were several filaments that lasted longer (up to 2-3 seconds), while during mother rotor fibrillation only short lived filaments accompanied the (long-lasting) mother rotor. Similar results were found for the simulations using other initial conditions that resulted in either multiple wavelet or mother rotor VF (see Table 7.1).

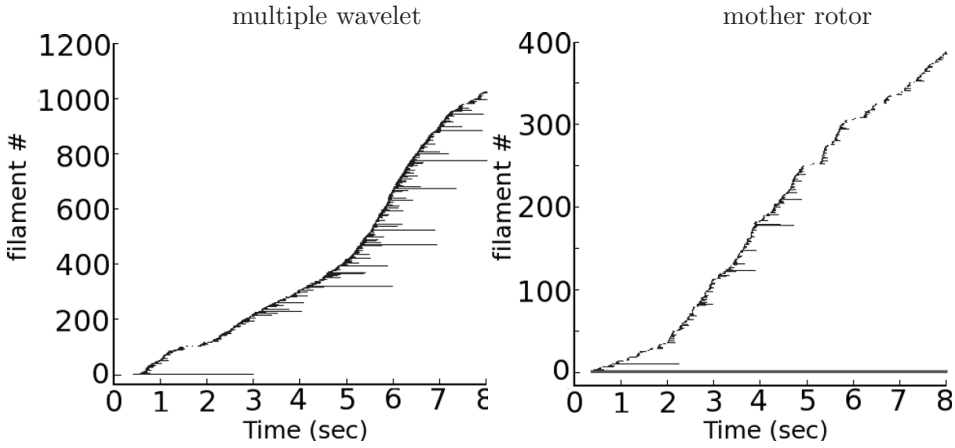

Figure 7.9: Filament history for multiple wavelet (left) and mother rotor (right) fibrillation. Horizontal lines correspond to individual filaments and start at the time a filament appears (through birth or bifurcation) and stop at the time a filament disappears (through death or amalgamation). The lengths of the lines denote the lifespan of each individual filament. For the multiple wavelet 1025 filaments were detected and 368 births, 525 deaths, 658 bifurcations and 501 amalgamation events were found. For the mother rotor fibrillation simulation, we detected 388 filaments and 223 births, 283 deaths, 166 bifurcations and 106 amalgamation events. The mother rotor filament can be clearly seen at the bottom of the graph (dark gray line), starting at the very beginning of the simulation and persisted until the end of the simulation (up to 12 seconds simulated).

7.3.4 Effect of Mother Rotor Frequency on VF Dynamics

If fibrillation is driven by a mother rotor, then influencing the frequency of the mother rotor should have a substantial effect on VF dynamics. We performed additional simulations in which we decreased the maximal conductance of the L-type Ca current in the region in which the mother rotor resided to 50, 35 and 25% of it's original value. This intervention increased the frequency of the mother rotor and resulted in flattening of the restitution slope in the region of the mother rotor. This did not change the type of rotation of the mother rotor, which remained stable after the intervention.

The results of these simulations are shown in Figure 7.10. Figure 7.10A shows the same period distribution as in Figure 7.6D for normal I_{CaL} conductance. We see a narrow unimodal period distribution with a mean period of 0.216 seconds. Spatially distinct frequency domains were not observed (see Figure 7.7C).

We see that for a 50% I_{CaL} reduction the mean period of VF decreased to 0.204 seconds (see Figure 7.10B). We also see that the period distribution became wider and that a small second peak arose around a period of 0.218 sec. When we decreased I_{CaL} to 35% of its normal conductance a bimodal period distribution arose (see Figure 7.10C), with a first peak around an mean period of 0.202 sec. and a second peak with a mean period of 0.210 sec. When we decreased I_{CaL} to 25% of its original conductance, the split in the period distribution became more

init	type	#filaments	avg. lifespan (sec)
LV	MR	388	0.068
LV-ANT	MR	518	0.061
LV-POST	MW	1268	0.081
POST	MW	1025	0.084
RV-POST	MW	952	0.082
RV	MW	978	0.079
SEP	MW	980	0.084

Table 7.1: Total number of filaments detected during 8 seconds of simulation time for different locations of the initial scroll wave (init). LV: left ventricle. RV: right ventricle. POST: posterior. ANT: anterior. SEP: septum. MR: mother rotor fibrillation, MW: multiple wavelet VF.

pronounced (see Figure 7.10D). The first peak had a mean period value of 0.197 sec., whereas the second peak increased to a mean of 0.252 sec., which is much larger than the mean period value for the original settings of G_{CaL} (0.216 sec).

The bimodal period distributions that occur for decreased I_{CaL} conductance reflects an underlying 3D spatial distribution of periods, as is shown in Figure 7.11A,B for the case were I_{CaL} is reduced to 25% of its original value. We clearly see that the heart is subdivided into different frequency domains: the mother rotor area (which has a period of 0.197 sec. (accounting for the left peak in Figure 7.10D)), and the area around the right ventricle where most of the wavebreaks occur and which has a much longer period of excitation (accounting for the right peak in Figure 7.10D). Such domains of different frequency of excitation are similar to those reported in experimental studies of atrial and ventricular mother rotor fibrillation [70, 200]. These domains arise when differences in refractory periods between different regions are large enough to cause Wenckebach like conduction blocks, which is presumed to be the sole mechanism for wavebreak formation during mother rotor type fibrillation.

We conclude that increasing the frequency of the mother rotor changes the process of the onset of breaks during VF. For normal I_{CaL} the wavebreaks are caused by dynamical instability: the first breaks occur only after a number of rotations of the initial spiral and the onset of these breaks was clearly associated with alternans in APD. This indicates that steep APD restitution mediated alternans was the mechanism for wavebreak formation. However, since these wavebreaks only occurred in steep regions far away from the initial spiral core, they led to a mother rotor type rather than a multiple wavelet type of VF. When I_{CaL} was decreased to more than 50%, breaks occured straight after the formation of the initial spiral without any alternans (which is an important characteristic for wavebreaks caused by dynamical heterogeneity). This is because the frequency of the mother rotor increased so much that differences in refractory period lead to local conduction block as was also reported in [86]. Thus, anatomical (and not dynamical) heterogeneity was responsible for wavebreak formation.

In addition, we found that due to the increased frequency of the mother rotor

the total number of filaments produced during 8 seconds increased from 388 ($I_{CaL} \times 1.0$) to 538 ($I_{CaL} \times 0.25$). Thus, speeding up of the mother rotor not only changes the mechanism of wavebreak formation but also increases the complexity of VF.

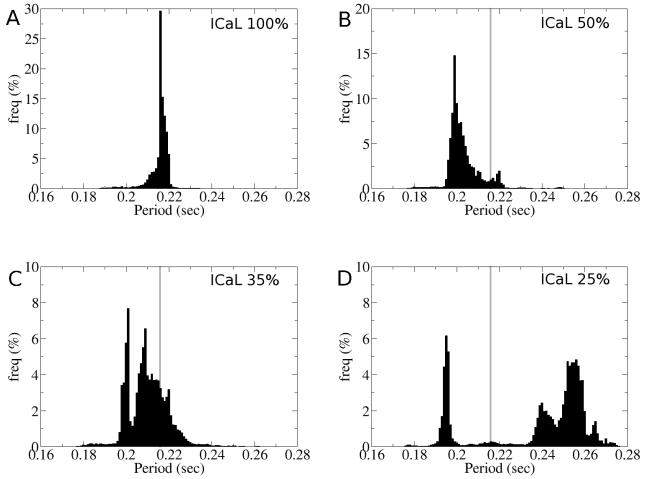

Figure 7.10: Normalized period distributions. Local mother rotor properties are changed (I_{CaL} times 1.0, 0.5, 0.35 and 0.25.). The gray vertical line denotes the mean period value of I_{CaL} times 1.0 (panel A).

7.4 Discussion

In this study, we report on mother rotor fibrillation in an electrophysiologically heterogeneous computational model of the human ventricles. We defined a mother rotor as a stationary, persistent source that actively drives VF, which terminates when the mother rotor is eliminated. However, it is also possible that a source driving VF is transient. We also call this a mother rotor if VF can be stopped by the removal of this source. It is understood that there may be special cases for which multiple wavelet VF can be eliminated by the removal of a single source. However, we think that in most cases true mother rotor VF will be correctly classified using this definition.

It should be noted that mother rotor like VF can occur without tissue substrate heterogeneity. Fenton and Cherry [32] showed that mother rotor like excitation patterns can occur as a result of discordant alternans-induced breakup far from the center of the spiral. In addition, rotors that anchor to inexcitable obstacles [153, 180, 193] (such as papillary muscles, fibrosis) may also result in mother rotor like VF. Furthermore, additional sources of heterogeneity (such as increased fibrosis) can lead to local conduction block and development of reentry, and are also important for the initiation and organization of VF [194].

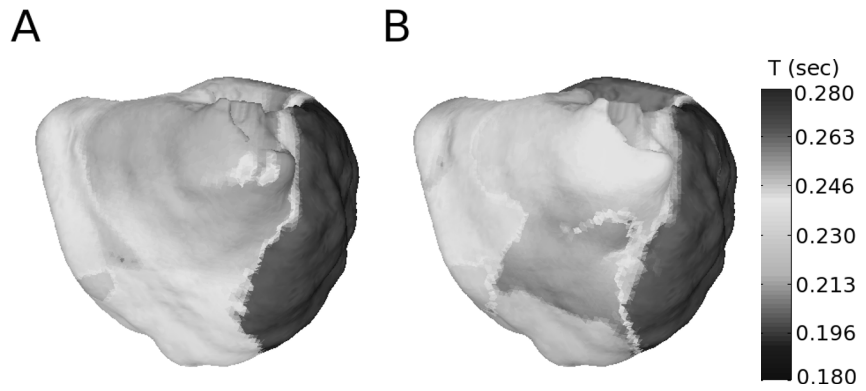

Figure 7.11: Spatial period distribution for the simulation with I_{CaL} times 0.25. (A) 2-4 seconds, (B) 4-6 seconds. The mother rotor was located in the dark blue region. Period values range from 0.18 s (blue) to 0.28 s (red). For color see page 209.

Our study shows that increased heterogeneity in the human heart can result in the onset of mother rotor VF. However, it should be emphasized that any type of heterogeneity, i.e. from local dynamic or fixed heterogeneities (including APD restitution), favors the formation of local wavebreaks and thus provides a substrate to sustain VF of any type (e.g. multiple wavelets) and not exclusively mother rotor VF.

Although our model is based on clinical data on heterogeneity and involves a detailed description of the structure of the heart and properties of cardiac cells, our conclusions should be further tested in experimental and clinical studies involving high spatial resolution recordings of wave activity in the human heart during VF.

In our model, we consistently reproduced mother rotor VF if the initial spiral wave was located in the left ventricle where APD was shortest and APD restitution shallowest. We found multiple wavelet VF when the initial spiral was located in the right ventricle where APD restitution was steep and APD was longer. In our model, shallow restitution curves were correlated with shorter APDs and periods, whereas steep restitution curves corresponded to longer APDs and periods (see [77]). Theoretically, it should be possible to have a model in which longer periods correspond to steeper restitution curves. However, in such a case we believe mother rotor fibrillation would not occur, since a rotor in a region of steep restitution would be unstable and would therefore lead to multiple wavelet type VF.

To demonstrate that the mother rotor was indeed responsible for driving the wavebreaks, we mimicked local ablation to remove the mother rotor spiral. After removing the tissue that supported the mother rotor, we found that all wavebreaks ended and the fibrillation was terminated within 0.5 seconds of simulation time. However, we do not think that local ablation of a mother rotor is of clinical use, as multiple mechanisms of VF can occur in the same heart depending on the initiation procedure. However, we cannot exclude the possibility that local

interventions may be used to stop a specific episode of VF. Note that if the mother rotor is terminated by other means, e.g. it slows down and is overrun by other wavelets, then VF is not necessarily terminated.

We then analyzed the differences in the underlying dynamics between mother rotor and multiple wavelet fibrillation. ECG signals for mother rotor and multiple wavelet VF were similar and resembled clinically observed ECG signals during VF. During multiple wavelet VF, we observed a broad period distribution that was mainly determined by dynamical processes, rather than underlying heterogeneity (see also [77]). In contrast, during mother rotor VF we observed that the periods were dominated by the period of the mother rotor, leading to a narrow distribution. Apart from the mother rotor, only short lived wavebreaks were present during mother rotor fibrillation, whereas during multiple wavelet VF several long lived filaments were present. In addition, during mother rotor VF, approximately 2-3 times less filaments were present compared to multiple wavelet VF. This difference is due to the fact that during mother rotor fibrillation the fast mother rotor dominates a large part of the cardiac tissue. Hence, other wavebreaks did not have enough time nor space to independently persist.

For the mother rotor fibrillation with the default I_{CaL} settings, we found that wavebreaks in the right ventricle occurred due to dynamical instabilities caused by steep APD restitution slopes (i.e., alternans). Wavebreaks occurred after several cycles of mother rotor rotation and at places where the breaks occurred there was alternans instability in APD. Excitation periods across the entire tissue were dictated by the mother rotor, and different frequency domains were not present.

We found that decreasing the period of the mother rotor (by decreasing the I_{CaL} conductance in the mother rotor region), and thus increasing anatomical heterogeneity, leads to Wenckebach like conduction blocks due to large differences in refractory period. Wavebreaks now occurred immediately after initiation of the mother rotor and were anatomically predefined. Consequently, different frequency domains were present, similar to experimental findings for mother rotor type VF [200].

We thus have shown that the formation of domains of different frequency is dependent on the frequency of the mother rotor and the degree of anatomical heterogeneity in refractory periods. Therefore, mother rotor type fibrillation is not necessarily associated with different frequency domains.

For multiple wavelet fibrillation, flattening restitution slope has been proposed as a promising therapeutic intervention [36]. However, for mother rotor fibrillation, besides absolute restitution slopes, heterogeneity in restitution slopes and APD is a major determinant for VF occurrence. This implies that reducing electrophysiological heterogeneity may also be a fruitful target for therapeutic intervention.

7.4.1 Limitations

Despite the fact that our model incorporates a detailed description of the electrophysiological properties of human ventricular cells, a realistic human ventricular geometry including fiber direction field, and a detailed description of ventricular electrophysiological heterogeneity, there are number of shortcomings of our study.

A first limitation is that clinical data were only available for the epicardial surface of the ventricles. There was no information on restitution properties in the mid-myocardium nor endocardium of these hearts. As a consequence, the epicardial restitution slope data had to be extrapolated across the entire ventricular walls using a diffusion-based algorithm as reported in [77]. The use of different parameters in our diffusion algorithm may lead to different gradients in slope values for the same set of clinical data. It remains to be investigated how these different heterogeneity profiles with different transmural slope gradients affect the results presented in this study.

Second, other heterogeneities, such as epi-, endocardial, and M-cells, Purkinje fibers, laminar sheets, and disease conditions (such as fibrosis and gap junction remodeling), were not taken into account in our model. Additional heterogeneities may further contribute to the complexity of excitation patterns during VF.

A third limitation to our study is that the ionic mechanisms responsible for the variation in APD restitution are presently unknown. It should be noted that the mapping of the TNNP model parameters to the restitution slope values that we used is not unique and that the same slopes may likely be obtained using other combinations of parameter settings. However, we believe that this non-uniqueness should not qualitatively affect the results of our study as long as shallow restitution curves correspond to shorter periods, and steep restitution curves correspond to longer periods.

Finally, the mechanisms of VF studied in this chapter are not the only mechanisms that may potentially cause VF. As an example, apart from steep APD restitution, other non-linear instabilities, e.g. in the intracellular calcium dynamics [137, 158, 159], may also lead to alternans and VF.

7.4.2 Conclusions

In this chapter, we report the finding of mother rotor VF in a computational model of the human ventricles. Furthermore, we showed that mother rotor and multiple wavelet VF can occur in the same heart depending on the initial location of reentry. We show that the underlying VF dynamics is markedly different between mother rotor and multiple wavelet VF. Mother rotor VF was more organized, with a smaller number of filaments and a more uniform distribution of rotor periods. Ablation of the mother rotor was sufficient to terminate VF. Studying the basic mechanisms responsible for maintaining and terminating VF in the human heart is important for understanding the pathogenesis of sudden cardiac death.

Acknowledgments

We would like to thank Prof. D.J. Paterson and the Wellcome Trust for assistance with the human heart APD restitution data. This research was funded by the Netherlands Organization for Scientific Research (NWO grant number 814.02.014). M.P.N. acknowledges previous support from the Marsden Fund Council from New Zealand government funding, administered by the Royal Society of New Zealand.

7.5 Supplementary Material

Figure 7.12

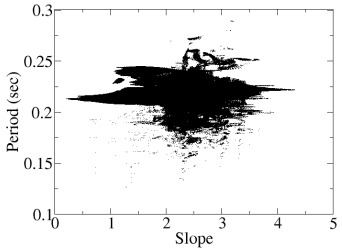

Figure 7.12: Correlation between mean period values measured and slope values for the multiple wavelet simulation. There is no correlation between period values measured and the underlying heterogeneity profile (slope value)(linear regression, F-test, $alpha = 0.01$). The period values are determined by dynamical processes.

Figure 7.13

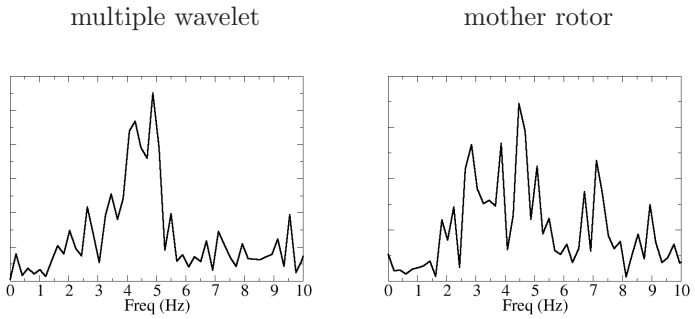

Figure 7.13: Fast Fourier transforms of the ECG signal for the multiple wavelet (left) and mother rotor simulation (right). The highest peak in the frequency spectrum of the mother rotor simulation corresponds to the frequency of the mother rotor.

CHAPTER 8

An Electro-Mechanical Model of the Human Left Ventricle and its Application to Study Mechanisms of Cardiac Arrhythmias

R.H. Keldermann[1*], M.P. Nash[2*], H. Gelderblom[3] and A.V. Panfilov[1]

[1] *Theoretical Biology/Bioinformatics Group*
Utrecht University
Padualaan 8, 3584 CH Utrecht, The Netherlands

[2] *Bioengineering Institute and Department of Engineering Science*
University of Auckland
Private Bag 92019, Auckland, New Zealand

[3] *Department of Biomedical Engineering*
Eindhoven University of Technology
The Netherlands

In preparation (2009)

[*] Both authors contributed equally to this study.

Abstract

We introduce an integrative 3D electro-mechanical model of the left ventricle of the human heart. Electrical activity is represented by the ionic TNNP model for human cardiac cells. It is embedded into an anatomical model of the left ventricle that contains a detailed description of cardiac anatomy and fiber orientation field. Mechanical activity is modeled using the active tension of the Niederer-Hunter-Smith model, that approximates active tension developed as a result of cellular cross-bridge cycling, and the passive mechanical response is determined via the Guccione transversely isotropic constitutive relations. The coupling between the electrical activity and the mechanical active tension is accomplished via the intracellular calcium concentration of the TNNP model. Mechano-electrical feedback is represented by the stretch-activated channels, which are modulated by local deformation.

The electro-mechanical model is integrated by a combination of an explicit finite difference approach for the excitation and a non-linear Galerkin finite element method for the mechanics. We verified our model by simulating a normal heart beat and compared the resulting strains in the cardiac wall with experimentally measured strains reported in the literature. We found fiber shortening and wall thickening during systolic contraction, and the cardiac and fiber strains were qualitatively similar to the experimentally measured strains.

We used this model to study the effect of mechano-electrical feedback on spiral wave excitation. We found that in some cases the spiral wavebreaks up into VF via mechano-electrical feedback of the stretch-activated channels. We identify the mechanisms of this transition and study the 3D organization of mechanically induced VF.

8.1 Introduction

Mechanical activity of the heart is initiated by electrical waves of excitation that propagate through the heart and initiate cardiac contraction. Abnormal excitation of the heart may result in cardiac arrhythmias and loss of mechanical pump function, which can be lethal. Sudden cardiac death caused by cardiac arrhythmias is the most common cause of death in the industrialized world and in most cases this is due to ventricular fibrillation (VF) [202]. It has been shown in clinical and experimental studies that VF occurs as a result of the onset of turbulent patterns of electrical activation of the heart which are underpinned by multiple re-entrant sources of excitation [29, 45, 62, 107, 178, 190]. Mechanisms behind the onset of reentrant sources in the heart and processes resulting in breakup of these sources into complex turbulent activation patterns are of great interest.

One of the important factors which affect electrical excitation of the heart is mechano-electrical feedback. It has been shown that mechanical deformation alters the electrical properties of myocytes [160] via the stretch-activated channels, which can change the shape of the action potential in response to stretch [76, 83].

Mechano-electric feedback has been studied in the clinical community for well over a century (see reviews [76, 83, 85]), and may have both pro-arrhythmic and anti-arrhythmic consequences. The mechanisms of these underlying phenomena are not well understood. One of the problems in experimental studies of mechano-electrical feedback is that it is difficult to control both electrical and mechanical properties of cardiac tissue, and to alter them in a systematic way. Therefore alternative methods should be used and one of them is mathematical modeling.

In our group we recently investigated effects of mechano-electrical feedback on wave propagation in 2D using a coupled electro-mechanical model. We found that it is possible to induce automatic pacemaker activity [129] and spiral wave breakup [130]. Both mechanisms are regulated by mechano-electrical feedback via the stretch-activated channels. However, in these studies we choose to use simple phenomenological model of cardiac excitation in a 2D isotropic medium. Active tension was generated using a simplified isotropic active tension transient. Furthermore, we used an isotropic Mooney-Rivlin material response to describe passive mechanical properties of the medium.

The aim of this study was twofold. First, we wanted to develop a more realistic model of the human ventricles to overcome most of the above limitations. Second, we wanted to study both the effect of wave dynamics on mechanical deformation, as well as the effect of mechano-electrical feedback on wave dynamics.

In this chapter, we introduce a new realistic 3D anisotropic electro-mechanical model of the human left ventricle that combines electrical waves of excitation and mechanical deformation. We validate our model by simulating a normal heart beat and qualitatively compared our strains with those found experimentally by Ashikaga et al. [6]. We use our model to study electrophysiological and mechanical dynamics during spiral waves in the presence of cardiac contraction. We found that turbulent patterns of excitation during ventricular tachycardia (VT) and VF resulted in desynchronized cardiac contraction compared to simulating a normal heart beat. Furthermore, we found that dynamical regions of stretch can cause an otherwise stationary spiral to breakup in smaller waves via mechano-electrical feedback of the stretch-activated channels.

8.2 Methods

We introduce a coupled 3D electro-mechanical model of the human left ventricle that combines electrical waves of excitation and mechanical deformation. In this model electrical waves of excitation are described using a detailed ionic cell model of the human ventricles [171, 174]. Mechanical deformations are calculated using finite elasticity theory combined with finite element analysis. Based on the local intracellular calcium concentration, active tension is approximated from the equations governing development of tension from cellular cross-bridge cycling [119]. This active tension is then used to solve the non-linear stress equilibrium equations using the finite element model. In turn, the resulting mechanical deformations have a feedback effect on the excitation properties of the medium via

the moving coordinate system and the stretch-activated channels. The electrical and mechanical part each have their own numerical discretization. For the electrophysiological part, we created a detailed anatomical finite difference geometry of the left ventricle that also contains fiber direction anisotropy. For the mechanical part, we created an equivalent tricubic Hermite finite element geometry that contains the same fiber direction anisotropy. Numerically, the coupled electromechanical model combines a finite difference method approach to integrate the excitation equations, with a Galerkin finite element method to solve the equations governing tissue mechanics.

8.2.1 Modeling Cardiac Excitation

Excitable behavior is modeled using a monodomain description of cardiac tissue using the following partial differential equation [74]:

$$C_m \frac{\partial V_m}{\partial t} = \frac{\partial}{\partial x_i}\left(D_{ij}\frac{\partial V_m}{\partial x_j}\right) - I_{ion} \tag{8.1}$$

$$\begin{aligned} I_{ion} &= I_{Na} + I_{to} + I_{CaL} + I_{Kr} + I_{Ks} + I_{K1} + I_{NaCa} \\ &\quad + I_{NaK} + I_{pCa} + I_{pK} + I_{Na,b} + I_{Ca,b} \end{aligned} \tag{8.2}$$

where V_m denotes the transmembrane voltage, C_m the membrane capacitance, D_{ij} the diffusion tensor accounting for the anisotropy of cardiac tissue, and I_{ion} the sum of the ionic transmembrane currents describing the excitable behavior of the individual ventricular cells. To represent human ventricular electrophysiological properties, we used the ionic model developed by Ten Tusscher et al. [174] and refer to this as the TNNP model (see full model description in Appendix A). This model provides a detailed description of voltage, ionic currents and intracellular ion concentrations, and is based on a wide range of human based electrophysiological data. The most recent version of the TNNP model [174] also includes a more extensive description of intracellular calcium dynamics. The model reproduces experimentally measured APD [108, 114] and conduction velocity restitution curves [41]. In this study, we used the "default" settings of the TNNP model (see Appendix A).

The diffusion tensor D_{ij} is derived from the fiber direction field. Assuming that the transverse conductivity is the same in all directions orthogonal to the direction of the muscle fiber axis, we described the ventricular conductivity tensor using the following equation:

$$D_{ij} = D_T * \delta_{i,j} + (D_L - D_T)\alpha_i\alpha_j \tag{8.3}$$

where, D_L and D_T are the longitudinal and transverse conductivity, respectively and α is the muscle fiber direction. For D_L we used 162 Ωcm and for D_T we used 40.5 Ωcm, which resulted in conduction velocities of 68 cm/s in the longitudinal direction and 32 cm/s in the transverse direction, similar to the values

reported by [167]. The resulting anisotropy ratio was approximately 2:1, which is also consistent with clinical measurements [71].

8.2.2 Modeling Cardiac Mechanics

In order to model deformation of the cardiac tissue, mechanical analysis is based on finite deformation elasticity theory. The normal sarcomere length of cardiac muscle cells is 2.0 μm [66, 134]. In mammals, sarcomere lengths operate in vivo usually between 1.7-2.15 μm [143] and in vitro maximally between 1.5-2.3 μm [13, 57, 175, 176]. Thus, cardiac cells change their length by 15-20% during contraction [103] and their maximal stretch is around 5-10%.

Following standard continuum mechanics, we use two types of coordinates to refer to a material point in space. Here, $\mathbf{x} = \{x_i\}$ describes the present (deformed) position in rectangular Cartesian coordinates of a material particle that occupied the location $\mathbf{X} = \{X_M\}$ in the reference (undeformed) configuration. The deformation gradient tensor, $\mathbf{F}$, transforms the undeformed line segment, $d\mathbf{X}$, into the deformed line segment, $d\mathbf{x}$, by $d\mathbf{x} = \mathbf{F}d\mathbf{X}$ with $F_M^i = \frac{\partial x_i}{\partial X_M}$. The right Cauchy-Green deformation tensor, $\mathbf{C}$, describes how each component of the undeformed line segment $d\mathbf{X}$ contributes to the squared length of the deformed line segment $d\mathbf{x}$ and is defined in terms of the deformation gradient tensor:

$$\mathbf{C} = \mathbf{F}^T\mathbf{F} \qquad \text{or} \qquad C_{MN} = \left\{ \frac{\partial x_k}{\partial X_M} \frac{\partial x_k}{\partial X_N} \right\} \tag{8.4}$$

The right Cauchy-Green deformation tensor is independent of rigid body motion. We can define three principal components, which remain unchanged under coordinate rotations at a given state of deformation: $I_1 = tr\mathbf{C}$, $I_2 = 1/2[(tr\mathbf{C})^2 - tr\mathbf{C^2}]$ and $I_3 = \det\mathbf{C}$. Next, we introduce the Lagrangian Green's strain tensor, $\mathbf{E}$, which is defined by:

$$\mathbf{E} = \frac{1}{2}(\mathbf{C} - \mathbf{I}) \qquad \text{or} \qquad E_{MN} = \frac{1}{2}(C_{MN} - I_{MN}) \tag{8.5}$$

where $\mathbf{I}$ is the unitary tensor. Note that both $\mathbf{C}$ and $\mathbf{E}$ are symmetric tensors by definition. To represent material behavior independent of rigid body motion, we use the second Piola-Kirchhoff stress tensor, T^{MN} [101], which represents the force per unit undeformed area, acting on an infinitesimal element of surface in the reference configuration.

Constitutive Equations

Constitutive equations are empirical relations used to represent stress-deformation behavior of a material, which are independent of the choice of the coordinate system, between experimentally observed stress and strain tensors. This can be accomplished by introducing a strain energy density function W that depends on the components of the right Cauchy-Green deformation tensor. Differentiation of

the strain energy density function W with respect to the strain $\mathbf{E}$ results in the second Piola-Kirchhoff stress tensor [46]:

$$T^{MN} = \frac{1}{2}\left(\frac{\partial W}{\partial E_{MN}} + \frac{\partial W}{\partial E_{NM}}\right) - p\delta^{MN}C^{-1}_{MN} \tag{8.6}$$

where W is a strain energy density function in terms of the strain $\mathbf{E}$ and p is the hydrostatic pressure computed based on a Lagrange multiplier approach to maintain incompressibility (i.e., the Galerkin incompressible constraint, see [115]). The passive myocardium can be modeled as an incompressible hyperelastic material, described by a transversely isotropic material law. In this study we used a material law adapted from Guccione et al. [49]:

$$\begin{aligned} W &= \frac{C_1}{2}e^{Q} \\ Q &= 2C_2(E_{ff}+E_{cc}+E_{rr}) + C_3E^2_{ff} + C_4(E^2_{cc}+E^2_{rr}+2E^2_{cr}) + 2C_5(E^2_{fc}+E^2_{fr}) \end{aligned} \tag{8.7}$$

where the subscripts f,c and r describe the strains in the fiber, cross-fiber (within the wall-plane perpendicular to the fiber direction) and radial (perpendicular to the wall-plane) directions, respectively (see Figure 8.1). The material parameters C_1-C_5 were obtained from estimations made by Schmid et al. [155] and are based on estimated material parameters from experimental data of six pig hearts for an orthotropic experimental material law [27]: $C_1 = 0.095$, $C_2 = 0$, $C_3 = 30.5$, $C_4 = 13.75$ and $C_5 = 13$. Material parameters in the sheet and sheet-normal directions were averaged to get equal material properties in the cross-fiber directions. Material properties are assumed to be homogeneous throughout the left ventricular wall.

Stress equilibrium

Due to active tension in the cardiac wall and the pressure load on the endocardial surface, the finite element model will be deformed until a new equilibrium state is reached. To find the new deformed state, the equilibrium equations are solved using the finite element method. These equations arise from the conservation of linear momentum following Newton's law of motion. In the absence of body forces the static equilibrium in terms of second Piola-Kirchhoff stress tensor reduces to:

$$\frac{\partial}{\partial X_M}\left(T^{MN}\frac{\partial x_j}{\partial X_N}\right) = 0 \tag{8.8}$$

where, T^{MN} is the second Piola-Kirchhoff stress tensor, $\mathbf{X}$ the coordinates in the undeformed state and $\mathbf{x}$ the coordinates in the deformed state.

By introducing a weighting field of virtual displacements, $\delta\mathbf{v} = \{\delta v_j\}$ (see [101]) the weak form of the stress equilibrium equations in absence of body forces can be transformed into an integral equation:

$$\int_{V_0} T^{MN} F_N^j \frac{\partial(\delta v_j)}{\partial X_M} dV_0 = \int_{S_2} \mathbf{s} \cdot \delta \mathbf{v} dS \tag{8.9}$$

where V_0 is the undeformed volume and S_2 is the portion of the boundary subjected to external surface loads $\mathbf{s}$.

Finite Element Approximation

For finite element analysis it is useful to approximate the undeformed (X_M) and deformed coordinates (x_i) using a Galerkin finite element interpolation scheme. Isoparametric element coordinates ξ_k, are local normalized material coordinates ($0 \leq \xi_k \leq 1$) that move with the deforming body and provide parametrization of the geometric variables for each element.

$$X_M = \Psi_n(\xi_k) X_M^n \tag{8.10}$$

$$x_i = \Psi_n(\xi_k) x_i^n \tag{8.11}$$

where $\Psi_n(\xi_k)$ are the interpolation functions defined at the finite element nodes n. For this study, we used tricubic Hermite elements. Using the same interpolation functions, the virtual displacement field in Eq. 8.9 can be approximated using:

$$\delta v_j = \Psi_n(\xi_k) \delta {v_j}^n \tag{8.12}$$

Substituting Eq. 8.12 into Eq. 8.9, and setting the coefficient of each arbitrary displacement component δv_j to zero gives:

$$\int_{V_e} T^{MN} F_N^j \frac{\partial \Psi_n}{\partial X_M} dV_0 = \int_{S_2} \mathbf{s} \cdot \Psi_n dS \tag{8.13}$$

where, V_e is the undeformed volume of each element. Equation 8.13 represents a set of global residual equations arising from the finite element model and is the start of the computational finite element solution. This system can be numerically solved by replacing the integrals using Gaussian quadrature. This results in a system of $K\mathbf{u} = \mathbf{f}$, with K, the stiffness matrix, $\mathbf{u}$, the vector of mesh parameters (geometric coordinates) and $\mathbf{f}$ the zero vector. For further details see [113, 115].

Boundary Conditions

For mechanics two common types of boundary conditions are used to constrain the finite element model.

- *Geometric constraints.* To prevent rigid body motion, deformed nodal coordinates and its derivatives are fixed to predetermined values. In our model, the entire basal ring of the left ventricle was fixed.

- *Surface pressures.* External tractions are applied to nodes to constraint the right hand side of Eq. 8.13.

If external surface pressures are applied, then the right-hand-side integral of Eq. 8.13 involving the surface traction vector $\mathbf{s}$ has to be evaluated for those portions of the boundary subjected to the loading condition. If we consider a deforming surface with unit normal $\mathbf{n} = n_j \mathbf{i}_j$ and assume that the surface is loaded with a pressure p_{appl} (a physical stress), then the surface traction vector has components $\mathbf{s} = p_{appl} n_j \mathbf{i}_j$.

8.2.3 Modeling Electro-Mechanical Coupling and Mechano-Electric Feedback

In order to mathematically couple the reaction diffusion system and the mechanical equations, the relationship between the equations of electrical activity (Eq. 8.1) and cardiac mechanics (Eq. 8.13) must be considered.

Modeling Electro-Mechanical Feedback

In normal cardiac tissue, the active components of stress depend on the intracellular concentration of calcium ions $[Ca^{2+}]_i$, the history of sarcomere length changes, and a range of other factors such as the kinetics of calcium binding to troponin C [66, 119].

In this study we choose to use the model of Niederer-Hunter-Smith (NHS) [119] to generate active tension T_a in cardiac tissue. The NHS contraction model uses three variables as input to generate T_a, which are: the intracellular calcium concentration $[Ca^{2+}]_i$, the fiber shortening λ and the velocity of fiber shortening $\dot{\lambda}$. The intracellular calcium concentration is generated by the TNNP model (Eq. 8.2), while the other two parameters are obtained from the finite element model. The model was fitted to experimental data from rats to calculate active tension (see Appendix B). The model is designed to operate under physiological sarcomere length (SL) changes for $1.8 < SL < 2.3\ \mu m$. For further information see [119].

In this study, active and passive (second Piola Kirchhoff) stress components are linearly superimposed to define the total state of stress in the tissue [67]. Mechanical properties of the tissue are defined by:

$$T^{MN} = \frac{1}{2}\left(\frac{\partial W}{\partial E_{MN}} + \frac{\partial W}{\partial E_{NM}}\right) - p\delta^{MN} C^{-1}_{MN} + T_a \delta^{M1}\delta^{1N} C^{-1}_{MN} \tag{8.14}$$

where C^{MN} are the components of the contravariant metric tensor, which can be computed from the covariant metric tensor (Eq. 8.4) using $C^{MN} = C^{-1}_{MN}$ (undeformed material coordinates are orthogonal). Note that active stress is only present in the fiber direction ($\delta^{M1}\delta^{1N}$).

Eq. 8.14 is further adapted to include numerical length and velocity dependent stability (for details see [120]).

Modeling Mechano-Electrical Feedback

In this study, we neglected the effect of mechanical deformation on capacitive and ionic currents. Instead, we focused on the effect of tissue deformation on wave propagation and mechano-electrical feedback via the stretch-activated channels.

Tissue Deformation
The equations describing electrical activity (Eq. 8.1) can be re-defined by taking local coordinate deformation into account. We can express the gradients with respect to the material coordinate system by changing Eq. 8.1:

$$C_m \frac{\partial V_m}{\partial t} = \frac{1}{\sqrt{C}} \frac{\partial}{\partial X_M} \left(\sqrt{C} D_N^M C^{NL} \frac{\partial V_m}{\partial X_L} \right) - I_{ion} \tag{8.15}$$

where $C^{NL} = \{C_{NL}\}^{-1}$ are again the components of the contravariant metric tensor, $C = det(C_{NL})$, is the determinant of the covariant metric tensor ($det(C_{NL}) = 1$ for an incompressible medium) and D_N^M are the components of the diffusion tensor.

Stretch-Activated Channels
The direct influence of deformation on the excitation properties is via the stretch-activated current I_s, which is added to Eq. 8.2. In general there are three groups of mechanically activated channels in the heart, but only two of them (the cation non-selective channels, and the potassium-selective channels) are activated by stretch [83]. The overall physiological action of these channels is depolarization of the membrane in response to stretch, as shown in the majority of experimental observations from isolated cardiac tissue. Experimental studies of the electrophysiological properties of stretch-activated channels show that they are instantly activated by mechanical stimulation, and that the current-voltage (I-V) relationship for the most important nonspecific cation channels is linear [61, 201, 203]. On basis of these observations, linear ionic models for I_s have been proposed [177, 181]. These linear models have been used to study effects of mechanical stretch on heart tissue using detailed ionic models of cardiac myocytes. Therefore, we believe that a linear time-independent description will be sufficient for our formulation of cardiac cells.

$$I_s = G_s \frac{(\lambda - 1)}{(\lambda_{max} - 1)} (V_m - E_s), \tag{8.16}$$

where G_s and E_s are the maximal conductance and reversal potential, respectively, of the stretch-activated channels, $\lambda = \sqrt{2E_{ff} + 1} = \sqrt{C_{ff}}$ is the extension ratio in the fiber direction, that is normalized for the maximum extension factor λ_{max}. We assume that cells can maximally stretch by 10% and hence $(\lambda_{max} - 1)$ is set to 0.1. Following [129], the I_s current in Eq. 8.16 is only present if $E_{ff} > 0$ (which indicates stretch in fiber direction). Otherwise I_s is set to zero.

The value of E_s in most biophysical models is assumed to be around -20 mV [61, 177, 181], and describes the experimentally observed depolarizing effect of

the stretch-activated current. The value of G_s varies between 0 and 100 $\mu S/\mu F$ [81, 83, 177]. However, there are only few experimental studies that report the value of G_s for single cells. Furthermore, whole cell currents are often normalized for cell capacitance without reporting the value of this cell capacitance. In adult rat myocytes, Zeng et al. [201] reported a value for G_s of 12 $\mu S/\mu F$ for 3% strain in cardiac myocytes. In [177], it was reported that G_s varies between 0 and 100 $\mu S/\mu F$ and was set to 30 $\mu S/\mu F$ by rationalizing the effect of various G_s values on action potential properties.

Various different single channel conductances of stretch-activated channels have been recorded in both the atria and ventricles for different species and vary from around 20 pS to above 100 pS (see an overview in [61]). The value of G_s can be calculated from the single channel conductance γ (pS), the channel density ρ (around $0.3/\mu m^2$) and the cell area A using $G_s = \gamma \rho A$ [61]. Since there are large variations of single channel conductances reported for the stretch-activated channels, it is reasonable to assume that the value of G_s also varies. In this study we used G_s values between zero and 75 $\mu S/\mu F$ to investigate the effects of stretch-activated current on excitation properties.

8.2.4 Human Ventricular Data Set

Geometric data describing the 3D ventricular anatomy and fiber direction field are derived from a normal healthy human heart [60] and is described in more detail in [170]. This data set contains 1693010 data points with an isotropic resolution of 0.5 mm. At each data point, three geometrical coordinates (x,y,z) are known. The muscle fiber direction field was constructed based on general knowledge on fiber architecture in the human heart [166] combined with detailed data on the fiber architecture of the canine heart [121]. This fiber orientation field has been validated by comparing it with recently obtained MR-diffusion tensor imaging data of the human heart [170].

In this study, we were interested in an electro-mechanical model of the left ventricle. Therefore, we removed the data points of the right ventricle of the human data set. After removal of the right ventricle the data set contained 1380946 data points (see Figure 8.2).

Based on this data set we constructed a finite element mesh for the mechanics, and a finite difference geometry for the electrophysiology.

8.2.5 Finite Element Model of the Human Left Ventricle

The anatomical finite element model of the left ventricle consists of two quantitative fields: the ventricular geometry and the fibrous structure orientations (i.e., muscle fiber and cross-fiber directions) throughout the myocardium. Each field has been fitted using least squares techniques based on the finite element method. A schematic overview of the LV is given in Figure 8.1.

The endocardial and epicardial surface data were extracted from the left ventricular data set. Additionally, some data points of the basal ring were removed

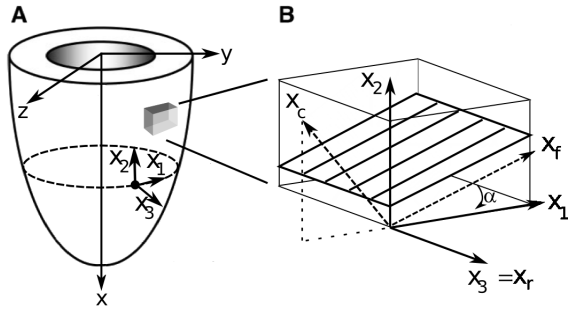

Figure 8.1: (Left) Schematic representation of the LV with cardiac coordinate system. Element coordinates: ξ_1, circumferential axis, ξ_2, longitudinal axis (base to apex) and ξ_3, transmural axis. (Right) Schematic representation of local fiber coordinate system. *f* is in the fiber direction, *c* is the cross-fiber direction in the wall-plane, perpendicular to the fiber direction, and *r* is the radial direction perpendicular to the wall-plane. α is the fiber angle between ξ_1 and the fiber axis ξ_f in the ξ_1,ξ_2 plane. Because there are no laminar sheets in our model $\xi_3 = \xi_r$.

so that the data set could be clearly partitioned. To create a fitted finite element mesh of this data, we first created an initial mesh in the shape of a truncated ellipsoid using tricubic Hermite elements. To create the apex of the finite element model we used collapsed nodes, i.e., placed more nodes of the same element at the same geometric location. For the apex, elements with two collapsed nodes were used, thereby creating a pointy apex shape using four apex elements with six nodes. The initial mesh contained four elements in the circumferential and longitudinal direction and one element in the radial direction.

The initial mesh was then fitted using a face fitting procedure in which the endocardial and epicardial surfaces were fitted to respectively the local endo- ($\xi_3 = 0$) and epicardial ($\xi_3 = 1$) faces of the finite elements. The endocardial and epicardial face of the mesh each contained 798 degrees of freedom, which were fitted to 34177 and 103319 data points, respectively. For this, we used an iterative method in which the Euclidean distance between all data points and their orthogonal projections to the model mesh were minimized. To improve the accuracy of the fit, the mesh was refined in the ξ_1 direction. The new mesh contained one element in the radial direction, four in the longitudinal direction and eight in the circumferential direction, resulting in a total of 32 tricubic Hermite finite elements.

The fixation of the basal nodes had a great influence on the numerical convergence of the mechanics in that region. Therefore, we decided to refine the upper layer of the basal ring into two sub-layers to create a small layer of basal elements where the displacement boundary conditions could be applied. This reduced the influence of the boundary conditions in the basal region of the finite element mesh. This resulted in an additional eight elements bringing the total number of finite elements to 40. The resulting mesh is shown in Figure 8.2.

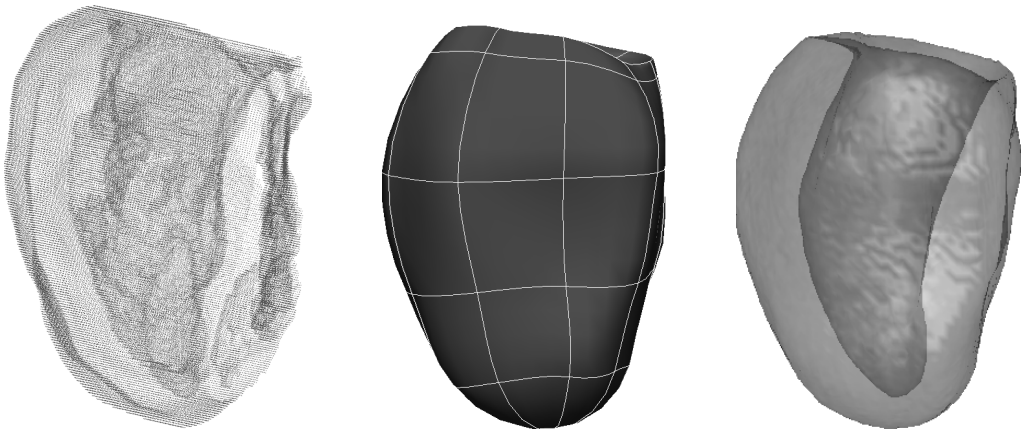

Figure 8.2: (Left) Human 3D voxel data set of the left ventricle (based on [60]). (Middle) Finite element model of the left ventricle. (Right) Finite difference model of the left ventricle. Posterior view shown.

Fiber Fitting

Two angles defining the muscle fiber orientation could be derived from the fiber data set. The first angle represents the elevation angle with respect to the horizontal section of the model, with 0° meaning the fiber is in the horizontal plane (yz-plane), and the second angle represents the azimuth angle with respect to the global x-axis (apex to base). For further details see [170].

For cardiac mechanics two angles are important. The first is the *fiber* angle α, which is defined as the angle between the fiber vector and the local circumferential direction (ξ_1) of the heart (see Figure 8.1). We assume that fibers lie in the (ξ_1, ξ_2)-coordinate plane and are tangential to the endocardial and epicardial surfaces. The second is the *sheet* angle, which is the orientation of the sheets that bundle the muscle fibers. Unfortunately, the data set did not contain sheet angle information. Furthermore, we assumed that the muscle fibers are aligned with the local surface tangent plane, i.e., they have no imbrication angle leaving only the fiber angle as a parameter to fit. To avoid misinterpretation that our model contains sheet directions, we rather use the term cross-fiber direction, which is the vector perpendicular to the fiber direction lying in the wall-plane of the ventricles.

To determine the fiber angles from the given fiber data set, we assume that the circumferential direction of the heart is aligned with the yz-plane in the cardiac coordinate system. The fiber angles α are calculated using:

$$\alpha = arcsin\left(\frac{-x}{\sqrt{x^2+y^2+z^2}}\right) \tag{8.17}$$

Note that angles between the yz-plane and the fiber vector pointing in the negative x-direction are defined as positive and are only unique between $-\frac{\pi}{2}$ and

$+\frac{\pi}{2}$. In order to represent the cardiac geometry more accurately, the ξ_1-direction of the model was not enforced to be in the *yz*-plane. Therefore, the calculated fiber angles had to be corrected for the angle between the *yz*-plane and the local (ξ_1) direction before fitting.

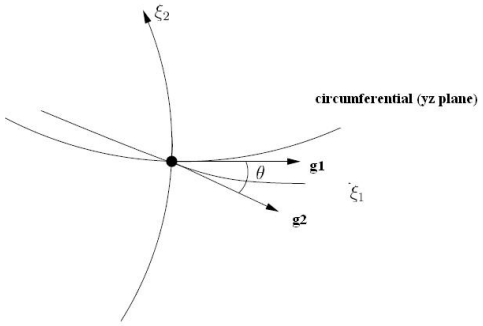

Figure 8.3: Fiber angle correction (adapted from [164])

To obtain this correction, we determined for each data point the ξ-coordinates in the corresponding element. Then, for each element a vector $\mathbf{g_1}$, lying in the *yz*-plane at the intersection with the $\xi_1\xi_2$-plane, and a vector $\mathbf{g_2}$, lying in the $\xi_1\xi_2$-plane aligned with the ξ_1 direction are determined:

$$\mathbf{g_1} = a\frac{\partial \mathbf{x_k}}{\partial \xi_1}\mathbf{i_k} + b\frac{\partial \mathbf{x_k}}{\partial \xi_2}\mathbf{i_k} \tag{8.18}$$

$$\mathbf{g_2} = \frac{\partial \mathbf{x_k}}{\partial \xi_1}\mathbf{i_k} \tag{8.19}$$

where $\mathbf{x_k} = (x, y, z)$ and $\mathbf{i_k}$ are unit vectors along the three rectangular Cartesian axes. $a = \frac{\frac{\partial x}{\partial \xi_2}}{\frac{\partial x}{\partial \xi_1}}$ and $b = 1$ to ensure $\mathbf{g_1}(1) = 0$, i.e., $\mathbf{g_1}$ lies in the *yz*-plane. The angle between $\mathbf{g_1}$ and $\mathbf{g_2}$ is the correction angle θ (see Figure 8.3), which represents the angle between the ξ_1-axis and its projection on the *yz*-plane:

$$\theta = arccos(\mathbf{g_1}, \mathbf{g_2}) \tag{8.20}$$

where $\mathbf{g_1}$ and $\mathbf{g_2}$ have been normalized to unit length.

If $\frac{\partial x}{\partial \xi_1}$ is negative, (i.e., $\mathbf{g_2}$ makes a positive angle with the *yz*-plane), π is subtracted from θ to form the correction angle. Last, the correction angle is added to the fiber angles of the data points lying in each finite element. After this correction, the fiber angle represents the angle of the fiber vector with respect to the local ξ_1-direction in the model.

An initial fiber field with zero fiber angles and fiber angle derivatives was set up. Since tricubic Hermite elements are used, one fiber angle and seven fiber

angle derivatives are specified in each node. The model fiber angles are then fitted using an iterative method by adapting the nodal fiber angles and their derivatives such that the least squares error between the fiber angles and model angles was minimized. The fiber angles field contained 1560 degrees of freedom, which were fitted to 10904 fiber angles.

The resulting root mean square error after fitting was 10.2°, and varied from 1.83° to 34.4° in individual elements. Through the left ventricular wall, the fiber angles varied from 13° (endocardium) to −55° (epicardium) at the anterior site, 72° to −32° at the posterior site, 62° to −57° in the free wall and 14° to −37.3° in the septum (angles with respect to local element circumferential direction). These fiber orientation were also found in goats [39]. In Figure 8.4 we show the fiber direction on the endo- and epicardium. Note that in the region of the septum some ambiguous fiber directions present.

For more information about how to create a mathematical model of geometry and fibrous structure of the heart we refer to [121, 164].

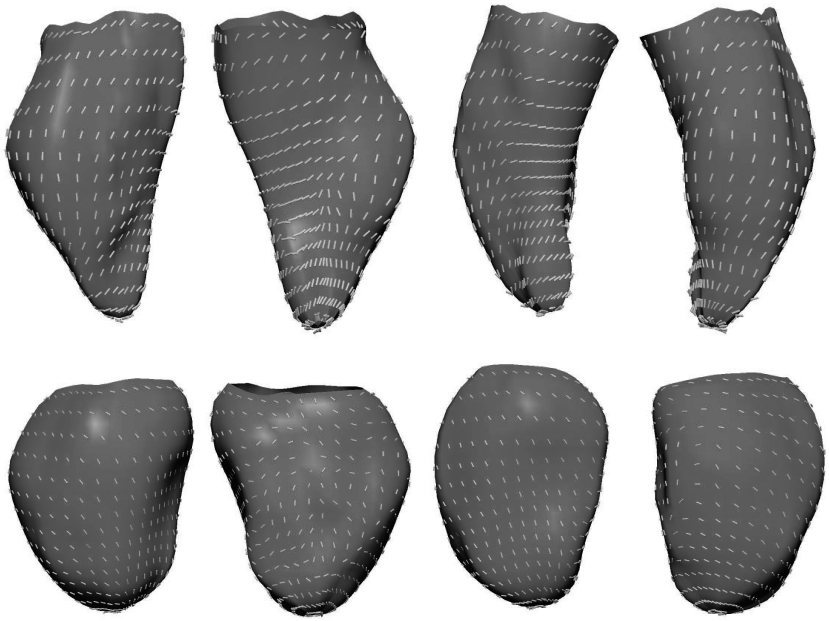

Figure 8.4: Fiber direction shown on the endo- (top) and epicardial (bottom) surfaces. From left to right: LV free wall, septum, posterior and anterior view shown.

Reference State and Passive Inflation

In large deformation mechanics, material deformation and derived stresses are calculated with respect to a well defined reference configuration, for which the material strain and stress components are assumed to be zero. We assume that

the residual stresses and strains can be neglected if the heart is in zero loading state, i.e., zero LV cavity pressure, and that the data set on which the model is based, is obtained from a heart that was in this state.

The first step of each simulation was filling of the heart until the end-diastolic volume was reached. To simulate this, we increased the pressure in the left ventricular cavity from 0 to 1 kPa (p_{appl}), by applying a load on the endocardial surface of the model (pressure boundary condition). To ensure convergence of this mechanical problem, the load was applied gradually by increasing the pressure in steps of 0.1 kPa. During all simulations the pressure boundary condition of 1 kPa is applied. The result of this passive inflation is not shown in the figures.

8.2.6 Finite Difference Model of the Human Left Ventricle

Below we describe how we created a 3D voxel anatomy of the human left ventricle.

Each finite element has a local coordinate system ξ_k which ranges from 0 to 1 (dimensionless). We discretized each local finite element using a space step of 0.025. This resulted in 40x40x40 data points per finite element. In each data point we extracted the global x,y,z-coordinates and the fiber direction vector from the finite element mesh. We then mapped and interpolated all these data points to their nearest voxels in the finite difference space using a resolution of 0.5 mm. This voxel description was modified to remove small obstacles and holes. The final voxel anatomy of the left ventricle contained 1118053 voxels. This is shown in Figure 8.2.

Next, based on the finite element fiber and cross-fiber directions a new fiber field was derived (see [60]). In Figure 8.5 we show a cross sectional plane showing the elevation and azimuth fiber angles between the endo- and epicardium of the left ventricle. This section corresponds very well to the cross sections shown in [170]. However, in the region of the septum it can be clearly seen that there are some ambiguous fiber directions present (see also Figure 8.4).

8.2.7 Numerical Approach

Solution Method

The coupled electro-mechanical model is solved using a hybrid approach that incorporates a finite difference method to solve the electrical problem and finite element techniques to compute the deformation of the tissue. The electro-mechanical simulations are typically solved for two distinct time scales, one for the electrophysiology and one for the mechanics.

Electrophysiology
Equations for the gating variables in the TNNP and NHS model were integrated using a Rush and Larsen integration scheme [149]. To integrate Equation 8.15, we used a forward Euler scheme with a time step of $\Delta t = 0.08$ ms and a space step of $\Delta x = 0.5$ mm. The upstroke of the action potential was calculated using a time

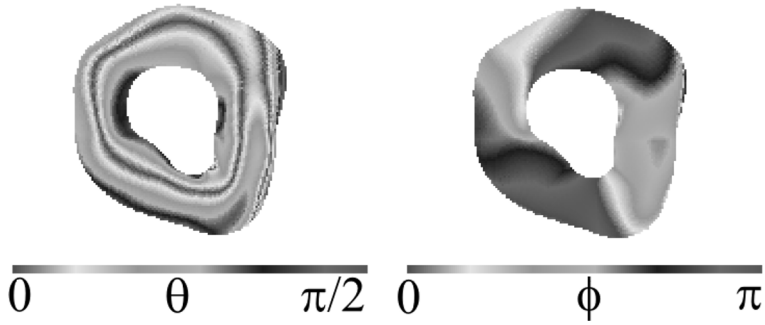

Figure 8.5: Short-axis view of fiber direction at approximately 50% base-apex. (Left) Elevation angle (i.e., the angle the fiber makes with the cross sectional plane). (Right) Azimuth angle (i.e., the angle the fiber makes with the x-axis). The septum is located on the right, and the anterior and the posterior LV free wall are located on the top and bottom side, respectively. For color see page 210.

step of $\Delta t = 0.02$ ms. The following Laplacian was evaluated at each point in the human ventricular geometry:

$$\Delta(i,j,k) = \frac{1}{\sqrt{C}} \frac{\partial}{\partial X_M} \left(\sqrt{C} D_N^M C^{NL} \frac{\partial V_m}{\partial X_L} \right) \tag{8.21}$$

which can be discretized using the following equation:

$$L(i,j,k) = \sum_{l=0}^{l=18} w_l V_m(l) \tag{8.22}$$

where l is an index running over the 18 neighbors of the point (i,j,k) and the point itself, and w_l are the weights defined for each neighbor point containing information about the voltage contributed to the Laplacian at each point (i,j,k). Weights are calculated at each point using the local conductivity and metric tensors calculated by Eq. 8.15. To impose no-flux boundary conditions the axial current flow from surface heart points to non-heart points was set to zero by using $w_l = 0$ for the weights of non-heart neighboring points [170].

Mechanics
Every N_{mech} integration steps (set to 100 for these simulations), the computed values of the active tension T_a (calculated at each finite difference point) are interpolated to the corresponding finite element Gauss points. To avoid numerical instability active tension was set to zero in the basal ring and in the inner layer of Gauss points of the apex element. These active Gauss point stresses serve as input to load the tissue mechanics model. Given the undeformed model geometry, mechanical properties and boundary conditions, the unknowns of the mechanical problem are then the deformed geometric coordinates, which have to be minimized with respect to the solution variable **u** and linearized using Taylor

expansion. Non-linear iterations are then performed to solve these stress equilibrium equations that govern tissue mechanics, i.e., the solution **u** for which the residuals are zero is approximated using the Newton-Raphson iterative method. The resulting set of equations can then be solved for each iteration using LU decomposition. Convergence is reached when both the ratio of constraints (i.e., for which the solution is known, e.g. boundary conditions) to the unconstraints residuals and the sum of the solution vector increments for the current Newton iteration are below a prescribed error tolerance. This iterative method requires an initial estimate of the deformed coordinates. A useful estimate is the undeformed geometry.

Once convergence is reached, deformation tensors are updated and passed on to the finite difference method at 41380 points. These 41380 metric tensor points are interpolated to the corresponding 1118053 voxels in the finite difference geometry. These metric tensors are then used to update the new weights properties of Eq. 8.22 and to calculate the current generated via the stretch-activated channels (Eq. 8.16).

Figure 8.6 schematically represents all of the components involved in the electro-mechanical coupled model.

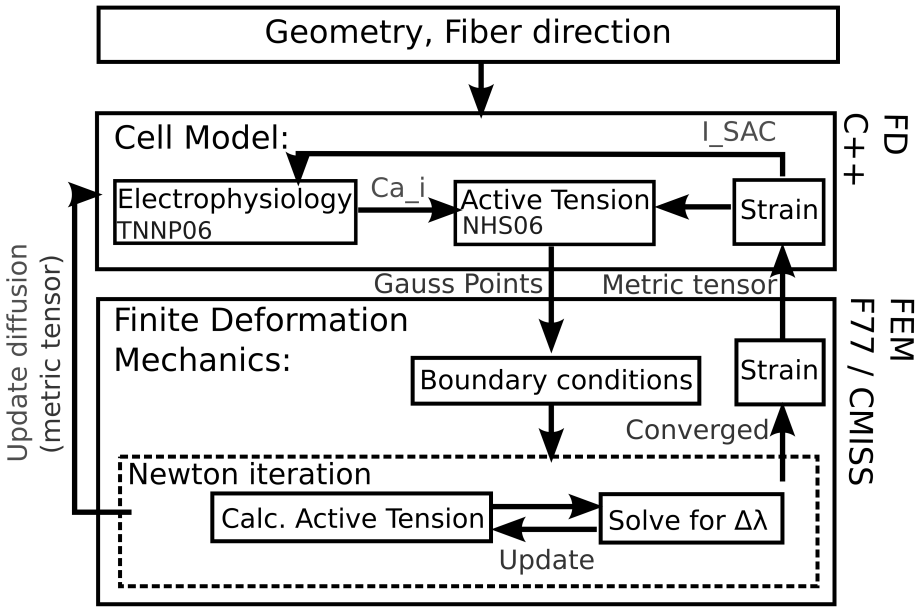

Figure 8.6: Flow diagram showing the processes involved in the 3D coupled electro-mechanical model (adapted from [120]).

Simulating a Normal Heart Beat and Ventricular Fibrillation

To simulate normal cardiac rhythm we stimulate the entire endocardium of the left ventricle for 10 ms each 0.6 seconds, using a stimulus current of twice the diastolic threshold value.

To initiate 3D scroll waves, we used a S1-S2 protocol, for which a S1 stimulus was applied in septum. The S2 stimulus was activated during the refractory tail of the S1 stimulus on the posterior side of the ventricles and was extended from the base for approximately 50% of the base-apex dimension, thereby creating a single scroll wave on the posterior side of the left ventricular wall. Stimulus currents were applied at twice the diastolic threshold value. Simulations were run for 4 seconds or were terminated if there was no activity present.

Electrograms

Assuming that the medium is an infinite volume conductor, electrograms were calculated using the dipole source density of the membrane potential in all voxel points using [135]:

$$ECG = \int_V \frac{D\nabla V_m \cdot \overrightarrow{r}}{r^3} dV \tag{8.23}$$

where, V is the domain of integration (i.e., the ventricular volume), and $\overrightarrow{r}$ is the vector from each point to the recording electrode, which was placed 10 cm from the center of the ventricles in the anterior direction of the transverse plane.

Filaments and Phase Singularities

Scroll wave filaments were detected using an algorithm proposed by Fenton and Karma [33]. If there is a spiral wave in 2D (a scroll wave in 3D) present, the core (filament) can be defined as the point(s) for which the excitation wavefront and waveback meet. This can be calculated as the intersection points of an isopotential line (we used -60 mV) and the $dV/dt = 0$ iso-line. Voxel data corresponding to these intersection points were then stored. Individual filaments were detected by iteratively joining neighboring voxels that were designated as filament points. All voxels that belonged to the same filament were assigned a unique identifier. Filaments were determined at 10 ms intervals.

Implementation

The finite difference simulations were coded in C++ and the finite element method was coded in Fortran using the CMISS (Continuum Mechanics, Image Analysis, Signal processing and System identification, www.cmiss.org) software package created by the Auckland Bioengineering Institute. Data transfer between the finite difference method and the finite element method was handled via file transfers. Simulations were run on a Dell Precision Workstation (dual Intel Xeon 2.8 GHz, 2GB RAM). Simulating 1 second of wave propagation and deformation of the left

ventricle took approximately 18 hours of wall-clock computation time. Ventricular geometry, wave patterns and scroll wave filaments were visualized using the marching cubes algorithms for isosurface detection in voxel data, and OpenGL for isosurface rendering. Mechanical deformation was visualized using the cmgui (www.cmiss.org/cmgui).

8.3 Model Validation and Results

8.3.1 The TNNP model

The electrophysiological model developed by Ten Tusscher et al. [171, 174] has been validated in [170].

8.3.2 The NHS Excitation-Contraction Coupling Model

For this study we choose to model active tension using the NHS model [120]. Although some data is available for humans as well, the NHS model parameters are mainly validated and rationalized based on rat experimental data.

We tested the outcome of this model (i.e., active tension) by simulating a normal heart beat by stimulating the full endocardium of the left ventricular model, and by simulating a stable spiral on the LV (both without mechanical feedback). We used the original NHS 2006 model to determine active tension traces and kept λ constant, i.e., active tension was only dependent on the intracellular calcium concentration. As in [119], various tension traces were calculated for different values of λ ($1 \leq \lambda \leq 1.1$, stepsize 0.02). Normally, λ is not constant and updates during the course of the simulation.

In Figure 8.7 we show the results for these two simulations using the default parameters of the NHS model. During a normal heart beat we see that active tension increases once intracellular calcium increases. Once intracellular calcium decreases it takes little more time for the active tension to reach its maximal value before returning to zero. The maximal value of the active tension is dependent on the intracellular calcium and λ. For larger λ values, active tension values increase as is shown in Figure 8.7 (see also Niederer et al. [119]). This is known as the Frank-Starling mechanism, which increases cardiac contractility thereby linking cardiac ejection with cardiac filling [157].

However, in this same figure we also see accumulation of active tension during a stable spiral wave, i.e., high frequency stimulation, while intracellular calcium values are almost restored to their resting values. The spiral rotated at a frequency of approximately 4.0 Hz. The main difference is that the time between two action potentials, and thus between two intracellular calcium transient peaks is now much shorter compared to simulating a normal heart beat. During this high frequency stimulation the NHS model has not enough time to restore active tension to zero. If too much tension is accumulated in every cell, then the mechanical pump function of the LV will be lost, i.e., the entire cardiac muscle will be in a contracted state.

The parameters of the NHS model are mainly based on rat experimental data. Rats have a normal cardiac rhythm of around 280 beats/min compared to humans who have approximately 60-80 beats/min at rest, and 180-200 beats/min during exercise. At these frequencies, one would not expect accumulation of active tension, because that would be lethal. Accumulation of active tension might be expected when frequencies would increase even more, e.g. during VF. However, this phenomenon has not been investigated in experimental or numerical studies.

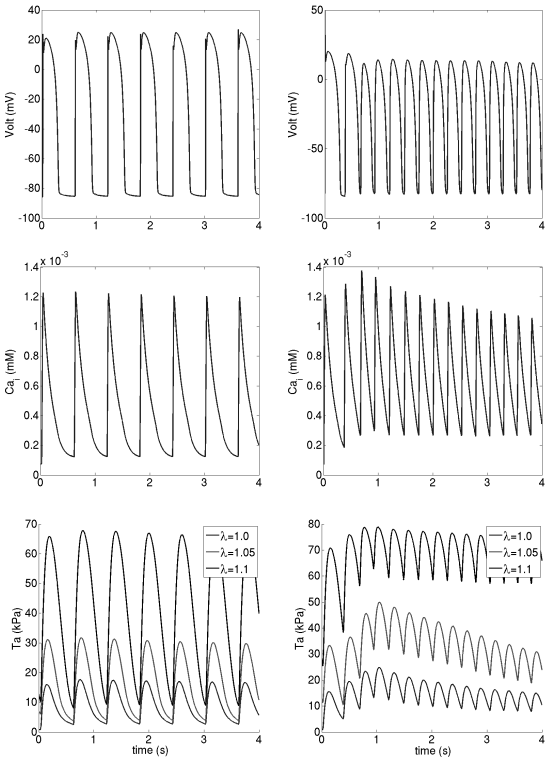

Figure 8.7: Validation of active tension traces in the NHS model. (Left) Normal heart beat. (Right) Stable spiral. From top to bottom: membrane potential, intracellular calcium concentration and active tension. For color see page 210.

Because of this we modified the NHS model in such way that also during spiral waves active tension is restored to zero. For this Equations B.9 and B.10 in Appendix B are important, which describe the relaxation kinetics of the active tension. Commonly, there are two stages found in experiments: a linear component describing the slow process and a non-linear Hill type component describing the fast process. The slow process is characterized by α_{r1} and the fast process by α_{r2}. Niederer et al. [119] reported various values for α_{r1} and α_{r2} in their paper, which are mainly based on rat and guinea pig experimental data. However, these values increase with increasing temperature and have not been

normalized for this effect. The relaxation parameters of the NHS model were fitted based on experimental data from Saeki et al. [151]. The default settings of the NHS model are $\alpha_{r1} = 2s^{-1}$ and $\alpha_{r2} = 1.75s^{-1}$, respectively. However Saeki et al. [151] reported a value of $12s^{-1}$ for α_{r2} in their paper. Piroddi et al. [134] reported kinetic parameters for full tension generation and development in human atrial and ventricular myofibrils. They reported values for atrial myocytes of $\alpha_{r1} = 0.52s^{-1}$ and $\alpha_{r2} = 16s^{-1}$, and for ventricular myocytes of $\alpha_{r1} = 0.15s^{-1}$ and $\alpha_{r2} = 2.90s^{-1}$, respectively. However, changing the NHS model into a human variant requires reparametrization of all parameters. We therefore chose to use the value of $\alpha_{r2} = 12s^{-1}$ as was reported initially by Saeki et al. [151]. However, increasing α_{r2} also decreases the maximal active tension.

Piroddi et al. [134] reported a maximal Ca^{2+} activated tension in human atrial and ventricular myofibrils of 125 and 108 kPa, respectively, while other studies reported values between 30-50 kPa [179, 191] (reported values for $\lambda = 1.1$). In our model with $\alpha_{r2} = 12s^{-1}$, maximal active tension values are less than 20 kPa ($\lambda = 1.1$). These low values result in lower strains during cardiac contraction. To compensate for this we increased T_{ref} from 56.2 kPa to 100 kPa, as was originally used in the model of Hunter et al. [66].

The result of changing these two parameters on active tension traces is shown in Figure 8.8. The membrane potential and intracellular calcium are the same as in Figure 8.7. We see no accumulation of active tension while simulating a stable spiral. However, maximal active tension values are are much lower (30-40 kPa) compared to the 100-120 kPa found during a normal cardiac cycle. Nonetheless, these values are sufficient for our model to contract, because in our model we use a constant end-diastolic LV cavity pressure of 1 kPa. For higher mid-contraction LV cavity pressures (5-10 kPa), it is required that T_a is approximately 100-120 kPa. This can be accomplished by increasing T_{ref}.

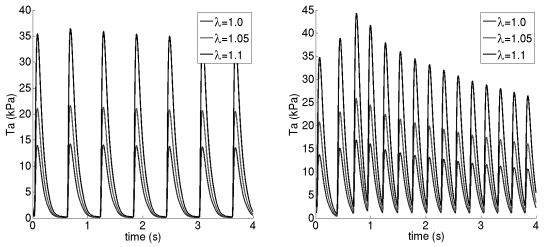

Figure 8.8: Modified NHS model with $\alpha_{r2} = 12s^{-1}$ and $T_{ref} = 100$ kPa. (Left) Normal heart beat. (Right) stable spiral. For color see page 210.

8.3.3 Simulating a Normal Heart Beat

To simulate a normal heart beat we stimulated the entire endocardium of the left ventricle with a period of 0.6 seconds. Note that λ is updated during the

course of the simulation and thus active tension is dependent on both λ and the intracellular calcium concentration.

In Figure 8.9 the pseudo ECG is shown, which resembles a normal ECG for a normal heart beat. The QRS-complex corresponds to the depolarization of the ventricles and lasted approximately 90 ms. The T-wave represents the repolarization (or recovery) of the ventricles. The QT interval was approximately 0.36 seconds. These values are similar to clinically recorded ECGs of normal heart beats [53]. Note that the sign of the T-wave does not coincide with the sign of the QRS-complex, as our model does not account for transmural variation in electrophysiological properties.

At the endocardium, active tension started to rise after the initiation of the action potential after approximately 0.01-0.03 seconds and reached its maximal value after approximately 0.10 seconds.

In Figure 8.10, we show the mechanical 3D deformations of the finite element model during a normal heart beat (top and posterior wall shown). The colors denote a fitted field of the membrane potential, with red denoting the maximal membrane potential of 20 mV and blue denoting the resting membrane potential of -80 mV. During the first few ms. ($t < 0.05$ seconds) we found axial shortening (ξ_2), i.e., a decrease in apex to base length. After approximately 0.05 seconds the entire left ventricle was depolarized, and active tension increased. As a result, the heart started to contract ($t = 0.06 - 0.08$ seconds): the apex started to twist, i.e., the orientation of the inner wall rotated clockwise, the wall thickened (ξ_3), and the radii of the endocardial and epicardial surfaces decreased (ξ_1). As a consequence the LV volume decreased. After approximately 0.10-0.12 seconds active tension started to decrease, and as a result the LV started to relax: the apex twisted back, i.e., the orientation of the inner wall rotated counter-clockwise, the wall became thinner, and in the axial direction the apex to base length increased until the apex reached its original position. The LV volume increased to its original end-diastolic volume ($t = 0.40$ seconds).

In Figure 8.9 we show the ejection fraction, which is the fraction of blood pumped out of the left ventricle with each heart beat. During the simulation the LV ejection fraction increased from 0 to 58%. This is in accordance with the LV ejection fraction of a normal person [53]. The small blip in the ejection fraction at the beginning of the simulation is a numerical artefact of the initial steady state of the mechanical geometry, and is corrected (converged) at the next mechanical time step. In subsequent heart beats this blip is no longer present.

Cardiac and Fiber Strains

In Figure 8.11 we show the mean epi-, mid- and endocardial *cardiac* and *fiber* strains in an element located on the anterior wall of the LV equator (approximately halfway base-apex), which were calculated while simulating a normal heart beat. We calculated six independent cardiac strains using the locale coordinate axis (see Figure 8.1, ξ_1, ξ_2, ξ_3): circumferential strain E_{11}, longitudinal strain E_{22}, transmural strain E_{33}, circumferential-longitudinal shear E_{12}, longitudinal-

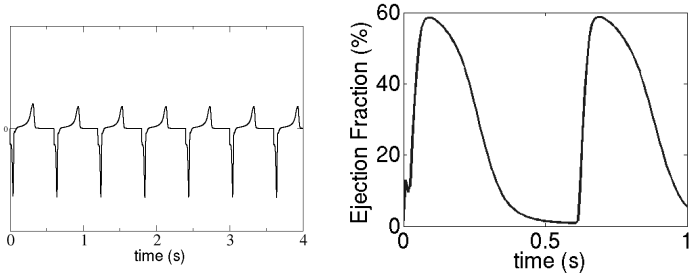

Figure 8.9: Normal heart beat simulation. (Left) ECG. (Right) Ejection fraction.

transmural shear E_{23}, and circumferential-transmural shear E_{13}. Furthermore, we also calculated another set of six finite strains using the local fiber-cross-fiber coordinate system (see Figure 8.1, ξ_f, ξ_s, ξ_n): fiber strain E_{ff}, cross-fiber strain E_{cc}, radial fiber strain E_{rr}, shear within the cross-fiber plane E_{fc}, cross-fiber shear E_{cr}, and radial shear E_{fc}.

In our model we use a transversely isotropic constitutive law and have no sheet angles, i.e. all the sheet angles are zero. However, zero sheet angles correspond to cross-fiber directions that are tangent to the epi- and endocardial surface. Thus, in the model the fiber radial strain (ξ_r) (perpendicular to the cross-fiber-plane) is the same as the cardiac radial strain , i.e., $E_{nn} = E_{33}$.

In our model we first inflated the zero reference state to the end-diastolic pressure (see methods, results not shown). As a consequence, the initial fiber and cross-fiber strains were slightly increased (E_{ff} and $E_{cc} > 0$) and the initial radial strain was decreased ($E_{rr} < 0$).

During endocardial pacing we found multiple phases of deformation, which were mainly exemplified by the fiber strain E_{ff}. In general we found fiber shortening ($E_{ff} < 0$) and wall thickening ($E_{rr} = E_{33} > 0$) during systolic contraction (see also Figure 8.10). Looking at the cardiac strains, we see shortening in the circumferential direction (E_{11}) and only small changes in the axial direction (apex-base, E_{22}). In general, we found small cardiac and fiber shear strains.

During systolic contraction we found only little variations in strain between epi-, mid- and endocardium E_{ff} strains. However, for E_{rr} we observed that $E_{endo} > E_{mid} > E_{epi}$.

If we increased the stiffness of the material e.g. by increasing C_1 we observed less fiber shortening and wall thickening, i.e., E_{ff} are E_{rr} had a smaller amplitude. If we increased the active tension of the model e.g. by increasing T_{ref}, we observed more fiber shortening and wall thickening, i.e., E_{ff} and E_{rr} had a larger amplitude (results not shown).

We compared our results with the cardiac and fiber-sheet strains reported by Ashikaga et al. [6]. They experimentally measured local cardiac and fiber-sheet strains in five dogs within the anterior wall of the LV (between the first and second diagonal branches of the left anterior descending coronary artery), while

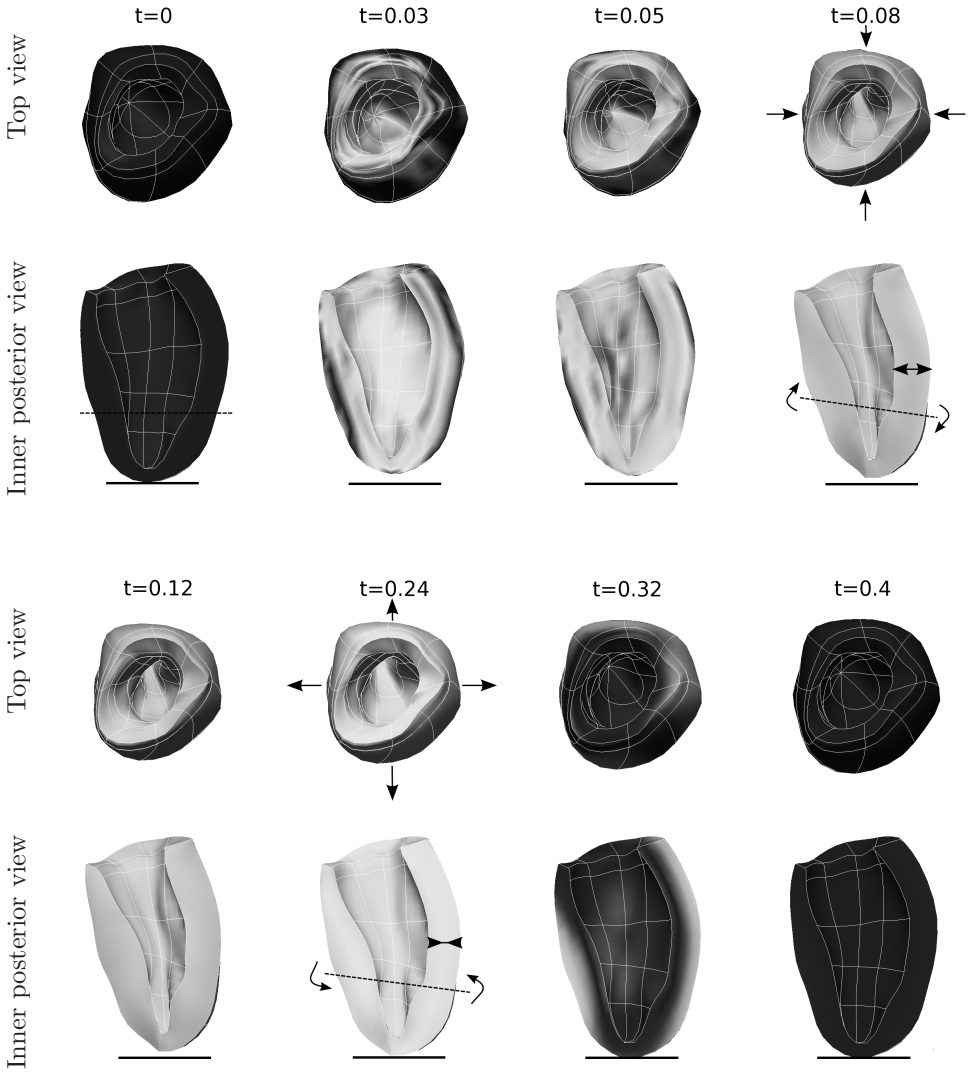

Figure 8.10: Mechanical deformation during a normal heart beat. Top view and inner posterior wall shown. The septum is located to the left. Snapshots are taken at time 0, 0.03, 0.05, 0.08, 0.12, 0.24, 0.32 and 0.40 seconds. Colors represent the membrane potential (blue=-80mV, red=+20mV). The solid black line denotes the initial position of the apex. The dashed line denotes the orientation of the wall segment. Arrows denote changes of the wall segment/orientations. For color see page 211.

stimulating the LV epicardium. In Figure 8.12 we show the cardiac and fiber-sheet strains of Ashikaga et al. [6]. The experimental results reported by Ashikaga et al. [6] have no time scale present on the time axis. They also calculated strains using a different reference state: the end-diastole (all initial strains are zero), which introduces a small systematic difference. Because our model lacks sheet angles, we can only compare the fiber strain E_{ff}. Cross-fiber and radial strains E_{cc} and E_{rr} cannot be compared with Ashikaga's measurements. Also, in our model $E_{rr} = E_{33}$. This means that we can directly compare E_{rr} from our model with E_{33} from Ashikaga et al. [6]. Cardiac strains can be directly compared.

Qualitatively our strains correspond very well to those reported by Ashikaga et al. [6]. As in our simulations, Ashikaga et al. [6] also report fiber shortening (E_{ff}) and wall thickening (E_{33}) during systolic contraction, with only small changes in axial direction (E_{22}). Furthermore, they found small variations between epi-, mid- and endocardial fiber strains E_{ff}, and for $E_{rr} = E_{33}$ they also observed that $E_{endo} > E_{mid} > E_{epi}$.

Differences in normal/shear strains can be explained by several factors. Ashikaga et al. [6] used dogs to experimentally measure all strains, while we used a human electrophysiological model and geometry, and components/parameters of other species for active tension and material parameters. Furthermore, our model is transversely isotropic while the measured experimental strains are orthotropic. This will affect strain predictions, especially in the apex and in the base [39]. Nevertheless, strains were qualitatively similar.

Note that our strains were measured in a segment of the anterior free wall of the LV similar to the experimental strains measured in the anterior element by Ashikaga et al. [6]. Many factors can give rise to regional variation in strains, such as fiber orientations, geometry (wall thickness), activation sequence and heterogeneous properties.

8.3.4 Simulating a Stable Spiral

To simulate a stable spiral we initiated a spiral on the posterior wall of the LV using a S1-S2 protocol. For this simulation $G_s = 0$. The spiral remained stable for the entire duration of the simulation.

In Figure 8.13 the pseudo ECG is shown. The ECG signal was periodic (dominant frequency of 4.0 Hz), which resembles ECG signals during ventricular tachycardia (VT). The dominant frequency corresponds to the period of the spiral. In Figure 8.13 we also show the change of the volume fraction, which is the fraction of the volume with respect to the end-diastolic volume measured during the course of time. The first two oscillations correspond to the initiation of the spiral wave during the S1-S2 protocol. After the spiral was initiated we observed that the volume of the LV decreased by approximately 50% and oscillated around 50% with an amplitude of 8-10% and had a dominant frequency of 4.0 Hz.

In Figure 8.14 we show the mechanical 3D deformations of the finite element model during a stable spiral. The first snapshot denotes the initial end-diastolic LV volume at $t = 0$. The other snapshots show the 3D deformations at $t = 3.2$,

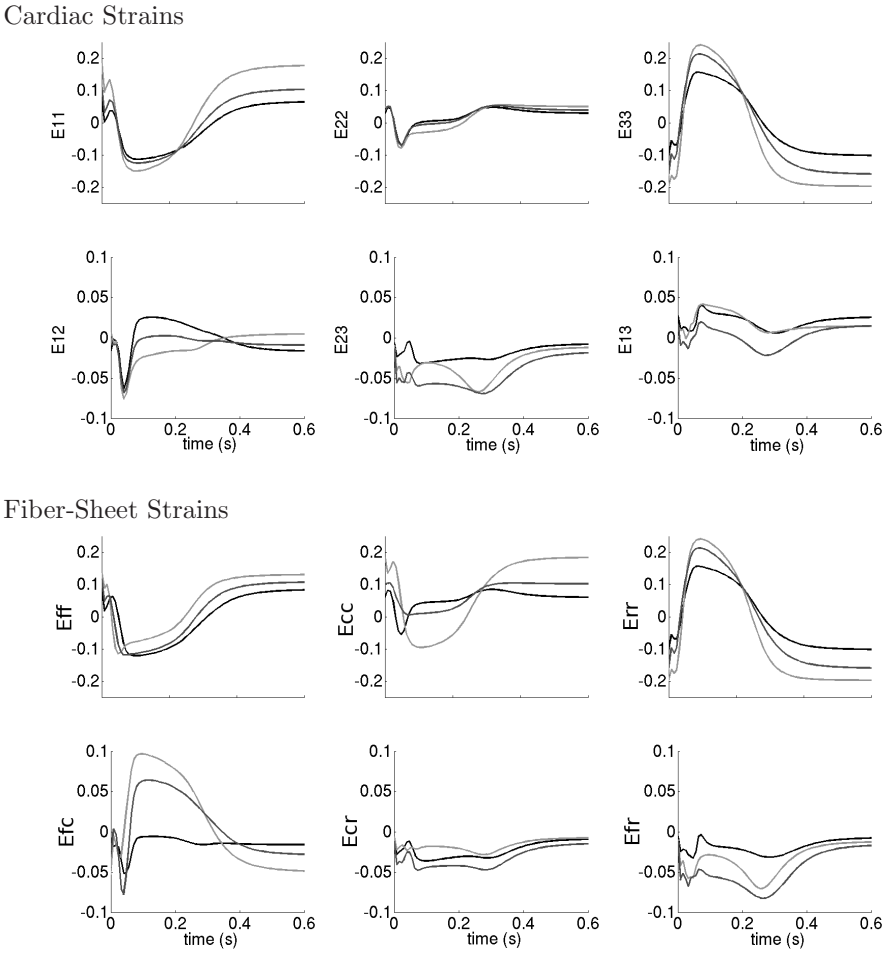

Figure 8.11: Mean cardiac (top) and fiber strains (bottom) measured on the anterior wall of the LV during a normal heart beat simulation. Subepicardium (black), midwall (red), and subendocardium (green) mean strains shown. Note the different scales for shear and normal strains. For color see page 212.

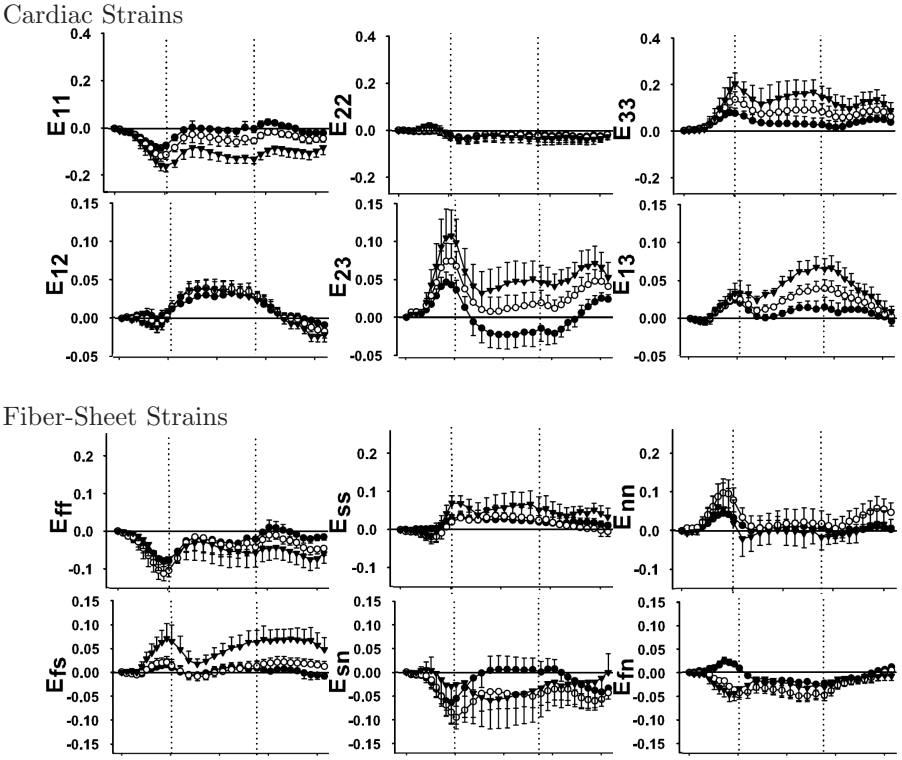

Figure 8.12: Experimental cardiac (top) and fiber-sheet strains (bottom) measured in dogs on the anterior wall of the LV. Subepicardium (filled circles), midwall (open circles), and subendocardium (filled triangles) mean strains ± SD shown (n=5 dogs). Note different scales for shear and normal strains (from Ashikaga et al. [6]).

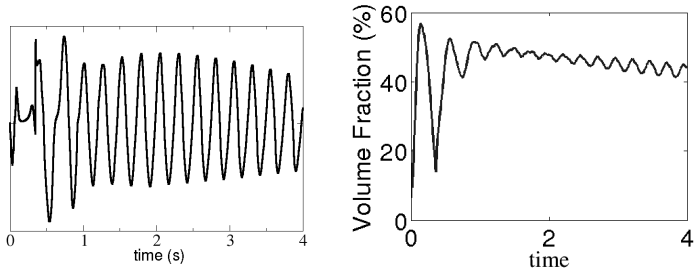

Figure 8.13: Stable spiral simulation. (Left) ECG. (Right) Volume Fraction with respect to the end-diastolic volume.

3.3 and 3.4 seconds. After the initiation of the spiral wave all deformations were similar to those shown in Figure 8.14, i.e., the LV is in a contracted state with little variations in LV volume. From Figure 8.14 it is clearly seen that the LV volume decreased with respect to the initial end-diastolic volume ($t = 0$).

In Figure 8.15 we show the mean epi-, mid- and endocardial normal fiber strains during a stable spiral wave in the same element as for the normal heart beat simulation. We compare the normal fiber strains from the normal heart beat simulation (Figure 8.11) with those of the stable spiral (Figure 8.15). In general we observed fiber shortening ($E_{ff} < 0$) and wall thickening ($E_{nn} > 0$) during the course of time. The fiber strains were oscillating with the same frequency as the frequency of the spiral wave. The amplitude of E_{ff}, E_{ss} and E_{nn} was smaller compared to the amplitude measured during a normal heart beat. Note that these strains only represent the strains in the anterior element, but that this does not represent the normal 3D fiber strain distributions. The entire LV was constantly in a contracted state. However, we also found that the 3D distribution of E_{ff} varied throughout the LV during the time course and that in some regions stretch of fibers ($E_{ff} > 0$) occurred. These regions of fiber stretch dynamically shifted across the LV myocardium and are dependent on the phase of the spiral / location of wavefronts and were often located in front of the wavefront (for similar results see Figure 8.19). However, we did not observe regions of fiber stretch close to the core of the spiral (results not shown).

8.3.5 Mechanically Induced Breakup

We repeated a similar simulation as for the stable spiral, but now we enabled the stretch-activated channels. We found that it is possible to mechanically induce wavebreaks via the mechano-electrical feedback of the stretch-activated channels. We found that stretch related processes are enhanced over time and that a steady state of filaments was not found within the 4 seconds of simulation time. We therefore decided to extend this simulation to 8 seconds.

In Figure 8.16 we show the ECG of this simulation. We see that the ECG is more irregular and complex compared to ECG of the stable spiral simulation. The

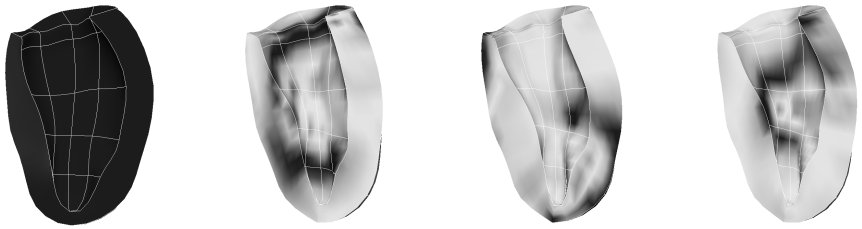

Figure 8.14: Mechanical deformation during a stable spiral. Inner posterior wall shown. The septum is located to the left. Snapshots are taken at time 0, 3.2, 3.3 and 3.4 seconds. Colors represent the membrane potential (blue=-80mV, red=+20mV). For color see page 213.

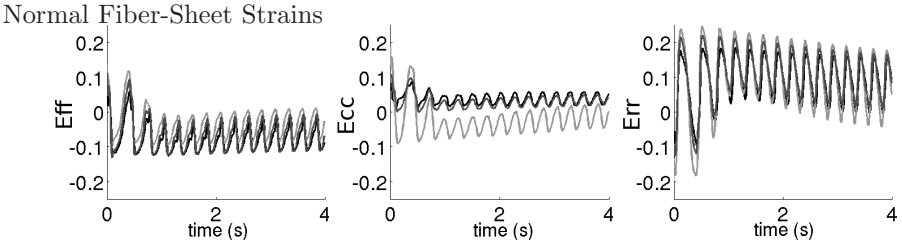

Figure 8.15: Normal fiber strains measured on the anterior wall of the LV during a stable spiral simulation. Subepicardium (black), midwall (red), and subendocardium (green) mean strains shown. For color see page 213.

dominant frequency was 3.6 Hz., which is similar to those frequencies reported in clinical [23, 112, 116, 195] and numerical studies [170]. The lower frequency can be explained by the activation of the stretch-activated current, which leads to regional lower conduction velocities (see below).

After the spiral was initiated and wavebreaks occurred, we found that the LV was constantly in a contracted state, similar to the stable spiral simulation. The end-diastolic volume decreased by approximately 50%. During wavebreaks, the change of volume fraction, mechanical 3D deformations and normal fiber strains were all similar compared to those results of the stable spiral simulation and only marginal differences were found (results not shown).

In Figure 8.17 we show the 3D wavefronts and filaments at the beginning and at end of the simulation. During the course of the simulation we observed fragmentation of wavefronts. In Figure 8.16 we show the time dynamics of the number of filaments found in the LV during 8 seconds of simulation. Over the first 4 seconds of time, the number of filaments steadily increased from 1 (the initial spiral) to over 15. Between 4 and 8 seconds of time we see that the number of filaments slightly decreased and in the end oscillated around 13. Normally, one would expect that e.g. during restitution induced breakup, the number of filaments to fluctuate around a certain value. In our mechano-electrical feedback simulations certain stretch related process are enhanced over time, thereby cre-

ating more filaments during the first 4 seconds. If we look closer at the filament dynamics in Figure 8.16 we also see an oscillatory component in the formation and destruction of filaments (dominant frequency of 3.6.Hz.). The average number of filaments found during the last second was 13.6.

We analyzed how filaments were created and destroyed over time through death, birth, bifurcation and amalgamation events. This is shown in Figure 8.18. Horizontal lines indicate individual filaments and their lifespan. The start of a line is determined by the birth of a filament or the bifurcation from another filament. The end of the line occurs when the filaments disappear, i.e., the death or the amalgamation of a filament with another filament. Short horizontal lines correspond to short living filaments, and long lines correspond to long living filaments. During the 8 second simulation we detected 1276 filaments and 453 births, 496 deaths, 824 bifurcations and 781 amalgamation events. In Figure 8.18 we also see that the initial spiral remained intact for 8 seconds (bottom red line). Most of the filaments existed only for a short period of time, although there were also a small number of persistent filaments present.

Such filament dynamics are similar to mother rotor fibrillation, however, the underlying mechanism of wavebreaks is different. During mother rotor fibrillation VF is thought to be driven by a dominant fast source of excitation [19, 69, 200]. This rapid reentrant electrical source (i.e., the mother rotor) is responsible for maintaining VF and causes conduction block in the surrounding tissue due to heterogeneity in refractory periods [8]. As a result, multiple small wavebreaks and irregular activation patterns are generated [69]. However, in our mechanical feedback simulations there was no heterogeneity in refractory period present.

In our simulations, the mechanism of wavebreaks can be explained by the accommodation phenomenon [58, 59, 130]. In Figure 8.19 we show the position of the wavefronts and the 3D distribution of extension factors λ for $t = 2.1$, 2.15 and 2.2 seconds. Overall, we predominantly see that most of the fibers are shortened ($\lambda < 1$), which caused the LV to be in a contracted state. However, in some regions we also observed stretch of fibers ($\lambda > 1$). These regions of stretch shifted over the myocardium during the course of time and were dependent on the phase of the spiral and/or positions of wavebreaks/wavefronts (see Figure 8.19). However, we did not observe regions of stretch close to the core of the initial spiral. Often regions of stretch were located in front of the wavefront (Figure 8.19). This means that the stretch-activated current I_s was activated in certain areas on the LV before the wavefront arrived. Hence, the membrane potential slowly depolarized within these regions. The amount of I_s-current generated is dependent on the value of λ and the amount of time λ was extended in these regions. If over time sufficient stretch-activated current was generated, and hence the membrane potential was sufficiently (slowly) depolarized before the next wavefront arrived, then this resulted in local inactivation of the sodium current and a decrease of the conduction velocity. We have previously investigated this effect using simpler 2D electro-mechanical models[130]. Note that the sodium current needs to be decreased by at least 80% in order to fail to generate a new action potential. This is dependent on the value of λ (> 1), the amount of time stretch is observed, and

the value of G_s.

We observed almost no stretch in the region close to the core of the initial spiral, therefore the I_{Na} current was not be blocked in this region, and as a consequence the initial spiral remained intact in this region during the simulation. Hence, the filament history is similar to mother rotor fibrillation.

We also investigated the effects of different G_s values on VF dynamics. For this, we repeated the above simulations with G_s equal to 0, 30, 45, 60 and 75 $\mu S/\mu F$ and analyzed the number of filaments present during the simulation. The results are shown in Figure 8.20. For $G_s = 30\ \mu S/\mu F$, we found that the simulation remained stable during 4 seconds of simulation time. Some small breaks were found at the end of the simulation. For larger G_s values we observed that the number of filaments steadily increased over time with more filaments created for larger value of G_s, thereby also increasing the complexity of the VF dynamics.

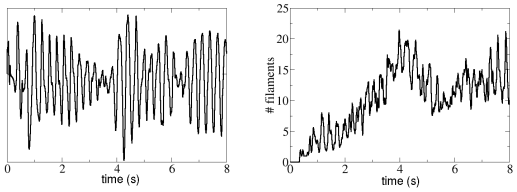

Figure 8.16: Mechanically induced breakup. (Left) ECG. (Right) Number of filaments. $G_s = 75\ \mu S/\mu F$.

8.4 Discussion

In this study, we developed a 3D electro-mechanical framework to investigate the effects of electrical waves on mechanical contraction, and the effects of contraction on wave dynamics. The 3D finite difference model contains a detailed description of human left ventricular anatomy, fiber direction anisotropy, and describes electrophysiological cell properties of human ventricular cells. The electrophysiological cell model has been developed by Tusscher et al. [171]. This model contains a detailed description of voltage, ionic currents and intracellular ion concentrations, and is based on a wide range of human based electrophysiological data. The most recent version of the TNNP model [174] also includes a more extensive description of intracellular calcium dynamics. In normal cardiac tissue, the active components of stress depend on the intracellular concentration of calcium ions $[Ca^{2+}]_i$, the history and the sarcomere length changes, and a number of other factors such as the kinetics of calcium binding to troponin C [66, 119]. The intracellular calcium concentration of the Ten Tusscher model is used as input for the biophysical NHS model [119], that approximates active tension from the equations governing development of tension from cellular cross-bridge cycling. The active tension is coupled to a 3D finite element model of passive elasticity and

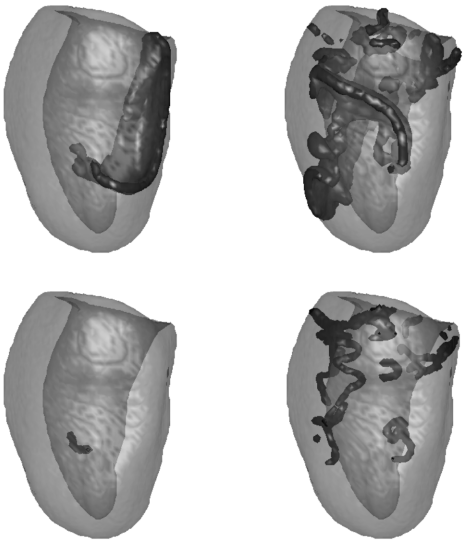

Figure 8.17: 3D Wavefronts (top) and filaments (bottom) found during mechanically induced breakup. $G_s = 75\ \mu S/\mu F$. Left: after the initialization of the spiral ($t = 0.6$ seconds). Right: at the end of the simulation ($t = 8.0$ seconds). Posterior view shown. The septum is located to the right. For color see page 213.

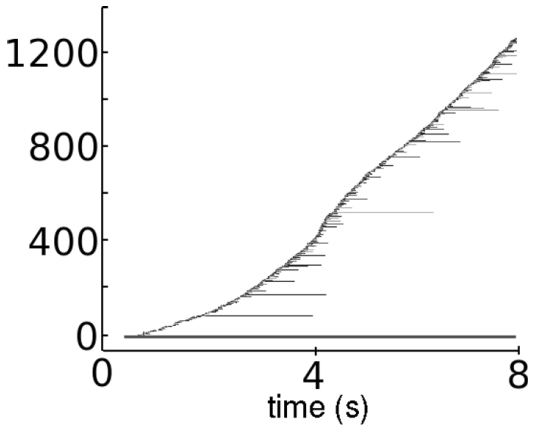

Figure 8.18: Filament history. $G_s = 75\ \mu S/\mu F$. Horizontal lines correspond to individual filaments and start at the time a filament appears (through birth or bifurcation) and stop at the time a filament disappears (through death or amalgamation). Filaments get assigned unique identity numbers that are not reused once a filament has died. Different colors are used to indicate clusters of filaments that can be traced back through bifurcation events to the same initial filament, which is the first filament of that color. We use different colors for filaments with the same ancestor only if the filament cluster has a size of 5 or more filaments. All other filaments that either have arisen through birth rather than bifurcation, or belong to a small cluster are colored black.The long gray line at the bottom represents the initial spiral, which persisted through the simulation.

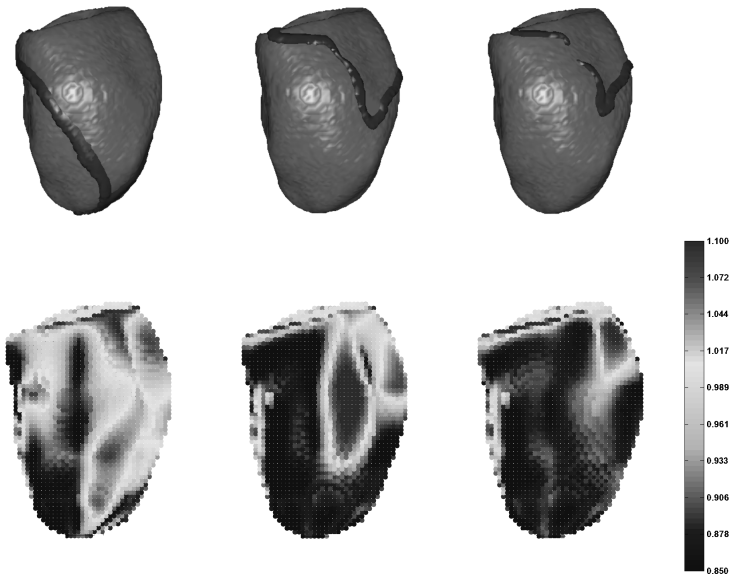

Figure 8.19: Mechanisms of breakup via stretch. $G_s = 75\ \mu S/\mu F$. In regions with stretch (i.e., $\lambda > 1$) the stretch-activated current is present. (Top) Wavefronts shown on the epicardial surface at 2.1, 2.18 and 2.2 seconds (from left to right). (Bottom) Extension ratio λ. Anterior view shown with the septum located to the left. For color see page 214.

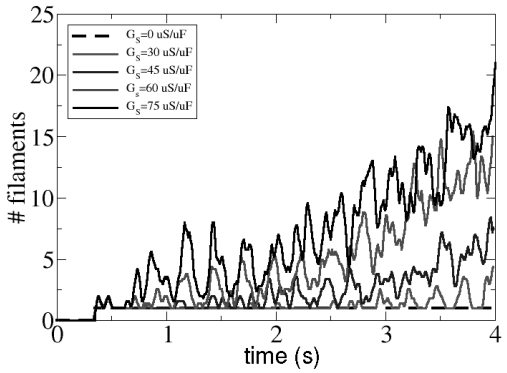

Figure 8.20: Number of filaments over time for $G_s = 0$, $G_s = 30$, 45, 60 and 75 $\mu S/\mu F$. For color see page 214.

contains a detailed description of the same human left ventricular anatomy and fiber direction anisotropy. The finite element model is subject to a transversely isotropic material response to describe the passive properties. Stress equilibrium equations are then solved to calculate the deformed state of the left ventricle and the corresponding local metric tensors. Mechano-electrical feedback is induced via these local metric tensors by updating the local coordinate system and by calculating the local deformation that modulates the stretch-activated current.

To illustrate the behavior of the 3D electro-mechanical LV model, we performed several simulations to verify and investigate the effects of our model.

We stimulated the entire left ventricular endocardium to simulate a normal heart beat. In general, we found fiber shortening and wall thickening during systolic contraction. The cardiac and fiber strains were qualitatively similar to the experimental strains reported by Ashikaga et al. [6]. The ejection fraction was approximately 58%, which corresponds well to the ejection fraction of a normal person.

Simulating a stable spiral on the posterior side of the left ventricle resulted in loss of contraction. The end-diastolic LV volume decreased by approximately 50%, and the entire LV was constantly in a contracted state, although we did observe regions of fiber stretch that shifted dynamically and were often located ahead of the wavefront.

When we activated mechano-electrical feedback via the stretch-activated current, we observed that these dynamical regions of stretch were responsible for creating wavebreaks. Because these stretch regions were often located ahead of the wavefront, a slow inward stretch-activated current was generated that depolarized the membrane potential. This slow rise in membrane potential resulted in the accommodation phenomenon, in which the sodium current was blocked and conduction velocity decreased. Once the wavefront arrived, no new upstroke of the action potential was generated and/or conduction velocity slowed down, leading to wavebreaks.

The complexity of the VF dynamics is dependent on the amount of stretch generated, (determined by e.g. λ, intracellular calcium, T_{ref}, passive material properties, etc) and the value of the stretch-activated current (determined by G_s and E_s). Indeed, we observed that the complexity of VF and the number of filaments increased when G_s increased.

These preliminary results suggest that mechano-electric feedback could potentially cause an otherwise stationary spiral wave to breakup. Note, however, that the effects found here should be considered as an indication of the importance of mechanics on wave dynamics and not as a firmly established mechanism. Further research involving studies for different parameter values, different initial conditions, numerical convergence, and different boundary conditions are needed to quantify the effects of mechano-electrical feedback in more detail.

8.4.1 Limitations

The primary aim of the present study was to investigate the fundamental effects of contraction on wave propagation in a realistic 3D model of the left ventricle. In this study we intended to describe the biophysical mechanisms underlying excitation and contraction as detailed as possible. Although our model is based on currently available models and experimental data, there are still some limitations that have to be addressed in future studies.

We used an endocardial LV pressure of 1 kPa, which corresponds to the end-diastolic pressure. As a consequence, lower active tension values are sufficient to cause contraction. Normally, there is a LV pressure-volume loop during cardiac contraction, in which pressure increases to above 10 kPa at the end-systolic phase. In the future, we also want to use higher mid-contraction LV cavity pressures (5-10kPa). This requires higher active tension development.

In this study we only used the anatomy of the left ventricle. Currently, we are developing a geometry based on DTMRI data that encompasses both the left and right ventricles.

We only incorporated fiber direction in our model. Since our data is based on DTMRI data, only the fiber orientations were known, and there was no information about sheet and imbrication angles. This affects local mechanics, especially in the transmural wall, and in the apex and the base [39].

Mechanical properties are described by a transversely isotropic material relation, and are based on experimental data from pigs..

We neglected the effects of mechanics on the passive electrical properties of cardiac cells. Should experimental data become available in the future then this can be straightforwardly incorporated into our model.

The parameters of the active tension model are mainly based experimental data from rats. Some of these parameters were adjusted to avoid tension accumulation during high frequency. This is only a temporarily solution, which resulted in lower active tension values. A human tension model needs to be developed, based on human experimental data, to determine the correct parameters, such that there is no accumulation and maximum active tension developed is around 100-120 kPa. It is possible to increase maximal tension by increasing T_{ref}. This requires a higher LV cavity pressure.

Mechano-electrical feedback is only modeled via the conduction system and the stretch-activated channels. It is also known that certain ionic currents can be affected via mechanical deformations. For example, it is known that the intracellular calcium transient is expected to vary for different sarcomere lengths. This feedback mechanism is not yet modeled in our framework. Currently, only limited experimental data is available to investigate such feedback mechanisms.

Acknowledgments

This research was funded by the Netherlands Organization for Scientific Research (NWO grant number 814.02.014). M.P.N. acknowledges previous support from the Marsden Fund Council from New Zealand government funding, administered by the Royal Society of New Zealand.

CHAPTER 9

Summarizing Discussion

9.1 A Review

This thesis is devoted to studying mechanisms of ventricular fibrillation (VF). Two main factors which may be responsible for the initiation and organization of VF are mechano-electrical feedback and tissue heterogeneity. Therefore, this thesis is divided into two parts.

Part I (chapters 2-5) deals with modeling the basic effects of mechano-electrical feedback using simple 2D tissue models. We focused on the effects of the depolarizing current of the stretch-activated channels, and studied automatic pacemaker activity and spiral wave breakup.

Part II (chapters 6-8) deals with the effects of heterogeneous action potential duration restitution and mechano-electrical feedback using anatomically based models of the human ventricles. In **chapter 6** we developed a method that incorporates clinically measured heterogeneous APD restitution data into our anatomical model of the human ventricles. In **chapters 6** and **7**, we used this model to study the effects of heterogeneous APD restitution on the organization of VF dynamics. Finally, in **chapter 8** we developed an anatomically detailed electro-mechanical model of the human left ventricle. We used this model to study two mechanisms: the effect of excitation-contraction coupling on tissue deformation, and the effect of mechano-electrical feedback on the initiation and organization of VF dynamics.

Part I

In **chapter 2** we presented a general review on modeling cardiac mechano-electrical feedback using 2D tissue models. We provided a general description of the framework used to model mechano-electrical feedback and described some of the fundamental effects of deformation on cardiac excitable behavior. The physiological mechanism underpinning mechano-electrical feedback occurs mainly via the so called mechano-sensitive ion channels, such as the stretch-activated channels, which have been identified in cardiac cells [61, 150]. In response to stretch, these channels produce an inward current that depolarizes the cell, and can initiate cardiac excitation [35]. Some of the most important effects of mechano-electrical feedback, which have been identified in both theoretical and experimental studies, are:

- Changes of action potential properties caused by the depolarizing current of the stretch-activated channels. These changes include a decrease of resting membrane potential, elongation of action potential duration, flattening of the restitution curve, and an increase in activation threshold [88, 141, 142, 177].
- Formation and drift of automatic pacemakers modulated via the depolarizing current of the stretch-activated channels [35, 129].
  (**chapters 3** and **4**)
- Spiral wave drift regulated by periodic deformations of the tissue via the resonant drift mechanism [1, 47, 130]. (**chapter 5**)
- Breakup of spiral waves caused by the depolarizing current of the stretch-activated channels via the accommodation phenomenon [58, 59, 130].
  (**chapters 5** and **8**)

These effects can play an important role in the induction of cardiac arrhythmias which are mechanically induced. For example, it is known that a mechanical impact on the chest can result in ventricular fibrillation; a condition known as Commotio Cordis [38, 96].

It is important to note that these studies regarding mechano-electrical feedback are still in their infancy and much needs to be done to further understand the resulting feedback dynamics on reaction-diffusion dynamics. In particular more realistic biophysical models need to be developed to more accurately describe the processes that occur during cardiac contraction and how these affect reaction-diffusion properties.

One of the basic effects of mechano-electrical feedback is the formation of automatic pacemakers due to depolarization of cardiac tissue via the stretch-activated channels. In **chapters 3** and **4** we investigated the organization and interaction of mechanically induced pacemakers.

We found that mechanical deformations can induce automatic pacemakers in an otherwise non-oscillatory medium, and that this effect is due to the depolarizing current of the stretch-activated channels. The mechanism of automatic pacemakers can be explained as follows. After propagation of an initial stimulus in the center of the tissue, we observed stretch in the center of the medium, which resulted in the activation of the depolarizing stretch-activated current I_s. If the tissue in this region is no longer refractory, then a new action potential will be generated once the threshold value is exceeded. We found that these self-organized pacemakers can drift throughout the medium to approach a stable attractor and that the locations of these attractors are dependent on the size of the medium, and the location of the initial stimulus.

Furthermore, we found that pacemakers can give rise to complex excitation patterns while drifting. We showed that multiple pacemakers initiated at both symmetrical and non-symmetrical locations interacted with each other to form one stable pacemaker that drifted to the center of the medium. Besides mechanical deformation and the stretch-activated current, we also found that electrophysiological parameters can influence the position of the stable attractors. In the presence of a parametric gradient of excitability, we found that pacemakers drifted to the region containing the lowest period.

The induction of pacemakers is dependent on the relation of the depolarizing effect of I_s and the excitation properties of cardiac cells. These properties differ substantially throughout the heart [83]. The most important pacemaker in the heart is the sino-atrial node, which consists of special cell types that are capable of generating electrical impulses and is responsible for maintaining sinus rhythm. Next to the sino-atrial node there are many other types of cardiac cells that show self-oscillating behavior, even in the absence of applied stretch. Therefore, given the wide variety of properties of cardiac cells and the depolarizing action of the stretch-activated channels in the heart, we propose that the effects of deformation on pacemaking activity can exist for some types of cardiac cells, particularly those that exhibit or are close to self-oscillation dynamics.

Indeed, as shown in detailed biophysical models of cardiac tissue [177], and in experimental studies [83], stretch-activated channels can depolarize cardiac tissue in a similar way as found in our computations. Furthermore, it was recently shown in neonatal rat ventricular cell cultures that calcium overload can lead to pacemaker activity and that in some cases these pacemakers drift throughout the medium [18].

Next to automatic pacemakers, mechano-electrical feedback can also induce drift and breakup of spiral waves, which is investigated in **chapter 5** and offers a possible new mechanism to explain the initiation of VF.

We found that tissue deformation has a pronounced effect on spiral wave rotation, which can result in drift and meandering of spiral waves. This can be explained by the *resonant drift* mechanism, in which drift and meandering of the spiral wave are caused by small periodic oscillations in electrophysiological parameters in synchrony with the period of the spiral wave. In this study, mechanical

deformation induced by a rotating spiral wave provides such a periodical modulation of the tissue with a period equal to that of the spiral wave. Resonant drift of spiral waves has been investigated in detailed models of cardiac tissue. Biktashev and Holden[15] showed that applying a spatially uniform periodic repetitive stimulation to a tissue containing a stable non-drifting spiral led to spiral wave drift. Resonant drift of spiral waves has also been investigated in experimental BZ reactions. Grill et al. [47] showed that applying a periodic sequence of short light impulses to a BZ reaction containing a spiral forced the spiral wave to drift. Both these studies applied external periodic stimuli resulting in drift of otherwise stable spiral waves. In contrast, the resonant drift observed in our model resulted from the periodic mechanical deformation regulated by the spiral wave itself. Therefore, it is likely that these effects of mechanics on spiral wave dynamics could also be reproduced using more detailed experimental and modeling studies in cardiac tissue.

Our main finding was that mechanical deformation can lead to spiral wave breakup into complex spatio-temporal patterns. Spiral wave breakup occurred due to the *accommodation phenomenon* [58, 59], in which the fast inward current I_{fi}, which is responsible for the upstroke of the action potential, was inactivated via the slow diastolic depolarization of the stretch-activated current I_s. Vetter and McCulloch [181] demonstrated in a Beeler-Reuter ionic model that stretch-activated current can block action potentials. They showed that increasing the conductance of the stretch-activated current resulted in failure of excitation of cardiac cells. A similar mechanism was also demonstrated in [87] for a one-dimensional setup using an accurate ionic model of atrial tissue (Courtemanche model [28]). However, both these models did not show that this block of action potentials can lead to wavebreaks resulting in 2D or 3D complex spatio-temporal patterns. We also found that spiral wave breakup could be reproduced using the detailed ventricular ionic model of Ten Tusscher et al. [171, 174]. Inactivation of the fast sodium current by depolarization has also been observed in experiments [58, 59].

Note that automatic pacemakers and spiral wave breakup via the accommodation phenomenon are two different mechanisms which rely both on the description of the sodium current. Automatic pacemakers are initiated by the activation of the sodium current, while spiral wave breakup via the accommodation phenomenon is mediated via the inactivation of the sodium current. If block of the sodium current would occur via the depolarizing current of the stretch-activated channels, then no new action potential can be generated in the center of the tissue and as a result no automatic pacemakers can be initiated. Hence, both pacemaker activity and block of sodium current cannot occur together using the same description of the sodium current. This does not mean that both mechanisms cannot occur in the heart, but they do not necessarily occur in the same cell.

One of the limitations in the above two-dimensional mechano-electrical studies is that we used low dimensional models to describe excitable behavior. Furthermore, we neglected the anisotropic behavior of cardiac tissue, which may be important for both the reaction-diffusion system as for the mechanical deformations.

We chose not to consider these effects in the two-dimensional studies, because the main aim of these studies was to investigate the basic effects of deformation in a general reaction-diffusion-mechanics system.

Part II

We studied the organization of VF using a heterogeneous anatomical model of the human ventricles in **chapter 6**. For this, we decided to create an anatomical model of the human ventricles that also incorporated clinically measured restitution data [114].

We introduced APD restitution heterogeneity into our model by incorporating clinically measured restitution data from patients who were undergoing surgery for aortic valve replacement as reported in [114]. Clinical restitution curves were mapped and interpolated to our 3D ventricular geometry [60] and reproduced by our cell model [171, 174] using appropriate regional variations of the parameters of the electrophysiological model.

Currently, data on the full three-dimensional organization of APD restitution in the human ventricles are not available. Furthermore, measuring restitution properties on the epi- and endocardium require different clinical methods. To date, either epicardial [114] or endocardial restitution properties [198] (but not both) have been reported for individual hearts. Given the different observations made in these studies regarding restitution slope patterns on the epi- and endocardial surfaces, it is likely that this heterogeneity has a three-dimensional structure. In the absence of experimental three-dimensional data, we extrapolated the two-dimensional surface patterns across the three-dimensional mass. Rather than using different data sets from two different studies, we used only the epicardial data from Nash et al. [114]. We believe that this is a reasonable first step until more detailed data on three-dimensional organization of human restitution becomes available.

We found that APD restitution heterogeneity is not only important for the initiation of wavebreaks and re-entry as was also reported by [22, 24], but also affects the number of filaments during VF. We observed that an increased level of APD restitution slope heterogeneity leads to more filaments and a broader and more dynamical distribution of excitation periods. We found that there is an interplay between the dynamical organization and complexity of VF, and the underlying APD restitution heterogeneity.

Our results show that an increase in wavebreaks caused by increasing heterogeneity is predominantly due to the presence of larger areas with steep restitution slope, rather than increased gradients in restitution slope or APD. However, we do not exclude that other factors such as geometric effects, anisotropy or more pronounced APD gradients potentially play a role in wavebreak formation.

Furthermore, we found that the number of epicardial phase singularities correlated well with the total number of filaments as was also shown by Ten Tusscher et al. [170], and that the distribution of epicardial excitation periods, provides a good estimate of the period distribution within the entire ventricular mass.

We continued our study of VF using the heterogeneous model of the human ventricles. In **chapter 7** we found that different initial conditions can lead to different mechanisms of VF: either mother rotor or multiple wavelet VF. Multiple mechanisms of VF in the same heart have also been observed in Langendorff perfused rabbit hearts by Wu et al. [193]. However, in their study mother rotor VF was induced by changing tissue properties via an increase in the D600 concentration. In our study, we found that both types of fibrillation can be simulated using the same parameter settings and that the type of VF is dependent on the initial startup position of the spiral wave.

The general idea behind mother rotor VF is that wavebreaks are driven by a dominant fast source of excitation [19, 69, 200] that causes conduction block in the surrounding tissue due to heterogeneity in refractory periods [8]. To demonstrate that we found mother rotor VF we removed that part of the ventricles which contained the mother rotor spiral, i.e. local ablation. Indeed, we found that after removal of the tissue all wavebreaks ended and wave activity terminated within 0.5 seconds.

We analyzed the differences in the underlying dynamics between mother rotor and multiple wavelet fibrillation. We found that the ECG signals for mother rotor and multiple wavelet VF were similar and resembled clinically observed ECG signals during VF as was also reported by [23, 112, 116, 195]. Interestingly, we observed that the fast Fourier transformation (FFT) of both the mother rotor and multiple wavelet ECG signals resulted in complex frequency patterns. One would expect a more narrow defined peak frequency for the mother rotor simulation, because the mother rotor drives the wavebreaks with a certain frequency. Partially, this can be explained by the position of the recording electrode, which is used to calculate the ECG signal. If the recording electrode is closest to the position of the mother rotor one would expect a more regular ECG signal, while if the position of the recording electrode is closer to the wavebreaks, one would expect a more complex ECG signal.

We also studied period distributions which were measured during the mother rotor and multiple wavelet simulations. During multiple wavelet VF, we observed a broad period distribution that was mainly determined by dynamical processes, rather than the underlying heterogeneity (see also [77]). As expected, during mother rotor VF we observed that the periods were dominated by the period of the mother rotor, leading to a narrow distribution.

Apart from the mother rotor, only short lived wavebreaks were present during mother rotor fibrillation, whereas during multiple wavelet VF several long lived filaments were present. In addition, during mother rotor VF, approximately 2-3 times less filaments were found compared to multiple wavelet VF. This can be explained by the fact that during mother rotor fibrillation the fast mother rotor dominates a large part of the cardiac tissue.

Normally, during mother rotor VF one would expect anatomically defined frequency domains, as was reported by [200]. However, this was not the case in our simulations, and we found that wavebreaks had the same period as the mother

rotor, and thus no frequency domains were observed. Wavebreaks occurred as a result of the high restitution slopes, rather than differences in refractory period caused by the underlying heterogeneity. To investigate this in more detail, we locally decreased the period of the mother rotor (by decreasing the I_{CaL} conductance in the mother rotor region), and thus increased anatomical heterogeneity. Indeed, this lead to Wenckebach like conduction blocks due to large differences in refractory period. Consequently, different frequency domains were present, similar to experimental findings for mother rotor type VF [200].

Thus, the formation of domains of different frequency is dependent on the frequency of the mother rotor and the degree of anatomical heterogeneity in refractory periods and, therefore, mother rotor fibrillation is not necessarily associated with different frequency domains.

Finally, in **chapter 8**, we studied the initiation and organization of VF due to mechano-electrical feedback in a detailed anatomical model of the left ventricle (LV). To overcome most of the limitations of the basic 2D electro-mechanical tissue models (**chapters 3-5**), we decided to create a more realistic 3D electromechanical model of the human left ventricle. Our model is the first model incorporating a detailed description of the human left ventricular anatomy (including fiber anisotropy) [60] and electrophysiological cell properties of human ventricular cells [171, 174], combined with a finite element model of passive elasticity to describe geometric deformations. As a result, we accurately can investigate the effects of wave dynamics on mechanical deformation, as well as the effect of mechano-electrical feedback on wave dynamics and VF organization.

We validated our model by stimulating the entire left ventricular endocardium to simulate a normal heart beat. In general, we found fiber shortening and wall thickening during systolic contraction. The cardiac and fiber strains were qualitatively similar to the experimental strains reported by Ashikaga et al. [6].

We found that during ventricular tachycardia loss of contraction occurred in which the end-diastolic LV volume decreased with approximately 50%. Although the entire LV is a contracted state, we observed regions of fiber stretch that shifted dynamically and were often located in front of the wavefront. We found that these regions of stretch were responsible for creating wavebreaks which resulted in VF as a result of the accommodation phenomenon of the inward depolarizing current of the stretch-activated channels.

The complexity of the VF dynamics depends on the amount of stretch generated and the parameters of the stretch-activated channels. Indeed, we observed that the complexity of VF and the number of filaments increased when G_s increased.

In a normal healthy heart one does not expect stretch-activated channels to be activated leading to wavebreaks and VF. In the above models our stretch-activated channels are homogeneously distributed and only activated if stretch occurs. Furthermore, wavebreaks only occurred for larger values of G_s. However, we believe that stretch-activated channels may be important in e.g. diseased hearts, in which local stiffness parameters can change as a result from excessive

fibrosis [7]. Recently, Sbrana et al. [154] experimentally demonstrated in cell cultures that an increase in tissue stiffness can lead to a decrease of the cell surface area caused by contraction. They showed that this may act as an amplifier of the stress tension generated in the plasma membrane, which in turn leads to a remarkable increase in the activation of the stretch-activated channels (530%).

Although the results of mechano-electrical feedback and tissue heterogeneity are not directly coupled, there are some points of interest. First, mechano-electrical feedback provides an additional source of heterogeneity in the tissue. This heterogeneity is dynamic and regulated by the underlying location of the wavefronts/scroll waves. Second, although the mechanism of wavebreak is different, the organization of VF in the mechano-electrical feedback simulations in the LV are comparable to the mother rotor VF dynamics found in the APD restitution heterogeneity simulations.

9.2 Model Complexity

In this thesis we used different models with different levels of complexity for modeling cardiac excitability, mechanics and geometry of cardiac tissue.

For cardiac excitability, there are two classes of models: low dimensional and ionic models. Low dimensional models can reproduce some important measurable characteristics of cardiac tissue, such as action potential restitution properties, the general shape of the action potential, and the effects of tissue anisotropy and heterogeneity. By adding one or two extra variables these models can also describe experimentally measured conduction velocity restitution and the exact shape of the action potential. However, low dimensional models do not describe detailed biophysical mechanisms of cardiac excitation that occur due to different dynamics of ionic channels on the cardiac membrane. To describe ionic channel dynamics one should use so-called ionic models for cardiac tissue that are based on the founding paper by Hodgkin and Huxley [59]. Ionic models describe the properties of each individual ionic channel and are based on experimental studies of voltage and time dynamics using voltage clamp techniques.

For cardiac mechanics, it is possible to use simple and detailed models to reproduce passive and active tension of cardiac tissue. For passive tension, simple models are based on simple elasticity laws, such the Neo-Hookian material law. One of them is a Mooney-Rivlin material response, which describe properties of soft rubbers and silicone gels and is used as a general description of passive properties of cardiac tissue [117]. A more detailed description is given by the Guccione constitutive material law [49], which describes passive material properties of the intact ventricular myocardium and is based on canine measurements. For active tension, simple models use a direct coupling of a state variable of the electrical model to calculate the active tension of cardiac fibers [117]. A more detailed description would define active fiber tension as function of the intracellular calcium

transient and the history of changes in cell length. One of the most recent models of this type is the Niederer-Hunter-Smith model [119], that approximates active tension developed as a result of cellular cross-bridge cycling.

For cardiac tissue geometry, simulations use either 2D or 3D rectangular sheets or an accurate anatomical description of the ventricles of the heart that incorporates fiber direction anisotropy.

Current flow at the tissue level can be represented using a mono-domain or bi-domain model [147]. In the mono-domain description only the transmembrane currents and potentials are represented, while in bi-domain models both intracellular and extracellular currents and potentials are described. It is widely accepted that bi-domain models are required in simulations for which an external stimulus is applied, e.g., defibrillation. For all our simulations, which did not include modeling of defibrillation, it was suffice to use a mono-domain description.

In this thesis we used a combination of various types of models. In particular:

In **part I** of this thesis, we used simple models to describe electrical and mechanical activity of cardiac tissue as well as simple rectangular geometries. We decided this, because our aim was to investigate basic mechanisms of mechano-electrical feedback.

To study pacemaker generation it was sufficient to use a two variable Aliev-Panfilov model [2]. However, in order to investigate spiral wave breakup a more detailed (but still low dimensional) model was needed that also includes a proper description of the inactivation kinetics of the sodium current. This is because the standard Aliev-Panfilov model [2] lacks a description of this inactivation kinetics. For this study, we have chosen to use a three-variable Fenton-Karma model [33], that contains a more detailed description of the sodium current (inactivation and activation kinetics).

In **part II** of this thesis, we were interested to investigate mechanisms of ventricular fibrillation in the human heart based on detailed clinical measurements of APD restitution properties in the human heart [114]. To reproduce these APD restitution properties in the best possible way, we choose to use a detailed ionic model describing the excitable behavior of human ventricular cells [174], which was fitted to clinically measured APD restitution data [114]. We combined this model with an anatomically based model of the human ventricles including fiber direction anisotropy [60]. Furthermore, we would like to find out if mechanically induced breakup (observed in part 1 of this thesis) could manifest itself in an accurate 3D model of the human left ventricle. We therefore needed a more realistic model that also included a detailed description of the active tension and deformation. For this, we used the Ten Tusscher model [171, 174] to describe the excitable behavior of cardiac cells, the Guccione constitutive material law [49] for passive tension and the Niederer-Hunter-Smith model [119] to approximate active tension.

In conclusion, for the main aim of this thesis: 'studying the effects of mechano-electrical feedback and tissue heterogeneity on the initiation and organization of

ventricular fibrillation', we used the most detailed and realistic representation of the human ventricles. However, to understand these complex models, the insights obtained from simple models proved to be indispensable.

9.3 Future Directions

In this thesis we studied the role of mechano-electrical feedback and tissue heterogeneity on the initiation and organization of ventricular fibrillation. We believe that the addition of mechano-electrical feedback and clinically measured tissue heterogeneity in our models is a step forward in anatomical modeling of the human heart. However, there are still important details which can be further improved in our models.

Currently, in our anatomical geometry of the human (left) ventricle(s), there are only fiber angles incorporated and no sheet and imbrication angles present, and thus these models are transversely isotropic. In reality the ventricles are orthotropically anisotropic [92, 93], in which the muscle fibers are organized in a laminar structure. Now that more data becomes available about orthotropic anisotropy, it would be interesting to incorporate this in future versions of existing three-dimensional models. Orthotropic anisotropy will likely affect mechanical and electrophysiological properties such as mechanical strains, filament dynamics and the stability and organization of VF.

We studied the effects of heterogeneous restitution data on the dynamics of VF using a detailed ionic model to describe electrophysiological cell properties of human ventricular cells, combined with an anatomically accurate human ventricular geometry. Currently, clinical restitution data is mostly available for the epi- or the endocardial surface of the ventricles [114, 198], but not measured simultaneously on the epi- and endocardium in the same patient. However, recently the group of Nanthakumar [102] studied VF in human patients and obtained simultaneous electrograms from both the epi- and endocardium in the left ventricular cardiomyopathy and from the endocardium in right ventricular myopathy. We believe that it is only a matter of time that restitution data measured simultaneously from both the epi- and endocardium will be published. This data can then be used to improve our model and study transmural restitution heterogeneity. It would also be interesting to repeat our simulations using more clinical restitution data of different patients to study VF dynamics between data sets, and compare these results with clinically observed VF dynamics in patients [102, 116].

Furthermore, we developed a detailed electro-mechanical model the human left ventricle. In the future we will also add the right ventricle to this model. In the current model, we used an endocardial LV cavity pressure of 1 kPa, which corresponds to the end-diastolic pressure. In reality, there is a LV pressure-volume loop present during the cardiac cycle that consists of a ventricular filling phase (diastole), isovolumetric contraction phase, ejection phase, and an isovolumetric relaxation. During the cardiac cycle the LV cavity pressure increases to above

10 kPa at the end-systolic phase. In the future, we want to use mid-contraction pressures (5-10 kPa) and pressure-volume loops to describe the LV cavity pressure. This also requires higher active tension development.

There are also other types of heterogeneity present in the human heart which were not taken into account in our models, which will likely contribute to the complexity of excitation patterns during VF, such as the Purkinje network, fibrosis, gap junction remodeling, and transmural variations between epi-, endo- and midmyocardial cell types. The Purkinje network can be important during cardiac arrhythmias in which the Purkinje network can provide new pathways to excitation waves which may result in reentry [54, 126]. Recently, Ten Tusscher and Panfilov [168] developed a human ventricular model that also incorporates the Purkinje network and showed that the Purkinje network can be important for more complex ventricular tachycardia's, such as bundle branch block or reentry. This Purkinje network can easily be incorporated into our model. The occurrence of cardiac arrhythmias is coupled to diseases such as myocardial infarction, cardiomyopathies and congestive heart failure. It is known that during these diseases extensive fibrosis formation [9] and gap junction remodeling [133] takes place, thereby increasing cardiac heterogeneity. Furthermore, in reality there are variations in cell types present in the myocardial wall: epi- endo- and midmyocardial cells, which lead to a substantial heterogeneity within the ventricular wall [4]. The above mentioned heterogeneity types will likely add additional effects which are important for the initiation and organization of VF. In the future we will study the individual effects of these heterogeneities.

9.4 Conclusion

In this thesis we investigated mechanisms of ventricular fibrillation, focusing on the role of mechano-electrical feedback and tissue heterogeneity. The most important conclusions regarding mechano-electrical feedback are that local tissue deformations can lead to automatic pacemaker activity via the stretch-activated channels, and that local stretch of fibers can cause an otherwise stable spiral wave to break up. The most important conclusion regarding tissue heterogeneity is that action potential duration restitution heterogeneity is not only important for the initiation of wavebreaks and re-entry, but also affects the dynamics of ventricular fibrillation. In addition, different initial conditions can lead to different mechanisms of ventricular fibrillation: either mother rotor or multiple wavelet ventricular fibrillation. These results indicate that mechano-electrical feedback and tissue heterogeneity may play an important role in the initiation and dynamics of ventricular fibrillation. Further research and development of mechano-electrical models is needed to quantify the effects of mechano-electrical feedback in more detail.

APPENDIX A

TNNP 2006 Model

This appendix contains the parameters and equations governing the TNNP 2006 model. For more information we refer to [171, 174].

Table A1 Default model parameter settings of the TNNP 2006 model.

Parameter	Definition	Value
R	Gas constant	8.3143 $JK^{-1}mol^{-1}$
T	Temperature	310 K
F	Faraday constant	96.4867 $Cmmol^{-1}$
C_m	Cell capacitance per unit surface area	2.0 $\mu F cm^{-2}$
S	Surface to volume ratio	0.2 μm^{-1}
ρ	Cellular resistivity	162 Ωcm
V_c	Cytoplasmic volume	16405 μm^3
V_{sr}	Sarcoplasmic reticulum volume	1094 μm^3
V_{ss}	Subspace volume	54.68 μm^3
K_o	Extracellular K^+ concentration	5.4 mM
Na_o	Extracellular Na^+ concentration	140 mM
Ca_o	Extracellular Ca^{2+} concentration	2 mM
G_{Na}	Maximal I_{Na} conductance	14.838 $nSpF^{-1}$
G_{K1}	Maximal I_{K1} conductance	5.405 $nSpF^{-1}$

Continued on next page

Continued from previous page

Parameter	Definition	Value
G_{to}	Epicardial I_{to} conductance	0.294 $nSpF^{-1}$
G_{Kr}	Maximal I_{Kr} conductance	0.153 $nSpF^{-1}$
G_{Ks}	Maximal epicardial I_{Ks} conductance	0.392 $nSpF^{-1}$
p_{KNa}	Relative I_{Ks} permeability to Na^{+}	0.03
G_{CaL}	Maximal I_{CaL}conductance	3.980^{-5} $cmms^{-1}\mu F^{-1}$
k_{NaCa}	Maximal I_{NaCa}	1000 $pApF^{-1}$
γ	Voltage dependence parameter of I_{NaCa}	0.35
K_{mCa}	Ca_i half saturation constant for I_{NaCa}	1.38 mM
K_{mNai}	Na_i half saturation constant for I_{NaCa}	87.5 mM
k_{sat}	Saturation factor for I_{NaCa}	0.1
α	Factor enhancing outward nature of I_{NaCa}	2.5
P_{NaK}	Maximal I_{NaK}	2.724 $pApF^{-1}$
K_{mK}	K_o half saturation constant of I_{NaK}	1 mM
K_{mNa}	Na_i half saturation constant of I_{NaK}	40 mM
G_{pK}	Maximal I_{pK} conductance	0.0146 $nSpF^{-1}$
G_{pCa}	Maximal I_{pCa} conductance	0.1238 $nSpF^{-1}$
K_{pCa}	Half saturation constant of I_{pCa}	0.0005 mM
G_{bNa}	Maximal I_{bNa} conductance	0.000290 $nSpF^{-1}$
G_{bCa}	Maximal I_{bCa} conductance	0.000592 $nSpF^{-1}$
V_{maxup}	Maximal I_{up} conductance	0.006375 $mMms^{-1}$
K_{up}	Half saturation constant of I_{up}	0.00025 mM
V_{rel}	Maximal I_{rel} conducatance	0.102 $mMms^{-1}$
k_1'	R to O and RI to I I_{rel} transition rate	0.15 $mM^{-2}ms^{-1}$
k_2'	O to I and R to RI I_{rel} transition rate	0.045 $mM^{-1}ms^{-1}$
k_3	O to R and I to RI I_{rel} transition rate	0.060 ms^{-1}
k_4	I to O and RI to I I_{rel} transition rate	0.005 ms^{-1}
EC	Ca_{SR} half saturation constant of k_{casr}	1.5 mM
max_{sr}	Maximum value of k_{casr}	2.5
min_{sr}	Minimum value of k_{casr}	1
V_{leak}	Maximal I_{leak} conductance	0.00036 $mMms^{-1}$
V_{xfer}	Maximal I_{xfer} conductance	0.0038 $mMms^{-1}$
Buf_c	Total cytoplasmic buffer concentration	0.2 mM
K_{bufc}	Ca_i half saturation constant for cytoplasmic buffer	0.001 mM
Buf_{sr}	Total sarcoplasmic buffer concentration	10 mM
K_{bufsr}	Ca_{SR} half saturation constant for sarcoplasmic buffer	0.3 mM
Buf_{ss}	Total subspace buffer concentration	0.4 mM
K_{bufss}	Ca_{SS} half saturation constant for subspace buffer	0.00025 mM

Reversal potentials

$$E_X = \frac{RT}{zF} log \frac{X_o}{X_i} \qquad \text{for} \quad X = Na^+, K^+, Ca^{2+} \tag{A.1}$$

$$E_{Ks} = \frac{RT}{F} log \frac{K_o + p_{KNa} Na_o}{K_i + p_{KNa} Na_i} \tag{A.2}$$

Fast Na^+ current

$$I_{Na} = G_{Na} m^3 h j (V - E_{Na}) \tag{A.3}$$

$$m_\infty = \frac{1}{(1. + e^{(-56.86 - V)/9.03})^2} \tag{A.4}$$

$$\alpha_m = \frac{1}{1. + e^{(-60. - V)/5.}} \tag{A.5}$$

$$\beta_m = \frac{0.1}{1. + e^{(V + 35.)/5.}} + \frac{0.1}{1. + e^{(V - 50.)/200.}} \tag{A.6}$$

$$\tau_m = \alpha_m \beta_m \tag{A.7}$$

$$h_\infty = \frac{1}{(1. + e^{(V + 71.55)/7.43})^2} \tag{A.8}$$

$$\alpha_h = \begin{cases} 0 & \text{if } V \geq -40, \\ 0.057 e^{-(V + 80.)/6.8} & \text{if } V < -40. \end{cases} \tag{A.9}$$

$$\beta_h = \begin{cases} \frac{0.77}{0.13(1. + e^{-(V + 10.66)/11.1})} & \text{if } V \geq -40, \\ 2.7 e^{0.079V} + 3.1 \times 10^5 e^{0.3485V} & \text{if } V < -40. \end{cases} \tag{A.10}$$

$$\tau_h = \frac{1}{\alpha_h + \beta_h} \tag{A.11}$$

$$j_\infty = \frac{1}{(1. + e^{(V + 71.55)/7.43})^2} \tag{A.12}$$

$$\alpha_j = \begin{cases} 0 & \text{if } V \geq -40, \\ \frac{(-2.5428 \times 10^4 e^{0.2444V} - 6.948 \times 10^{-6} e^{-0.04391V})(V + 37.78)}{1. + e^{0.311(V + 79.23)}} & \text{if } V < -40. \end{cases} \tag{A.13}$$

$$\beta_j = \begin{cases} \frac{0.6 e^{0.057V}}{1. + e^{-0.1(V + 32.)}} & \text{if } V \geq -40, \\ \frac{0.02424 e^{-0.01052V}}{1. + e^{-0.1378(V + 40.14)}} & \text{if } V < -40. \end{cases} \tag{A.14}$$

$$\tau_j = \frac{1}{\alpha_j + \beta_j} \tag{A.15}$$

L-type Ca^{2+} current

$$I_{CaL} = G_{CaL} d f f_2 f_{cass} 4 \frac{(V-15)F^2}{RT} \frac{0.25 Ca_{SS} e^{2(V-15)F/RT} - Ca_o}{e^{2(V-15)F/RT} - 1} \tag{A.16}$$

$$d_\infty = \frac{1}{1+e^{(-8-V)/7.5}} \tag{A.17}$$

$$\alpha_d = \frac{1.4}{1+e^{(-35-V)/13}} + 0.25 \tag{A.18}$$

$$\beta_d = \frac{1.4}{1+e^{(V+5)/5}} \tag{A.19}$$

$$\gamma_d = \frac{1}{1+e^{(50-V)/20}} \tag{A.20}$$

$$\tau_d = \alpha_d \beta_d + \gamma_d \tag{A.21}$$

$$f_\infty = \frac{1}{1+e^{(V+20)/7}} \tag{A.22}$$

$$\alpha_f = 1102.5 e^{-(\frac{V+27}{15})^2} \tag{A.23}$$

$$\beta_f = \frac{200}{1+e^{(13-V)/10}} \tag{A.24}$$

$$\gamma_f = \frac{180}{1+e^{(V+30)/10}} + 20 \tag{A.25}$$

$$\tau_f = \alpha_f + \beta_f + \gamma_f \tag{A.26}$$

$$f_2\infty = \frac{0.67}{1+e^{(V+35)/7}} + 0.33 \tag{A.27}$$

$$\alpha_{f2} = 600 e^{-\frac{(V+25)^2}{170}} \tag{A.28}$$

$$\beta_{f2} = \frac{31}{1+e^{(25-V)/10}} \tag{A.29}$$

$$\gamma_{f2} = \frac{16}{1+e^{(V+30)/10}} \tag{A.30}$$

$$\tau_{f2} = \alpha_{f2} + \beta_{f2} + \gamma_{f2} \tag{A.31}$$

$$f_{cass\infty} = \frac{0.6}{1+(\frac{CaSS}{0.05})^2} + 0.4 \tag{A.32}$$

$$\tau_{fcass} = \frac{80}{1+(\frac{CaSS}{0.05})^2} + 2 \tag{A.33}$$

Transient outward current

$$I_{to} = G_{to} r s (V - E_K) \tag{A.34}$$

For all cell types:

$$r_\infty = \frac{1}{1. + e^{(20-V)/6.}} \tag{A.35}$$

$$\tau_r = 9.5e^{-(V+40)^2/1800} + 0.8 \tag{A.36}$$

$$s_\infty = \frac{1}{1. + e^{(V+20)/5}} \tag{A.37}$$

$$\tau_s = 85.e^{-(V+45)^2/320} + \frac{5}{1. + e^{(V-20.)/5.}} + 3 \tag{A.38}$$

Slow delayed rectifier current

$$I_{Ks} = G_{Ks} x_s^2 (V - E_{Ks}) \tag{A.39}$$

$$x_{s\infty} = \frac{1}{1 + e^{(-5-V)/14}} \tag{A.40}$$

$$\alpha_{xs} = \frac{1400}{\sqrt{1 + e^{(5-V)/6}}} \tag{A.41}$$

$$\beta_{xs} = \frac{1}{1 + e^{(V-35)/15}} \tag{A.42}$$

$$\tau_{xs} = \alpha_{xs}\beta_{xs} + 80 \tag{A.43}$$

Rapid delayed rectifier current

$$I_{Kr} = G_{Kr}\sqrt{\frac{K_o}{5.4}} x_{r1} x_{r2} (V - E_K) \tag{A.44}$$

$$x_{r1\infty} = \frac{1}{1. + e^{(-26.-V)/7.}} \tag{A.45}$$

$$\alpha_{xr1} = \frac{450.}{1. + e^{(-45.-V)/10.}} \tag{A.46}$$

$$\beta_{xr1} = \frac{6.}{1. + e^{(V+30.)/11.5}} \tag{A.47}$$

$$\tau_{xr1} = \alpha_{xr1}\beta_{xr1} \tag{A.48}$$

$$x_{r2\infty} = \frac{1}{1. + e^{(V+88.)/24.}} \tag{A.49}$$

$$\alpha_{xr2} = \frac{3.}{1. + e^{(-60.-V)/20.}} \tag{A.50}$$

$$\beta_{xr2} = \frac{1.12}{1. + e^{(V-60.)/20.}} \tag{A.51}$$

$$\tau_{xr2} = \alpha_{xr2}\beta_{xr2} \tag{A.52}$$

Inward rectifier K^+ current

$$I_{K1} = G_{K1}\sqrt{\frac{K_o}{5.4}}x_{K1\infty}(V - E_K) \tag{A.53}$$

$$\alpha_{K1} = \frac{0.1}{1. + e^{0.06(V-E_K-200)}} \tag{A.54}$$

$$\beta_{K1} = \frac{3.e^{0.0002(V-E_K+100)} + e^{0.1(V-E_K-10)}}{1. + e^{-0.5(V-E_K)}} \tag{A.55}$$

$$x_{K1\infty} = \frac{\alpha_{K1}}{\alpha_{K1} + \beta_{K1}} \tag{A.56}$$

Na^+/Ca^{2+} exchanger current

$$I_{NaCa} = k_{NaCa}\frac{e^{\frac{\gamma VF}{RT}}Na_i^3Ca_o - e^{\frac{(\gamma-1)VF}{RT}}Na_o^3Ca_i\alpha}{(K_{mNai}^3 + Na_o^3)(K_{mCa} + Ca_o)(1 + ksat e^{\frac{(\gamma-1)VF}{RT}})} \tag{A.57}$$

Na^+/K^+ pump current

$$I_{NaK} = P_{NaK}\frac{K_o}{K_o + K_{mK}}\frac{Na_i}{Na_i + K_{mNa}}\frac{1}{1 + 0.1245e^{-0.1VF/RT} + 0.0353e^{-VF/RT}} \tag{A.58}$$

I_{pCa} current

$$I_{pCa} = G_{pCa}\frac{Ca_i}{Ca_i + K_{pCa}} \tag{A.59}$$

I_{pK} current

$$I_{pK} = G_{pK}\frac{V - E_K}{1. + e^{(25-V)/5.98}} \tag{A.60}$$

Background currents

$$I_{bNa} = G_{bNa}(V - E_{Na}) \tag{A.61}$$

$$I_{bCa} = G_{bCa}(V - E_{Ca}) \tag{A.62}$$

Calcium dynamics

$$J_{leak} = V_{leak}(Ca_{SR} - Ca_i) \tag{A.63}$$

$$J_{up} = \frac{V_{maxup}}{1 + K_{up}^2/Ca_i^2} \tag{A.64}$$

$$J_{rel} = V_{rel} O (Ca_{SR} - Ca_{SS}) \tag{A.65}$$

$$J_{xfer} = V_{xfer}(Ca_{SS} - Ca_i) \tag{A.66}$$

$$O = \frac{k_1 Ca_{SS}^2 \bar{R}}{k_3 + k_1 Ca_{SS}^2} \tag{A.67}$$

$$\frac{d\bar{R}}{dt} = -k_2 Ca_{SS} \bar{R} + k_4(1 - \bar{R}) \tag{A.68}$$

$$k_1 = \frac{k_{1'}}{k_{casr}} \tag{A.69}$$

$$k_2 = k_{2'} k_{casr} \tag{A.70}$$

$$k_{casr} = max_{sr} - \frac{max_{sr} - min_{sr}}{1 + (EC/Ca_{SR})^2} \tag{A.71}$$

$$Ca_{ibufc} = \frac{Cai \times Buf_c}{Cai + K_{bufc}} \tag{A.72}$$

$$dCa_{itotal}/dt = -\frac{I_{bCa} + I_{pCa} - 2I_{NaCa}}{2V_c F} + \frac{V_{sr}}{V_c}(J_{leak} - J_{up}) + J_{xfer} \tag{A.73}$$

$$Ca_{srbufsr} = \frac{Ca_{sr} \times Buf_{sr}}{Ca_{sr} + K_{bufsr}} \tag{A.74}$$

$$dCa_{SRtotal}/dt = (J_{up} - J_{leak} - J_{rel}) \tag{A.75}$$

$$Ca_{ssbufss} = \frac{Ca_{ss} \times Buf_{ss}}{Ca_{ss} + K_{bufss}} \tag{A.76}$$

$$dCa_{SStotal}/dt = -\frac{I_{CaL}}{2V_{ss}F} + \frac{V_{sr}}{V_{ss}} J_{rel} - \frac{V_c}{V_{ss}} J_{xfer} \tag{A.77}$$

Sodium and potassium dynamics

$$dNa_i/dt = -\frac{I_{Na} + I_{bNa} + 3I_{NaK} + 3I_{NaCa}}{V_c F} \tag{A.78}$$

$$dK_i/dt = -\frac{I_{K1} + I_{to} + I_{Kr} + I_{Ks} - 2I_{NaK} + I_{pK} + I_{stim} - I_{ax}}{V_c F} \tag{A.79}$$

APPENDIX B

NHS 2006 Model

This appendix contains the parameters and equations governing the NHS 2006 model. For more information we refer to [119, 120].

Table B1 Default model parameter settings of the NHS 2006 model.

Parameter	Definition	Value
k_{on}	Rate of binding of Ca^{2+} to troponin C	100 $mM^{-1}ms^{-1}$
k_{off}	Tension dependent rate of unbinding of Ca^{2+} from troponin C	0.2 ms^{-1}
β_0	Tension coefficient	4.9
β_1	Half activation length dependent coefficient	-4.0
Ca_{50ref}	$[Ca^{2+}]_i$ reference half activation concentration	0.00105 mM
$Ca_{TRPN_{Max}}$	Ca^{2+} bound to TnC half activation concentration	0.07 mM
γ_{trpn}	Tension dependence	2.0
α_0	Rate of activation	0.008 ms^{-1}
α_{r1}	Slow rate of relaxation	0.002 ms^{-1}
α_{r2}	Fast rate of relaxation	0.0017 ms^{-1}
n_{Hill}	Activation coefficient (Hill coefficient)	3.0
n_{Rel}	Relaxation coefficient	3.0
K_z	Relaxation parameter	0.15

Continued on next page

Continued from previous page

Parameter	Definition	Value
A_1	Weighting coefficient	-29
A_2	Weighting coefficient	138
A_3	Weighting coefficient	129
α_1	Exponential rate constants	0.03 ms^{-1}
α_2	Exponential rate constants	0.13 ms^{-1}
α_3	Exponential rate constants	0.625 ms^{-1}
a	Curvature of the force velocity curve	0.35
z_p	Variable needed for linearization procedure	0.85
T_{ref}	Maximum tension at resting sarcomere length	56.2 kPa

Intracellular Calcium

Ca_i from TNNP model (see Appendix A)

$$Ca_b = Ca_{TRPN_{MAX}} - TRPN \tag{B.1}$$

$$\frac{dTRPN}{dtime} = J_{TRPN} \tag{B.2}$$

Tropomysosin

$$K_1 = \frac{\alpha_{r2} * (z_p)^{(n_{Rel}-1)} * n_{Rel} * (K_z)^{n_{Rel}}}{((z_p)^{n_{Rel}} + (K_z)^{n_{Rel}})^2} \tag{B.3}$$

$$K_2 = \frac{\alpha_{r2} * (z_p)^{n_{Rel}}}{((z_p)^{n_{Rel}} + (K_z)^{n_{Rel}})} * (1 - \frac{n_{Rel} * (K_z)^{n_{Rel}}}{((z_p)^{n_{Rel}} + (K_z)^{n_{Rel}})}) \tag{B.4}$$

$$z_{max} = \frac{\frac{\alpha_0}{\frac{Ca_{TRPN_{50}}}{Ca_{TRPN_{MAX}}})^{n_{Hill}})} - K_2}{\alpha_{r1} + K_1 + \frac{\alpha_0}{\frac{Ca_{TRPN_{50}}}{Ca_{TRPN_{MAX}}}^{n_{Hill}}}} \tag{B.5}$$

$$Ca_{50} = Ca_{50ref} * (1 + \beta_1 * (\lambda - 1)) \tag{B.6}$$

$$Ca_{TRPN_{50}} = \frac{Ca_{50} * Ca_{TRPN_{MAX}}}{Ca_{50} + \frac{k_{Ref_{off}}}{k_{on}} + (1 - \frac{(1+\beta_0*(\lambda-1))*0.5}{\gamma_{trpn}})} \tag{B.7}$$

$$\alpha_{Tm} = \alpha_0 * (\frac{Ca_b}{Ca_{TRPN_{50}}})^{n_{Hill}} \tag{B.8}$$

$$\beta_{Tm} = (\alpha_{r1} + \frac{\alpha_{r2} * z^{n_{Rel}-1}}{((z_p)^{n_{Rel}} + (K_z)^{n_{Rel}})}) \tag{B.9}$$

$$\frac{dz}{dtime} = \alpha_{Tm} * (1 - z) - \beta_{Tm} * z \tag{B.10}$$

Troponin

$$k_{off} = \begin{cases} k_{Ref_{off}} * (1 - \frac{T_a}{\gamma_{trpn} * T_{ref}}) & \text{if } (1 - \frac{T_a}{\gamma_{trpn} * T_{ref}}) > 0.1, \\ k_{Ref_{off}} & \text{if } (1 - \frac{T_a}{\gamma_{trpn} * T_{ref}}) \leq 0.1. \end{cases} \tag{B.11}$$

$$J_{TRPN} = (Ca_{TRPN_{MAX}} - TRPN) * k_{off} - Ca_i * TRPN * k_{on} \tag{B.12}$$

Myofilaments

$$\lambda, d\lambda \ (from\ FEM/CMISS) \tag{B.13}$$

Filament overlap

$$overlap = (1 + \beta_0 * (\lambda - 1)) \tag{B.14}$$

Length Dependent tension

$$T_{Base} = \frac{T_{ref} * z}{z_{max}} \tag{B.15}$$

Isometric tension

$$T_0 = T_{Base} * overlap \tag{B.16}$$

Cross bridges

$$Q = Q_1 + Q_2 + Q_3 \tag{B.17}$$

$$K(Q) = \begin{cases} \frac{(a*Q+1)}{1-Q} & \text{if } Q \leq 0, \\ \frac{(1+(a+2)*Q)}{1+Q} & \text{if } Q > 0. \end{cases} \tag{B.18}$$

$$\frac{dQ_i}{dtime} = A_i * d\lambda - \alpha_i * Q_i \tag{B.19}$$

Active Tension

$$T_a = T_0 K(Q) \tag{B.20}$$

Bibliography

[1] **Agladze, K.I., Davydov, V.A. & Mikhailov, A.S.** An observation of resonance of spiral waves in distributed excitable medium. *JETP Lett.* 45: 767–769 (1987).

[2] **Aliev, R.R. & Panfilov, A.V.** A simple two-variable model of cardiac excitation. *Chaos, Solitons and Fractals* 7: 293–301 (1996).

[3] **Allessie, M.A., Bonke, F.I.M. & Schopman, F.J.G.** Circus movement in rabbit atrial muscle as a mechanism of tachycardia. *Circ. Res.* 33: 54–62 (1973).

[4] **Antzelevitch, C., Sicouri, S., Litovsky, S.H., Lukas, A., Krishnan, S.C., Diego, J.M.D., Gintant, G.A. & D., Liu**. Heterogeneity within the ventricular wall. *Circ. Res.* 69: 1427–1449 (1991).

[5] **Ashihara, T., Yao, T., Namba, T., Ito, M., Ikeda, T., Kawase, A., Toda, S., Suzuki, T., Inagaki, M., Sugimachi, M., Kinoshita, M. & Nakazawa, K.** Electroporation in a model of cardiac defibrillation. *J. Cardiovasc. Electrophysiol.* 12: 1393–1403 (2001).

[6] **Ashikaga, H., Omens, J.H., Ingels, N.B. & Covell, J.W.** Transmural mechanics at left ventricular epicardial pacing site. *Am. J. Physiol. Heart Circ. Physiol.* 286: H2401–H2407 (2004).

[7] **Atance, J., Yost, M.J. & Carver, W.** Influence of the extracellular matrix on the regulation of cardiac fibroblast behavior by mechanical stretch. *J. Cell. Physiol.* 200: 377–386 (2004).

[8] **Baher, A., Qu, Z., Hayatdavoudi, A., Lamp, S.T., Yang, M.J., Xie, F., Turner, S., Garfinkel, A. & Weiss, J.N.** Short-term cardiac memory and mother rotor fibrillation. *Am. J. Physiol. Heart Circ. Physiol.* 292: H180–H189 (2007).

[9] **de Bakker, J.M. & van Rijen, H.V.** Electrocardiographic manifestation of anatomical substrates underlying post-myocardial infarction tachycardias. *J. Electrocardiol.* 40: S21–S25 (2007).

[10] **Banville, I., Chattipakorn, N. & Gray, R.A.** Restitution dynamics during pacing and arrhythmias in isolated pig hearts. *J. Cardiovasc. Electrophysiol.* 15: 455–463 (2004).

[11] **Banville, I. & Gray, R.A.** Effect of action potential duration and conduction velocity restitution and their spatial dispersion on alternans and the stability of arrhythmias. *J. Cardiovasc. Electrophysiol.* 13: 1141–1149 (2002).

[12] **Beeler, G.W. & Reuter, H.J.** Reconstruction of the action potential of ventricular myocardial fibers. *J. Physiol.* 268: 177–210 (1977).

[13] **Bers, D.M.** *Excitation-Contraction Coupling and Cardiac Excitation Force.* 3rd Edition. Kluwer Academic Publishers, Dordrecht, The Netherlands (2001).

[14] **Biktashev, V.N.** Dissipation of the excitation wave fronts. *Phys. Rev. Lett.* 89: 168102 (2002).

[15] **Biktashev, V.N. & Holden, A.V.** Control of re-entrant activity in a model of mammalian atrial tissue. *Proc. Roy. Soc. Lond. B* 260: 211–217 (1995).

[16] **Biktashev, V.N. & Holden, A.V.** Resonant drift of autowave vortices in two dimensions and the effect of boundaries and inhomogeneities. *Chaos, Solitons and Fractals* 5: 575–562 (1995).

[17] **Biktashev, V.N., Holden, A.V., Tsyganov, M.A., Brindley, J. & Hill, N.A.** Excitation wave breaking in excitable media with linear shear flow. *Phys. Rev. Lett.* 81: 2815–2818 (1998).

[18] **Chang, M.G., Tung, L., Sekar, R., Cysyk, J., Qi, Y.R., Xu, L., Marban, E. & Abraham, R.M.** Calium overload induces tachyarrhythmias in a 2D ventricular myocyte experimental model. *Heart Rhythm* 3: S109–S110 (2006).

[19] **Chen, J., Mandapati, R., Berenfeld, O., Skanes, A.C. & Jalife, J.** High-frequency periodic sources underlie ventricular fibrillation in the isolated rabbit heart. *Circ. Res.* 86: 86–93 (2000).

[20] **Cherry, E.M. & Fenton, F.** Suppression of alternans and conduction blocks despite steep APD restitution: electrotonic, memory, and conduction velocity restitution effects. *Am. J. Physiol. Heart Circ. Physiol.* 286: H2332–H2341 (2004).

[21] **Clayton, R.H. & Holden, A.V.** A method to quantify the dynamics and complexity of re-entry in computational models of ventricular fibrillation. *Phys. Med. Biol.* 47: 225–238 (2002).

[22] **Clayton, R.H. & Holden, A.V.** Dispersion of cardiac action potential duration and the initiation of re-entry: A computational study. *Biomed. Eng. Online* 4: 1–15 (2005).

[23] **Clayton, R.H., Murray, A. & Campbell, R.W.** Objective features of the surface electrocardiogram during ventricular tachyarrhythmias. *Eur. Heart J.* 16: 1115–1119 (1995).

[24] **Clayton, R.H. & Taggart, P.** Regional differences in APD restitution can initiate wavebreak and re-entry in cardiac tissue: A computational study. *Biomed. Eng. Online* 4(54): 1–14 (2005).

[25] **Clayton, R.H., Zhuchkova, E.A. & Panfilov, A.V.** Phase singularities and filaments: Simplifying complexity in computational models of ventricular fibrillation. *Prog. Biophys. Mol. Biol.* 90: 378–398 (2006).

[26] **Compton, S.** Ventricular tachycardia [online]. *eMedicine* http://www.emedicine.com/med/topic2367.htm (2002).

[27] **Costa, K.D., Holmes, J.W. & McCulloch, A.D.** Modelling cardiac mechanical properties in three dimensions. *Phil. Trans. Roy. Soc. Lond. A.* 359: 1233–1250 (2001).

[28] **Courtemanche, M., Ramirez, R.J. & Nattel, S.** Ionic mechanisms underlying human atrial action potential properties: insights from a mathematical model. *Am. J. Physiol.* 275: H301–H321 (1998).

[29] **Davidenko, J.M., Pertsov, A.M., Salomonsz, R., Baxter, W. & Jalife, J.** Stationary and drifting spiral waves of excitation in isolated cardiac muscle. *Nature* 355: 349–351 (1992).

[30] **DiFrancesco, D. & Noble, D.** A model of cardiac electrical activity incorporating ionic pumps and concentration changes. *Phil. Trans. Roy. Soc. Lond.* 307: 353–398 (1985).

[31] **Epstein, A.E.** Ventricular fibrillation. In *Cardiac electrophysiology. From cell to bedside, 4th edition*, edited by D. P. Zipes & J. Jalife, pp. 705–710. Saunders, Philadelphia (2004).

[32] **Fenton, F., Cherry, E.M., Hastings, H.M. & Evans, S.J.** Multiple mechanisms of spiral wave breakup in a model of cardiac electrical activity. *Chaos* 12: 852–892 (2002).

[33] **Fenton, F. & Karma, A.** Vortex dynamics in three-dimensional continuous myocardium with fiber rotation: filament instability and fibrillation. *Chaos* 8: 20–47 (1998).

[34] **FitzHugh, R.** Impulses and physiological states in theoretical models of nerve membrane. *Biophys. J.* 1: 445–465 (1961).

[35] **Franz, M.R., Cima, R., Wang, D., Profitt, D. & Kurz, R.** Electrophysiological effects of myocardial stretch and mechanical determinants of stretch-activated arrhythmias. *Circulation.* 86: 968–978 (1992).

[36] **Garfinkel, A., Kim, Y.H., Voroshilovsky, O., Qu, Z., Kil, J.R., Lee, M.H., Karagueuzian, H. S., Weiss, J.N. & Chen, P.S.** Preventing ventricular fibrillation by flattening cardiac restitution. *Proc. Natl. Acad. Sci. U.S.A.* 97: 6061–6066 (2000).

[37] **Garfinkel, A. & Qu, Z.** Nonlinear dynamics of excitation and propagation in cardiac tissue. In *Cardiac electrophysiology. From cell to bedside, 3rd edition*, edited by D. P. Zipes & J. Jalife, pp. 315–320. Saunders, Philadelphia (1999).

[38] **Garny, A. & Kohl, P.** Mechanical induction of arrhythmias during ventricular repolarization: modeling cellular mechanisms and their interaction in two dimensions. *Ann. N. Y. Acad. Sci.* 1015: 133–143 (2004).

[39] **Geerts, L., Bovendeerd, P.H.M., Nicolay, K. & Arts, T.** Characterization of normal cardiac myofiber field in goat measured with MR-diffusion tensor imaging. *Am. J. Physiol. Heart Circ. Physiol.* 283: H139–H145 (2002).

[40] **Gerish, G.** Standienpezifische aggregationsmuster bei distyostelium discoideum. *Wihelm Roux Arch. Entwick Org* 156: 127–144 (1965).

[41] **Girouard, S.D., Pastore, J.M., Laurita, K.R., Gregory, K.W. & Rosenbaum, D.S.** Optical mapping in a new guinea pig model of ventricular tachycardia reveals mechanisms for multiple wavelengths in a single reentrant circuit. *Circulation* 93: 603–613 (1996).

[42] **Gorelova, N.A. & Bures, J.J.** Spiral waves of spreading depression in the isolated chicken retina. *J. Neurobiol.* 14: 353–363 (1983).

[43] **Gray, R.A. & Jalife, J.** Ventricular fibrillation and atrial fibrillation are two different beasts. *Chaos* 8: 65–78 (1998).

[44] **Gray, R.A., Jalife, J., Panfilov, A., Baxter, W.T., Cabo, C. & Pertsov, A.M.** Non-stationary vortex-like reentrant activity as a mechanism of polymorphic ventricular tachycardia in the isolated rabbit heart. *Circulation* 91: 2454–2469 (1995).

[45] **Gray, R.A., Pertsov, A.M. & Jalife, J.** Spatial and temporal organization during cardiac fibrillation. *Nature* 392: 75–78 (1998).

[46] **Green, A.E. & Adkins, J.E.** *Large Elastic Deformations.* 2nd Edition. Clarendon Press, Oxford, United Kingdom (1970).

[47] **Grill, S., Zykov, V.S. & Müller, S.C.** Feedback-controlled dynamics of meandering spiral waves. *Phys. Rev. Lett.* 75: 3368–3371 (1995).

[48] **Grindrod, P.** *Patterns and Waves: The Theory and Applications of Reaction-Diffusion Equations.* Clarendon Press, Oxford, United Kingdom (1991).

[49] **Guccione, J.M., McCulloch, A.D. & Waldman, L.K.** Passive material properties of intact ventricular myocardium determined from a cylindrical model. *J. Biomech. Eng.* 113: 42–55 (1991).

[50] **Guevara, M.R., Ward, A., Shrier, A. & Glass, L.** Electrical alternans and period doubling bifurcations. *IEEE Comp. Cardiol.* 562: 167–170 (1984).

[51] **Gurev, V., Maleckar, M.M. & Trayanova, N.A.** Cardiac defibrillation and the role of mechanoelectric feedback in postshock arrhythmogenesis. *Ann. N. Y. Acad. Sci.* 1080: 320–333 (2006).

[52] **Guyton, A.C. & Hall, J.E.** *Textbook of Medical Physiology,.* 9th Edition. Elsevier Health Sciences (1996).

[53] **Guyton, A.C. & Hall, J.E.** *Textbook of Medical Physiology.* 11th Edition. Elsevier Health Sciences (2005).

[54] **Haissaguerre, M., Shah, D.C., Jais, P., Shoda, M., Kautzner, J., Arentz, T., Kalushe, D., Kadish, A., Griffith, M., Gaita, F., Yamane, T., Garrigue, S., Hocini, M. & Clementy, J.** Role of Purkinje conducting system in triggering of idiopathic ventricular fibrillation. *Lancet* 359: 677–678 (2002).

[55] **Hansen, D.E., Borganelli, M., Stacy, Jr, G.P. & Taylor, L.K.** Dose-dependent inhibition of stretch-induced arrhythmias by gadolinium in isolated canine ventricles. Evidence for a unique mode of antiarrhythmic action. *Circ. Res.* 69: 820–831 (1991).

[56] **Haws, C.W. & Lux, R.L**. Correlation between in vivo transmembrane action potential durations and activation-recovery intervals from electrograms. Effects of interventions that alter repolarization time. *Circulation* 81: 281–88 (1990).

[57] **Herrmann, C., Houadjeto, M., Travers, F. & Barman, T.** Early steps of the Mg^{2+}-ATPase of relaxed myofibrils. A comparison with Ca^{2+}-activated myofibrils and myosin subfragment 1. *Biochemistry.* 31: 8036–8042 (1992).

[58] **Hill, A.V.** Excitation and accommodation in nerve. *Proc. R. Soc. Lond.* 119: 305–355 (1936).

[59] **Hodgkin, A.L. & Huxley, A.F.** A quantitative description of membrane current and its application to conduction and excitation in nerve. *J.Physiol* 117: 500–544 (1952).

[60] **Hren, R.** *A realistic model of the human ventricular myocardium: Application of the study of ectopic activation.* PhD thesis, Dalhouse University, Halifax (1996).

[61] **Hu, H. & Sachs, F.** Stretch-activated ion channels in the heart. *J Mol Cell Cardiol.* 29: 1511–1523 (1997).

[62] **Huang, J., Rogers, J.M., Killingsworth, C.R., Sting, K.P., Smith, W.M. & Ideker, R.** Evolution of activation patterns during long-duration ventricular fibrillation in dogs. *Am J Physiol Heart Circ Physiol.* 101: H1139–1200 (2004).

[63] **Huang, J., Rogers, J.M., Killingsworth, C.R., Walcott, G.P., KenKnight, B.H., Smith, W.M. & Ideker, R.E.** Improvement of defibrillation efficacy and quantification of activation patterns during ventricular fibrillation in a canine heart failure model. *Circulation.* 103: 1473–1478 (2001).

[64] **Huang, J., Walcott, G.P., Killingsworth, C.R., Melnick, S.B., Rogers, J.M. & Ideker, R.E.** Quantification of activation patterns during ventricular fibrillation in open-chest porcine left ventricle and septum. *Heart Rhythm* 2: 720–728 (2005).

[65] **Hunter, P. & Nielsen, P.** A strategy for integrative computational physiology. *Physiology. (Bethesda).* 20: 316–325 (2005).

[66] **Hunter, P.J., McCulloch, A.D. & ter Keurs, H.E.** Modelling the mechanical properties of cardiac muscle. *Prog. Biophys. Mol. Biol.* 69: 289–331 (1998).

[67] **Hunter, P.J., Nash, M.P. & Sands, G.B.** Computational Electromechanics of the Heart. In *Computational Biology of the Heart*, edited by A.V. Panfilov & A.V. Holden, pp. 345–407. Wiley, Chichester, United Kingdom (1997).

[68] **Imbihl, R. & Ertl, G.** Oscillatory kinetics in heterogeneous catalysis. *Chem. Rev.* 95: 697–733 (1995).

[69] **Jalife, J.** Ventricular fibrillation: mechanisms of initiation and maintenance. *Annu. Rev. Physiol.* 62: 25–50 (2000).

[70] **Jalife, J., Berenfeld, O. & Mansour, M.** Mother rotors and fibrillatory conduction: a mechanism of atrial fibrillation. *Cardiovasc. Res.* 54: 204–216 (2002).

[71] **Jongsma, H.J. & Wilders, R.** Gap junctions in cardiovascular disease. *Circ. Res.* 86: 1193–1197 (2000).

[72] **Kay, M.W. & Rogers, J.M.** Epicardial rotors in panoramic optical maps of fibrillating swine ventricles. *Conf. Proc. IEEE. Eng. Med. Biol. Soc.* 1: 2268–2271 (2006).

[73] **Kay, M.W., Walcott, G.P., Gladden, J.D., Melnick, S.B. & Rogers, J.M.** Lifetimes of epicardial rotors in panoramic optical maps of fibrillating swine ventricles. *Am. J. Physiol. Heart Circ. Physiol.* 291: H1935–41 (2006).

[74] **Keener, J. & Sneyd, J.** *Mathematical physiology.* Springer-Verlag, New York, Heidelberg, Berlin (1998).

[75] **Keldermann, R.H., Nash, M.P. & Panfilov, A.V.** Pacemakers in a reaction diffusion mechanics systems. *J. Stat. Phys.* 128: 375–392 (2006).

[76] **Keldermann, R.H., Nash, M.P. & Panfilov, A.V.** Modeling cardiac mechano-electrical feedback using reaction-diffusion-mechanics systems. *Physica D* Accepted for Publication (2008).

[77] **Keldermann, R.H., Ten Tusscher, K.H., Nash, M.P., Hren, R., Taggart, P. & Panfilov, A.V.** Effect of heterogeneous APD restitution on VF organization in a model of the human ventricles. *Am. J. Physiol. Heart Circ. Physiol.* 294: H764–H774 (2008).

[78] **Kelly, D., Mackenzie, L., Hunter, P., Smaill, B. & Saint, D.A.** Gene expression of stretch-activated channels and mechanoelectric feedback in the heart. *Clin. Exp. Pharmacol. Physiol.* 33: 642–648 (2006).

[79] **Kerckhoffs, R.C.P., Healy, S.N., Usyk, T.P. & McCulloch, A.D.** Computational methods for cardiac electromechanics. *Proc. IEEE* 94(4): 769–783 (2006).

[80] **Kohl, P., Bollensdorff, C. & Garny, A.** Effects of mechanosensitive ion channels on ventricular electrophysiology: experimental and theoretical models. *Exp. Physiol.* 91(2): 307–321 (2006).

[81] **Kohl, P., Day, K. & Noble, D.** Cellular mechanisms of cardiac mechano-electric feedback in a mathematical model. *Can. J. Cardiol.* 14: 111–119 (1998).

[82] **Kohl, P., Franz, M.R. & Sachs, F.** *Cardiac Mechano-Electric Feedback and Arrhythmias.* Elsevier Health Sciences (2005).

[83] **Kohl, P., Hunter, P.J. & Noble, D**. Stretch-induced changes in heart rate and rhythm: Clinical observations, experiments and mathematical models. *Prog. Biophys. Molec. Biol.* 71: 91–138 (1999).

[84] **Kohl, P., Nesbitt, A.D., Cooper, P.J. & Lei, M.** Sudden cardiac death by commotio cordis: role of mechano-electric feedback. *Cardiovasc. Res.* 50: 280–289 (2001).

[85] **Kohl, P. & Ravens, U.** (editors). *Mechano-Electric Feedback and Cardiac Arrhythmias*, volume 82(1-3), pp. 1–266. Prog. Biophys. Molec. Biol., Elsevier Ltd (2003).

[86] **Krinsky, V.I.** Spread of excitation in an inhomogeneous medium (state similar to cardiac fibrillation). *Biofizika* 11: 776–784 (1966).

[87] **Kuijpers, N.H., Ten Eikelder, H.M., Bovendeerd, P.H., Verheule, S., Arts, T. & Hilbers, P.A.** Mechanoelectric feedback leads to conduction slowing and block in acutely dilated atria: a modeling study of cardiac electromechanics. *Am. J. Physiol. Heart Circ. Physiol.* 292: H2832–H2853 (2007).

[88] **Lab, M.J.** Transient depolarization and action potential alterations following mechanical changes in isolated myocardium. *Cardiovasc. Res.* 14: 624–637 (1980).

[89] **Lab, M.J.** Contraction-excitation feedback in myocardium. Physiological basis and clinical relevance. *Circ. Res.* 50: 757–766 (1982).

[90] **Lab, M.J.** Mechanoelectric feedback (transduction) in heart: concepts and implications. *Cardiovasc. Res.* 32: 3–14 (1996).

[91] **Lechleiter, J., Girard, S., Peralta, E. & Clapham., D.** Spiral calcium wave propagation and annihilation in Xenopus laevis oocytes. *Science* 252: 123–126 (1991).

[92] **LeGrice, I.J., Hunter, P.J. & Smaill, B.H.** Laminar structure of the heart: a mathematical model. *Am. J. Physiol.* 272: H2466–H2476 (1997).

[93] **LeGrice, I.J., Smaill, B.H., Chai, L.Z., Edgar, S.G., Gavin, J.B. & Hunter, P.J.** Laminar structure of the heart: ventricular myocyte arrangement and connective tissue architecture in the dog. *Am. J. Physiol.* 269: H571–H582 (1995).

[94] **Li, W., Kohl, P. & Trayanova, N.** Induction of ventricular arrhythmias following mechanical impact: a simulation study in 3D. *J. Mol. Histol.* 35: 679–686 (2004).

[95] **Li, W., Kohl, P. & Trayanova, N.** Myocardial ischemia lowers precordial thump efficacy: an inquiry into mechanisms using three-dimensional simulations. *Heart Rhythm* 3: 179–186 (2006).

[96] **Link, M.S., Wang, P.J., Pandian, N.G., Bharati, S., Udelson, J.E., Lee, M.Y., Vecchiotti, M.A., VanderBrink, B.A., Mirra, G., Maron, B.J. & Estes, N.A.** An experimental model of sudden death due to low-energy chest-wall impact (commotio cordis). *N. Engl. J. Med.* 338: 1805–1811 (1998).

[97] **Lucy, S.D., Jones, D.L. & Klein, G.J.** Pronounced increase in defibrillation threshold associated with pacing-induced cardiomyopathy in the dog. *Am. Heart J.* 127: 366–376 (1994).

[98] **Luo, C.H. & Rudy, Y.** A model of the ventricular cardiac action potential. Depolarization, repolarization, and their interaction. *Circ. Res.* 68: 1501–1526 (1991).

[99] **Luo, C.H. & Rudy, Y.** A dynamic model of the cardiac ventricular action potential. I. Simulations of ionic currents and concentration changes. *Circ. Res.* 74: 1071–1096 (1994).

[100] **Madias, C., Maron, B.J., Weinstock, J., Estes, N.A.M. & Link, M.S.** Commotio cordis: sudden cardiac death with chest wall impact. *J. Cardiovasc. Electrophysiol.* 18: 115–122 (2007).

[101] **Malvern, L.E.** *Introduction to the Mechanics of a Continuous Medium*. Prentice Hall, Englewood Cliffs (1969).

[102] **Masse, S., Downar, E., Chauhan, V., Sevaptsidis, E. & Nanthakumar, K.** Ventricular fibrillation in myopathic human hearts: mechanistic insights from in vivo global endocardial and epicardial mapping. *Am. J. Physiol. Heart Circ. Physiol.* 292: H2589–H2597 (2007).

[103] **McCulloch, A.D., Smaill, B.H. & Hunter, P.J.** Left ventricular epicardial deformation in the isolated arrested dog heart. *Am. J. Physiol.* 252: H233–H241 (1987).

[104] **Mikhailov, A.S., Zanette, D.H., Zhai, Y.M., I.Z., Kiss & Hudson, J.L.** Cooperative action of coherent groups in broadly heterogeneous populations of interacting chemical oscillators. *Proc. Natl. Acad. Sci. U.S.A.* 101: 10890–10894 (2004).

[105] **Moe, G.K.** On the multiple wavelet hypothesis of atrial fibrillation. *Arch. Int. Pharmacodyn. Ther.* 140: 183–188 (1962).

[106] **Moe, G.K., Rheinbolt, W.C. & Abildskov, J.A.** A computer model of atrial fibrillation. *Am. Heart J.* 67: 200–220 (1964).

[107] **Moreno, J., Zaitsev, A.V., Warren, M., Berenfeld, O., Kalifa, J., Lucca, E., Mironov, S., P., Guha. & Jalife, J.** Effect of remodelling, stretch and ischaemia on ventricular fibrillation frequency and dynamics in a heart failure model. *Cardiovasc. Res.* 65: 158–166 (2005).

[108] **Morgan, J.M., Cunningham, D. & Rowland, E.** Dispersion of monophasic action potential duration: demonstrable in humans after premature ventricular extrastimulation but not in steady state. *J. Am. Coll. Cardiol.* 19: 1244–1253 (1992).

[109] **Muñuzuri, A.P., Innocenti, C., Flesselles, J., Gilli, J., Agladze, K.I. & Krinsky, V.I.** Elastic excitable medium. *Phys. Rev. E* 50: R667–R670 (1994).

[110] **Murray, J.D.** *Mathematical Biology.* 3rd Edition. Springer (2002).

[111] **Nanthakumar, K., Jalife, J., Masse, S., Downar, E., Pop, M., Asta, J., Ross, H., Rao, V., Mironov, S., Sevaptsidis, E., Rogers, J., Wright, G. & Dhopeshwarkar, R.** Optical mapping of Langendorff-perfused human hearts: establishing a model for the study of ventricular fibrillation in humans. *Am. J. Physiol. Heart Circ. Physiol.* 293: H875–H880 (2007).

[112] **Nanthakumar, K., Walcott, G.P., Melnick, S., Rogers, J.M., Kay, M.W., Smith, W.M., Ideker, R.E. & Holman, W.** Epicardial organization of human ventricular fibrillation. *Heart Rhythm* 1: 14–23 (2004).

[113] **Nash, M.P.** *Mechanics and Material Properties of the Heart using an Anatomically Accurate Mathematical model.* PhD thesis, University of Auckland, New Zealand (1998).

[114] **Nash, M.P., Bradley, C.P., Sutton, P.M., Clayton, R.H., Kallis, P., Hayward, M.P., Paterson, D.J. & Taggart, P.** Whole heart action potential duration restitution properties in cardiac patients: a combined clinical and modelling study. *Exp. Physiol.* 91: 339–354 (2006).

[115] **Nash, M.P. & Hunter, P.J.** Computational mechanics of the heart: from tissue structure to ventricular function. *J. Elasticity* 61: 113–141 (2000).

[116] **Nash, M.P., Mourad, A., Clayton, R.H., Sutton, P.M., Bradley, C.P., Hayward, M., Paterson, D.J. & Taggart, P.** Evidence for multiple mechanisms in human ventricular fibrillation. *Circulation* 114: 536–42 (2006).

[117] **Nash, M.P. & Panfilov, A.V.** Electromechanical model of excitable tissue to study reentrant cardiac arrhythmias. *Prog. Biophys. Mol. Biol.* 85: 501–522 (2004).

[118] **Nickerson, D.P., Nash, M.P., Nielsen, P.M.F., Smith, N.P. & Hunter, P.J.** Computational multiscale modeling in the physiome project: modeling cardiac electromechanics. *IBM J. Res. Dev.* 50: 617–630 (2006).

[119] **Niederer, S.A., Hunter, P.J. & Smith, N.P.** A quantitative analysis of cardiac myocyte relaxation: a simulation study. *Biophys. J.* 90: 1697–1722 (2006).

[120] **Niederer, S.A. & Smith, N.P.** An improved numerical method for strong coupling of excitation and contraction models in the heart. *Prog. Biophys. Mol. Biol.* 96: 90–111 (2008).

[121] **Nielsen, P. M., Le Grice, I. J., Smaill, B. H. & Hunter, P. J.** Mathematical model of geometry and fibrous structure of the heart. *Am. J. Physiol.* 260: H1365–H1378 (1991).

[122] **Noble, D.** A modification of the Hodgkin−Huxley equation applicable to Purkinje fiber action and pacemaker potential. *J. Physiol.* 160: 317–352 (1962).

[123] **Noble, D. & Rudy, Y.** Models of cardiac ventricular action potentials: Iterative interaction between experiment and simulation. *Phil. Trans. Roy. Soc. Lond.* 359(1783): 1127–1142 (2001).

[124] **Noble, D., Varghese, A., Kohl, P. & Noble, P.** Improved guinea-pig ventricular model incorporating diadic space, I_{kr} and I_{ks}, length and tension-dependent processes. *Can. J. Cardiol.* 14: 123–134 (1998).

[125] **Nolasco, J.B. & Dahlen, R.W.** A graphic method for the study of alternation in cardiac action potentials. *J. Appl. Physiol.* 25: 191–196 (1968).

[126] **Ouyang, F., Cappato, R., Ernst, S., Goya, M., Volkmer, M., Hebe, J., Antz, M., Vogtmann, T., Schaumann, A., Fotuhi, P., Hoffmann-Riem, M. & Kuck, K.H.** Electroanatomic substrate of idiopathic left ventricular tachycardia: unidirectional block and macroreentry within the purkinje network. *Circulation.* 105: 462–469 (2002).

[127] **Panfilov, A.V.** Three-dimensional organization of electrical turbulence in the heart. *Phys. Rev. E* 59: R6251–R6254 (1999).

[128] **Panfilov, A.V. & Holden, A.V.** Self-generation of turbulent vortices in a two-dimensional model of cardiac tissue. *Phys. Lett. A* 147: 463–466 (1990).

[129] **Panfilov, A.V., Keldermann, R.H. & Nash, M.P.** Self-organized pacemakers in a coupled reaction-diffusion-mechanics system. *Phys. Rev. Lett.* 95: 258104 (2005).

[130] **Panfilov, A.V., Keldermann, R.H. & Nash, M.P.** Drift and breakup of spiral waves in reaction-diffusion-mechanics systems. *Proc. Natl. Acad. Sci. U.S.A.* 104: 7922–7926 (2007).

[131] **Panfilov, A.V. & Pertsov, A.M.** Ventricular fibrillation: evolution of the multiple wavelet hypothesis. *Phil. Trans. Roy. Soc. Lond. A.* 359: 1315–1325 (2001).

[132] **Pertsov, A.M., Davidenko, J.M., Salomontsz, R., Baxter, W. & Jalife, J.** Spiral waves of excitation underlie reentrant activity in isolated cardiac muscle. *Circ. Res.* 72: 631–650 (1993).

[133] **Pinto, J.M. & Boyden, P.A.** Electrical remodeling in ischemia and infarction. *Cardiovasc. Res.* 42: 284–297 (1999).

[134] **Piroddi, N., Belus, A., Scellini, B., Tesi, C., Giunti, G., Cerbai, E., Mugelli, A. & Poggesi, C.** Tension generation and relaxation in single myofibrils from human atrial and ventricular myocardium. *Pflügers Arch.* 454: 63–73 (2007).

[135] **Plonsey, R. & Barr, R.C.** *Bioelectricity.* Plenum Publishing Corporation, NY (1989).

[136] **Pool, R**. Heart like a wheel. *Science* 247: 1294–1295 (1990).

[137] **Pruvot, E.J. Katra, R.P., Rosenbaum, D.S. & Kaurita, K.R.** Role of calcium cycling versus restitution in the mechanism of repolarization alternans. *Circ. Res.* 94: 1083–1090 (2004).

[138] **Qu, Z., Garfinkel, A., Chen, P.S. & Weiss, J.N.** Mechanisms of discordant alternans and induction of reentry in simulated cardiac tissue. *Circulation.* 102: 1664–70 (2000).

[139] **Qu, Z. & Weiss, J.N.** The chicken or the egg? Voltage and calcium dynamics in the heart. *Am. J. Physiol. Heart Circ. Physiol.* 293: H2054–2055 (2007).

[140] **Qu, Z., Weiss, J.N. & Garfinkel, A.** Cardiac electrical restitution properties and stability of reentrant spiral waves: a simulation study. *Am. J. Physiol.* 276: H269–H283 (1999).

[141] **Riemer, T.L., Sobie, E.A. & Tung, L.** Stretch-induced changes in arrhythmogenesis and excitability in experimentally based heart cell models. *Am. J. Physiol.* 275: H431–H442 (1998).

[142] **Riemer, T.L. & Tung, L.** Stretch-induced excitation and action potential changes of single cardiac cells. *Prog. Biophys. Mol. Biol.* 82: 97–110 (2003).

[143] **Rodriguez, E.K., Hunter, W.C., Royce, M.J., Leppo, M.K., Douglas, A.S. & Weisman, H.F.** A method to reconstruct myocardial sarcomere lengths and orientations at transmural sites in beating canine hearts. *Am. J. Physiol.* 263: H293–H306 (1992).

[144] **Rogers, J.** Combined phase singularity and wavefront analysis for optical maps of ventricular fibrillation. *IEEE Trans. Biomed. Eng.* 92: 56–65 (2004).

[145] **Rogers, J., Huang, J., Melnick, S.B. & Ideker, R.E.** Sustained reentry in the left ventricle of fibrillating pig hearts. *Circ. Res.* 92: 539–545 (2003).

[146] **Rogers, J., Huang, J., Smith, W.M. & Ideker, R.E.** Incidence, evolution and spatial distribution of functional reentry during ventricular fibrillation in pigs. *Circ. Res.* 84: 945–954 (1999).

[147] **Roth, B.J. & Wikswo, J.P.** A bidomain model for the extracellular potential and magnetic filed of cardiac tissue. *IEEE Trans. Biomed. Eng.* 33: 467–469 (1985).

[148] **Rudy, Y. & Silva, J.R.** Computational biology in the study of cardiac ion channels and cell electrophysiology. *Q. Rev. Biophys.* 39: 57–116 (2006).

[149] **Rush, S. & Larsen, H.** A practical algorithm for solving dynamic membrane equations. *IEEE Trans. Biomed. Eng.* 25: 389–392 (1978).

[150] **Sachs, F.** Molecular Transduction in Cardiac Electrophysiology. In *From Cell to Bedside*, edited by D.P. Zipes & J. Jalife, pp. 96–102. 4th Edition. Saunders, Philadelphia, United States (1995).

[151] **Saeki, Y., Kobayashi, T., Yasuda, S., Nishimura, S., Sugiura, S., Yamashita, H. & Sugi, H.** Role of Ca^{2+} in determining the rate of tension development and relaxation in rat skinned myocardium. *J. Mol. Cell Cardiol.* 36: 371–380 (2004).

[152] **Samie, F.H., Berenfeld, O., Anumonwo, J., Mironov, S.F., Udassi, S., Beaumont, J., Taffet, S., Pertsov, A.M. & Jalife, J.** Rectification of the background potassium current: a determinant of rotor dynamics in ventricular fibrillation. *Circ. Res.* 89: 1216–1223 (2001).

[153] **Samie, F.H. & Jalife, J.** Mechanisms underlying ventricular tachycardia and its transition to ventricular fibrillation in the structurally normal heart. *Cardiovasc. Res.* 50: 242–250 (2001).

[154] **Sbrana, F., Sassoli, C., Meacci, E., Nosi, D., Squecco, R., Paternostro, F., Tiribilli, B., Zecchi-Orlandini, S., Francini, F. & Formigli, L.** Role for stress fiber contraction in surface tension development and stretch-activated channel regulation in C2C12 myoblasts. *Am. J. Physiol. Cell Physiol.* 295: C160–C172 (2008).

[155] **Schmid, H., O'Callaghan, P., Nash, M.P., Lin, W., Legrice, I.J., Smaill, B.H., Young, A.A. & Hunter, P.J.** Myocardial material parameter estimation : A non-homogeneous finite element study from simple shear tests. *Biomech. Model. Mechanobiol.* 7: 161–173 (2008).

[156] **Selfridge, O.** Studies on flutter and fibrillation. Some notes on the theory of flutter. *Arch. Inst. Cardiol. Mex.* 18: 177–187 (1948).

[157] **Shiels, H.A. & White, E.** The Frank-Starling mechanism in vertebrate cardiac myocytes. *J. Exp. Biol.* 211: 2005–2013 (2008).

[158] **Shiferaw, Y., Watanabe, M.A., Garfinkel, A., Weiss, J.N. & Karma, A.** Model of intracellular calcium cycling in ventricular myocytes. *Biophys. J.* 85: 3666–3686 (2003).

[159] **Shimizu, W. & Antzelevitch, C.** Cellular and ionic basis for T-wave alternans under long-QT conditions. *Circulation.* 99: 1499–1507 (1999).

[160] **Sigurdson, W., Ruknudin, A. & Sachs, F.** Calcium imaging of mechanically induced fluxes in tissue-cultured chick heart: Role of stretch-activated ion channels. *Am. J. Physiol.* 262: H1110–H1115 (1992).

[161] **Smaill, B.H. & Hunter, P.J.** Structure and Function of the Diastolic Heart: Material Properties of Passive Myocardium. In *Theory of Heart: Biomechanics, Biophysics and Non-Linear Dynamics of Cardiac Function*, edited by L. Glass, P.J. Hunter & A.D. McCulloch, pp. 1–29. Springer, New York, United Stated (1991).

[162] **Spach, M.S. & Heidlage, J.F.** The stochastic nature of cardiac propagation at a microscopic level. electrical description of myocardial architecture and its application to conduction. *Circ. Res.* 76: 366–380 (1995).

[163] **Spencer, A.J.M.** *Continuum Mechanics.* Longman Group Limited, London, United kingdom (1980).

[164] **Stevens, C.** *An anatomically based computational study of cardiac mechanics and myocardial infarction.* PhD thesis, University of Auckland, New Zealand (2002).

[165] **Stich, M., Ipsen, M. & Mikhailov, A.S.** Self-organized stable pacemakers near the onset of birhythmicity. *Phys. Rev. Lett.* 86: 4406–4409 (2001).

[166] **Streeter, D.D.** Gross morphology of the heart. In *Handbook of Physiology, Section 2: The Cardiovascular System, Volume 1: The Heart*, edited by R.M. Berne & N. Sperelakis, pp. 61–112. Bethesda, American Physiology Society (1979).

[167] **Taggart, P., Sutton, P.M., Opthof, T., Coronel, R., Trimlett, R., Pugsley, W. & Kallis, P.** Inhomogeneous transmural conduction during early ischaemia in patients with coronary artery disease. *J. Mol. Cell Cardiol.* 32: 621–630 (2000).

[168] **Ten Tusscher, K. H. & Panfilov, A. V.** Modelling of the ventricular conduction system. *Prog. Biophys. Mol. Biol.* 96: 152–170 (2008).

[169] **Ten Tusscher, K.H.** *Spiral wave dynamics and ventricular arrhythmias.* PhD thesis, Utrecht University, Utrecht (2004).

[170] **Ten Tusscher, K.H., Hren, R. & Panfilov, A.V.** Organization of ventricular fibrillation in the human heart. *Circ. Res.* 100: e87–101 (2007).

[171] **Ten Tusscher, K.H., Noble, D., Noble, P.J. & Panfilov, A.V.** A model for human ventricular tissue. *Am. J. Physiol. Heart Circ. Physiol.* 286: H1573–H1589 (2004).

[172] **Ten Tusscher, K.H., Noble, D., Noble, P.J. & Panfilov, A.V.** A model for human ventricular tissue. *Am. J. Physiol. Heart Circ. Physiol.* 286: H1573–H1589 (2004).

[173] **Ten Tusscher, K.H. & Panfilov, A.V.** Influence of nonexcitable cells on spiral breakup in two-dimensional and three-dimensional excitable media. *Phys. Rev. E* 68: 062902–1–062902–4 (2003).

[174] **Ten Tusscher, K.H. & Panfilov, A.V.** Alternans and spiral breakup in a human ventricular tissue model. *Am. J. Physiol. Heart Circ. Physiol.* 291: H1088–100 (2006).

[175] **Ter Keurs, H.E., Rijnsburger, W.H., Van Heuningen, R. & Nagelsmit, M.J.** Tension development and sarcomere length in rat cardiac trabeculae. Evidence of length-dependent activation. *Circ. Res.* 46: 703–714 (1980).

[176] **Ter Keurs, H.E., Shinozaki, T., Zhang, Y.M., Zhang, M.L., Wakayama, Y., Sugai, Y., Kagaya, Y., Miura, M., Boyden, P.A., Stuyvers, B.D. & Landesberg, A.** Sarcomere mechanics in uniform and non-uniform cardiac muscle: A link between pump function and arrhythmias. *Prog. Biophys. Mol. Biol.* 97: 312–331 (2008).

[177] **Trayanova, N., Li, W., Eason, J. & Kohl, P.** Effect of stretch activated channels on defibrillation efficacy. *Heart Rhythm* 1: 67–77 (2004).

[178] **Valderrabano, M., Chen, P. & Lin, S.F.** Spatial distribution of phase singularities in ventricular fibrillation. *Circulation* 108: 354–359 (2003).

[179] **Van Der Velden, J., Klein, L.J., Zaremba, R., Boontje, N.M., Huybregts, M.A., Stooker, W., Eijsman, L., De Jong, J.W., Visser, C.A., Visser, F.C. & Stienen, G.J.** Effects of calcium, inorganic phosphate, and pH on isometric force in single skinned cardiomyocytes from donor and failing human hearts. *Circulation.* 104: 1140–1146 (2001).

[180] **Vaquero, M., Calvo, D. & Jalife, J.** Cardiac fibrillation: from ion channels to rotors in the human heart. *Heart Rhythm* 5: 872–879 (2008).

[181] **Vetter, F.J. & McCulloch, A.D.** Mechanoelectric feedback in a model of the passively inflated left ventricle. *Ann Biomed Eng.* 29: 414–426 (2001).

[182] **Vigh, A., Lowder, J. & Deantonio, H.** Does acute volume overloading in the setting of left ventricular dysfunction and pulmonary hypertension affect the defibrillation threshold? *Pacing. Clin. Electrophysiol.* 22: 759–764 (1999).

[183] **Weijer, C.J.** Dictyostelium morphogenesis. *Curr Opin Genet Dev.* 14: 392–398 (2004).

[184] **Weiss, J.N., Garfinkel, A., Karagueuzian, H.S., Qu, Z. & Chen, P.S.** Chaos and the transition to ventricular fibrillation: a new approach to antiarrhythmic drug evaluation. *Circulation.* 99: 2819–2826 (1999).

[185] **Weiss, J.N., Karma, A., Shiferaw, Y., Chen, P.S., Garfinkel, A. & Qu, Z.** From pulsus to pulseless: the saga of cardiac alternans. *Circ. Res.* 98: 1244–1253 (2006).

[186] **Whiteley, J.P., Bishop, M.J. & Gavaghan, D.J.** Soft tissue modelling of cardiac fibres for use in coupled mechano-electric simulations. *Bull. Math. Biol.* 69: 2199–2225 (2007).

[187] **Wiener, N. & Rosenblueth, A.** The mathematical formulation of the problem of conduction of impulses in a network of connected excitable elements, specifically in cardiac muscle. *Arch. Inst. Cardiol. Mex.* 16: 205–265 (1946).

[188] **Winfree, A.T.** *The Geometry of Biological Time*. Springer, New York, USA (1980).

[189] **Winfree, A.T. & Strogatz, S.H.** Organizing centers for three-dimensional chemical waves. *Nature* 311: 611–615 (1984).

[190] **Witkowski, F.X., Leon, L.J., Penkoske, P.A., Giles, W.R., Spano, M.L., Ditto, E.L. & Winfree, A.T.** Spatiotemporal evolution of ventricular fibrillation. *Nature* 392: 78–82 (1998).

[191] **Wolff, M.R., Buck, S.H., Stoker, S.W., Greaser, M.L. & Mentzer, R.M.** Myofibrillar calcium sensitivity of isometric tension is increased in human dilated cardiomyopathies: role of altered β-adrenergically mediated protein phosphorylation. *J. Clin. Invest.* 98: 167–176 (1996).

[192] **Wu, T., Lin, S., Weiss, J.N., Ting, C. & Chen, P.** Two types of ventricular fibrillation in isolated rabbit hearts. *Circulation* 106: 1859–1866 (2002).

[193] **Wu, T.J., Lin, S.F., Baher, A., Qu, Z., Garfinkel, A., Weiss, J.N., Ting, C.T. & Chen, P.S.** Mother rotors and the mechanisms of D600-induced type 2 ventricular fibrillation. *Circulation.* 110: 2110–2118 (2004).

[194] **Wu, T.J., Ong, J.J., Hwang, C., Lee, J.J., Fishbein, M.C., Czer, L., Trento, A., Blanche, C., Kass, R.M., Mandel, W.J., Karagueuzian, H.S. & Chen, P.S.** Characteristics of wave fronts during ventricular fibrillation in human hearts with dilated cardiomyopathy: role of increased fibrosis in the generation of reentry. *J. Am. Coll. Cardiol.* 32: 187–196 (1998).

[195] **Wu, T.J., Ong, J.J.C., Hwang, C., Lee, J.J., Fishbein, M.C., Czer, L., Tento, A., Blanche, C., Kass, R.M., Mandel, W.J., Karagueuzuan, H.S. & Chen, P.** Characteristics of wave fronts during ventricular fibrillation in human hearts with dilated cardiomyopathy: Role of increased fibrosis on the generation of reentry. *J. Am. Coll. Cardiol.* 32: 187–196 (1998).

[196] **Xie, F., Qu, Z., Garfinkel, A. & Weiss, J.N.** Electrophysiological heterogeneity and stability of reentry in simulated cardiac tissue. *Am. J. Physiol. Heart Circ. Physiol.* 280: H535–H545 (2001).

[197] **Yoshida, R., Takahashi, T., Yamaguchi, T. & Ichijo, H.** Self-oscillating gel. *J. Am. Chem. Soc.* 118: 5134–5135 (1996).

[198] **Yue, A.M., Franz, M.R., Roberts, P.R. & Morgan, J.M.** Global endocardial electrical restitution in human right and left ventricles determined by noncontact mapping. *J. Am. Coll. Cardiol.* 46: 1067–75 (2005).

[199] **Zaikin, A.N. & Zhabotinsky, A.M.** Concentration wave propagation in two-dimensional liquid-phase self-organising system. *Nature* 225: 535–537 (1970).

[200] **Zaitsev, A.V., Berenfeld, O., Mironov, S.F., Jalife, J. & Pertsov, A.M.** Distribution of excitation frequencies on the epicardial and endocardial surfaces of fibrillating ventricular wall of the sheep heart. *Circ. Res.* 86: 408–417 (2000).

[201] **Zeng, T., Bett, G.C. & Sachs, F.** Stretch-activated whole cell currents in adult rat cardiac myocytes. *Am. J. Physiol. Heart Circ. Physiol.* 278: H548–H557 (2000).

[202] **Zevitz, M.E.** Ventricular fibrillation [online]. *eMedicine* http://www.emedicine.com/med/topic2363.htm (2004).

[203] **Zhang, H., Holden, A.V., Kodama, I., Honjo, H., Lei, M., Varghese, T. & Boyett, M.R.** Mathematical models of action potentials in the periphery and center of the rabbit sinoatrial node. *Am J Physiol Heart Circ Physiol* 279: H397–H421 (2000).

[204] **Zheng, Z.J., Croft, J.B., Giles, W.H. & Mensah, G.A.** Sudden cardiac death in the United States, 1989 to 1998. *Circulation* 104: 2158–2163 (2001).

[205] **Zykov, V.S.** *Simulation of Wave Processes in Excitable Media.* Manchester University Press, Manchester, United Kingdom (1987).

Nederlandse Samenvatting

Introductie

Het hart is een holle spier die door samen te trekken ervoor zorgt dat het bloed door het lichaam wordt gepompt. Het menselijk hart trekt ongeveer een keer per seconde samen, wat uiteindelijk resulteert in meer dan 2.5 biljoen samentrekkingen in 80 jaar. Als het hart niet goed meer samen trekt kan het bloed niet meer door het lichaam gepompt worden en zal na een paar minuten de dood intreden. De aandoening waarbij het hart niet meer in staat is om voldoende bloed uit te pompen om aan de behoeften van de weefsels te voldoen wordt hartfalen genoemd. In de westerse wereld is hartfalen een van de meest voorkomende doodsoorzaken en in de meeste gevallen gaat het om een hartritmestoornis genaamd ventrikelfibrilleren (ook wel kamerfibrilleren of VF genoemd). Tijdens VF kunnen de kamers van het hart niet meer gecoördineerd samentrekken, waardoor er geen pompfunctie meer is. De enige manier om dit te behandelen is door een elektrische schok toe te dienen aan het hart.

In dit proefschrift onderzoeken we mechanismen van VF door middel van numerieke simulaties van wiskundige modellen die de eigenschappen van het hartweefsel beschrijven. In de laatste decennia zijn veel wiskundige modellen ontwikkeld om onderzoek te doen naar hartritmestoornissen. Deze modellen variëren van modellen die de eigenschappen van een enkele hartcel beschrijven tot complexe drie-dimensionale orgaan modellen. We zijn met name geïnteresseerd in de terugkoppeling van de vervorming van het hart op het elektrische geleidingssysteem. Verder onderzoeken we ook het effect van elektrische weefselheterogeniteit op het ontstaan en de organisatie van VF.

Het Hart

Het hart wordt aangestuurd door een pompgedeelte en een elektrisch gedeelte, die nauw met elkaar verbonden zijn, maar functioneel onderscheiden moeten worden. Het hart is een holle spier bestaande uit twee boezems (de atria) en twee kamers (de ventrikels). De rechter boezem ontvangt zuurstofarm bloed van het lichaam, en de linker boezem ontvangt zuurstofrijk bloed van de longen. De functie van de boezems is om het bloed te pompen naar de kamers. De rechter kamer pompt zuurstofarm bloed naar de longen toe, en de linker kamer pompt zuurstofrijk bloed via de aorta naar de rest van het lichaam. Voor een effectieve pompwerking van het hart is het belangrijk dat zowel de boezems als de kamers gecoördineerd samentrekken. Onder normale omstandigheden wordt de timing van samentrekken van individuele hartcellen gereguleerd door een voorafgaand elektrisch signaal (ook wel actiepotentiaal of excitatie genoemd). De actiepotentiaal wordt gevormd door ion-stromen die door ion-kanalen gelegen in het celmembraan van een hartspiercel lopen, en geeft een signaal aan de hartspiercel om samen te trekken.

In de wand van de rechter boezem ligt een klein stukje weefsel met speciale hartcellen die spontaan een actiepotentiaal met een bepaalde frequentie genereren. Dit wordt de sinusknoop genoemd. Onder normale omstandigheden kunnen hartspiercellen alleen een actiepotentiaal genereren als deze gestimuleerd worden door een elektrisch stroompje afkomstig van een buurcel. Van de sinusknoop plant het elektrisch signaal zich voort naar de rest van het hartweefsel. Als eerste worden de boezems geëxciteerd, met als gevolg dat deze samentrekken en het bloed naar de kamers gepompt wordt. Vervolgens plant het signaal zich met een kleine vertraging voort naar de kamers en zullen deze samentrekken en het bloed naar de longen en de rest van het lichaam pompen.

Het samentrekken van het hart heeft ook invloed op de vorm en de eigenschappen van de actiepotentiaal. Dit wordt mechano-elektrische terugkoppeling genoemd. In hartcellen zijn speciale ion-kanalen aanwezig die open gaan op het moment dat een cel uitrekt (stretch), met als gevolg dat de eigenschappen van de actiepotentiaal veranderden. Deze ion-kanalen heten stretch-geactiveerde kanalen en kunnen belangrijke zijn in het ontstaan van hartritmestoornissen.

Hartritmestoornissen

Een hartritmestoornis is een situatie waarbij het hart niet meer met een regelmatige frequentie kan samentrekken. De hartslag van een volwassen persoon in rust ligt tussen de 60-100 slagen per minuut. Bij meer dan 100 slagen per minuut wordt gesproken van een tachycardie en bij meer dan 250 slagen per minuut wordt gesproken van fibrillatie. Echter tijdens fibrillatie zullen de boezems of de kamers ongecoördineerd samentrekken met als gevolg dat de pompwerking van het hart verstoord wordt. Hartritmestoornissen in de kamers zijn gevaarlijker omdat deze meestal overgaan in ventrikelfibrilleren met als gevolg dat het bloed niet meer rondgepompt wordt door het lichaam. In de meeste hartritmestoornissen is een verstoring in de voortgeleiding van de actiepotentiaal de oorzaak voor afwijkin-

gen in het samentrekken van het hart. Mechano-elektrische terugkoppeling en weefselheterogeniteit spelen hierbij dan ook een belangrijke rol.

Veel hartritmestoornissen worden gedreven door *cirkelgeleiding* (ook wel reentry genoemd). Tijdens reentry draait de actiepotentiaal met een hoge frequentie rond in een cirkel, waarbij de kop van het signaal voortdurend de staart volgt. In twee en drie-dimensionale weefsels kan een actiepotentiaal ronddraaien om een niet-geleidend anatomisch obstakel waardoor er een golf ontstaat in de vorm van een spiraal. Spiralen kunnen ook roteren rondom hun eigen kern. Spiralen roteren met een hoge frequentie en het bijzondere van deze golven is dat ze niet zoals een normale actiepotentiaal golf maar een keer langskomen, maar steeds opnieuw het weefsel exciteren. Als een spiraal ontstaat in de kamers dan wordt het samentrekken van het hart niet meer bepaald door het initiële signaal van de sinusknoop, maar door de spiraal golf. De hoge frequentie van deze spiraal golven leidt dan ook tot hogere frequenties van samentrekken. Tijdens een tachycardie is er maar een spiraal golf aanwezig, terwijl tijdens fibrillatie er meerdere spiraal golven tegelijkertijd aanwezig zijn. Deze spiralen botsen voortdurend op elkaar en fragmenteren in nieuwe spiralen met als gevolg dat er chaotische patronen ontstaan en het hart niet meer gecoördineerd kan samentrekken.

In de kamers zal een enkele spiraal meestal opbreken in kleinere (chaotische) spiralen. Weefsel heterogeniteit en actiepotentiaal eigenschappen spelen hierbij een belangrijke rol. Bepaalde hartziekten, maar ook ouderdom, kunnen ervoor zorgen dat er structurele en elektrische veranderingen optreden met als gevolg dat de heterogeniteit in weefseleigenschappen toe neemt. Hierdoor neemt ook de kans toe om een hartritmestoornis te krijgen.

In dit proefschrift onderzoeken we twee typen van ventrikelfibrilleren. Het eerste type staat bekend als *multiple wavelet* fibrillatie en wordt gekarakteriseerd door de aanwezigheid van meerdere langdurige zelf organiserende spiralen. Dit type fibrillatie kan ontstaan door de aanwezigheid van weefselheterogeniteit of door dynamische instabiliteit in het elektrische systeem. Het tweede type staat bekend als *mother rotor* fibrillatie. Hierbij wordt fibrillatie gedreven door de aanwezigheid van een dominante snelle spiraal. Deze snelle spiraal (de “moeder rotor”) is zo snel dat het omliggende weefsel de snelheid van deze spiraal niet altijd kan volgen. Hierdoor breekt op deze plaatsen het golffront van de moeder rotor op in kleinere fragmenten, met als gevolg dat er complexe onregelmatige golfpatronen ontstaan. Lokale verschillen in actiepotentiaal eigenschappen en de snelheid van de moeder rotor spelen hierbij een belangrijke rol.

Hoewel de complexe golfpatronen die optreden tijdens multiple wavelet en mother rotor fibrillatie op elkaar lijken, zijn er ook belangrijke verschillen tussen deze twee typen te vinden. Zo wordt aangenomen dat mother rotor fibrillatie stopt als de snelle spiraal niet meer aanwezig is. Dit geldt niet voor multiple wavelet fibrillatie.

Naast weefselheterogeniteit speelt mechano-elektrische terugkoppeling ook een belangrijke rol in het ontstaan van hartritmestoornissen. Mechano-elektrische terugkoppeling kan ervoor kan zorgen dat het elektrische geleidingssysteem van het hart verstoord wordt en als gevolg hiervan kan een golf opbreken in spiralen.

Een van de meeste bekende voorbeelden hiervan is Commotio Cordis, waarbij een plotselinge impact van een klein object op de borst een hartritmestoornis kan veroorzaken. Het is aangetoond dat het ontstaan van deze hartritmestoornis gereguleerd wordt door de vervorming van het hart en de activatie van de zogenaamde stretch-geactiveerde kanalen. Verder beïnvloedt mechano-elektrische terugkoppeling ook de onderliggende organisatie van VF.

Door numerieke wiskundige modellen te gebruiken kunnen we meer inzicht krijgen in de onderliggende mechanismen die plaatsvinden tijdens ventrikelfibrilleren.

Dit Proefschrift

In dit proefschrift zijn we met name geïnteresseerd in het effect van mechano-elektrische terugkoppeling en weefselheterogeniteit op de organisatie van ventrikelfibrilleren (VF). In het eerste deel van dit proefschrift, bestaande uit **hoofdstukken 2-5**, bestuderen we de basis mechanismen van mechano-elektrische terugkoppeling in twee-dimensionale weefsels, waarbij we gebruik maken van simpele wiskundige modellen die het elektrische gedrag van het hartweefsel beschrijven. In het tweede gedeelte van dit proefschrift, bestaande uit **hoofdstukken 6-8**, maken we gebruik van drie-dimensionale anatomische modellen die de kamers van het menselijk hart beschrijven en onderzoeken we wat de effecten zijn van weefselheterogeniteit en mechano-elektrische terugkoppeling op de organisatie van VF.

Deel I

In **hoofdstuk 2** geven we een algemeen overzicht van mechano-elektrische terugkoppeling in twee-dimensionale weefsels. We geven een algemene beschrijving van hoe mechano-elektrische terugkoppeling gemodelleerd kan worden. De meest basale effecten van mechano-elektrische terugkoppeling zijn:

- Veranderingen van actiepotentiaal eigenschappen door de stretch-geactiveerde kanalen. Denk hierbij o.a. aan een verandering van de vorm en de duur van de actiepotentiaal.
- Het genereren van spontane actiepotentialen via de activatie van de stretch-geactiveerde kanalen, ook wel *automatische pacemakers* genoemd. (**hoofdstukken 3** en **4**)
- Het verplaatsen van spiraal golven door het periodiek samentrekken van het weefsel (**hoofdstuk 5**).
- Het opbreken van een spiraal in meerdere kleinere spiralen door de activatie van de stretch-geactiveerde kanalen (**hoofdstukken 5** and **8**).

In **hoofdstuk 3** en **4** onderzoeken we de invloed van mechano-elektrische terugkoppeling op het ontstaan van spontane actiepotentialen, en bestuderen we

de organisatie en de eigenschappen van deze automatische pacemakers. Het ontstaan van spontane actiepotentialen is als volgt. Doordat het weefsel initieel in het midden gestimuleerd wordt, trekt het weefsel hier samen en daardoor zal het weefsel aan de rand uitrekken. Als de actiepotentiaal verplaatst in het weefsel, verplaatsen ook de gebieden van samentrekken en uitrekken. Als de actiepotentiaal de rand bereikt, zal de rand samentrekken en zal het weefsel in het midden uitrekken. Als er voldoende rek in het midden is zullen de stretch-geactiveerde kanalen een stroompje genereren en zal er een nieuwe actiepotentiaal ontstaan. Het ontstaan van deze spontane actiepotentialen is autonoom en herhaalt zich met een bepaalde frequentie.

Naast de sinusknoop bevat het hart ook verschillende andere celtypes die zelf-oscillerend gedrag tonen in de afwezigheid van rek. Gegeven de verscheidenheid aan eigenschappen van hartcellen en het feit dat stretch-geactiveerde kanalen een nieuwe actiepotentiaal kunnen genereren, is het aannemelijk dat automatische pacemakers kunnen ontstaan voor celtypes die van nature zelf-oscillerende eigenschappen hebben.

Naast automatische pacemakers kan mechano-elektrische terugkoppeling ook zorgen voor het verplaatsen en opbreken van spiraal golven. Dit hebben we onderzocht in **hoofdstuk 5**. In het weefsel is een elektrische spiraal golf aanwezig die met een bepaalde frequentie roteert en golven uitzendt. Deze elektrische spiraal zorgt ervoor dat het weefsel met dezelfde frequentie zal vervormen. Door de mechano-elektrische terugkoppeling zal deze periodieke vervorming zorgen voor kleine veranderingen in de elektrische eigenschappen van het weefsel. Als gevolg hiervan zal de spiraal langzaam verplaatsen.

Mechano-elektrische terugkoppeling kan ook leiden to het opbreken van een enkele spiraal golf in meerdere kleine spiralen (fibrillatie) en dit biedt dan ook een nieuw mechanisme voor het ontstaan van hartritmestoornissen. Doordat het weefsel periodiek vervormt zullen in sommige gebieden de stretch-geactiveerde kanalen geactiveerd worden die vervolgens een klein elektrisch stroompje genereren. Dit stroompje is echter te klein om een automatische pacemaker te generen, maar is groot genoeg om de lokale elektrische eigenschappen zodanig te veranderen dat er geen nieuwe actiepotentiaal gegenereerd kan worden. Doordat er tijdelijk geen nieuwe actiepotentiaal gegenereerd kan worden op deze specifieke locatie kan het golffront niet verder verplaatsen en zal de spiraal opbreken in meerdere kleinere spiralen.

Deel II

In **hoofdstuk 6** bestuderen we de organisatie van ventrikelfibrilleren (VF) door gebruik te maken van een anatomisch gedetailleerde wiskundige beschrijving van de menselijke kamers (geometrie) dat heterogene weefseleigenschappen bevat. We gebruiken hiervoor een (in onze groep recent ontwikkeld) actiepotentiaal model dat het exciteerbare gedrag van menselijke kamer cellen beschrijft en combineren dit met een anatomisch gedetailleerde geometrie van de menselijke kamers. Echter, in dit model heeft iedere cel in de kamers dezelfde elektrische eigenschappen.

In werkelijkheid bevat het menselijk hart een diversiteit aan weefselheterogeniteit en hebben cellen verschillende elektrische eigenschappen. Hierdoor ontstaan er verschillen in de vorm en duur van de actiepotentiaal. Bepaalde hartziekten kunnen de aanwezige heterogeniteit versterken. In dit onderzoek zijn we met name geïnteresseerd wat de effecten van heterogene elektrische eigenschappen zijn op de organisatie van VF.

We hebben ons bovenstaande (homogene) model uitgebreid met unieke heterogene elektrische weefseleigenschappen. Een groep uit Engeland (in samenwerking met een groep uit Nieuw-Zeeland) heeft heterogene elektrische eigenschappen gemeten van het menselijk hart tijdens open-hart operaties. Door tijdens de operatie een sok met 256 elektroden over het hart heen te trekken, was het mogelijk om lokale elektrische eigenschappen van de kamers te meten. Deze data werd beschikbaar gesteld voor ons onderzoek.

Als eerste stap hebben we ons menselijke model uitgebreid door deze 256 data punten te plaatsen op de juiste posities in ons anatomische model van de kamers. Als tweede stap hebben we deze 256 eigenschappen uitgebreid naar alle 13.5 miljoen hartpunten in ons model. Deze waarden zijn vervolgens gekoppeld aan het wiskundige model dat de actiepotentiaal berekend voor menselijke kamercellen. Door verschillende parameters te gebruiken voor (lokaal) verschillende elektrische eigenschappen wordt in elk punt een unieke actiepotentiaal berekend. Hierdoor ontstaan er onderliggende verschillen in de duur en vorm van de actiepotentiaal.

Voor de standaard parameter setting, die een actiepotentiaal in een gezonde hartcel beschrijft, zien we dat een kunstmatig geïnduceerde spiraal stabiel blijft. Echter, voor andere parameter settings zien we dat een enkele spiraal opbreekt in meerdere kleinere spiralen. De elektrische eigenschappen gevonden in de patiënten verschillen onderling en beschrijven parameter settings die stabiele en onstabiele spiralen ondersteunen.

We hebben gevonden dat aanwezigheid van deze weefselheterogeniteit niet alleen verantwoordelijk is voor het opbreken van spiralen, maar ook bepaalt hoeveel spiralen er tegelijkertijd ondersteund worden in het weefsel. Als de kamers veel gebieden bevatten die langzamer herstellen, en dus minder snel klaar zijn om het volgende signaal te geleiden, dan zien we dat er meer spiralen ondersteund kunnen worden en dat de organisatie van VF complexer wordt. Verder laten we zien dat het ECG en het frequentiespectrum van deze simulaties overeenkomen met die van patiënten met ventrikelfibrilleren.

In **hoofdstuk 7** vervolgen we onze studie van de organisatie van VF door gebruik te maken van ons heterogene model van de menselijke kamers. Voor deze studie hebben we gebruik gemaakt van specifieke patiënt data: de linker kamer heeft een parameter setting die een stabiele spiraal ondersteunt, en de rechter kamer heeft een setting waarvoor een spiraal opbreekt. We hebben gevonden dat als we de kunstmatig geïnduceerde spiraal opstarten in verschillende gebieden van de kamers dit verschillende typen van VF geeft.

Als we de spiraal opstarten in de linker kamer zien we dat deze spiraal stabiel blijft tijdens de hele simulatie. De golven die deze spiraal uitzendt komen terecht in de rechter kamer en doordat daar andere elektrische eigenschappen zijn breekt

deze golf op in kleine golven. Dit komt overeen met *mother rotor* fibrillatie. Deze fibrillatie wordt dan ook gedreven door de aanwezig van de snelle stabiele spiraal in de linker kamer. Om aan te tonen dat dit inderdaad het geval was, hebben we tijdens de simulatie een stuk van de linker kamer verwijderd zodat de moeder spiraal afgeknipt wordt. We hebben gevonden dat zodra de moeder spiraal niet meer aanwezig is in het weefsel de fibrillatie en het opbreken van golven in de rechter kamer ook stopt. De organisatie van dit type van fibrillatie wordt onder andere bepaald door de snelheid van de moeder spiraal en de onderliggende weefselheterogeniteit.

Als we de spiraal opstarten in de rechter kamer, zien we dat deze spiraal meteen aan het begin van de simulatie opbreekt in kleinere spiralen en dat deze spiralen voldoende tijd hebben om hun rotatie te voltooien. Door de elektrische eigenschappen van het weefsel worden er voortdurend spiralen gecreëerd en afgebroken. Dit resulteert in chaotische golfpatronen en dit type van fibrillatie komt dan ook overeen met *multiple wavelet* fibrillatie. We hebben gevonden dat zodra we een gedeelte afknippen van de kamers dit type van fibrillatie niet stopt en dat de spiralen die nog aanwezig zijn blijven fragmenteren om nieuwe spiralen te creëren. De organisatie van dit type van fibrillatie wordt niet zozeer bepaald door de onderliggende weefselheterogeniteit, maar meer door de onderliggende interacties van spiralen.

We hebben vervolgens de verschillen in onderliggende eigenschappen van deze twee typen van fibrillatie geanalyseerd. We hebben gevonden dat de ECG signalen van zowel de mother rotor als de multiple wavelet VF simulatie vergelijkbaar zijn met klinisch geobserveerde ECG signalen. De golfpatronen die we tijdens de mother rotor simulatie gevonden hebben zijn echter minder complex vergeleken met de patronen die we gevonden hebben voor de multiple wavelet simulatie. Tijdens de mother rotor simulatie zien we dat de nieuwe spiralen die ontstaan een korte levensduur hebben, terwijl er in de multiple wavelet simulatie meerdere spiralen gevonden zijn die een langere levensduur hebben. Bovendien zien we dat er tijdens de multiple wavelet simulatie veel meer spiralen zijn dan in de mother rotor simulatie.

In **hoofdstuk 8** hebben de we organisatie van VF in een anatomisch model van de linker kamer en het effect van mechano-elektrische terugkoppeling onderzocht. Ons doel was om een zo realistisch mogelijk model te gebruiken dat ook vervormingen van de kamer ondersteunt. Hiervoor hebben we ons anatomisch model van de linker kamer gekoppeld met een mechanisch gedetailleerd model dat ook kan vervormen. Hierdoor is het mogelijk om de effecten van elektrische golven op vervormingen te onderzoeken, en de effecten van vervorming op de golfdynamica en organisatie van VF. We hebben dit nieuwe model gevalideerd door een normale hartslag te simuleren en de resultaten te vergelijkingen met data uit de literatuur.

We hebben gevonden dat, als we een initiële kunstmatig opgewekte stabiele spiraal simuleren, de linker kamer voortdurend samengetrokken is en nauwelijks kan ontspannen. Ondanks dat zijn er ook gebieden te vinden waar het weefsel uitrekt. Deze gebieden verplaatsen zich met dezelfde periode als die van de spiraal

en bevinden zich vaak voor het golffront. Deze gebieden zijn echter niet te vinden dichtbij de kern van de spiraal. Zodra we de mechano-elektrische terugkoppeling activeren via de stretch-geactiveerde kanalen, zien we dat een deel van deze spiraal in kleinere spiralen fragmenteert en ontstaat er fibrillatie. De oorzaken van het fragmenteren van deze spiraal zijn hetzelfde als boven beschreven in **hoofdstuk 5**. Verder zien we dat tijdens ventrikelfibrilleren ook de linker kamer voortdurend samengetrokken is en niet kan ontspannen.

We zien dat er meer spiralen ontstaan en dat de organisatie van VF complexer wordt als de terugkoppeling van de stretch-geactiveerde kanalen sterker aanwezig is. Verder zien we dat dit mechanisme van ventrikelfibrilleren lijkt op dat van mother rotor fibrillatie. Omdat het weefsel dichtbij de kern van de initiële spiraal altijd samengetrokken is, worden de stretch-geactiveerde kanalen in dit gebied nooit actief. Hierdoor zal de initiële spiraal dichtbij de kern nooit opbreken in kleinere spiralen. Echter de golven die deze spiraal uitzendt naar verderop gelegen gebieden komen terecht in gebieden waar cellen wel uitrekken, met als gevolg dat hier de actiepotentiaal geblokkeerd wordt en opbreekt in kleinere spiralen. Het mechanisme van het ontstaan van deze nieuwe spiralen is dus anders dan bij mother rotor fibrillatie.

Conclusie

In dit proefschrift hebben we onderzoek gedaan naar mechanismen van ventrikelfibrilleren, waarbij we ons gericht hebben op de rol van mechano-elektrische terugkoppeling en weefselheterogeniteit. Aan de hand van de analyses van weefselheterogeniteit concluderen we dat heterogene elektrische eigenschappen niet alleen belangrijk zijn voor het opbreken van spiralen, maar ook de onderliggende organisatie van fibrillatie beïnvloedt. Verder hebben we laten zien dat als we een kunstmatig geïnduceerde spiraal op verschillende lokaties opstarten in hetzelfde heterogene model, dit kan leiden tot zowel mother rotor als multiple wavelet fibrillatie. De belangrijkste conclusies wat betreft mechano-elektrische terugkoppeling zijn dat lokale vervormingen kunnen leiden tot het ontstaan van pacemakers via de activatie van de stretch-geactiveerde kanalen en dat lokale rek ervoor kan zorgen dat een anders stabiele spiraal fragmenteert. Deze modellen zijn een eerste studie naar het effect van mechano-elektrische terugkoppeling, en hebben nieuwe inzichten opgeleverd over het ontstaan en de organisatie van ventrikelfibrilleren. Het verder ontwikkelen van deze modellen is belangrijk om de effecten van mechano-elektrische terugkoppeling tijdens hartritmestoornissen in meer detail te kunnen quantificeren.

Color Plates

Color plates from Chapter 2

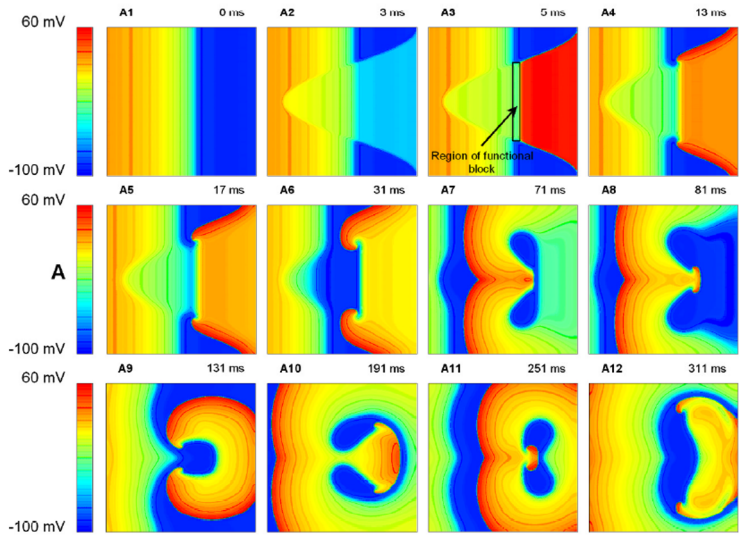

Figure 2.8 on page 30. Initiation of spiral waves after mechanical impact. Reprinted with permission from [38].

Color plates from Chapter 6

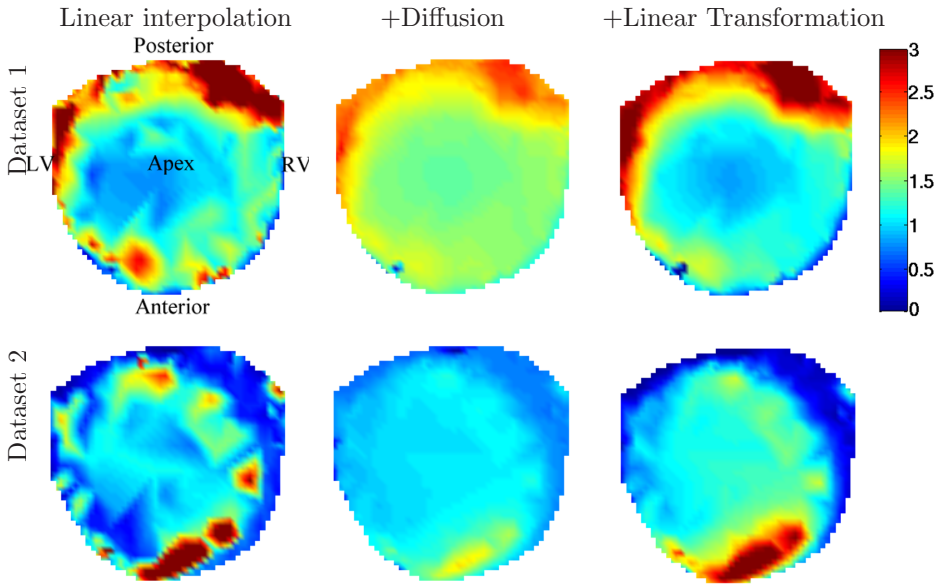

Figure 6.1 on page 84. Distribution of epicardial restitution, S_{max} shown on the polar projection, with the epicardial apex at the center of each plot and the ventricular base at the outer circumference.

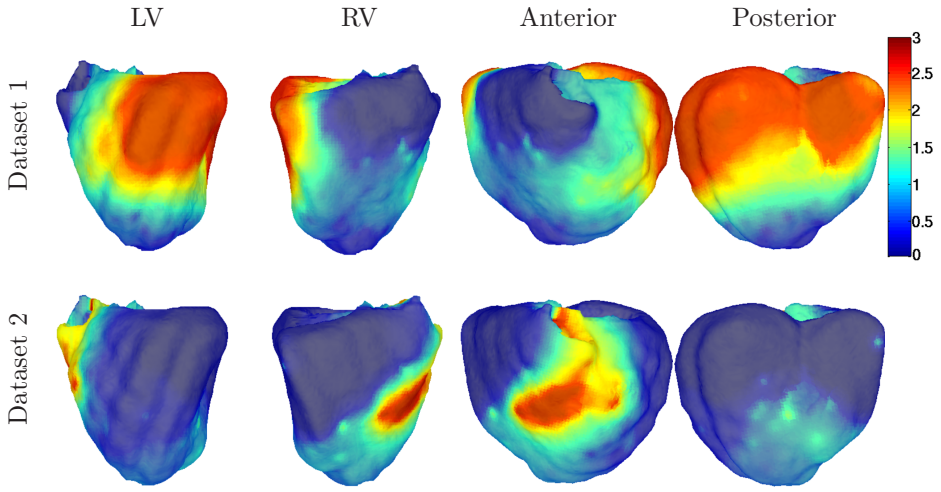

Figure 6.3 on page 85. 3D plots of restitution S_{max}. (Top) Dataset 1. (Bottom) Dataset 2. From left to right: LV, RV, anterior and posterior views.

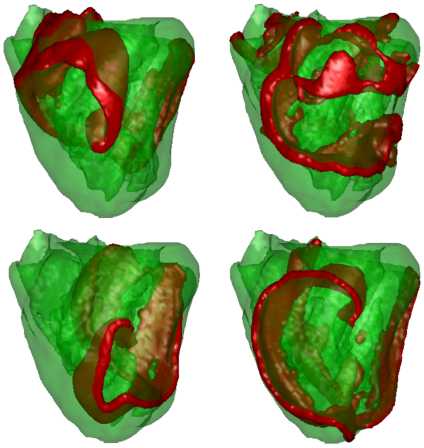

Figure 6.6 on page 89. Wavefronts in red. (Top) Dataset 1. (Bottom) Dataset 2. The first snapshot shows the spiral after initiation on the left ventricular free wall and the second snapshot shows wavefronts after 5 seconds of simulation time.

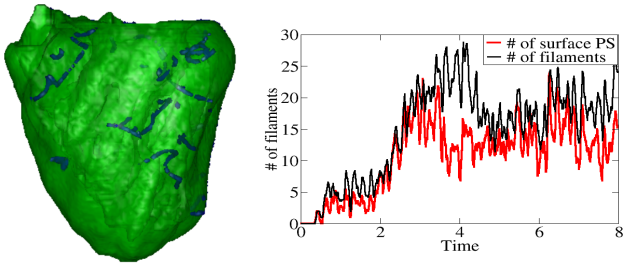

Figure 6.8 on page 90. Filaments of dataset 1. (A) Snapshot after 5 seconds of simulation time. (B) Number of PSs (red) and filaments (black) over time.

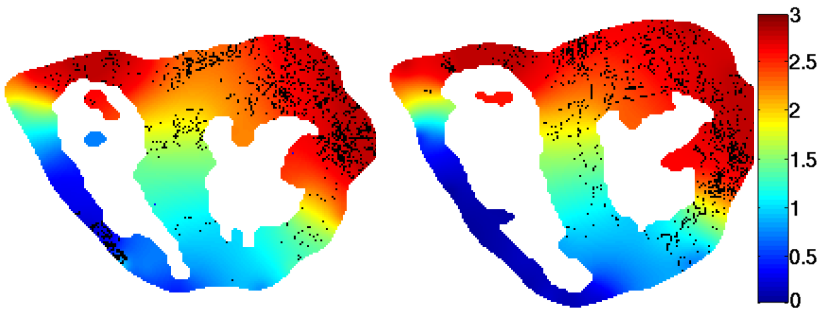

Figure 6.11 on page 93. Location of filament voxels (black) for the entire 8 seconds run. Maximum restitution slopes are represented using a pseudo-color spectrum.

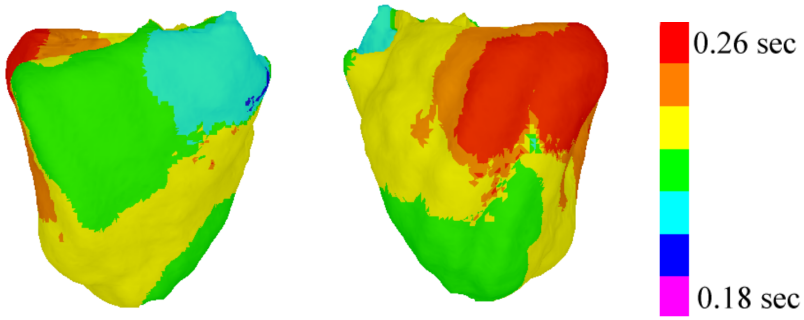

Figure 6.12 on page 94. Average excitation periods for $\varepsilon = 1$ in a time interval between 2-4 seconds of simulation time. LV (left) and RV (right) views are shown.

Color plates from Chapter 7

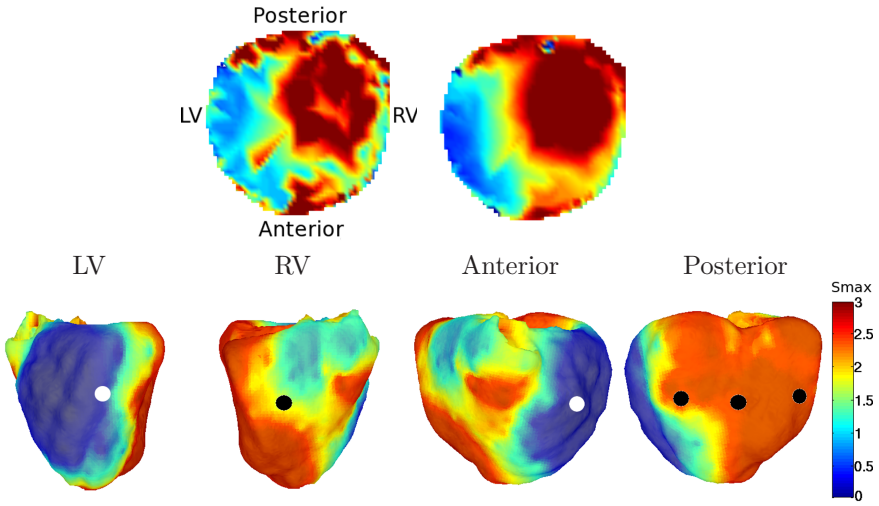

Figure 7.1 on page 103. Polar and 3D plots of maximum restitution slope values S_{max}. (Top) Distribution of epicardial restitution, S_{max} shown on polar projections, with the epicardial apex at the center of each plot and the ventricular base at the outer circumference. (Top left) 243 *experimental* S_{max} values interpolated across the polar plot using MATLAB's griddata. (Top right) *model* S_{max} values after the diffusion based algorithm. (Bottom) *model* 3D plots of maximum restitution curves S_{max}. From left to right: LV, RV, anterior and posterior views. The circles denote the positions of initial wave breaks leading to the formation of the first spiral wave. Black circles indicate positions of the first wavebreak that lead to multiple wavelet VF dynamics, whereas white circles indicate positions of first wavebreak that lead to mother rotor fibrillation type dynamics. Maximum restitution slope values range from 0.5 (blue) to 3 (red).

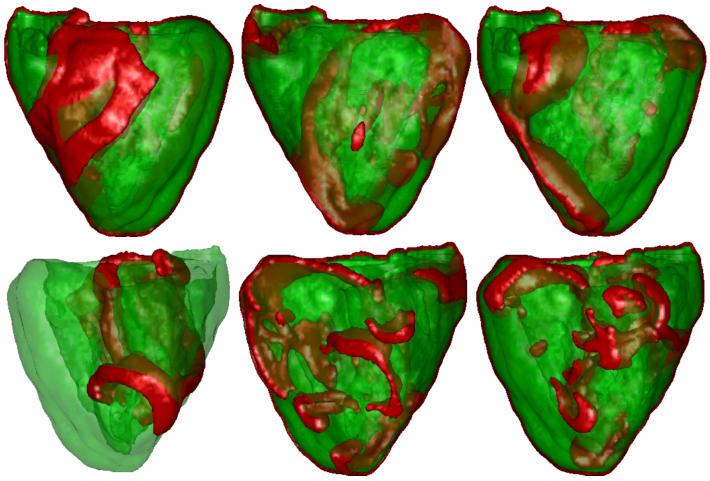

Figure 7.2 on page 106. Multiple wavelet VF. Wavefronts are shown in red. (Top) LV view. (Bottom) RV view. (First column) Location of the initial spiral. (Second column) After 5 seconds. (Third column) After 7 seconds.

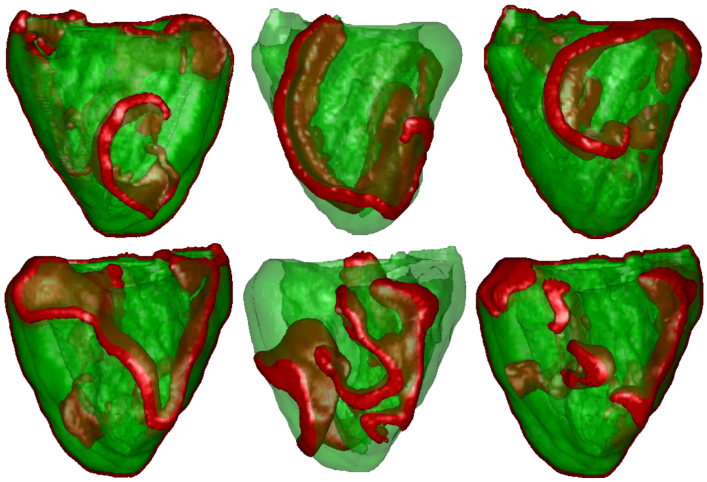

Figure 7.3 on page 107. Mother rotor fibrillation. Wavefronts are shown in red. (Top) LV view. (Bottom) RV view. (First column) Location of the initial spiral. (Second column) After 3.5 seconds. (Third column) After 10 seconds. Note the stable spiral in the LV free wall, while breaks occurred in the RV free wall.

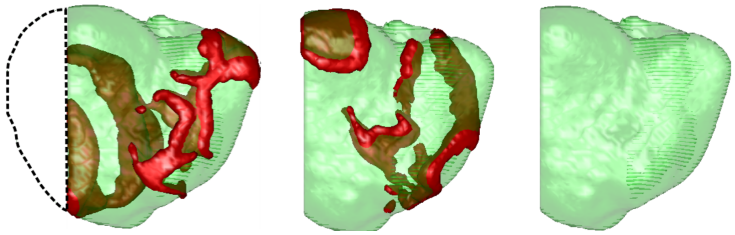

Figure 7.4 on page 108. Ablation of the mother rotor spiral in the LV (posterior view). The black dashed line denotes the part of the ventricles that was removed. The first snapshot is at approximately 3 seconds of simulation time (i.e., the time when part of the LV was removed), the second snapshot at 3.3 seconds and the third snapshot is at 3.5 seconds.

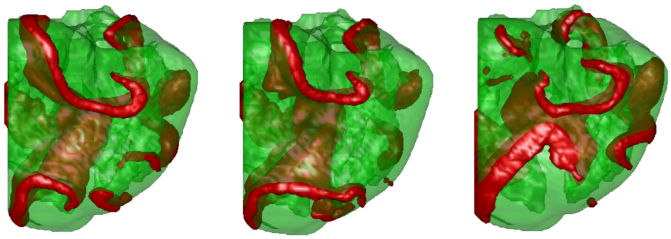

Figure 7.5 on page 108. Ablation of the LV (posterior view) during multiple wavelet VF. The first snapshot is at approximately 3 seconds of simulation time (i.e., the time when part of the LV was removed), the second snapshot at 3.5 seconds and the third snapshot is at 4.0 seconds.

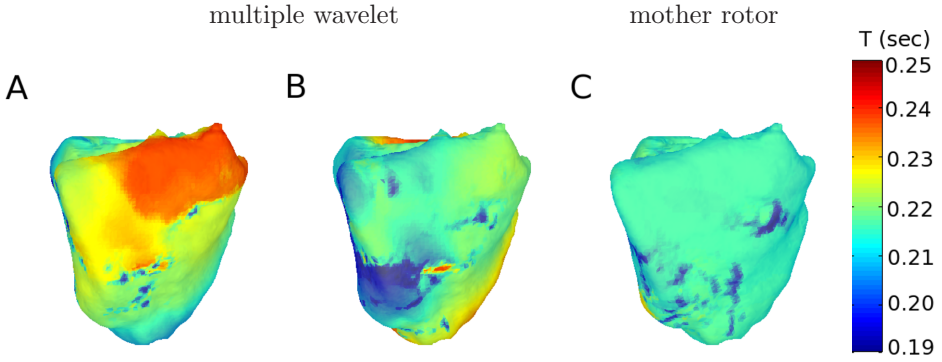

Figure 7.7 on page 110. Spatial distribution of mean period values. (A) and (B) Multiple wavelet simulation, period distribution shown between 2-4 and 4-6 seconds. (C) Mother rotor simulation, period distribution shown between 2-4 seconds. Similar pattern occurs for the time interval between 4-6 seconds. Right ventricular free wall is shown. Period values range from 0.19 s (blue) to 0.25 s (red).

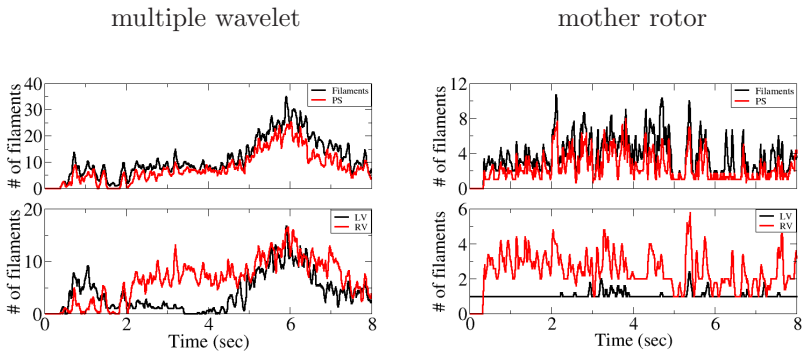

Figure 7.8 on page 111. Total number of filaments and epicardial PSs. (Left) Multiple wavelet VF. (Right) Mother rotor fibrillation. (Top) Total number of filaments and epicardial PSs. (Bottom) Number of filaments in the LV and RV are shown (filaments in the septum not included).

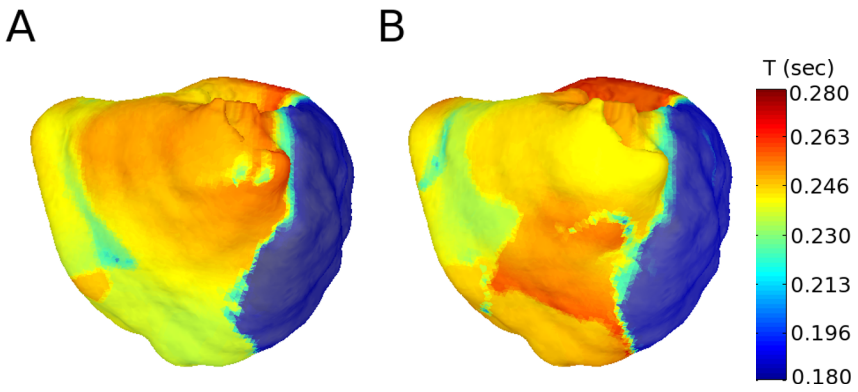

Figure 7.11 on page 115. Spatial period distribution for the simulation with I_{CaL} times 0.25. (A) 2-4 seconds, (B) 4-6 seconds. The mother rotor was located in the dark blue region. Period values range from 0.18 s (blue) to 0.28 s (red).

Color plates from Chapter 8

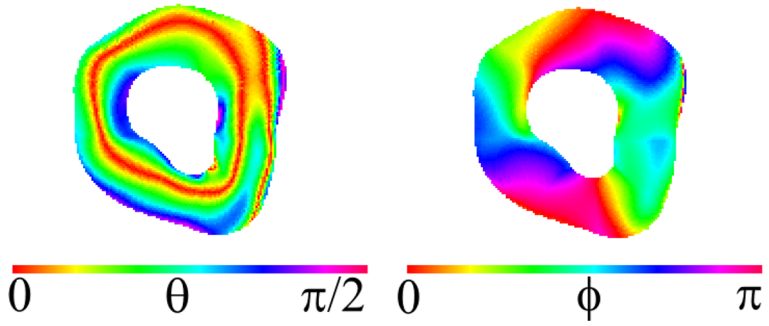

Figure 8.5 on page 134. Short-axis view of fiber direction at approximately 50% base-apex. (Left) Elevation angle (i.e., the angle the fiber makes with the cross sectional plane). (Right) Azimuth angle (i.e., the angle the fiber makes with the x-axis). The septum is located on the right, and the anterior and the posterior LV free wall are located on the top and bottom side, respectively.

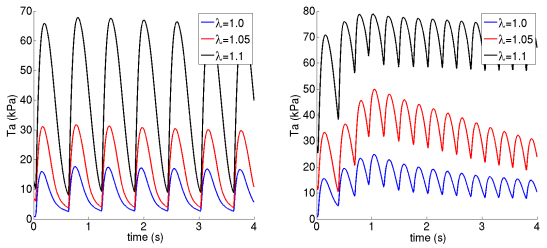

Figure 8.7 on page 138. Validation of active tension traces in the NHS model. (Left) Normal heart beat. (Right) Stable spiral.

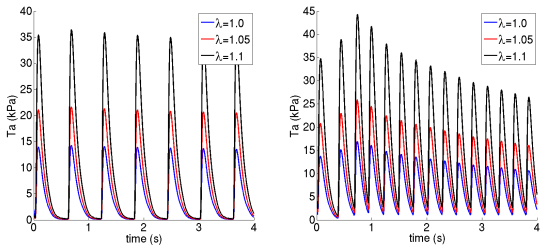

Figure 8.8 on page 139. Modified NHS model with $\alpha_{r2} = 12s^{-1}$ and $T_{ref} = 100$ kPa. (Left) Normal heart beat. (Right) stable spiral.

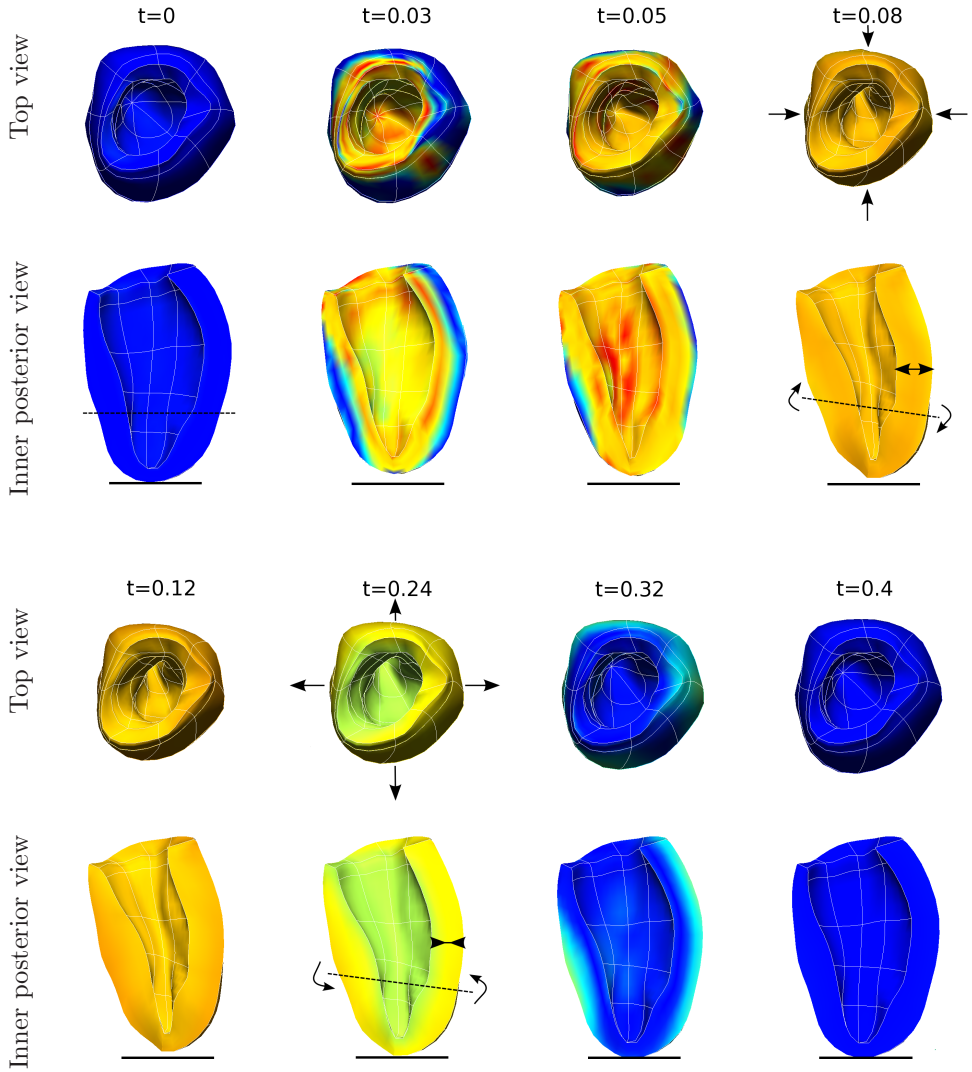

Figure 8.10 on page 142. Mechanical deformation during a normal heart beat. Top view and inner posterior wall shown. The septum is located to the left. Snapshots are taken at time 0, 0.03, 0.05, 0.08, 0.12, 0.24, 0.32 and 0.40 seconds. Colors represent the membrane potential (blue=-80mV, red=+20mV). The solid black line denotes the initial position of the apex. The dashed line denotes the orientation of the wall segment. Arrows denote changes of the wall segment/orientations.

Cardiac Strains

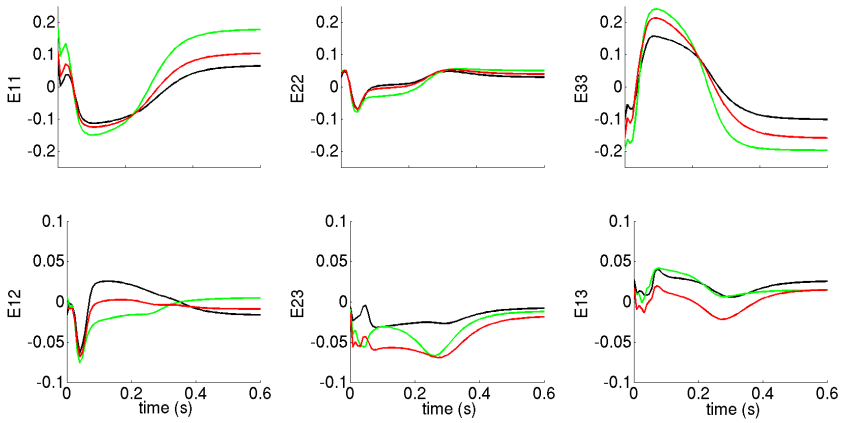

Fiber-Sheet Strains

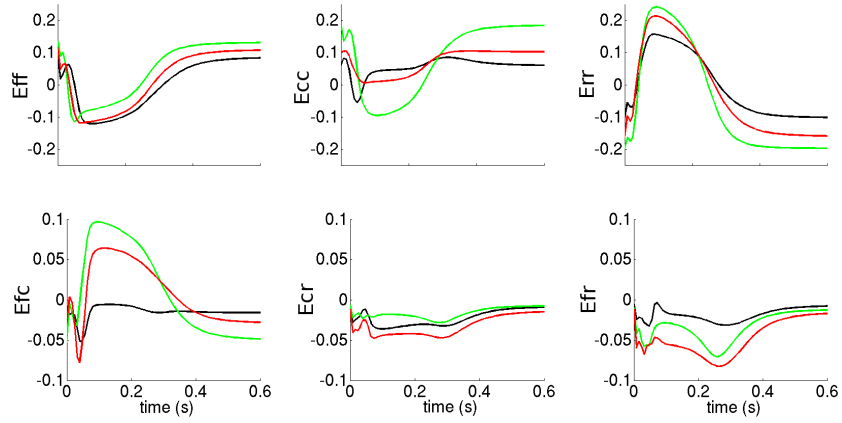

Figure 8.11 on page 144. Mean cardiac (top) and fiber strains (bottom) measured on the anterior wall of the LV during a normal heart beat simulation. Subepicardium (black), midwall (red), and subendocardium (green) mean strains shown. Note the different scales for shear and normal strains.

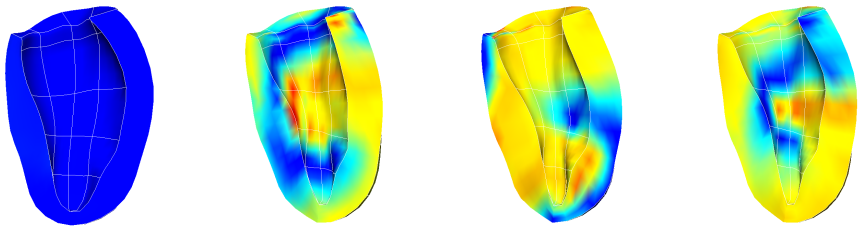

Figure 8.14 on page 147. Mechanical deformation during a stable spiral. Inner posterior wall shown. The septum is located to the left. Snapshots are taken at time 0, 3.2, 3.3 and 3.4 seconds. Colors represent the membrane potential (blue=-80mV, red=+20mV).

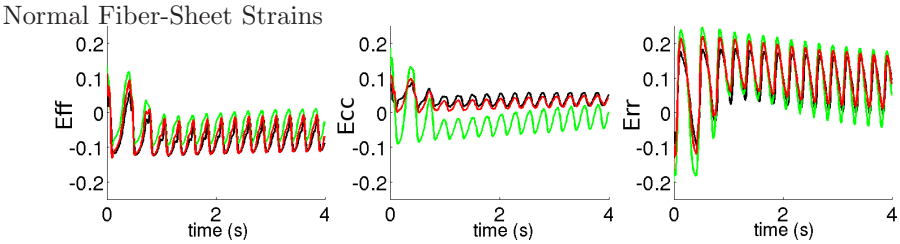

Figure 8.15 on page 147. Normal fiber strains measured on the anterior wall of the LV during a stable spiral simulation. Subepicardium (black), midwall (red), and subendocardium (green) mean strains shown.

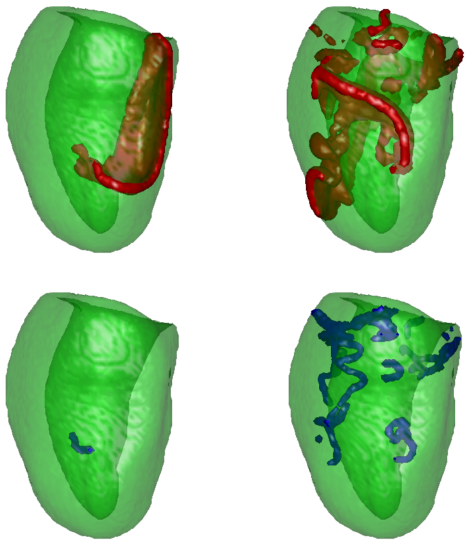

Figure 8.17 on page 150. 3D Wavefronts (top) and filaments (bottom) found during mechanically induced breakup. $G_s = 75\ \mu S/\mu F$. Left: after the initialization of the spiral ($t = 0.6$ seconds). Right: at the end of the simulation ($t = 8.0$ seconds). Posterior view shown. The septum is located to the right.

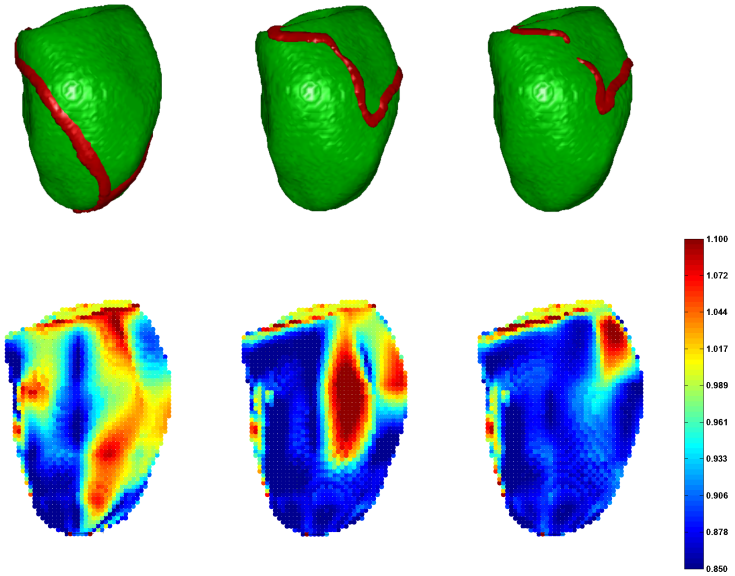

Figure 8.19 on page 151. Mechanisms of breakup via stretch. $G_s = 75\ \mu S/\mu F$. In regions with stretch (i.e., $\lambda > 1$) the stretch activated current is present. (Top) Wavefronts shown on the epicardial surface at 2.1, 2.18 and 2.2 seconds (from left to right). (Bottom) Extension ratio λ. Anterior view shown with the septum located to the left.

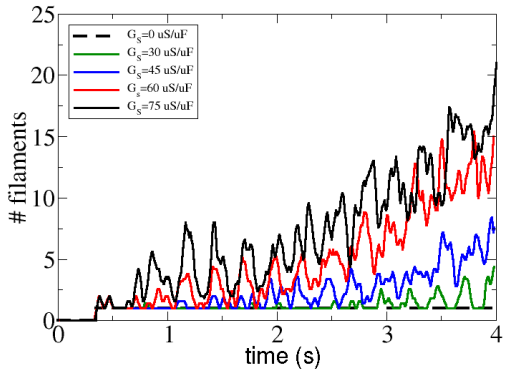

Figure 8.20 on page 151. Number of filaments over time for $G_s = 0$, $G_s = 30$, 45, 60 and 75 $\mu S/\mu F$.

Curriculum Vitae

De auteur van dit proefschrift, Rik Hubert Keldermann, werd op 9 april 1980 geboren in Heerlen. Vanaf 1992 was hij leerling op het Sintermeertencollege te Heerlen, waar hij in 1998 zijn VWO diploma behaalde. In hetzelfde jaar begon hij met de studie Biomedische Technologie aan de Universiteit van Eindhoven en in 1999 behaalde hij daar zijn propedeuse. In 2001 koos hij als specialisatie voor de richting BioModeling and BioInformatics in de groep van Prof. dr. P.A.J. Hilbers. In deze groep studeerde hij in 2004 af bij Dr. N. Kuijpers met een scriptie getiteld "Computer Simulations of Electrophysiology in Pathological Atrial Tissue". Na zijn studie kwam hij terecht bij de vakgroep Theoretische Biologie / Bioinformatica van Prof. Dr. P. Hogeweg aan de Universiteit Utrecht. Vanaf 2005 was hij werkzaam als assistent in opleiding (AIO) bij deze vakgroep, begeleid door Dr. A.V. Panfilov en Prof. dr. P. Hogeweg. De resultaten van dit onderzoek staan beschreven in dit proefschrift.

The author of this thesis, Rik Hubert Keldermann was born on April 9, 1980 te Heerlen, The Netherlands. In 1992 he attended the Sintermeertencollege te Heerlen where he gained his VWO diploma in 1998. In the same year he started his studies in Biomedical Engineering at the University of Eindhoven and he obtained his propedeuse in 1999. In 2001 he decided to join the group of Prof. dr. P.A.J. Hilbers and specialized in BioModeling and BioInformatics. In this group he obtained his Master's degree in 2004 under the supervision of Dr. N. Kuijpers with a thesis titled "Computer Simulations of Electrophysiology in Pathological Atrial Tissue". After his graduation, he joined the Theoretical Biology / Bioinformatics group of Prof. dr. P. Hogeweg at the Utrecht University. In 2005 he started his doctoral research in this group, supervised by Dr. A.V. Panfilov and Prof. dr. P. Hogeweg. The results of this research are described in this thesis.

List of Publications

Peer-Review Journal Publications

Kuijpers, N.H.L., Keldermann, R.H., Arts, T., Hilbers, P. Computer simulations of successful defibrillation in decoupled and non-uniform cardiac tissue. *Europace* 2: 166-177 (2005).

Panfilov, A.V., Keldermann, R.H., Nash, M.P. Self-organized pacemakers in a coupled reaction-diffusion-mechanics system. *Phys. Rev. Lett.* 95: 258104 (2005).

Kuijpers, N.H.L., Keldermann, R.H., Ten Eikelder, H.M.M., Arts, T., Hilbers, P. The role of the hyperpolarization-activated current I_f in arrhythmogenesis: a computer model study. *IEEE Trans. Biomed. Eng.* 53: 1499-1511 (2006)

Keldermann, R.H., Nash, M.P., Panfilov, A.V. Pacemakers in a reaction diffusion mechanics system. *J. Stat. Phys.* 128: 375-392 (2007).

Panfilov, A.V., Keldermann, R.H., Nash, M.P. Drift and breakup of spiral waves in reaction-diffusion-mechanics-system. *Proc. Natl. Acad. Sci. U.S.A.* 104: 7922-7926 (2007).

Keldermann, R.H., Ten Tusscher, K.H.W.J., Nash, M.P., Hren, R., Taggart, P., Panfilov, A.V. Effect of heterogeneous APD restitution on VF organization in a model of the human ventricles. *Am. J. Physiol. Heart Circ. Physiol.* 294: H764-H774 (2008).

Keldermann, R.H., Nash, M.P., Panfilov, A.V. Modeling cardiac mechano-electrical feedback using reaction-diffusion-mechanics systems. *Physica D.* Accepted for publication (2008). DOI:10.1016/j.physd.2008.08.017

Keldermann, R.H., Ten Tusscher, K.H.W.J., Nash, M.P., Bradley, C.P., Hren, R., Taggart, P., Panfilov, A.V. A computational study of mother rotor VF in the human ventricles. *Am. J. Physiol. Heart Circ. Physiol.* 296: H370-H379 (2009).

Keldermann, R.H., Nash, M.P., Gelderblom, H., Panfilov, A.V. An electro-mechanical model of the human left ventricle and its application to study mechanisms of cardiac arrhythmias. *In preparation* (2009).

Peer-Review Conference Proceedings

Keldermann, R.H., Kuijpers, N.H.L., Hilbers, P.A.J. Computer simulations of the initiation of atrial fibrillation. *Europace* 6: 137P/7 (2004).

Nash, M.P., Keldermann, R.H., Panfilov, A.V. Re-entrant waves in contracting excitable ventricular tissue to study mechano-electric feedback and arrhythmias. *FASEB J.* 19: A.554 (2005).

Keldermann, R.H., Ten Tusscher, K.H.W.J., Hren, R., Panfilov, A.V. Re-entrant arrhythmias in a heterogeneous model of the human ventricles. *Heart Rhythm* 3: S185 (2006).

Keldermann, R.H., Ten Tusscher, K.H.W.J., Hren, R., Panfilov, A.V. Mother rotor fibrillation in a heterogeneous anatomically based model of the human ventricles. *Heart Rhythm* 4: S160 (2007).

Dankwoord

Wat is de tijd toch snel voorbij gegaan! Ik heb met veel plezier gewerkt aan het onderzoek dat beschreven staat in dit proefschrift. Ondanks dat, was het niet altijd even makkelijk als dat het van de buitenkant leek en heb ik toch ook moeilijke momenten gehad. Op deze plek wil ik graag iedereen bedanken die een bijdrage heeft geleverd aan het tot stand komen van dit proefschrift. Allereerst wil ik graag mijn directe begeleider en co-promotor Sasha Panfilov bedanken. Ik heb veel van je geleerd in de aflopen jaren en ik kon altijd bij je aankloppen als ik iets wilde weten of bepaalde ideeën of resultaten had. Ik wil je graag ook bedanken voor de mogelijkheden die je me geboden hebt om mijn onderzoek een eigen draai te geven. Ik hoop dat we onze samenwerking succesvol kunnen voortzetten in de nabije toekomst. Als tweede wil ik graag mijn promotor Paulien Hogeweg bedanken. Danzij jou heb ik een andere kijk op wetenschap gekregen en jouw creatieve manier van denken inspireert mensen. Verder wil ik je ook graag bedanken dat je altijd vroeg hoe het met mij en mijn vrouw ging toen we een moeilijke tijd doormaakten op het persoonlijke vlak.

Verder wil ik Kirsten ten Tusscher bedanken. Jij stond altijd klaar voor me tijdens mijn onderzoek en ik heb veel van je geleerd. Bedankt ook voor de gezellige tripjes naar de winkel. Ik wens je veel succes in Noorwegen en ik hoop nog veel met je samen te mogen werken.

Martyn, thank you for supervising me. I will not forget keeping you awake on the other side of the world, by spamming you with many email questions. Email replies sent at 04:00 were quite normal. Get some sleep! I also want to thank you and your family for the great time during my stay in New Zealand. I hope we continue to work together in the future.

I also would like to thank Arkady Pertsov, Jacques de Bakker, Marc Vos, Ronald Wilders and Martyn Nash for being on my reading committee and finding the time and interest to read my thesis.

Verder wil ik graag Hanneke Gelderblom bedanken. Zonder jouw werk was

het niet mogelijk om een 3D mechano-elektrisch model te ontwikkelen. Bedankt ook voor het lezen en verbeteren van hoofdstuk 8. Ik zou ook graag Nico Kuijpers willen bedanken. Jij hebt er 5.5 jaar geleden voor gezorgd dat ik verslaafd ben geraakt aan dit onderwerp. Door ons onderzoek voor mijn master thesis kon ik een snelle start maken voor mijn PhD.

Ik wil mijn kamergenoten van het *Warme Zuiden* bedanken: Milan, Marian en Daniel. Ik denk dat onze versie van het zingen van *Only You* waarschijnlijk nooit op CD uitgebracht zal worden. Milan, bedankt voor het helpen met wiskundige problemen, de vele wetenschappelijke en politieke discussies die we gevoerd hebben en voor de gezellige spelavonden. Marian, bedankt voor al je persoonlijk advies, LaTeX-tips en de fijne tripjes naar de winkel. Daniel, bedankt voor de fijne tijd, de steun en het knoflooksaus recept dat je me gegeven hebt.

Daarnaast, wil ik ook de vakgroep bedanken voor de gezellige tijd. Rob, ik zal niet vergeten dat we een keer samen 4 uur lang op station Geldermalsen hebben zitten kleumen van de kou. Stan, bedankt voor alle LaTeX-tips. Jan Kees, bedankt dat mijn computer en het cluster altijd in orde waren zodat ik mijn simulaties kon draaien. Ik wil Boris bedanken voor alle discussies en het introduceren van World of Warcraft. Ik vroeg me af of je me ook kan vertellen hoe ik erweer vanaf kom. Henk-Jan, bedankt voor je steun en de gezellige gesprekken die we gehad hebben. Jos, bedankt voor het relativeren van mijn stress momenten. Daniel W., lets keep up those chess games! Ik bedank Henk-Jan, Jos en Daniel W. ook voor het lezen en verbeteren van mijn proefschrift. Verder bedank ik iedereen voor de fijne tijd, de lunchpauzes en het zetten van koffie.

Sander en René, bedankt voor het zijn van mijn paranimfen en de gezellige momenten tijdens onze LAN parties. Ik hoop dat we deze traditie nog lang blijven voortzetten. Het wordt ook weer eens tijd om uit eten te gaan in Trafalgar Pub. Marijn, bedankt voor het zijn van mijn beste vriend en dat ik altijd op je kan rekenen. We zullen elkaar nog regelmatig voorbijlopen in World of Warcraft.

Dan wil ik graag mijn vrienden en familie bedanken. In het bijzonder wil ik mijn ouders en schoonouders bedanken voor het steunen van mijn onderzoek. Loes en Nelline, ook al zijn jullie niet meer aanwezig, bedankt voor alles dat jullie ons geleerd en gegeven hebben. Ik draag dit proefschrift daarom op aan jullie. Pa en Arend, ook bedankt voor de steun, de mooie momenten en alle adviezen. Met name het uit eten gaan moeten we zeer zeker niet afschaffen! Arco bedankt voor alles, we moeten zeer zeker nog eens een keertje DragonBallZ kijken. Verder wil ik ook mijn broertje Bram bedanken voor alle steun die hij me geeft. Ik heb vaak over de telefoon mijn verhaal aan je kwijt gekund. Samen maken we zo heel wat mee en ik zal er altijd voor je zijn.

Tot slot wil ik graag mijn vrouw Ariska bedanken. Bedankt voor al je liefde, steun en voornamelijk het geduld dat je soms moest opbrengen als ik weer eens in de stress zat. We hebben samen moeilijke tijden doorgemaakt, maar ook hele mooie momenten. Met jou trouwen blijft het beste moment in mijn leven en ik ben je dankbaar voor alles dat jij me geeft om die pijnlijke periodes boven te komen. Ik hoop hetzelfde aan jou terug te kunnen geven en ik beloof je dat de zon weer zal schijnen in ons leven.